



UNIVERSITÀ  
DEGLI STUDI  
FIRENZE

DOTTORATO DI RICERCA IN  
SCIENZE CHIMICHE

CICLO XXVII

COORDINATORE Prof. Goti Andrea

**Formic Acid Homogeneous Catalytic Activation  
by Transition Metal Polydentate Phosphine Complexes  
for Hydrogen Storage and Production**

Settore Scientifico Disciplinare CHIM/03

**Dottorando**  
Dott. Mellone Irene

---

*(firma)*

**Tutore**  
Dr. Gonsalvi Luca

---

*(firma)*

**Coordinatore**  
Prof. Goti Andrea

---

*(firma)*

**Cotutore**  
Dr. Rosi Luca

---

*(firma)*

*A Marco  
per esserci sempre*

## INDEX

Frequently used abbreviations	I
X-ray crystal structures: atom colour code	II
Optimized structures: atom colour code	II
List of complexes	III
<b>Chapter 1: Introduction</b>	<b>1</b>
1.1 Overview	1
1.2 Hydrogen	2
1.2.1 Properties and industrial use of hydrogen	2
1.2.2 Methods for producing hydrogen in view of its use as energy carrier	4
1.2.3 Hydrogen storage	8
1.3 Decomposition of formic acid in the presence of heterogeneous catalysis	15
1.4 Decomposition of formic acid in the presence of homogeneous catalysis	21
1.5 Aim of the work	34
1.6 References	36
<b>Chapter 2: Formic acid dehydrogenation catalysed by ruthenium complexes bearing the tripodal ligands triphos and NP<sub>3</sub></b>	<b>41</b>
2.1. Overview	41
2.2. Introduction	42
2.3. Synthesis of Ru complexes bearing triphos and NP <sub>3</sub>	46
2.4. Catalytic formic acid (FA) dehydrogenation tests	50
2.5. VT-NMR mechanistic studies	54
2.6. DFT calculations	60
2.6.1. The Mechanism of Formic Acid Dehydrogenation Catalyzed by [Ru( $\kappa^3$ triphos)(MeCN) <sub>3</sub> ] <sup>2+</sup> ( <b>1</b> )	60
2.6.2. The mechanism of Formic Acid dehydrogenation catalyzed by [Ru( $\kappa^4$ -NP <sub>3</sub> )Cl <sub>2</sub> ] ( <b>2</b> )	68
2.7. Conclusions	78
2.8. Experimental section	79
2.8.1. General methods and materials	79
2.8.2. Synthesis of [Ru( $\kappa^3$ -triphos)(MeCN) <sub>3</sub> ](PF <sub>6</sub> ) <sub>2</sub> ( <b>1'</b> )	80
2.8.3. Reaction of [Ru( $\kappa^3$ -triphos)(MeCN) <sub>3</sub> ](PF <sub>6</sub> ) <sub>2</sub> ( <b>1'</b> ) with CO (1 atm)	80
2.8.4. Catalytic tests	81

## ***Index***

2.8.5.	Variable temperature NMR experiments	82
2.8.6.	Reactivity of [Ru( $\kappa^4$ -NP <sub>3</sub> )(H)Cl] ( <b>6</b> ) with HCO <sub>2</sub> NHEt <sub>3</sub>	82
2.8.7.	Computational methodology	83
2.9.	References	83
<b>Chapter 3: Hydrogen Storage and Release by HCOOH Dehydrogenation and NaHCO<sub>3</sub> Hydrogenation Catalyzed by Ru(II) Complexes Bearing Bulky Polydentate Phosphines</b>		<b>87</b>
3.1.	Overview	87
3.2.	Introduction	88
3.3.	Synthesis of Ru and Fe complexes bearing P <sup>2</sup> P <sub>3</sub> <sup>Cy</sup> , P <sup>3</sup> P <sub>3</sub> <sup>iPr</sup> , PhP <sup>2</sup> P <sub>2</sub> <sup>tBu</sup> and <sup>H</sup> C <sup>2</sup> P <sub>3</sub> <sup>Cy</sup>	89
3.4.	Catalytic formic acid and formic acid/amine dehydrogenation	98
3.5.	Catalytic bicarbonate hydrogenation	102
3.6.	Conclusions	103
3.7.	Experimental section	104
3.7.1.	General methods and materials	104
3.7.2.	Formic acid dehydrogenation procedures	104
3.7.3.	Sodium bicarbonate hydrogenation procedures	104
3.8.	References	105
<b>Chapter 4: Iron(II) Complexes of the Linear <i>rac</i>-tetraphos-1 Ligand as Efficient Homogeneous Catalysts for Sodium Bicarbonate Hydrogenation and Formic Acid Dehydrogenation.</b>		<b>107</b>
4.1.	Overview	107
4.2.	Introduction	108
4.3.	Syntheses and characterization of Fe(II) complexes	109
4.4.	Reactivity of Fe(II) complexes toward H <sub>2</sub>	115
4.5.	Reactivity of Fe(II) hydride complexes toward CO <sub>2</sub>	116
4.6.	Fe-Catalyzed Formic Acid Dehydrogenation	118
4.7.	Fe-Catalyzed Sodium Bicarbonate Hydrogenation	121
4.8.	NMR Mechanistic studies	123
4.9.	Conclusions	128
4.10.	Experimental section	128
4.10.1.	General methods and materials	128
4.10.2.	Synthetic procedures	129
4.10.3.	Catalytic tests	134
4.11.	References	134
<b>Appendix</b>		<b>137</b>
<b>Curriculum Vitae</b>		<b>179</b>

## FREQUENTLY USED ABBREVIATIONS

${}^{\text{H}}\text{C}^2\text{P}_3^{\text{Cy}}$   $\text{HC}(\text{CH}_2\text{CH}_2\text{PCy})_3$

DFT Density functional theory

DMC Dichloromethane

ESI-MS ElectroSpray ionization Mass Spectrometry

FT-IR Infrared spectroscopy

GC Gas-chromatography

iPrOH Isopropanol

BuLi n-buthyllithium

NMR Nuclear magnetic resonance

NP<sub>3</sub> tris(2-diphenylphosphinoethyl) amine

OTf  $\text{OSO}_2\text{CF}_3$

PC Propylene Carbonate

$\text{PhP}^2\text{P}_2^{\text{tBu}}$   $\text{PhP}(\text{CH}_2\text{CH}_2\text{P}^{\text{tBu}})_2$

$\text{P}^2\text{P}_3^{\text{Cy}}$   $\text{P}(\text{CH}_2\text{CH}_2\text{PCy})_3$

$\text{P}^3\text{P}_3^{\text{iPr}}$   $\text{P}(\text{CH}_2\text{CH}_2\text{CH}_2\text{P}^{\text{iPr}})_3$

P4 1,1,4,7,10,10-hexaphenyl-1,4,7,10-tetraphosphadecane

RT Room temperature

tBuOK Tert-potassium butoxide

TH Transfer hydrogenatio

THF Tetrahydrofuran

TOF Turnover frequency

TON Turnover number

Triphos 1,1,1-tris(diphenylphosphinomethyl)ethane

XRD Single-crystal X-ray diffraction

## **X-RAY CRYSTAL STRUCTURES: ATOM COLOUR CODE**

Carbon	Gray
Chlorine	Violet Red
Iron	Blue
Hydrogen	White
Nitrogen	Green
Oxygen	Red
Phosphorous	Orange

## **OPTIMIZED STRUCTURES: ATOM COLOUR CODE**

Carbon	Black
Chlorine	Green
Iron	Blue
Hydrogen	Grey
Nitrogen	Dark blue
Oxygen	Red
Phosphorous	Violet
Ruthenium	Blue

## LIST OF COMPLEXES

1	$[\text{Ru}(\kappa^3\text{-triphos})(\text{MeCN})_3](\text{OTf})_2$
1'	$[\text{Ru}(\kappa^3\text{-triphos})(\text{MeCN})_3](\text{PF}_6)_2$
2	$[\text{Ru}(\kappa^4\text{-NP}_3)\text{Cl}_2]$
3	<i>cis</i> - $[\text{Ru}(\kappa^3\text{-triphos})(\text{CO})(\text{H})_2]$
4	$[\text{Ru}(\kappa^3\text{-triphos})(\eta^1\text{-OOCH})(\eta^2\text{-OOCH})]$
4'	$[\text{Ru}(\kappa^3\text{-triphos})(\text{MeCN})(\eta^2\text{-OOCH})]$
5	$[\text{Ru}(\kappa^4\text{-NP}_3)\text{Cl}(\eta^1\text{-OOCH})]$
6	$[\text{Ru}(\kappa^4\text{-NP}_3)\text{Cl}(\text{H})]$
7	$[\text{Ru}(\kappa^4\text{-NP}_3)(\text{H})(\eta^2\text{-H}_2)]^+$
8	$[\text{Ru}(\kappa^4\text{-NP}_3)\text{Cl}(\eta^2\text{-H}_2)]^+$
9	$[\text{Ru}(\kappa^3\text{-triphos}^{\text{Me}})(\text{MeCN})_2(\eta^1\text{-OOCH})]^+$
10	$[\text{Ru}(\kappa^3\text{-triphos}^{\text{Me}})(\text{MeCN})(\eta^1\text{-OCH}_2)]$
11	$[\text{Ru}(\kappa^3\text{-triphos}^{\text{Me}})(\eta^1\text{-OOCH})_3]^-$
12	$[\text{Ru}(\kappa^3\text{-triphos}^{\text{Me}})(\eta^1\text{-OC}(\text{OH})\text{H})(\eta^1\text{-OOCH})_2]$
13	$[\text{Ru}(\kappa^4\text{-NP}_3)\text{H}(\eta^1\text{-OOCH})]$
14	$[\text{Ru}(\kappa^4\text{-NP}_3)(\eta^2\text{-H}_2)(\eta^1\text{-OOCH})]$
15	$[\text{Ru}(\text{P}^3\text{P}_3^{\text{IPr}})\text{Cl}][\text{BPh}_4]$
16	$[\text{Ru}(\text{P}^3\text{P}_3^{\text{IPr}})(\text{H})_2]$
17	$[\text{Ru}(\text{PhP}^2\text{P}_2^{\text{tBu}})\text{Cl}_2]$
18	$[\text{Ru}(\text{P}^2\text{P}_3^{\text{Cy}})\text{H}(\text{N}_2)][\text{BF}_4]$
19	$[\text{Ru}(\text{H}^1\text{C}^2\text{P}_3^{\text{Cy}})\text{H}(\text{CO})]$
20	$[\text{Fe}(\text{P}^2\text{P}_3^{\text{Cy}})(\text{N}_2)]$
21	$[\text{Fe}(\text{P}^2\text{P}_3^{\text{Cy}})(\text{N}_2)][\text{BPh}_4]$
22	$[\text{Fe}(\text{P}^2\text{P}_3^{\text{Cy}})(\text{H})_2]$
23	$[\text{Fe}(\text{P}^2\text{P}_3^{\text{Cy}})\text{H}(\text{N}_2)][\text{BF}_4]$
24	$[\text{Fe}(\text{rac-P4})(\eta^1\text{-FBF}_3)](\text{BF}_4)$
25	<i>cis-α</i> - $[\text{Fe}(\text{rac-P4})(\text{CH}_3\text{CN})_2](\text{BF}_4)_2$
26	$[\text{Fe}(\text{rac-P4})\text{H}][\text{BPh}_4]$
27	<i>cis-α</i> - $[\text{Fe}(\text{rac-P4})(\text{H})_2]$
28	<i>cis-α</i> - $[\text{FeH}(\text{NCMe})(\text{rac-P4})](\text{BF}_4)$
29	<i>cis-α</i> - $[\text{Fe}(\text{rac-P4})(\eta^2\text{-O}_2\text{CH})](\text{BPh}_4)$
30	<i>cis-α</i> - $[\text{Fe}(\eta^2\text{-O}_2\text{CO})(\text{rac-P4})]$
30'	$\{\mu^2\text{-}[\text{Fe}(\text{MeOH})_4]\text{-}\kappa^1\text{-O-}[\text{Fe}(\eta^2\text{-O}_2\text{CO})(\text{rac-P4})]_2\}(\text{BPh}_4)_2$
31	<i>cis-α</i> - $[\text{Fe}(\text{rac-P4})\text{H}(\text{CO})](\text{BF}_4)$



# Chapter 1

## Introduction

### 1.1 Overview

This chapter provides a literature overview on the development and use of new methods for the production and storage of hydrogen as promising energy vector of the future. After a brief description of properties and use of hydrogen, its different production and storage methods are reported, in particular focusing on the concept of using formic acid as a hydrogen storage material. The state of the art on the formic acid activation by its dehydrogenation pathway in heterogeneous and homogeneous catalysis is also given. In the last part of the Chapter, the main objectives of the present PhD project are described.

## 1.2 Hydrogen

The constant and rapidly growing world population and the rising standards of living are causing a dramatic increase the world's energy consumption. In addition to that, production of energy by burning carbon-based fuels inevitably leads to an increasing level of carbon dioxide in the atmosphere, thus aggravating the greenhouse effect with all its environmental and socio-economic consequences.

For these reasons, sustainable and benign energy sources as well as efficient ways of energy distribution are necessary. Therefore, one of the most important scientific and technological challenges nowadays is finding new energy vectors, possibly derived from renewable sources, that can contribute to the worldwide demand for energy in a sustainable manner with advantageous costs. Various renewable energy sources (e.g. wind and solar) have seen large scale applications over the last decade and capacities are steadily increasing.<sup>1</sup>

In this respect, H<sub>2</sub> is expected to play an important role as secondary energy carrier, as it allows an efficient conversion of chemical to electrical energy using fuel cells, producing only water as by-product without releasing CO<sub>2</sub> and none of the other pollutants formed by burning fossil fuels as in the current fossil fuel-based economy. A pre-requisite for the large scale utilization of hydrogen is the development of efficient technologies for hydrogen generation from renewable sources and its storage in a safe and reversible manner.<sup>2</sup>

### 1.2.1 Properties and industrial use of hydrogen

Hydrogen is one of the most widespread and plentiful elements on earth. Owing to its high reactivity, however, hydrogen combines with other elements and thus cannot be collected as such for combustive energy production. As a consequence, to produce hydrogen a significant amount of energy must be applied, to obtain it as pure from the molecules in which it is associated in chemical bonds. Hydrogen is therefore not a primary energy source but only an energy carrier. Some of its physical and chemical characteristics, however, are not well-suited for this purpose, especially as a transportation fuel. The lightness of hydrogen represents a handicap for its storage, transmission and use in its gaseous form. The small H<sub>2</sub> molecules also diffuse

through most materials and makes steel brittle, especially at high pressure or/ and temperature. In spite of this, there is presently great interest for its applications.

**Table 1.1.** Properties of hydrogen.<sup>3</sup>

<b>Chimica formula</b>	<b>H<sub>2</sub></b>
Molecular weight	2.0159
Appearance	Colorless and odorless gas
Melting point	-259.1 °C
Boiling point	-252.9 °C
Density at 0 °C	0.09 kg m <sup>-3</sup>
Density as a liquid at -253 °C	70.8 kg m <sup>-3</sup>
Energy content	28 670 kcal kg <sup>-1</sup> 57.7 kcal mol <sup>-1</sup>
Octane number	130+
Autoignition temperature	520 °C
Flammability limits in air	4-74%
Explosive limits in air	15-59%
Ignition energy	0.005 mcal (milli-calorie)

Today, hydrogen production is about 50 million tonnes yearly worldwide,<sup>3</sup> corresponding to less than 2% of the world's primary energy demand. Mostly, hydrogen is used as a feedstock in the chemical and petrochemical industry, to produce principally ammonia, refined fossil fuels by hydrocracking, and a variety of chemicals. Only smaller amounts of hydrogen are delivered to end users.

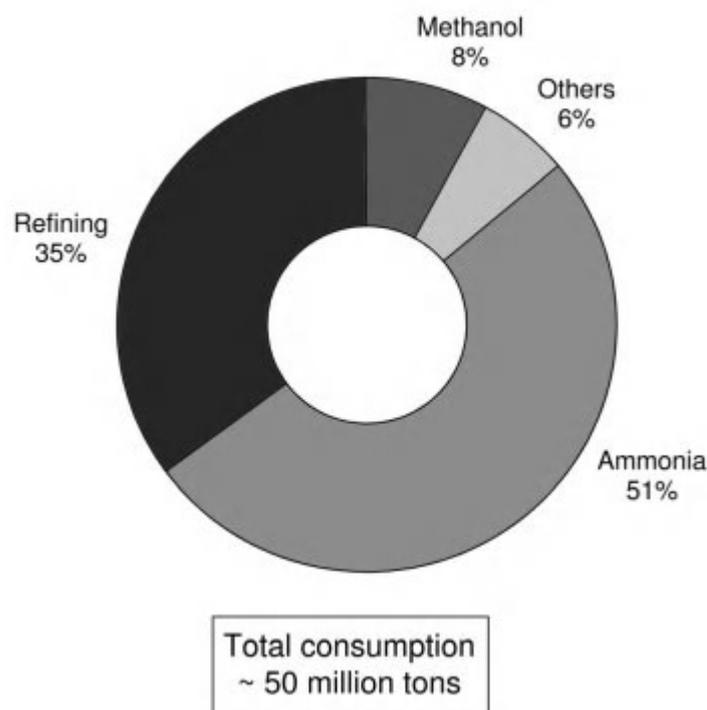
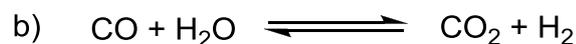
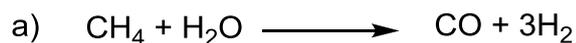


Figure 1.1. Main hydrogen-consuming sectors in the world.<sup>3</sup>

### 1.2.2 Methods for producing hydrogen in view of its use as energy carrier

Currently, more than 95% of hydrogen is produced from fossil fuels. Among them, methane has the highest hydrogen-to-carbon ratio (25 %w) and it is also the most suitable feedstock for hydrogen production due to its wide availability and ease of handling. There are several processes to convert methane into hydrogen, such as steam reforming (SMR), partial oxidation with oxygen (POX), or their combination (autothermal reforming).

SMR is the preferred method affording ca. 50% of the hydrogen produced worldwide.<sup>3</sup> In SMR, methane reacts with steam over a metal catalyst in a reactor at high temperatures and pressures to yield hydrogen and carbon monoxide (Scheme 1.1a). In a second step, additional hydrogen can be produced by a lower-temperature water gas-shift reaction (WGSR, Scheme 1.1b).



**Scheme 1.1.** Steps of steam reforming of methane.

SMR produces a hydrogen rich gas mixture that is typically in the order of 70-75% hydrogen on a dry mass basis, along with smaller amounts of methane (2-6%), carbon monoxide (7-10%), and carbon dioxide (6-14%).

Hydrogen purification is then necessary, particularly when it must be used in fuel cells where high hydrogen purity is required to avoid poisoning of the catalysts. This is usually achieved by capture and sequestration of CO<sub>2</sub>, generally venting into the atmosphere. However, the cost of CO<sub>2</sub> capture and disposal is currently high.

In the POX and autothermal reforming process, hydrogen can be produced from a range of hydrocarbon feedstocks, including coal, heavy residual oils, and other low-value refinery products. These methods are more efficient than simple steam reforming, but require oxygen, whose separation from air at low cost and its safe use in methane oxidation is still technically difficult (Scheme 1.2).

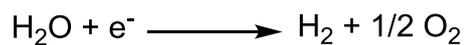


**Scheme 1.2.** Partial oxidation of carbon.

This problem can be overcome producing hydrogen through pyrolysis-based hydrocarbon gasification processes in the absence of oxygen.

Producing hydrogen from petroleum oil and natural gas would only be a temporary solution and would not solve the energy dependence on fossil fuels and related environmental problems. Thus, more sustainable methods are needed, such as generating hydrogen from biomass or from water by electrolysis using renewables as well as wind and solar energy sources.

*Water electrolysis* consists in the splitting of water into hydrogen and oxygen molecules using electricity and an electrolyzer device (Scheme 1.3).<sup>4</sup>



**Scheme 1.3.** Electrolysis of water.

The two most common types of electrolyzers are alkaline (using a potassium hydroxide electrolyte) and PEM (using a solid polymer membrane electrolyte). Commercial electrolysis is a mature technology used to produce high-purity hydrogen, and in addition the oxygen produced as by-product can be employed in several industrial applications. Electrolysis is thus the best method of producing hydrogen from carbon-free feedstocks, and can be economically viable if electricity can be obtained from renewable energy sources. However, the production of hydrogen by electrolysis is currently more expensive than the production of hydrogen from fossil fuels (Figure 1.2).

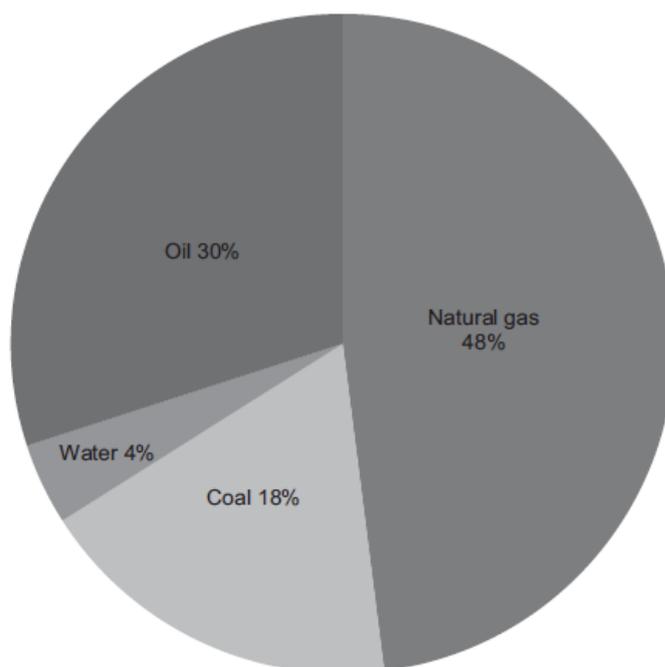


**Figure 1.2.** Sources of hydrogen production, currently used in the world.<sup>5</sup>

In view of a hydrogen-based economy, hydrogen is produced to generate electric power through fuel cells so apparently it is irrational to use electricity to make hydrogen and then use it back to generate electricity. However, this strategy can be adopted as a possible way to store hydrogen, as storage of electrical power is a difficult task.

Basically, any energy source that produces electricity can be used to produce hydrogen by water electrolysis. By burning fossil fuels a sufficiently large power capacity is generated, but producing hydrogen in this way is not convenient from an economical as well as ecological viewpoint. On the other hand, generating such a huge amount of electric power is even more difficult if we have to make use of renewable energy sources only, including hydropower, wind power, solar photovoltaic or nuclear power.

Nowadays, *hydroelectric power* is the largest renewable electricity source providing about 3 TWh, or 16% of the world's electricity need.<sup>6</sup> Hydroelectric power has been extensively exploited in Europe and the USA, where about 70% of its potential is already utilized.<sup>7</sup> Although in several countries the expansion of hydroelectric energy is currently based on low-cost small plants and its availability is limited by reason of technical, environmental, and legal restrictions, in the last years the number of such installations grew up. However, the increase in exploitation of hydroelectric power can give only a small contribution towards a hydrogen economy.

An other important contribution towards the development of a clean hydrogen economy could be found in the exploitation of *wind power*. Because of its great potential, wind power can be considered as the most efficient renewable energy source for hydrogen production at a reasonable cost in the foreseeable future. Wind is non-polluting, plentiful and the electricity generated in this way is already competitive with power from fossil fuels in some areas of the world. The disadvantage is the intermittent nature of wind energy, furthermore electrolyzers for hydrogen production coupled with wind farms operate at full capacity only for limited periods of time. In this direction, significant efforts are necessary for convenient hydrogen generation.

Like wind, *solar energy* is a non-polluting and plentiful source of energy but, being also an intermittent source, it suffers from the same drawbacks as wind energy. Moreover the production cost of hydrogen generated by photovoltaic systems with crystalline silicon solar cells is more expensive than that based on fossil fuels and other renewable energy sources. New concepts based on the use of thin-film technology, conductive organic polymers and nanostructured films,<sup>8</sup> are considered to improve the efficiency and to reduce the costs of hydrogen production.<sup>9</sup> Another

possibility is the use of photoelectrochemical and photochemical devices for water splitting using directly solar energy, avoiding the coupling with an electrolyzer. Unfortunately, for the foreseeable future this also is too expensive.<sup>10</sup>

*Biomass* could potentially become an important source of hydrogen, due to the large variety of materials which could serve as feedstock, such as agricultural residues from farming and wood processing or dedicated bioenergy crops.<sup>11</sup> Biomass can also be used for the production of liquid fuels such as ethanol, methanol and biodiesel. The advantages of the use of biomass consists of its conversion into hydrogen by gasification or pyrolysis coupled with steam reforming. Moreover, in this case, the CO<sub>2</sub> released can be captured from the atmosphere by natural photosynthetic cycle, so that the net CO<sub>2</sub> emission is near to zero. However, due to the related economic, ecological and land-use problems, this approach can only be expected to supply a part of the large quantities of hydrogen required.

In contrast, enzyme-based biochemical “digester” type processes are at present mainly limited to wet, sugar-based feedstocks but could include cellulosic feedstocks in the future with continued improvements in process techniques and systems.<sup>12</sup> Usually, hydrogen-evolving enzymes are poisoned by the oxygen that is produced along with hydrogen. For this reason it is necessary either to find microorganisms that are more tolerant to oxygen, or to create new genetically-modified forms of known bacteria that are unaffected by the presence of oxygen. In the last years, many efforts and finances were also invested in photobiological methods to produce hydrogen from water using algae.<sup>13</sup>

### **1.2.3 Hydrogen storage**

As previously said, the development of efficient technologies for hydrogen generation from renewable energy sources and for hydrogen storage in a safe and reversible manner is a pre-requisite for the utilization of hydrogen on a large scale in small- and middle-size mobile or stationary devices. Compared to other fuels, hydrogen has a high gravimetric energy density, but its volumetric energy density at atmospheric pressure is too low for most envisioned applications. Therefore, it is necessary to obtain an improved volumetric hydrogen storage density (Table 1.2).

**Table 1.2.** Properties of hydrogen compared with those of some common fuels.<sup>14</sup>

	Hydrogen	Petroleum (gasoline)	Methane	Methanol
Boiling point/K	20.3	350-400	111.7	337
<sup>a</sup> Liquid density/kg m <sup>-3</sup>	70.8	~ 700	425	797
<sup>b</sup> Gas density/kg m <sup>-3</sup>	0.08	~ 4.7	0.66	-
Vaporization heat/MJ kg <sup>-1</sup>	444	~ 300	577	1168
<sup>c</sup> Combustion heat/MJ kg <sup>-1</sup>	120	44.5	50.0	20.1
<sup>d</sup> Combustion heat/MJ m <sup>-3</sup>	8960	31170	21250	16020
<sup>e</sup> Ignition temperature/K	858	495	807	658

<sup>a</sup>At boiling point. <sup>b</sup>At STP. <sup>c</sup>Neglecting the energy in the exhaust (combustion) gases. <sup>d</sup>Referred to the liquid fuel. <sup>e</sup>In air.

Currently, *hydrogen compression* is the preferred solution to hydrogen storage and use in most hydrogen fuel cell-powered prototype cars. Hydrogen can now be held under 350 or even 700 atm in tanks made from new lightweight materials, such as carbonfiber- reinforced composites.

However, even in this pressure range, hydrogen per-volume energy content is 4.6 times lower than gasoline, and thus requires more voluminous tanks. Furthermore, about 10–15% of the energy content of hydrogen is required by compression.

Working with such high pressures, special vessel designs are also required. Generally, compressed hydrogen tanks have a fixed cylindrical shape and the integration into existing car architectures remains an important challenge. Moreover, hydrogen can diffuse through many materials, including metals. During prolonged exposure to hydrogen, some metals can also become brittle. Thus, it is important to avoid that material failure could cause hydrogen loss with a major safety hazard, being a highly flammable and explosive gas when exposed to air.

The high-pressure hydrogen storage systems made from high-tech materials and with special design are also complex and very expensive, therefore technological improvements are necessary to reduce production costs.

Only very recently, *liquid hydrogen* was evaluated as a viable on-board storage option for the automotive industry. A potential advantage of liquid hydrogen systems

is the high mass density of hydrogen at  $-253\text{ }^{\circ}\text{C}$  and  $0.1\text{ MPa}$  in comparison to  $70\text{ MPa}$  for compressed hydrogen systems. On the other hand, heat flowing from the environment into the tank vessel leads to hydrogen evaporation. As a consequence, the pressure inside the vessel increases, and after a certain maximum pressure is reached, hydrogen has to be vented. These significant hydrogen losses are unacceptable for a future use of this technology. Moreover, hydrogen, with a boiling point of  $-253\text{ }^{\circ}\text{C}$ , is after helium the most difficult gas to liquefy. Complex and expensive multi-stage cooling systems are necessary to obtain liquid hydrogen and require 30–40% of the energy content of the hydrogen.

The cost and energy invested into production and storage of liquid hydrogen are unsatisfactory both from an economic and from an environmental viewpoint.

*Hydrogen adsorption* is a borderline situation between physical and chemical storage. At ambient conditions, due to weak interactions between hydrogen molecules and adsorbents, none of the currently-known adsorbents has a satisfactory storage capacity so cryogenic and/or pressure systems are necessary as adsorptive storage solutions. Furthermore, ideal materials for hydrogen uptake should have a high surface area and pores in the micropore range.

Several porous solid materials for potential hydrogen storage are under investigation, such as activated carbon, graphene, carbon nanotubes, fullerenes, and polymers with intrinsic microporosity or suitably functionalized.<sup>15</sup> Fullerenes and carbon nanotubes have attracted much attention, but practical and economic problems are presented. Metal-organic frameworks (MOFs), a new class of highly porous materials with high surface areas, have also been recently discovered and show promise as high-capacity hydrogen storage media because their pore structure can be chemically tuned.<sup>16</sup>

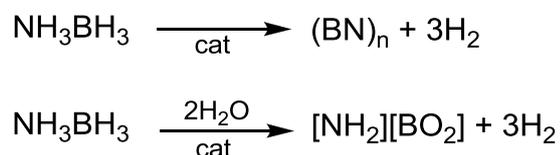
Contrary to physical storage methods, *chemical storage* media contain hydrogen either in chemically bonded or complexed forms, or incorporated into small organic molecules. In principle they can be divided in solid and liquid “molecular containers” of hydrogen. Among the different solid hydrogen storage media, metal hydrides, their alloys and their complex were extensively investigated.

Many metals and metallic alloys have the ability to absorb hydrogen, like a sponge, to form hydrides.<sup>17</sup> This process can be either reversible or irreversible, depending on the nature of the chemical bond between hydrogen and metal atoms. Hydrogen stored

irreversibly is released by a chemical reaction with another compound, generally water. Thus, for practical purpose reversible hydrides are more attractive, in which hydrogen is adsorbed and desorbed. Moreover, the uptake and release of hydrogen is typically controlled by temperature and pressure, which are different for various hydrides, making them poorly suitable for practical applications. Nevertheless, an advantage of metal hydrides is that they require less space than compressed hydrogen, being very compact.

Today, research into metal hydrides is focused mainly on light compounds such as  $\text{NaAlH}_4$ ,  $\text{Na}_3\text{AlH}_6$ ,  $\text{LiAlH}_4$ ,  $\text{NaBH}_4$ ,  $\text{LiBH}_4$  and  $\text{MgH}_2$ , which offer higher hydrogen contents per unit of mass.<sup>2d, 17b, 18</sup>

Lithium imide/lithium amide systems<sup>19</sup> and amine–borane adducts<sup>20</sup> are other promising materials for hydrogen storage. In particular *amine-borane adducts* are unique materials with a very high hydrogen content (ca. 20 wt%) but, for a complete desorption of hydrogen, high temperatures are necessary and by-products are produced, thus excluding so far their use in practical applications (Scheme 1.4). Studies for the use of amine-borane derivatives under ambient conditions are underway.<sup>21</sup>



**Scheme 1.4.** Hydrogen production from amine-borane adducts.

Hydrogen storage in liquid materials offers several benefits, including compatibility with existing transport and refueling infrastructure, and more attractive containment solutions operating under ambient temperature or pressure.

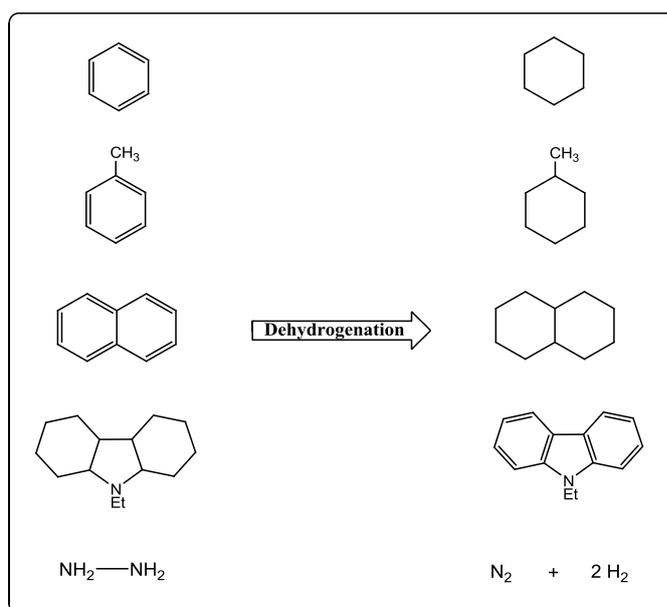
A number of *liquid organic hydrogen carriers* (LOHC) are proposed as potential sources of hydrogen, including methylcyclohexane, various hydrocarbons, hydrazine, 2-methylthiophene, BN-methylcyclopentane, carbazoles and their derivatives.

Among hydrocarbons, cyclic molecules such as benzene/cyclohexane, toluene/methylcyclohexane, or naphthalene/decalin, are proposed as reversible systems to store and release hydrogen. These compounds have an elevated

gravimetric and volumetric capacity storage but high temperature (over 300 °C) are required for a complete dehydrogenation.<sup>22</sup>

Carbazoles and substituted carbazoles are other organic materials with potential hydrogen storage properties. In particular, N-ethylperhydrocarbazole<sup>23</sup> can release a maximum of 6 mol equivalents of hydrogen and at 170 °C it is completely dehydrogenated over a Pd/C catalyst with TOF = 60 h<sup>-1</sup>. One disadvantage carbazole materials is their high decomposition temperature and high melting point.

*Hydrazine* has also a high hydrogen content and it is a liquid at room temperature. Hydrous hydrazine, N<sub>2</sub>H<sub>4</sub>·H<sub>2</sub>O contains 7.9 wt % of hydrogen, which can be efficiently released using Rh-Ni alloy nanoparticles.<sup>24</sup> The advantages of use hydrous hydrazine are the easy recharging and the only production of nitrogen as by product. However, hydrazine is a highly toxic compound (scheme 1.5).

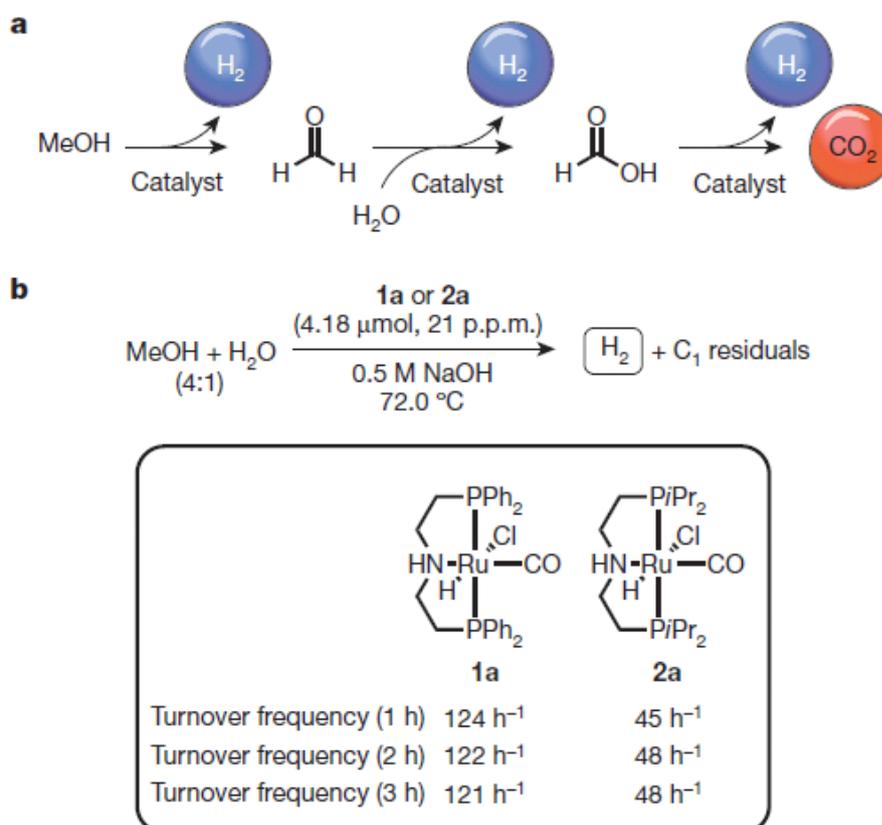


**Scheme 1.5.** Liquid organic hydrogen carriers (LOHC) abovementioned.

*Alcohols* are a promising alternative for hydrogen production. The first studies investigated the dehydrogenation of secondary and/or longer chain alcohols but more recent breakthroughs include even small primary alcohols, ethanol and methanol.<sup>25</sup>

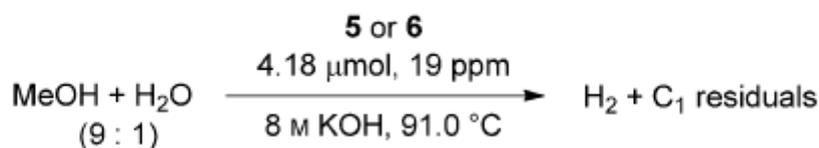
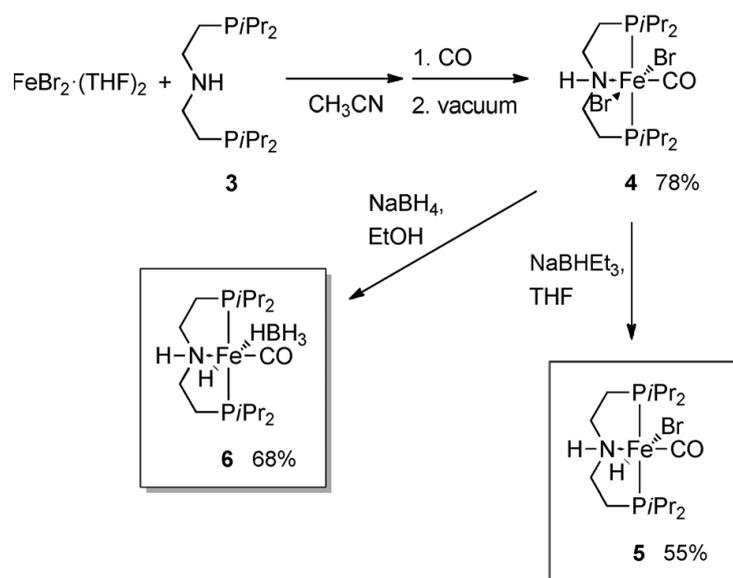
Ruthenium-based complexes are prominent catalysts for alcohol dehydrogenation procedures.<sup>26</sup> Recently, Beller *et al.* described an efficient low temperature aqueous-phase methanol dehydrogenation process, which is promoted by ruthenium

complexes. Hydrogen generation by this method proceeds at 65–95 °C and ambient pressure with excellent catalyst turnover frequencies (4700 h<sup>-1</sup>) and turnover numbers exceeding 350000 (Scheme 1.6).<sup>27</sup>



**Scheme 1.6.** a) Schematic pathway for a homogeneously catalysed methanol reforming process via three discrete dehydrogenation steps. b) Best-performing catalyst for aqueous-phase methanol dehydrogenation.<sup>27</sup>

Other platinum group metals, primarily iridium<sup>28</sup> and osmium,<sup>29</sup> are also applicable to this chemistry. More recently, non-noble metal systems based on iron and cobalt were reported with promising catalytic activity. Beller and co-workers reported that some iron pincer-type complexes are able to promote dehydrogenation of methanol at low temperatures with high TOFs. (Scheme 1.6).<sup>30</sup>



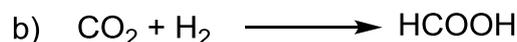
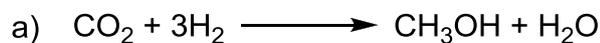
	<b>5</b>	<b>6</b>
TOF <sub>1h</sub>	414 h <sup>-1</sup>	702 h <sup>-1</sup>
TOF <sub>2h</sub>	385 h <sup>-1</sup>	594 h <sup>-1</sup>
TOF <sub>3h</sub>	353 h <sup>-1</sup>	510 h <sup>-1</sup>

**Scheme 1.7.** Synthesis and catalytic activity of Fe(II) complexes **5** and **6** active in dehydrogenation of aqueous methanol.<sup>30</sup>

An interesting feature of using MeOH as hydrogen source is that it can be regenerated by CO<sub>2</sub> reduction. In this way CO<sub>2</sub> can be used as a renewable feedstock and hydrogen storage material and a zero-carbon demand and emission catalytic cycle can be invoked, avoiding the use of fossil fuels for energy production. This principle can be applied not only to MeOH but also to another important LOHC such as *formic acid*.

Even if methanol has a higher storage capacity of two hydrogen molecules compared to one in formic acid, the use of carbon dioxide to synthesize formic acid should be preferred for higher atom efficiency.<sup>3</sup> The need for three equivalents of hydrogen to produce one equivalent of methanol results in the loss of one equivalent of hydrogen,

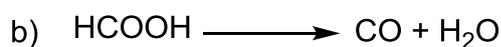
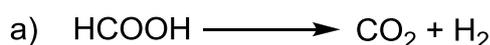
since water is formed (Scheme 1.8a). In contrast, a transfer rate of 100% is possible for formic acid formation (Scheme 1.8b).<sup>31</sup>



**Scheme 1.8.** Reduction of CO<sub>2</sub> to produce methanol and formic acid.

*Formic acid* contains 4.4 wt% of hydrogen, is a cheap liquid under ambient conditions and can be handled, stored and transported safely.

Formic acid decomposition can occur following two different pathways, known as *dehydrogenation* (Scheme 1.9a) and *dehydration* reactions (Scheme 1.9b), of which only the former can be used to produce fuel cell grade (CO free) hydrogen.



**Scheme 1.9.** Dehydrogenation (a) vs. dehydration (b) pathways for formic acid decomposition.

High selectivities to formic acid dehydrogenation can be obtained in the presence of transition metal catalysts. These are able not only to reduce the energy demand of the processes, allowing for lower activation energies, but also steer the decomposition pathway to the desired dehydrogenation reaction. In the following section, the state-of-the-art of formic acid activation in the presence of heterogeneous and homogeneous catalysts will be described.

### 1.3 Formic acid dehydrogenation using heterogeneous catalysts

The dehydrogenation of formic acid to hydrogen and carbon dioxide, in the presence of heterogeneous catalysts, has been reported for the first time by Sabatier in 1912.<sup>32</sup>

Initially, this reaction has been used to study adsorption and desorption processes during the decomposition of formic acid vapors as a model substrate on surfaces.<sup>33</sup>

Rienacker *et al.* investigated the decomposition of formic acid vapors to measure the activity of many types of heterogeneous catalysts (Table 1.3), mainly metals (Ni, Pd, Pt, Cu, Ag, Au) and alloys of transition metals (Cu-Au, Ag-Au, Cu-Pd, Cu-Ni).<sup>34</sup>

Whereas carbon monoxide was only produced when Au was part of the catalyst, alloys comprising Cu and Ag led to selective dehydrogenation to CO<sub>2</sub> and H<sub>2</sub>. Dowden and Reynold reported the activity of Ni, Cu and alloys of those metals for the decomposition of formic acid at 253 °C but no information of the purity of the produced gas was given.<sup>35</sup>

**Table 1.3.** Decomposition of formic acid in the presence of metals and alloys.<sup>36</sup>

Catalyst	$E_{akt}/\text{kJ mol}^{-1}$	Selectivity [% H <sub>2</sub> ]
Cu (110)	ca. 130	100
Cu, polycrystalline	115-130	100
Cu, wire, tempered	ca. 98	100
Cu, sheet, tempered	ca. 98	100
Au, sheet, tempered	ca. 122	93-94
Ag, sheet, tempered	ca. 109	100
Pd, sheet, tempered	ca. 34	>99
Cu <sub>25</sub> Au <sub>75</sub> -Cu <sub>75</sub> Au <sub>25</sub> , sheet, tempered	ca. 101-103	n.s.
Pd <sub>17</sub> Cu <sub>83</sub> -Pd <sub>92</sub> Cu <sub>8</sub> , sheet, tempered	ca. 50-92	n.s.
Pd <sub>17</sub> Cu <sub>83</sub> -Pd <sub>92</sub> Cu <sub>8</sub> , sheet, rapidly solidified	50-68	n.s.
Fe <sub>80</sub> B <sub>20</sub> , meltspun	110-160	50-80
Fe <sub>80</sub> B <sub>20</sub> , crystalline	ca. 50	10-30

In the late 1970's Williams *et al.* investigated the decomposition of formic acid at room temperature. In the presence of Pd/C (1 wt% Pd), the hydrogen production of 60 mL of H<sub>2</sub> were obtained from 4 mol/L of aqueous formic acid after 10 min. Carbon dioxide was trapped in a column filled with potassium hydroxide pellets.<sup>37</sup>

Wiener *et al.* improved the performance of this catalytic system, using a loading of 10 wt% Pd, obtaining 900 mL of hydrogen from a 4 M aqueous sodium formate

solution within 20 min at 70 °C, with a barium hydroxide solution used as carbon dioxide trap.<sup>38</sup>

Later on, studies were carried out to tune the selectivity of formic acid decomposition to dehydrogenation. Sexton *et al.* investigated the decomposition of formic acid on Cu(100) with electron energy loss spectroscopy (EELS).<sup>39</sup> At 127 °C a surface layer of formate was observed, which decomposed to H<sub>2</sub> and CO<sub>2</sub> within a temperature range between 152 and 227 °C.

In a review, Madix reported the selectivity of formic acid decomposition in the presence of several transition metals such as Ni, Fe, Cu, Pt and Ag. Ni(110) and Ni(100) promoted the dehydration reaction whereas Fe(100), Cu(110), Cu(100), Ru(100), Pt(111) and Ag(110) lead to formation of surface formate as intermediate of the decomposition to either CO or CO<sub>2</sub> and H<sub>2</sub>.<sup>40</sup>

Kisfaludi *et al.* investigated the effect of crystallite size on CO–CO<sub>2</sub> selectivity in the decomposition of formic acid over meltspun amorphous ribbons and ribbons with crystalline Fe particles.<sup>41</sup> The crystallized ribbons prefer dehydration as decomposition pathway whereas the amorphous ribbons produce mainly H<sub>2</sub> and CO<sub>2</sub>. Recently, Ojeda and Iglesia reported the selective dehydrogenation of formic acid at 80 °C catalyzed by dispersed gold nanoparticles supported on Al<sub>2</sub>O<sub>3</sub>.<sup>42</sup> Only small amounts of CO were detected (< 10 ppm). In addition, they showed that the activity and selectivity of this system depend on the Au domains size.

Solymosi and co-workers employed a range of monometallic noble metal catalysts (Ir, Pd, Pt, Ru and Rh) supported on activated high specific surface area (SSA) to study the decomposition of formic acid at elevated temperatures (70–477 °C).<sup>43</sup> Among the investigated catalysts, only the Ir based systems presented high activity at 100 °C. High selectivity to CO<sub>2</sub> and H<sub>2</sub> (>99%) was reached only at 200°C with addition of water, showing that under these conditions CO formation on Ir was suppressed. Comparable catalytic performances was achieved with Au (1%) on different support materials (SiO<sub>2</sub>, CeO<sub>2</sub> and AC, active carbon).<sup>44</sup>

Other studies considered the effect of the addition of a second metal on the process selectivity. This addition is known to change the electronic properties of the active phase, its adsorption behavior and the metal dispersion/particle size (Table 1.4).

**Table 1.4.** Recent heterogeneous catalyst for the decomposition of formic acid.<sup>45</sup>

Active phase/support	Solvent/medium	Performance	Temperature (K)
0.61% Au%Al <sub>2</sub> O <sub>3</sub>	He/gas phase	TOF = 25 600 h <sup>-1</sup> , <10 ppm CO	353
20 wt% PdAu/C-CeO <sub>2</sub>	Aqueous	TOF = 832 h <sup>-1</sup> , <140 ppm CO	375
1% Pd/C	He/gas phase	TOF = 255 h <sup>-1</sup> , S <sub>H<sub>2</sub></sub> = 99%	373
Mo <sub>2</sub> C/C	Ar/gas phase	TOF = 437 h <sup>-1</sup> , S <sub>H<sub>2</sub></sub> = 95-98%	423
PdAu@Au//C (core-shell)	Aqueous	130 ppm CO	356
5% Au/CeO <sub>2</sub>	Ar/gas phase	TOF = 295 h <sup>-1</sup> , S <sub>H<sub>2</sub></sub> = 100% <sup>a</sup>	473
Ir/C	Ar/gas phase	TOF = 960h <sup>-1</sup> , S <sub>H<sub>2</sub></sub> = 99%	373
Ag@Pd/C (core-shell)	Aqueous	TOF = 125 h <sup>-1</sup> , S <sub>H<sub>2</sub></sub> = 100%	293 363
		TOF = 626 h <sup>-1</sup> , 84 ppm CO	
Pd-S-SiO <sub>2</sub>	Aqueous	TOF = 803 h <sup>-1</sup> , S <sub>H<sub>2</sub></sub> = 100%	358

<sup>a</sup>Incomplete formic acid conversion.

Xing *et al.* reinvestigated the decomposition of formic acid/sodium formate solutions with several alloys composed of palladium on charcoal and elements from the copper group (Cu, Ag, Au) and compared with unmodified palladium on charcoal. While Pd/C quickly deactivated, Pd–Au/C and Pd–Ag/C produced high hydrogen quality at 92 °C. The effect of gold and silver was explained by the formation of smaller nanoparticles and a lower rate of carbon monoxide adsorption.<sup>46</sup>

The best result was obtained with Pd–Au–CeO<sub>2</sub> (Pd 10 wt%, 50 wt% and Pd:Au = 3:3) producing 1640 mL min<sup>-1</sup> g<sup>-1</sup> of gas, with a maximum TOF of 227 h<sup>-1</sup> at 92 °C

increasing to  $832 \text{ h}^{-1}$  at  $102 \text{ }^\circ\text{C}$ . The effect of  $\text{CeO}_2$  on the activity of Pd-based catalysts is probably due to  $\text{CeO}_2$  changing the electronic properties of the active Pd alloy phase.<sup>47</sup>

Xu and co-workers studied the performance of a number of mono and bimetallic nanoparticles immobilized inside metal organic frameworks (MOFs) as FA decomposition catalysts.<sup>48</sup> Of all the catalysts tested, only Au–Pd/MOF (20.4 wt% metal loading, Au:Pd = 2.46) showed promising FA decomposition activity at moderate reaction temperatures (average TOF of  $125 \text{ h}^{-1}$  at  $90 \text{ }^\circ\text{C}$ ). The catalyst is stable over four reaction cycles, but no detailed measurements of CO level were reported.

Chan *et al.* reported an interesting trimetallic system consisting of Pt, Ru and bismuth oxide. This catalytic system dehydrogenate formic acid in water at ambient temperature with high rates, yielding exclusively hydrogen and carbon dioxide with a very low activation energy. A TOF of  $312 \text{ h}^{-1}$  was achieved at  $80 \text{ }^\circ\text{C}$  without CO formation. The BiO is co-impregnated with the other metals on an activated carbon carrier. It was shown Pt-Ru systems without BiO were not active in formic acid dehydrogenation.<sup>49</sup>

As an alternative to metal alloys, bimetallic core-shell structures were shown to have unique physical and chemical properties. Xing *et al.* tested PdAu@Au core-shell nanoparticles supported on activated carbon in the decomposition of formic acid. The catalyst exhibited high activity, high selectivity, and stability at a low temperature and the catalytic performance was much better than that observed for the corresponding monometallic Au/C and Pd/C catalysts. During a continuous feed stability test, only 34 ppm of CO were produced after 30 h on stream.<sup>50</sup>

Recently, Tsang and co-workers carried out a systematic study of M–Pd core-shell nanoparticles (M = Ru, Rh, Pt, Ag, Au) reporting the high activity of Ag–Pd (1:1) core-shell nanoparticles. As compared to monometallic Pd, the TOF increased by an almost six-fold factor at room temperature ( $125 \text{ h}^{-1}$ ) to a maximum of  $626 \text{ h}^{-1}$  at  $90 \text{ }^\circ\text{C}$ . A maximum CO concentration of 84 ppm was observed only at high temperatures. Furthermore, the immobilization on high SSA AC enhanced the catalytic activity of the resulting Ag@Pd/C catalyst ( $196 \text{ h}^{-1}$  at  $25 \text{ }^\circ\text{C}$ ) keeping the  $\text{H}_2$  selectivity and allowing separation.<sup>51</sup>

As opposed to deposited metal nanoparticles, a practical strategy is to immobilize active organometallic catalysts onto compatible supports, to combine the advantages of both organometallic complexes and heterogeneous catalysts. Laurency and co-workers immobilized their highly active Ru-mTPPTS catalyst<sup>52</sup> via ion exchange polymer immobilization and physical adsorption on various supports obtaining heterogeneous catalysts for selective formic acid dehydrogenation.<sup>53</sup> In all cases high initial activity was followed by severe deactivation.

Recently, Guo and co-workers employed single-atom Pd and Ru dispersed on functionalized SiO<sub>2</sub> supports in the decomposition of aqueous HCOOH–HCOONa solution.<sup>54</sup> Using a mercapto-functionalized Pd–S–SiO<sub>2</sub> system as catalyst, a TOF of 719 h<sup>-1</sup> was achieved at 85 °C and the activity was stable after multiple catalyst recycles.

The only competitive alternative to noble metal catalysts in heterogeneous approaches, with similar activity and H<sub>2</sub> selectivity so far remains molybdenum carbide. Solymosi and co-workers investigated the activity of Mo<sub>2</sub>C supported on carbon nanotubes (CNT), high SSA AC and SiO<sub>2</sub> at reaction temperatures between 77 and 477 °C for both the decomposition and steam reforming of formic acid.<sup>55</sup> The product distribution and the selectivity of hydrogen formation depended on the nature of the supports and on the reaction temperature. The best catalytic performance was obtained with 1% Mo<sub>2</sub>C on AC giving full formic acid conversion at 150 °C (TOF of 437 h<sup>-1</sup>, based on bulk Mo<sub>2</sub>C as the active phase), with H<sub>2</sub> selectivities of 95-98%, whereas Mo<sub>2</sub>C/SiO<sub>2</sub> gave lower decomposition activity and H<sub>2</sub> selectivity (<70%). The addition of water to formic acid completely suppressed CO formation and gave CO-free H<sub>2</sub> on Mo<sub>2</sub>C/carbon catalysts, probably due to a shift in the WGS equilibrium towards H<sub>2</sub>/CO<sub>2</sub>. Another feature of the Mo<sub>2</sub>C catalyst is its high stability. No changes in activity or selectivity were observed within 10 h.<sup>56</sup> Recently, the photocatalytic decomposition of formic acid was studied in the presence of Fe(II) (photo-Fenton reaction with H<sub>2</sub>O<sub>2</sub>), pure TiO<sub>2</sub> in water<sup>57</sup> and in the gas phase,<sup>58</sup> as well as with alkaline earth titanates in water,<sup>59</sup> mainly for wastewater treatment.

An interesting alternative to the thermal decomposition of formic acid over heterogeneous catalysts is the electrochemical H<sub>2</sub> generation by formic acid

electrolysis. The used electrocatalysts are generally pure noble metal or noble metal alloys supported on carbon, in the latter case promising results were achieved.<sup>60</sup> However, this approach suffers from a number of inherent drawbacks.

#### 1.4 Formic acid dehydrogenation using homogeneous catalysts

The study of formic acid dehydrogenation in the presence of homogeneous catalysts was pioneered by Coffey in the late 1960s. Of a series of Pt, Ru and Ir phosphine complexes tested,  $[\text{IrH}_2\text{Cl}(\text{PPh}_3)_3]$  gave the highest rate of decomposition with a TOF of  $1187 \text{ h}^{-1}$  in refluxing acetic acid as solvent. Although metal carbonyl species were formed, no free carbon monoxide was detected in the evolved gas.<sup>61</sup>

**Table 1.5.** Decomposition/dehydrogenation of formic acid in the presence of homogeneous catalysts.<sup>36</sup>

Catalyst	Performance	$T/^\circ\text{C}$
$[\text{PtCl}_2(\text{Pbu})_3]$	$0.02 \text{ mol L}^{-1} \text{ h}^{-1}$	118
$\text{RuHBrCO}(\text{Pet}_2\text{Ph})_3$	$2.8 \text{ mol L}^{-1} \text{ h}^{-1}$	118
$\text{RuHCl}(\text{Et}_2\text{PC}_2\text{H}_4\text{PEt}_2)_2$	$2.0 \text{ mol L}^{-1} \text{ h}^{-1}$	118
$\text{IrCl}_3(\text{PEt}_2\text{Ph})_3$	$0.3 \text{ mol L}^{-1} \text{ h}^{-1}$	118
$[\text{IrCl}_3(\text{PBu}_3)_3]$	$0.7 \text{ mol L}^{-1} \text{ h}^{-1}$	118
$[\text{IrH}_2\text{Cl}(\text{PPh}_3)_3]$	$7.4 \text{ mol L}^{-1} \text{ h}^{-1}$	118
$[\text{IrH}_3(\text{PPh}_3)_3]$	$80 \text{ mol L}^{-1} \text{ h}^{-1}$	118
$[\text{Rh}(\text{CO})_2\text{Cl}]_2$	$31 \text{ mol L}^{-1} \text{ h}^{-1}$	100
$[\text{Pt}\{\text{P}(\text{iPr})_3\}_3]$	TOF = $100 \text{ h}^{-1}$	20
$[\text{Rh}(\text{C}_6\text{H}_4\text{PPh}_2)(\text{PPh}_3)_2]$	$3.3 \times 10^{-10} \text{ mol L}^{-1} \text{ h}^{-1}$	20
$[\text{Pt}_2\text{H}_3(\text{PEt}_3)_4][\text{BPh}_4]$	TON = 3.3	20
$[\text{Cp}^*\text{Mo}(\text{PMe}_3)_2(\text{CO})\text{H}]$	—	—
$[\text{Rh}(\text{H}_2)(\text{PMe}_2\text{Ph})_4]\text{BF}_4$	—	—
$[\text{Ru}_3(\text{CO})_{12}]$	TOF = $102 \text{ h}^{-1}$	75
$[\text{Ru}_2(\mu\text{-CO})(\text{CO})_4(\mu\text{-dppm})_2]$	TOF = $500 \text{ h}^{-1}$	rt
$[\text{Ru}(\text{H}_2\text{O})_6](\text{tos})_2$	TOF = $460 \text{ h}^{-1}$	120
$[\text{RuCl}_2(p\text{-cymene})_2]$	TON = 42	40
$[\text{RuCl}_2(\text{PPh}_3)_3]$	TOF = $2688 \text{ h}^{-1}$	40
$\text{RuBr}_3 \cdot \text{H}_2\text{O}/3\text{PPh}_3$	TOF = $3630 \text{ h}^{-1}$	40
$[\text{RuCl}_2(\text{benzene})_2]/\text{dppe}$	TON = 852	40
$[\text{RuCl}_2(\text{benzene})_2]/\text{dppp}$	TON = 1376	40
$[\text{Rh}(\text{Cp}^*)\text{bpy}(\text{H}_2\text{O})]\text{SO}_4$	TON = >80	25
$[\text{Ru}_2\text{Cl}_2(\text{DMSO})_4]$	TOF = $17\,800 \text{ h}^{-1}$	120
$[\text{RuCl}_2(\text{NH}_3)_6]$	TOF = $18\,000 \text{ h}^{-1}$	120
$[\text{RuCl}_3]$	TOF = $17\,400 \text{ h}^{-1}$	120
$[\text{Ru}_2(\text{HCO}_2)_2(\text{CO})_4]$	TOF = $17\,800 \text{ h}^{-1}$	120

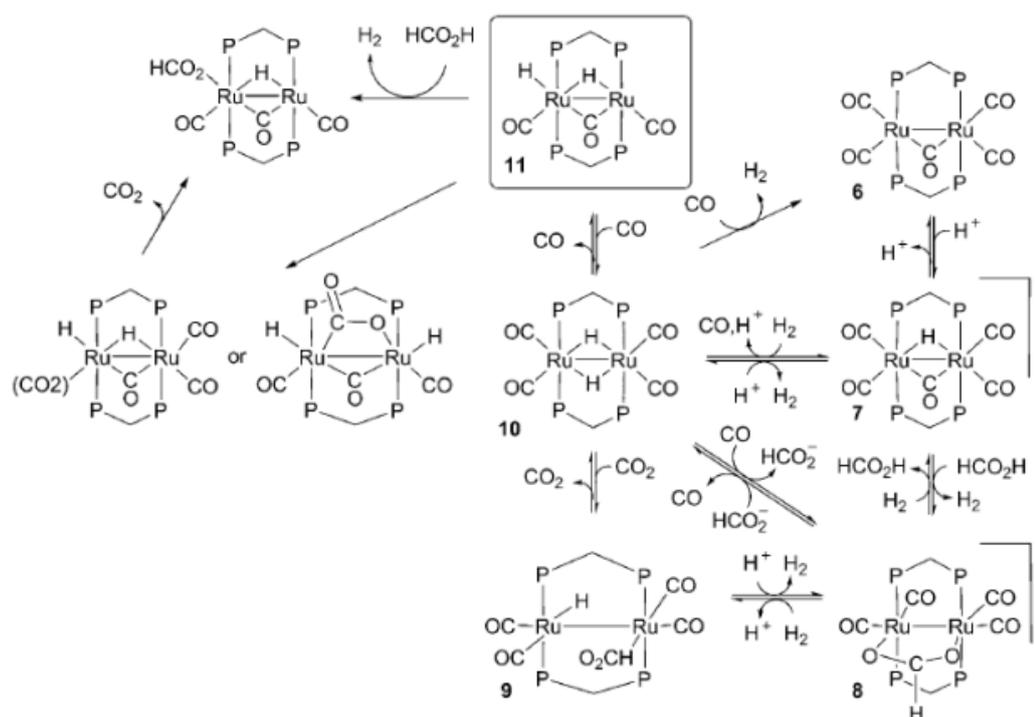
Forster and Beck used rhodium and iridium iodocarbonyl compounds in the presence of hydroiodic acid, achieving a TOF of  $4.4 \text{ h}^{-1}$  in 70% aqueous formic acid at  $100 \text{ }^\circ\text{C}$ .<sup>62</sup>

Studying homogeneously catalyzed WGS, it was found that  $\text{Ru}_3(\text{CO})_{12}$  catalyzes the decomposition of formate in basic media at  $75 \text{ }^\circ\text{C}$ .<sup>63</sup>

Strauss *et al.* reported the use of  $[\text{Rh}(\text{C}_6\text{H}_4\text{PPh}_2)(\text{PPh}_3)_2]$  as precursor. The Rh–C  $\sigma$ -bond present in the complex promoted the formation of a formate species as stable intermediate that subsequently catalysed formic acid dehydrogenation.<sup>64</sup>

Later works by Otsuka,<sup>65</sup> Paonessa and Trogler<sup>66</sup> reported the decomposition of formic acid using different Pt complexes. Catalyst activity was generally low, with the exception platinum phosphine catalyst  $[\text{Pt}\{\text{P}(\text{iPr})_3\}_3]$  reaching a TOF =  $100 \text{ h}^{-1}$  at room temperature.<sup>65</sup> Moreover, the authors isolated the active catalytic intermediates  $[\text{Pt}(\text{O}_2\text{CH})\{\text{P}(\text{iPr})_3\}_2\text{H}]$  and  $[\text{Pt}\{\text{P}(\text{iPr})_3\}_2(\text{H})_2]$ .

Puddephatt and co-workers investigated in depth the activity of the binuclear ruthenium phosphine complex  $[\text{Ru}_2(\mu\text{-CO})(\text{CO})_4(\mu\text{-dppm})_2]$  in formic acid dehydrogenation. Using this catalyst, selective and quantitative formic acid dehydrogenation was achieved with a TOF of  $500 \text{ h}^{-1}$  after 20 min, without the addition of a base. Mechanistic studies were carried out by NMR spectroscopy and various intermediate hydride and formate complexes were identified.  $[\text{Ru}_2\text{H}(\mu\text{-H})(\mu\text{-CO})(\text{CO})_2(\mu\text{-dppm})_2]$  was isolated and characterised by X-ray crystallography. In the presence of triethylamine the reverse reaction ( $\text{CO}_2$  hydrogenation) was successfully performed, achieving a maximum  $\text{HCO}_2\text{H}:\text{NEt}_3$  ratio of 1.2:1.<sup>67</sup>



**Scheme 1.9.** Catalytic cycle proposed for formic acid dehydrogenation in the presence of  $[\text{Ru}_2(\mu\text{-CO})(\text{CO})_4(\mu\text{-dppm})_2]$ .<sup>67a</sup>

In the last years several research groups focused their research on the potential of formic acid low temperature dehydrogenation as a hydrogen source. In 2008 Beller and co-workers investigated different homogeneous catalyst precursors such as  $\text{RhCl}_3 \cdot x\text{H}_2\text{O}$ ,  $[\{\text{RuCl}_2(\text{p-cymene})\}]_2$ ,  $[\text{RuCl}_2(\text{PPh}_3)_3]$ ,  $[\{\text{RuCl}_2(\text{benzene})_2\}]_2$  and  $\text{RuBr}_3 \cdot x\text{H}_2\text{O}$  at 40 °C, establishing the influence of different amines and different phosphine ligands on the activity and productivity of the catalytic systems.<sup>68</sup>

Activation of formic acid by an appropriate base was required at first. In the extensive study on nitrogen bases, Beller's group demonstrated that tertiary alkyl amines such as triethylamine ( $\text{NEt}_3$ ), *N,N*-dimethyl-*n*-hexylamine, and *N,N*-dimethylethanolamine allow for significantly higher catalyst activities compared to pyridine, piperidine, urea, *N,N,N',N'*-tetramethylurea, *N,N*-dimethylglycine as well as diethanolamine and ethanolamine. The rate of hydrogen production was correlated with the  $\text{pK}_a$  of the corresponding  $\text{R}_3\text{NH}^+$  ions of each base, concluding that the increase of amine content resulted in an increase of activity (Figure 1.3).<sup>68c</sup>

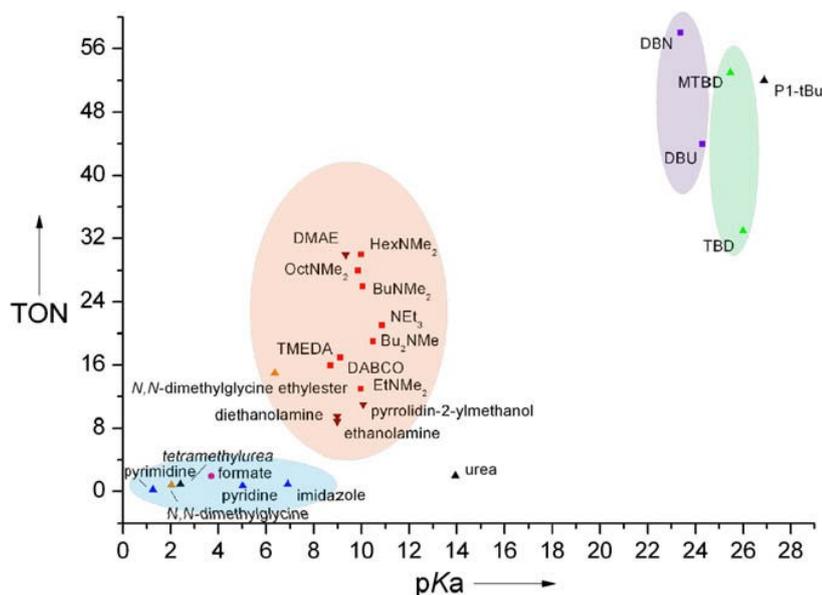


**Figure 1.3.** Relationship between  $pK_a$  of  $R_3NH^+$  ions and TON values in FA dehydrogenation in the presence of  $[\{RuCl_2(benzene)_2\}]_2/dppe$  catalyst.<sup>68c</sup>

Furthermore, it was shown that the type and concentration of ligands play an important role. Bidentate phosphine ligands with short alkyl groups like 1,2-bis(diphenylphosphino)ethane (dppe) gave generally better activity than their equivalents with longer carbon chains (e.g. 1,2-bis(diphenylphosphino)butane (dppb)).

The commercially available complex  $[RuCl_2(PPh_3)_3]$  showed a TOF of  $446.5\text{ h}^{-1}$  after 3 h, in  $HCO_2H/NEt_3$  (FA/TEA = 5:2) at  $40\text{ }^\circ\text{C}$ . The rates were similar at  $26.5\text{ }^\circ\text{C}$ , with TOF =  $181\text{ h}^{-1}$  and  $204\text{ h}^{-1}$  after 2 h and 6 h, respectively. Interestingly, with a pretreatment of the ruthenium complex in DMF for 2h at  $80\text{ }^\circ\text{C}$ , a TOF of  $2688\text{ h}^{-1}$  was achieved after the first 20 minutes. The system was demonstrated to run a PEM fuel cell with a maximum power of 47 mW at a voltage of 374 mV for more than 29 h. Later, the catalytic performance was improved with a catalyst produced *in situ* from  $RuBr_3$  and 3 equivalents of  $PPh_3$ , yielding an initial TOF of  $3630\text{ h}^{-1}$ .<sup>68b</sup>

The best results were obtained with the catalytic system generated *in situ* from  $[RuCl_2(benzene)]_2$  with  $N,N$ -dimethyl-*n*-hexylamine and 6 equiv. of dppe, yielding a total TON of 260000 over a period of two months with an average TOF =  $900\text{ h}^{-1}$ . More recently, under optimized conditions the same catalytic system showed TON up to 800000 and a TOF of  $48000\text{ h}^{-1}$  at  $80\text{ }^\circ\text{C}$ , setting the benchmark test for Ru catalysts for this reaction so far (Figure 1.4).<sup>69</sup>

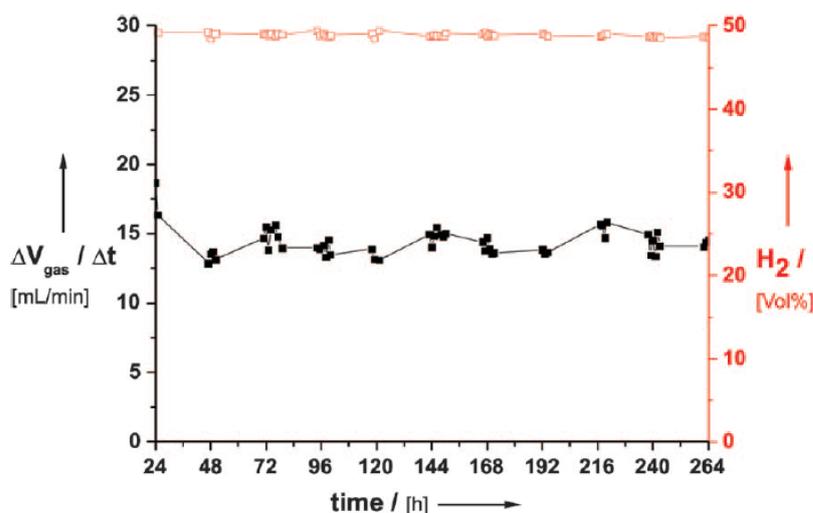


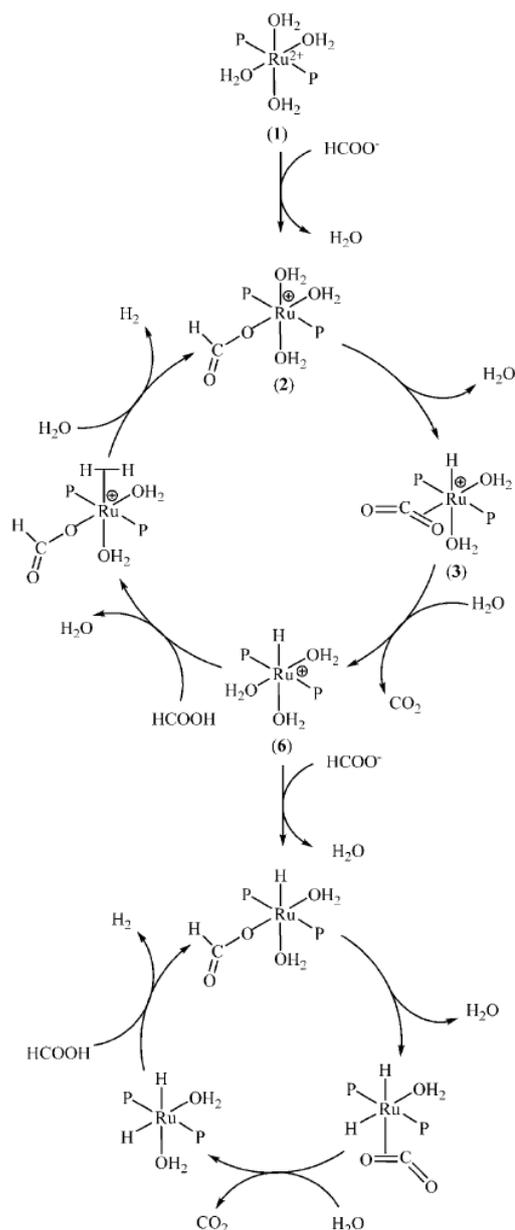
**Figure 1.4.** Continuous hydrogen production at room temperature using in situ  $[\text{RuCl}_2(\text{benzene})]_2/\text{dppe}$  (1:6) with *N,N*-dimethyl-*n*-hexylamine at 80 °C.<sup>69</sup>

The same authors also reported that the decomposition of formic acid over selected Ru-based catalysts can be accelerated or even triggered by irradiation with light (light source a PerkinElmer Cermax 300 W xenon-arc lamp with a filter cutting off UV below 380 nm and IR wavelengths between 780 and 1200 nm).<sup>70</sup>

At the same time, Laurency and co-workers reported a continuous ruthenium-based system for the catalytic dehydrogenation of a mixture of formic acid/sodium formate (9:1) in aqueous solution, in a range temperature between 70 and 120 °C.<sup>52</sup>

In this system, formic acid is added into a reactor containing a solution of  $[\text{Ru}(\text{H}_2\text{O})_6](\text{OTs})_2$  with *meta*-trisulfonated triphenylphosphine (*m*TPPTS) in water with a small quantity of sodium formate to activate the catalyst. At lower temperatures only small amounts of hydrogen were observed, while at 120 °C a TOF up to 460 h<sup>-1</sup> was achieved, reaching more than 40000 cycles. In all cases a conversion of 90–95% was obtained. Notably, hydrogen could be produced at pressures between 1 and 220 bar, and no loss of catalytic activity is observed up to 750 bar. No CO contamination was shown during the analysis of the evolved hydrogen gas, which than can be used directly in fuel cells.

Later on, the reaction mechanism of the formic acid dehydrogenation was studied and several intermediates of the catalytic cycle were identified by spectroscopic investigations.<sup>71</sup>

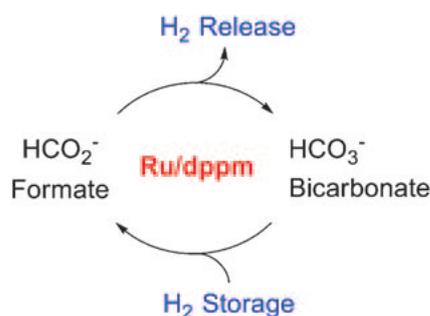


**Scheme 1.10.** Proposed mechanism for FA dehydrogenation by the Ru/*m*TPPTS system in water involving two competing cycles (P = *m*TPPTS).<sup>71</sup>

Following studies were then carried out on the influence of different sulfonato aryl and aryl/alkylphospine<sup>72a</sup> and biaryl sulfonated ligands<sup>72b</sup> as well as the Ru concentration on the formic acid dehydrogenation activity using RuCl<sub>3</sub> and [RuCl<sub>2</sub>(benzene)]<sub>2</sub> as the catalyst precursors. The results showed that ligand basicity, hydrophilicity and steric effects are the main parameters to promote the highest catalyst activity. Maximum formic acid decomposition rates were obtained with *meta*-disulfonated triphenylphosphine (*m*TPPDS) and *meta*-trisulfonated

triphenylphosphine(*m*TPPTS) and a TOF = 476 h<sup>-1</sup> at 90 °C was calculated for an Ru(III) precursor concentration of 28 mmol L<sup>-1</sup> together two equivalents of *m*TTPDS.<sup>72a</sup>

The possibility to couple FA dehydrogenation and bicarbonate hydrogenation as “hydrogen battery” device was recently assessed. Beller *et al.*<sup>73</sup> investigated the feasibility of a formate/bicarbonate cycle as reversible hydrogen storage system using [ $\{\text{RuCl}_2(\text{benzene})\}_2$ ] as the catalyst precursor in the presence of 1,2-bis(diphenylphosphino)methane (dppm) in water/DMF (5:1) in both hydrogen release and uptake of various carbonates, bicarbonates and hydroxides with the corresponding formates. The system NaHCO<sub>3</sub>/HCOONa showed good activity and formate/carbonate yields in a range temperature of 40–60 °C and H<sub>2</sub> pressure of 8 MPa. In both reactions the catalytic activity dropped in the second cycle.



**Scheme 1.10.** Hydrogen uptake and hydrogen release in the bicarbonate/ formate system.<sup>73a</sup>

Joó and co-workers<sup>74</sup> studied a rechargeable hydrogen storage device based on the hydrogenation of bicarbonate and decomposition of formate in aqueous solution with [ $\{\text{RuCl}_2(\textit{m}\text{TPPMS})_2\}_2$ ]<sup>+</sup> (*m*TPPMS = sodium diphenylphosphinobenzene-3-sulfonate), in both directions without the need of isolating either the formate or bicarbonate to start a new cycle. No organic solvents were needed and the reaction mixture showed excellent stability upon prolonged use.

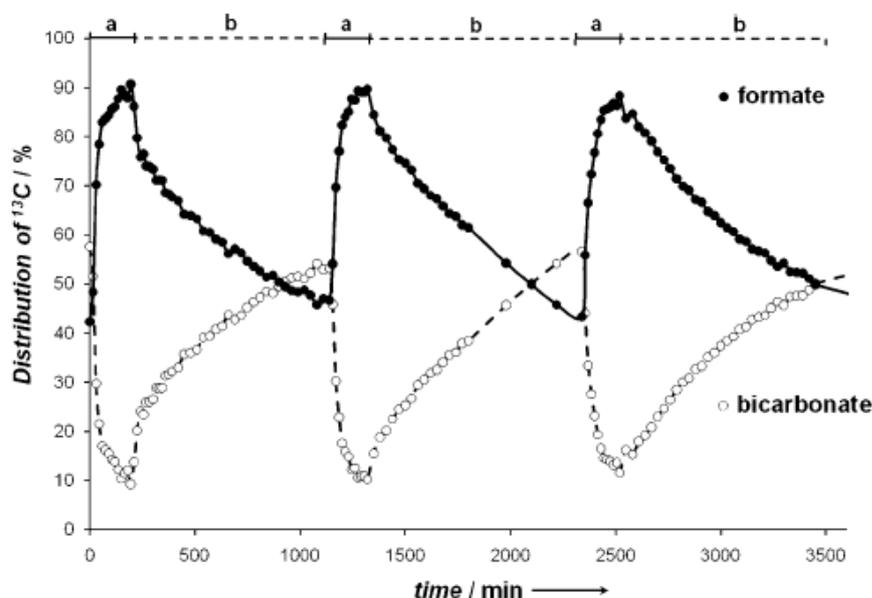
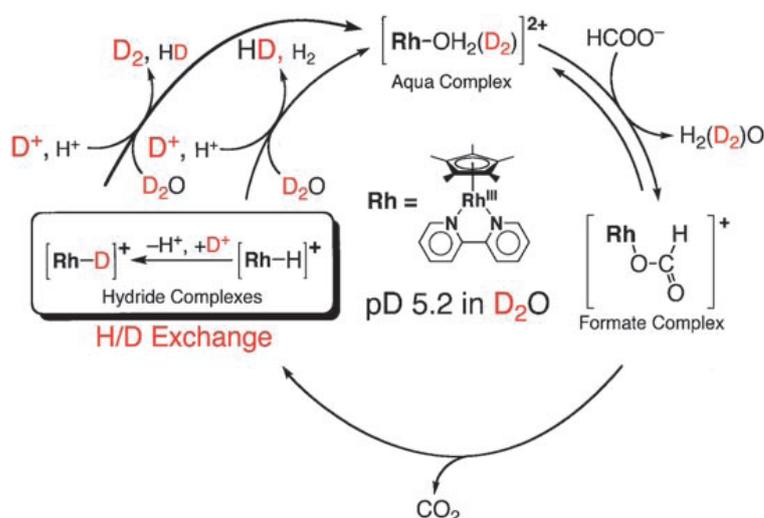


**Figure 1.5.** Relative amounts (%) of formate and bicarbonate during cycles of a) storage and b) generation of H<sub>2</sub> in a closed reactor. Catalyst: [ $\{\text{RuCl}_2(m\text{TPPMS})_2\}_2\text{]}^+$ ,  $[\text{Ru}] = 10 \text{ mM}$ ;  $[\text{H}^{13}\text{CO}_3\text{Na}] = 0.257 \text{ M}$ ;  $V(\text{D}_2\text{O}) = 2 \text{ mL}$ ;  $V(\text{total}) = 7 \text{ mL}$ ;  $T = 83 \text{ }^\circ\text{C}$ ; a)  $P(\text{H}_2) = 100 \text{ bar}$ ; b)  $P(\text{H}_2, \text{initial}) = 1 \text{ bar}$ .<sup>74</sup>

Another water-soluble catalyst, in this case the rhodium complex  $[\text{Cp}^*\text{Rh}(\text{bpy})(\text{H}_2\text{O})]\text{SO}_4$  ( $\text{Cp}^*$  = pentamethylcyclopentadienyl; bpy = bipyridine) has been described by Fukuzumi and co-workers to be very efficient for formic acid dehydrogenation at  $25 \text{ }^\circ\text{C}$ .<sup>75</sup>  $\text{CO}_2/\text{H}_2$  gas mixtures were produced from an aqueous solution of formic acid/sodium formate, reaching a maximum TOF  $> 80 \text{ h}^{-1}$  at  $\text{pH} = 3.8$ . There was no evidence of CO generation and the catalyst showed good activity and stability after repeated additions of formic acid. A detailed study of H/D exchange and deuterium kinetic isotope effect showed that hydrogen is formed via the formate complex  $[\text{Cp}^*\text{Rh}\{\text{OC}(\text{O})\text{H}\}(\text{bpy})]^+$  followed by the rate determining  $\beta$ -hydrogen elimination to provide the hydride complex  $[\text{Cp}^*\text{RhH}(\text{bpy})]^+$  (Scheme 1.11).



**Scheme 1.11.** Catalytic cycle for formic acid dehydrogenation catalyzed by  $[\text{Cp}^*\text{Rh}(\text{bpy})(\text{H}_2\text{O})]\text{SO}_4$  in  $\text{D}_2\text{O}$ .<sup>75</sup>

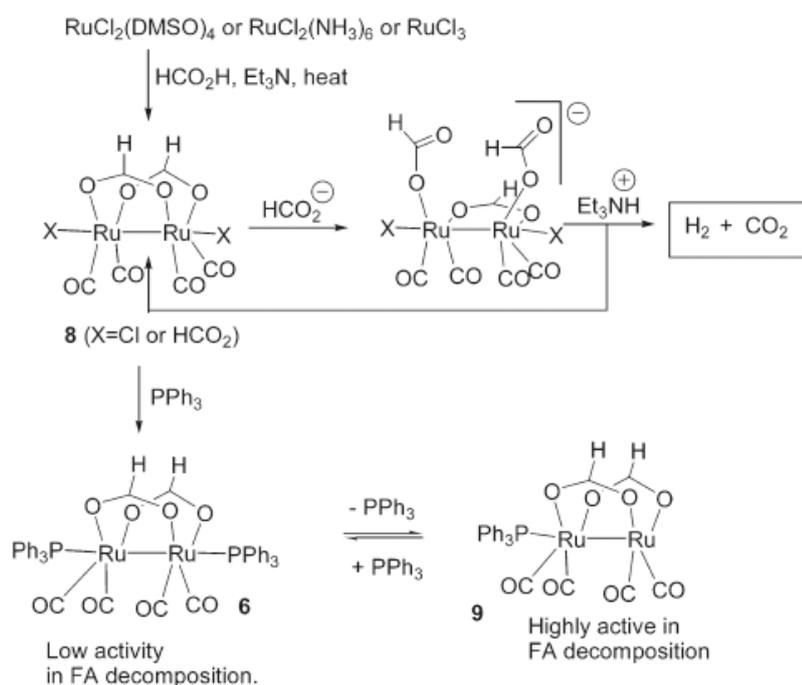
Recently, the same group reported FA dehydrogenations with TOF values up to 426  $\text{h}^{-1}$  in the presence of the heterodinuclear iridium–ruthenium complex  $[\text{Cp}^*\text{Ir}(\text{H}_2\text{O})(\text{bpm})\text{Ru}(\text{bpy})_2]_4^+$  (bpm = 2,2'-bipyrimidine) using aqueous  $\text{HCOOH}$ – $\text{HCOONa}$  solutions at room temperature and an optimized  $\text{pH} = 3.8$ .<sup>76</sup>

On the basis of previous work on  $\text{CO}_2$  hydrogenation,<sup>77</sup> Himeda and co-workers studied the activity of different Ru, Rh and Ir based catalysts with 4,4'-substituted 2,2'-bipyridine ligands in the dehydrogenation of aqueous solutions of formic acid.<sup>78</sup> Only the  $[\text{Cp}^*\text{Ir}(4,4'\text{-hydroxy-2,2'-bipyridine})]^{2+}$  complex showed a substantial activity with  $\text{TOF} = 2800 \text{ h}^{-1}$  at 60 °C, increasing to  $1.4 \times 10^4 \text{ h}^{-1}$  at 90 °C. No CO formation or catalyst degradation was observed. Moreover, the authors showed a strong pH influence due to the acid–base equilibrium of the hydroxyl group on the ligand, which was kept responsible for the high catalyst activity by increased solubility and positive electronic effects on the metal centre.

Recently, Himeda *et al*<sup>79</sup> reported the use of the  $[\text{Cp}^*\text{Ru}(\text{DHBP})]^+$  and  $[\text{Cp}^*\text{Rh}(\text{DHBP})]^{2+}$  (DHBP = 4,4'-bis(hydroxy)bipyridine) complexes in the interconversion between formic acid and  $\text{H}_2/\text{CO}_2$ . The best results were obtained with the Ru catalyst in both reactions. Also in this case, the pH play an important role on the catalytic activity.

Wills and co-workers found that hydrogen can be generated from formic acid/amine adducts (FA/TEA) using several Ru(II) and Ru(III) catalyst precursors such as

$[\text{RuCl}_2(\text{DMSO})_4]$ ,  $[\text{RuCl}_2(\text{NH}_3)_6]$ ,  $[\text{RuCl}_3]$  and  $[\text{Ru}_2(\text{HCO}_2)_2(\text{CO})_4]$  at  $120\text{ }^\circ\text{C}$  without the addition of phosphine ligands.<sup>80</sup> In the presence of these catalysts, the selective dehydrogenation of formic acid was very rapid (TOF ca.  $1.8 \times 10^4\text{ h}^{-1}$ ) and highly selective, with low levels of CO (ca. 0.02 mol%) detected in the outflows. The authors suggested that the precatalyst formed under reaction conditions a bis-ruthenium complex containing bridging formate and carbonyl ligands such as  $[\text{Ru}_2(\mu\text{-HCO}_2)_2(\text{CO})_4(\text{X})_2]$  common regardless to the Ru precursors used.



**Scheme 1.12.** Proposed catalytic cycle in  $\text{H}_2$  generation from FA using ruthenium complexes.<sup>80</sup>

Later on, the same authors demonstrated the efficient continuous generation of hydrogen and  $\text{CO}_2$  from a mixture of formic acid and triethylamine with  $[\text{RuCl}_2(\text{DMSO})_4]$  catalyst by using either a temperature- or impedance-based feed system to control the rate of formic acid replenishment.<sup>81</sup>

Olah *et al.* observed a different group of Ru carbonyl complexes whilst investigating the behavior of  $\text{RuCl}_3$  in an aqueous formic acid solution, in presence of  $\text{HCOONa}$ .<sup>82</sup> After the addition of formate,  $\text{H}_2$  and  $\text{CO}_2$  evolved with  $\text{TOF} = 275\text{ h}^{-1}$  at  $100\text{ }^\circ\text{C}$ . A considerable amount of CO (0.21%) was detected. The active catalyst species was identified as a tetranuclear ruthenium complex  $[\text{Ru}_4(\text{CO})_{12}\text{H}_4]$ , indicating that the Ru

species react with CO from formic acid decarbonylation to form the catalyst. Replacing water with DMF as reaction solvent, the solubility of  $[\text{Ru}_4(\text{CO})_{12}\text{H}_4]$  was improved and the activity was observed to increase ( $\text{TOF} = 1470 \text{ h}^{-1}$  at  $107 \text{ }^\circ\text{C}$ ). Unfortunately, recycling experiments showed a substantial deactivation after the first run.

More recently, the same group investigated for the first time the catalytic dehydrogenation of formic acid using  $\text{RuCl}_3 \cdot x\text{H}_2\text{O}$  and  $\text{PPh}_3$  as catalyst precursors in emulsion and in biphasic (aqueous/organic) systems. It was found that both the activity and the selectivity of the reported catalysts were enhanced by adding surfactants, especially sodium dodecyl sulfate to the toluene/water biphasic system.<sup>83</sup> Ruthenium carbonyls, such as  $[\text{Ru}(\text{HCO}_2)_2(\text{CO})_2(\text{PPh}_3)_2]$ ,  $[\text{Ru}(\text{CO})_3(\text{PPh}_3)_2]$ , and  $[\text{Ru}_2(\text{HCO}_2)_2(\text{CO})_4(\text{PPh}_3)_2]$ , have been isolated from the crude reaction mixtures and structurally characterized.

The presence of solvent, amine and formic acid vapor in the generated hydrogen from formic acid decomposition can cause a dramatically decreased fuel cell efficiency. The use of ionic liquids (ILs) as the reaction medium is an interesting approach to avoid solvent evaporation. Ionic liquids have a melting point below  $100 \text{ }^\circ\text{C}$  and their properties can be tuned according to the system requirements. In recent years, several studies were reported using different Ru-based catalyst in combination with different ILs for the formic acid dehydrogenation under mild conditions.<sup>84</sup>

An important target in organometallic catalysis is the replacement of noble metal-based catalysts, such as ruthenium, iridium, palladium, and rhodium, with non-precious metal catalysts such as iron compounds.

In 2009, the first examples of active homogeneous iron catalysts,  $\text{FeCl}_3$  and  $\text{FeCl}_2$ , for the generation of hydrogen from formic acid under ambient conditions were reported by Wills and co-worker as well as by Beller's group.<sup>69a</sup> However, these catalysts suffered from low activity and poor selectivity.

Recently, Beller and co-workers presented a different light-driven Fe based organometallic catalyst capable of generating hydrogen from formic acid under ambient conditions.<sup>85</sup> By studying the effects of various P- and N-ligands in the presence of metal carbonyl complexes, the initial  $\text{Fe}_3(\text{CO})_{12}$  precursor with 6,6''-(phenyl)-2,2':6,2''-terpyridine and  $\text{PPh}_3$  exhibited an initial TOF of  $200 \text{ h}^{-1}$  at  $60 \text{ }^\circ\text{C}$ .

It was demonstrated that in the presence or absence of visible light irradiation, hydrogen evolution can be either promoted or stopped. This implies that the precatalysts are activated into their active form only when irradiated. However, irreversible loss of CO from the metal precursor leads to a quick deactivation of the catalytic system.

In a following study, the same authors developed a new system for non-noble-metal-catalyzed formic acid dehydrogenation. Replacing  $\text{PPh}_3$  with two benzyl-substituted phosphines, benzyldiphenylphosphine ( $\text{PPh}_2\text{Bn}$ ) and tribenzylphosphine ( $\text{PBn}_3$ ), a tenfold improvement in catalytic activity was obtained (from  $\text{TOF} = 22$  to  $46 \text{ h}^{-1}$ ). The key to the success of the new system is the use of benzylphosphine as a ligand, which undergoes a remarkable ortho-metalation reaction upon irradiation with visible light.<sup>86</sup>

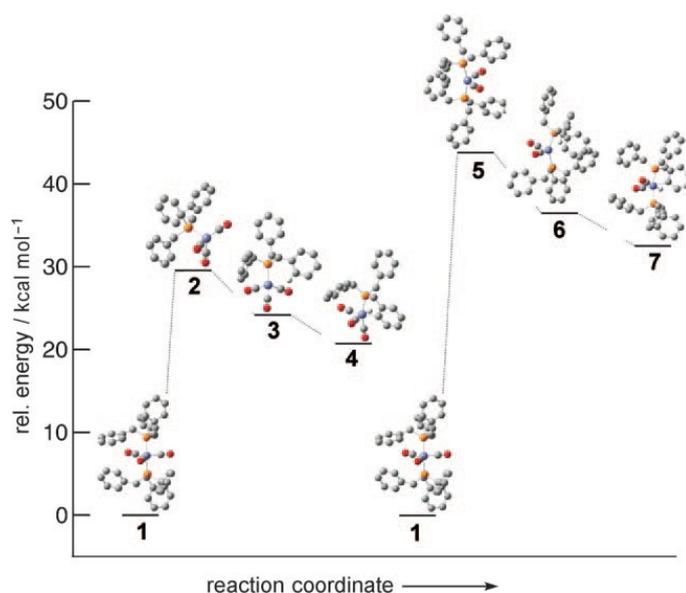
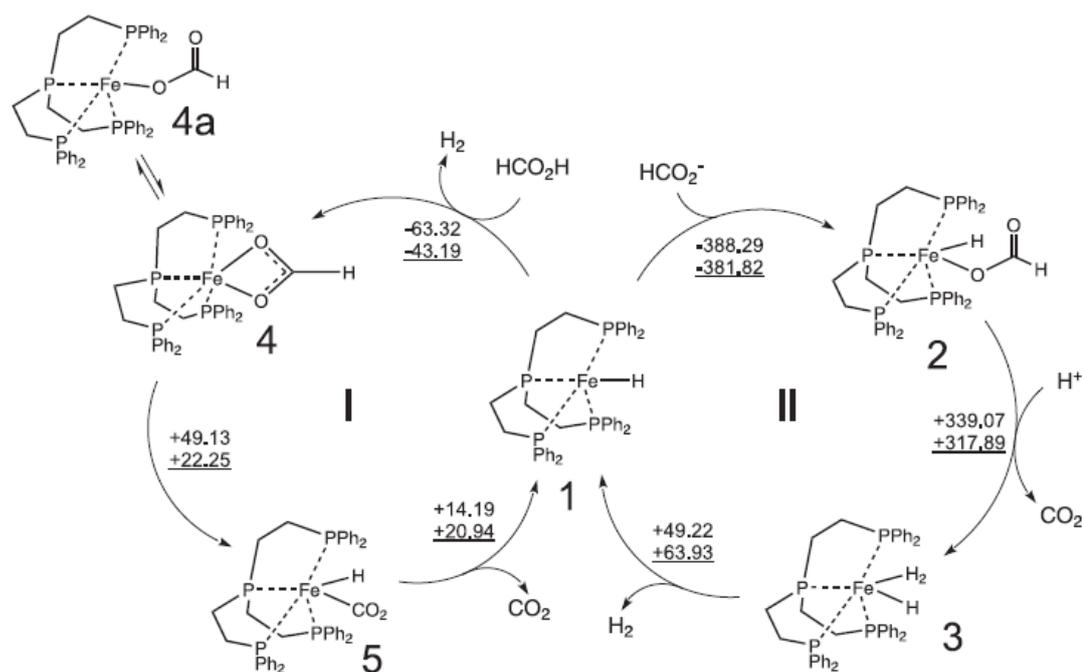


**Figure 1.6.** Relative energies for the conversion of  $[\text{Fe}(\text{CO})_3(\text{PBn}_3)_2]$  (1) into the metalated species  $[\text{HFe}(\text{C}_6\text{H}_4\text{CH}_2\text{PBn}_2)(\text{CO})_3]$  (4) and  $[\text{HFe}(\text{C}_6\text{H}_4\text{CH}_2\text{PBn}_2)(\text{PBn}_3)(\text{CO})_2]$  (7) via the intermediates  $[\text{Fe}(\text{PBn}_3)_2(\text{CO})_2]$  (5) or  $[\text{Fe}(\text{PBn}_3)(\text{CO})_3]$  (2).<sup>86</sup>

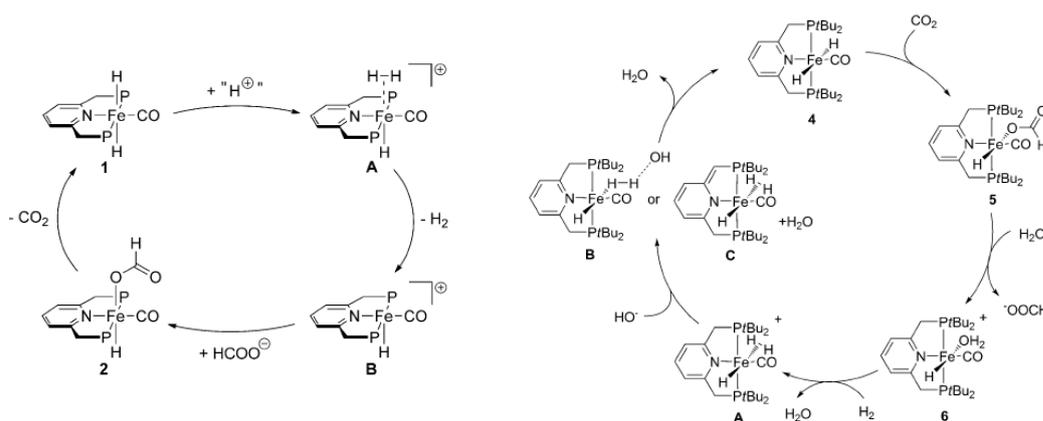
More recently, Beller's group reported the efficient hydrogen generation from formic acid catalyzed either by the combination  $\text{Fe}(\text{BF}_4)_2 \cdot 6\text{H}_2\text{O}/\text{PP}_3$  ( $\text{PP}_3 = \text{tris}[2\text{-(diphenylphosphino)ethyl}]$  phosphine) or the pre-isolated complexes  $[\text{FeH}(\text{PP}_3)]\text{BF}_4$ ,  $[\text{FeH}(\text{H}_2)(\text{PP}_3)]\text{BF}_4$ ,  $[\text{FeH}(\text{H}_2)(\text{PP}_3)]\text{BPh}_4$  and  $[\text{FeCl}(\text{PP}_3)]\text{BF}_4$  in propylene carbonate as a solvent, without the need for an additional base.<sup>87</sup> Except for  $[\text{FeCl}(\text{PP}_3)]\text{BF}_4$ , excellent activities were observed for all the systems, with a maximum TOF of 1942

$\text{h}^{-1}$  after 3 h at 40 °C using  $\text{Fe}(\text{BF}_4)_2 \cdot 6\text{H}_2\text{O}$  with an equivalent of  $\text{PP}_3$ . Remarkably, this system showed in a continuous hydrogen production experiment at 80 °C an outstanding performance with  $\text{TON} = 92000$  and  $\text{TOF} = 9425 \text{ h}^{-1}$ . A mechanism for the selective iron-catalyzed hydrogen generation from formic acid was proposed, based on NMR studies and DFT calculations (Scheme 1.12).



**Scheme 1.12.** Proposed mechanism for the selective iron-catalyzed hydrogen generation from formic acid with calculated relative energies for key complexes ( $\text{kJ mol}^{-1}$ ).<sup>87</sup>

Milstein and co-workers described an iron dihydride *pincer* complex  $[\text{Fe}(\text{t}^{\text{Bu}}\text{PNP})(\text{H})_2(\text{CO})]$  ( $\text{t}^{\text{Bu}}\text{PNP} = 2,6\text{-bis}(\text{di-tert-butylphosphinomethyl})\text{pyridine}$ ) which showed a good activity and selectivity in formic acid dehydrogenation at 40 °C in the presence of trialkylamines, with TON of up to 100000.<sup>88</sup> The same complex was reported earlier as an efficient catalyst for the low-pressure hydrogenation of carbon dioxide to sodium formate in aqueous solutions of sodium hydroxide.<sup>89</sup>



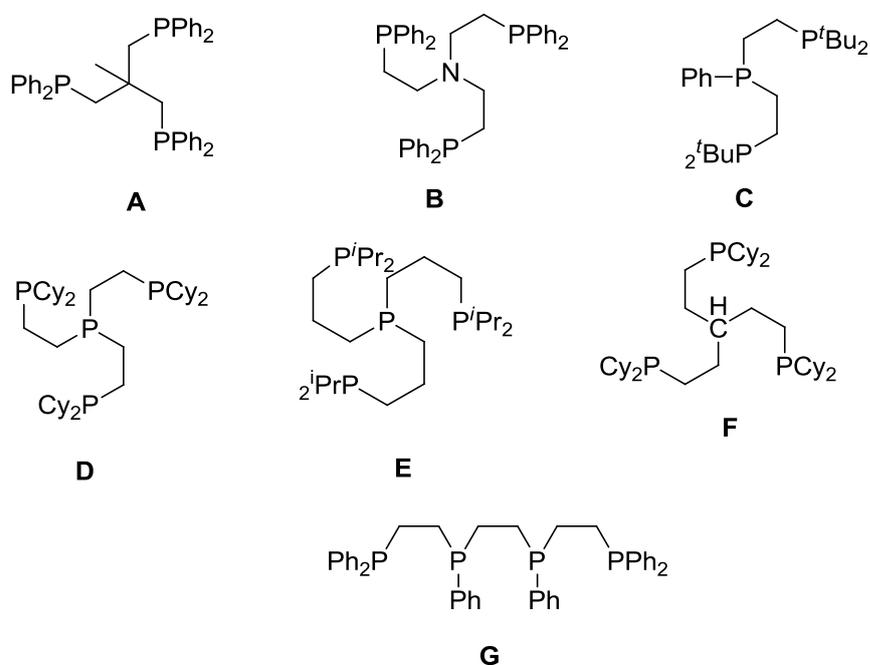
**Scheme 1.13.** Proposed mechanisms for the dehydrogenation of formic acid<sup>88</sup> and hydrogenation of  $\text{CO}_2$ <sup>89</sup> catalyzed by complex  $[\text{Fe}(\text{tBu})\text{PNP}](\text{H})_2(\text{CO})$ .

More recently, Schneider and co-workers reported a new pincer-type iron catalyst that, in the presence of a Lewis acid (LA) co-catalyst (10 mol%), achieves the highest TON (1000000) reported for formic acid dehydrogenation using a first-row transition metal catalyst. Preliminary experiments indicated that the LA assists in the decarboxylation of a key iron formate intermediate and can also be used to enhance the reverse process of  $\text{CO}_2$  hydrogenation.<sup>90</sup>

## 1.5 Aim of the work

The primary aim of this work has been to target new homogeneous catalysts for the selective dehydrogenation of formic acid to hydrogen and carbon dioxide. For this purpose, a variety of different transition metal complexes stabilized by polydentate phosphine ligands has been evaluated, also through collaborative work with other groups leading the research in this field. Polydentate phosphines are recognized as one of the most important classes of ligands having widespread applications in coordination chemistry. Such ligands provide an important advantage over monodentate phosphines with respect to greater control of the coordination number, stoichiometry and stereochemistry of their complexes. Moreover, polyphosphine complexes have two or more chelate rings which may help to reduce the number of possible inactive isomers in complexes, and therefore, can be expected to convey better catalyst stability and higher catalytic activities.

Most of the state-of-the-art results described above was described in the literature in the same years of this doctoral project. Until now, the best results for formic acid dehydrogenation was obtained in the case of Ru-catalyzed processes with the  $[\text{RuCl}_2(\text{benzene})]_2/\text{dppe}$  ( $\text{dppe} = 1,2\text{-bis}[\text{diphenylphosphino}]\text{ethane}$ ) system in the presence of *N,N*-dimethyl-*n*-hexylamine, under solventless conditions<sup>69</sup> and recently, many efforts were done to develop cheaper and equally efficient systems based on non-noble transition metals such as Fe/ $\text{PP}_3$ .<sup>87</sup> Our main interest was thus focused on the dehydrogenation of formic acid catalyzed by ruthenium and iron species both obtained *in situ* and pre-synthesized as molecularly defined complexes bearing tridentate and tetradentate phosphines (Scheme 1.14).



**Scheme 1.14.** Tridentate and tetradentate phosphines used in this work.

Mechanistic NMR studies and DFT calculations have often complemented the catalytic studies in order to understand the mechanism of substrate activation and pre-catalyst modifications during the catalytic cycle and to highlight differences which could be related to metal and ligand effects.

Chapters 2 and 3 describe our results obtained with Ru(II) complexes containing ligands **A-G**. Chapter 4 summarizes the synthesis, reactivity and application of a

series of Fe(II) complexes bearing ligand **G**. Finally, the Appendix section contains all major Supporting Information related to the previous chapters.

## 1.6 References

- <sup>1</sup> a) Bockris, J. *Science* **1972**, *176*, 1323; b) Crabtree, G.W.; Dresselhaus, M.S.; Buchanan, M. V. *Phys Today* **2004**, *57*, 39; c) Armaroli, N.; Balzani, V. *Angew, Chem. Int. Ed.* **2007**, *46*, 52
- <sup>2</sup> a) Zuttel, A.; Borgschulte A.; Schlapbach, L. *Hydrogen as a Future Energy Carrier*, Wiley VCH, Weinheim, **2008**; b) Armaroli, N.; Balzani, V. *ChemSusChem* **2011**, *4*, 21; c) Lubitz, W.; Tumas, B. *Chem. Rev.* **2007**, *107*, 3900; d) Eberle, U.; Felderhoff M.; Schüth, F. *Angew. Chem., Int. Ed.* **2009**, *48*, 6608; e) Thomas, M. K. *Catal. Today* **2007**, *120*, 389.
- <sup>3</sup> G. A. Olah, A. Goepfert, G. K. S. Prakash, *Beyond Oil and Gas: The Methanol Economy*, Wiley-VCH, Weinheim, **2006**.
- <sup>4</sup> Balzani, V.; Credi, A.; Venturi, M. *ChemSusChem* **2008**, *1*, 26.
- <sup>5</sup> Koumi Ngoh, S.; Njomo, D. *Renewable and Sustainable Energy Reviews* **2012**, *16*, 6782.
- <sup>6</sup> WEC, 2010 Survey of Energy Resources Interim, **2010**. Available from <http://www.worldenergy.org/> (accessed November 2010).
- <sup>7</sup> Stone, R. *Science* **2008**, *321*, 628.
- <sup>8</sup> Pagliaro, M.; Ciriminna, R.; Palmisano, G. *ChemSusChem* **2008**, *1*, 880.
- <sup>9</sup> a) Johnson, J. *Chem. Eng. News* **2008**, *86*, 40; b) Service, R. F. *Science* **2008**, *319*, 718.
- <sup>10</sup> a) Fujishima, A.; Honda, K. *Nature* **1972**, *238*, 37; b) Youngblood, W. J.; Lee, S. H. A.; Kobayashi, Y.; Hernandez-Pagan, E. A.; Hoertz, P. G.; Moore, T. A.; Moore, A. L.; Gust, D.; Mallouk, T. E. *J. Am. Chem. Soc.* **2009**, *131*, 926.
- <sup>11</sup> (a) Kapdan, I.; Kargi, F. *Enzyme Microb. Technol.* **2006**, *38*, 56; (b) Barreto, L.; Makihira, A.; Riahi, K. *Int. J. Hydrogen Energy*, **2003**, *28*, 267.
- <sup>12</sup> (a) Turner, J.; Sverdrup, G.; Mann, M.; Maness, P.; Kroposki, B.; Ghirardi, M.; Evans R.; Blake, D. *Int. J. Energy Res.* **2008**, *32*, 379; (b) Moriarty, P.; Honnery, D. *Int. J. Hydrogen Energy*, **2009**, *34*, 31.
- <sup>13</sup> a) Magnuson, A.; Anderlund, M.; Johansson, O.; Lindblad, P.; Lomoth, R.; Polivka, T.; Ott, S.; Stensjöt, K.; Styring, S.; Sundström, V.; Hammarström, *Acc. Chem. Res.* **2009**, *42*, 1899; b) Voith, M. *Chem. Eng. News* **2009**, *87*, 22.
- <sup>14</sup> van den Berg, A. W. C.; Arèan C. O. *Chem. Comm.* **2008**, 668.
- <sup>15</sup> Svec, F.; Germain, J.; Frechet, J. M. J. *Small* **2009**, *5*, 1098.
- <sup>16</sup> De Lacey, A.; Fernandez, A. *Chem. Rev.* **2007**, *107*, 4304.
- <sup>17</sup> a) Orimo, S. I.; Nakamori, Y.; Eliseo, J. R.; Zuttel, A.; Jensen, C. M. *Chem. Rev.* **2007**, *107*, 4111; b) Graetz, *J. Chem. Soc. Rev.* **2009**, *38*, 73.
- <sup>18</sup> Yang, J.; Sudik, A.; Wolverton, C.; Siegel, D. J. *Chem. Soc. Rev.* **2010**, *39*, 656.
- <sup>19</sup> Chen, P.; Xiong, Z.; Luo, J.; Lin, J.; Tan, K. L. *Nature* **2002**, *420*, 302.
- <sup>20</sup> a) Marder, T. B. *Angew. Chem.* **2007**, *119*, 8262; *Angew. Chem. Int. Ed.* **2007**, *46*, 8116; b) F. H. Stephens, V. Pons, R. T. Baker, *Dalton Trans.* **2007**, 2613.
- <sup>21</sup> Alcaraz, G.; Sabo-Etienne, S. *Angew. Chem. Int. Ed.* **2010**, *48*, 7170.
- <sup>22</sup> Okada, Y.; Sasaki, E.; Watanabe, E.; Hyodo, S.; Nishijima, H. *Int. J. Hydrogen Energy* **2006**, *31*, 1348.
- <sup>23</sup> Wang, Z.; Tonks, I.; Belli, J.; Jensen, C. M. *J. Organomet. Chem.* **2009**, *694*, 2854.
- <sup>24</sup> Wang, J.; Zhang, X-B.; Wang, Z-L.; Wanga, L-W.; Zhang, Y. *Energy Environ. Sci.* **2012**, *5*, 6885.

- <sup>25</sup> Johnson, T. C.; Morris, D. J.; Wills, M. *Energy Environ. Sci.* **2010**, *3*, 1207.
- <sup>26</sup> Alsabeh, P. G.; Mellmann, D.; Junge, H.; Beller, M. *Top. Organomet. Chem.* **2014**, *48*, 45.
- <sup>27</sup> Nielsen, M.; Alberico, E.; Baumann, W.; Drexler, H.-J.; Junge, H.; Gladiali, S.; Beller, M. *Nature* **2013**, *495*, 85.
- <sup>28</sup> a) Zeng, G.; Sakaki, S.; Fujita, K.-I.; Sano, H.; Yamaguchi, R. *ACS Catal.* **2014**, *4*, 1010; b) Polukeev, A.V.; Petrovskii, P.V.; Peregudov, A.S.; Ezernitskaya, M.G.; Koridze, A.A. *Organometallics* **2013**, *32*, 1000; c) Kawahara, R.; Fujita, K.-I.; Yamaguchi, R. *J. Am. Chem. Soc.* **2012**, *134*, 3643.
- <sup>29</sup> a) Spasyuk, D.; Smith, S.; Gusev, D.G. *Angew. Chem. Int. Ed.* **2012**, *51*, 2772; b) Putignano, E.; Bossi, G.; Rigo, P.; Baratta, W. *Organometallics* **2012**, *31*, 1133; c) Bertoli, M.; Choualeb, A.; Lough, A.J.; Moore, B.; Spasyuk, D.; Gusev, D.G. *Organometallics* **2011**, *30*, 3479; d) Baratta, W.; Boss, G.; Putignano, E.; Rigo, P. *Chem. Eur. J.* **2011**, *17*, 3474.
- <sup>30</sup> Alberico, E.; Sponholz, P.; Cordes, C.; Nielsen, M.; Drexler, H. J.; Baumann, W.; Junge, H.; Beller, M.; *Angew. Chem. Int. Ed.* **2013**, *52*, 14162.
- <sup>31</sup> (a) Jessop, P. G.; Ikariya, T.; Noyori, R. *Chem. Rev.* **1995**, *95*, 261; (b) Jessop, P. G.; Joó, F.; Tai, C. C. *Coord. Chem. Rev.* **2004**, *248*, 2425; (c) Jessop, P. G. in *The Handbook of Homogeneous Hydrogenation*, ed. J. G. de Vries and C. J. Elsevier, Wiley-VCH, Weinheim, **2007**, 489; (d) Leitner, W.; *Angew. Chem. Int. Ed.* **1995**, *34*, 2207; e) Enthaler, S. *ChemSusChem* **2008**, *1*, 801; f) Joó, F. *ChemSusChem* **2008**, *1*, 805.
- <sup>32</sup> Sabatier, P.; Mailhe, A. *Compt. Rend.* **1912**, *152*, 1212.
- <sup>33</sup> a) Trillo, J.M.; Munuera, G.; Criado, J.M.; *Catal. Rev.* **1972**, *7*, 51; b) Columbia, M.R.; Thiel, P.A. *J. Electroanal. Chem.* **1994**, *369*, 1; c) Tamaru, K. *Appl. Catal. A* **1997**, *151*, 167; d) Jarvi, T.D.; Stuve, E.M. *Electrocatalysis* **1998**, *75*; e) Hinshelwood, C.N.; Hartley, H. J. *Chem. Soc. Trans.* **1923**, *123*, 1333.
- <sup>34</sup> a) Rienäcker, G. *Z. Anorg. Allg. Chem.* **1936**, *227*, 353; b) Rienäcker, G.; Wessing, G.; Trautmann, G. *Z. Anorg. Allg. Chem.* **1938**, *236*, 252; c) Rienäcker, G.; Bade, H. *Z. Anorg. Allg. Chem.* **1941**, *248*, 45.
- <sup>35</sup> Dowden, D. A., Reynold, P. W. *Discuss. Faraday Soc.* **1950**, *8*, 184.
- <sup>36</sup> Enthaler, S.; von Langermann, J.; Schmidt, T. *Energy Environ. Sci.* **2010**, *3*, 1207.
- <sup>37</sup> Williams, R.; Crandall, R.S.; Bloom, A. *Appl. Phys. Lett.* **1978**, *33*, 381.
- <sup>38</sup> Wiener, H.; Sasson, Y.; Blum, J.; *J. Mol. Catal.* **1986**, *35*, 277.
- <sup>39</sup> Sexton, B. A. *Surf. Sci.* **1979**, *88*, 319.
- <sup>40</sup> Madix, R. *Catal. Rev. Sci. Eng.* **1984**, *26*, 281.
- <sup>41</sup> Kisfaludi, G.; Matusek, K.; Schay, Z.; Guczy L.; Lovas, A. *Mater. Sci. Eng. B* **1988**, *99*, 547.
- <sup>42</sup> Ojeda, M.; Iglesia, E. *Angew. Chem. Int. Ed.* **2009**, *48*, 4800.
- <sup>43</sup> Solymosi, F.; Koos, A.; Liliom, N.; Ugrai, I. *J. Catal.* **2011**, *279*, 213.
- <sup>44</sup> Gazsi, A.; Bansagi, T.; Solymosi, F. *J. Phys. Chem. C* **2011**, *115*, 15459.
- <sup>45</sup> Grasmann, M.; Laurency, L. *Energy Environ. Sci.* **2012**, *5*, 8171.
- <sup>46</sup> X. Zhou, Y. Huang, W. Xing, C. Liu, J. Liao and T. Lu, *Chem. Commun.* **2008**, 3540.
- <sup>47</sup> a) Senanayake, S. D.; Mullins, D. R. *J. Phys. Chem. C* **2008**, *112*, 9744; b) Xu, Y.; Gordon, W. O.; Senanayake, S. D.; Mullins, D. R.; Overbury, S. H. *Abstr. Pap. Am. Chem. Soc.* **2009**, 237; c) Zhou, X.; Huang, Y.; Liu, C.; Liao, J.; Lu, T.; Xing, W. *ChemSusChem* **2010**, *3*, 1379.
- <sup>48</sup> Gu, X.; Lu, Z.H.; Jiang, H.L.; Akita, T.; Xu, Q. *J. Am. Chem. Soc.* **2011**, *133*, 11822.
- <sup>49</sup> Ting, S.W.; Cheng, S.; Tsang, K.Y.; van der Laak, N.; Chan, K.Y. *Chem. Commun.* **2009**, 7333.
- <sup>50</sup> Huang, Y.; Zhou, X.; Yin, M.; Liu, C.; Xing, W. *Chem. Mater.* **2010**, *22*, 5122.
- <sup>51</sup> Tedsree, K.; Li, T. *Nat. Nanotechnol.* **2011**, *6*, 302.
- <sup>52</sup> Fellay, C.; Dyson, P. J.; Laurency, G. *Angew. Chem. Int. Ed.* **2008**, *47*, 3966.

- <sup>53</sup> Gan, W.; Dyson, P. J.; Laurencyzy, G. *React. Kinet. Catal. Lett.* **2009**, *98*, 205.
- <sup>54</sup> Zhao, Y.; Deng, L.; Tang, S.Y.; Lai, D.M.; Liao, B.; Fu, Y.; Guo, Q.X. *Energy Fuels* **2011**, *25*, 3693.
- <sup>55</sup> Koos, A.; Solymosi, F. *Catal. Lett.* **2010**, *138*, 23.
- <sup>56</sup> Flaherty, D. W.; Berglund, S. P.; Mullins, C. B. *J. Catal.* **2010**, *269*, 33.
- <sup>57</sup> a) Dey, G. R.; Nair, K. N. R.; Pushpa, K. K. *J. Nat. Gas Chem.* **2009**, *18*, 50; b) Yun, H. J.; Lee, H.; Joo, J. B.; Kim, W.; Yi, J. J. *Phys. Chem. C* **2009**, *113*, 3050; c) Iwasawa, Y. *Abstr. Pap. Am. Chem. Soc.* **2007**, 233.
- <sup>58</sup> Miller, K. L.; Lee, C. W.; Falconer, J. L.; Medlin, J. W. *J. Catal.* **2010**, *275*, 294.
- <sup>59</sup> Zielinska, B.; Borowiak-Palen, E.; Kalenczuk, R. *J. Int. J. Hydrogen Energy* **2008**, *33*, 1797.
- <sup>60</sup> a) Aldous, L.; Compton, R. G. *Energy Environ. Sci.* **2010**, *3*, 1587; b) Guo, W. L.; Li, L.; Tian, S.; Liu, S. L.; Wu, Y. P. *Int. J. Hydrogen Energy* **2011**, *36*, 9415; c) Lamy, C.; Devadas, A.; Simoes, M.; Coutanceau, C. *Electrochim. Acta* **2012**, *60*, 112.
- <sup>61</sup> Coffey, R. S. *Chem. Commun.* **1967**, 923.
- <sup>62</sup> Forster, D.; Beck, G.R. *Chem Commun.* **1971**, 994, 1072
- <sup>63</sup> Laine, R.M.; Rinker, R.G.; Ford, P.C. *J. Am. Chem. Soc.* **1977**, *99*:252
- <sup>64</sup> Strauss, S. H.; Whitmire, K. H.; SShriver, D. F. *J. Organomet. Chem.* **1979**, *174*, C59.
- <sup>65</sup> Yoshida, T.; Yamagata, T.; Tulip, T. H.; Ibers, J. A.; Otsuka, S. *J. Am. Chem. Soc.* **1978**, *100*, 2063.
- <sup>66</sup> Paonessa, R. S.; Trogler, W. C. *J. Am. Chem. Soc.* **1982**, *104*, 3529.
- <sup>67</sup> a) Gao, Y.; Kuncheria, J.; Yap, G.P.A.; Puddephatt, R.J. *Chem. Commun.* **1998**, 2365; b) Gao, Y.; Kuncheria, J.K.; Jenkins, H.A.; Puddephatt, R.J.; Yap G.P.A. *J. Chem. Soc. Dalton Trans.* **2000**, 3212.
- <sup>68</sup> a) Loges, B.; Boddien, A.; Junge, H.; Beller, M.; *Angew. Chem. Int. Ed.* **2008**, *47*, 3962; b) Boddien, A.; Loges, B.; Junge, H.; Beller, M. *ChemSusChem* **2008**, *1*, 751; c) H. Junge, Boddien, A.; Capitta, F.; Loges, B.; Noyes, J. R.; Gladiali, S.; Beller, M. *Tetrahedron Lett.* **2009**, *50*, 1603.
- <sup>69</sup> Boddien, A.; Loges, B.; Junge, H.; Gaertner, F.; Noyes, J. R.; Beller, M. *Adv. Synth. Catal.* **2009**, *351*, 2517.
- <sup>70</sup> Loges, B.; Boddien, A.; Junge, H.; Noyes, J. R.; Baumann, W.; Beller, M. *Chem. Commun.* **2009**, 4185.
- <sup>71</sup> Fellay, C.; Yan, N.; Dyson, P. J.; Laurencyzy, G. *Chem. Eur. J.* **2009**, *15*, 3752.
- <sup>72</sup> a) Gan, W.; Fellay, C.; Dyson, P. J.; Laurencyzy, G. *J. Coord. Chem.* **2010**, *63*, 2685; b) Guerriero, A.; Bricout, H.; Sordakis, K.; Peruzzini, M.; Monflier, E. Hapiot, F.; Laurencyzy, G.; Gonsalvi, L. *ACS Catal.* **2014**, *4*, 3002-3012.
- <sup>73</sup> a) Boddien, A.; Gaertner, F.; Federsel, C.; Sponholz, P.; Mellmann, D.; Jackstell, R.; Junge, H.; Beller, M. *Angew. Chem. Int. Ed.* **2011**, *50*, 6411; b) Federsel, C.; Jackstell, R.; Boddien, A.; Laurencyzy, G.; Beller, M. *ChemSusChem* **2010**, *3*, 1048.
- <sup>74</sup> Papp, G.; Csorba, J.; Laurencyzy G.; Joó, F. *Angew. Chem. Int. Ed.* **2011**, *50*, 10433.
- <sup>75</sup> Fukuzumi, S.; Kobayashi, T.; Suenobu, T. *ChemSusChem* **2008**, *1*, 827.
- <sup>76</sup> Fukuzumi, S.; Kobayashi, T.; Suenobu, T. *J. Am. Chem. Soc.* **2010**, *132*, 1496.
- <sup>77</sup> Himeda, Y. *Eur. J. Inorg. Chem.* **2007**, 3927.
- <sup>78</sup> Himeda, Y. *Green Chem.* **2009**, *11*, 2018.
- <sup>79</sup> Himeda, Y.; Miyazawa, S.; Hirose, T. *ChemSusChem* **2011**, *4*, 487.
- <sup>80</sup> Morris, D. J.; Clarkson, G. J.; Wills, M. *Organometallics* **2009**, *28*, 4133.
- <sup>81</sup> Majewski, A.; Morris, D. J.; Kendall, K.; Wills, M. *ChemSusChem* **2010**, *3*, 431.
- <sup>82</sup> Czaun, M.; Goeppert, A.; May, R.; Haiges, R.; Prakash, G. K. S.; Olah, G. A. *ChemSusChem* **2011**, *4*, 1241.
- <sup>83</sup> Czaun, M.; Goeppert, A.; Kothandaraman, J.; May, R.B.; Haiges, R.; Prakash, G. K.S.; Olah, G. A. *ACS Catal.* **2014**, *4*, 311.

- 
- <sup>84</sup> a) Li, X.; Ma, X.; Shi, F.; Deng, Y. *ChemSusChem* **2010**, *3*, 71; b) Scholten, J. D.; Precht, M. H. G.; Dupont, J. *ChemCatChem* **2010**, *2*, 1265; c) Yasaka, Y.; Wakai, C.; Matubayasi, N.; Nakahara, M. *J. Phys. Chem. A* **2010**, *114*, 3510; Berger, M. E. M.; Assenbaum, D.; Taccardi, N.; Spiecker, E.; Wasserscheid, P. *Green Chem.* **2011**, *13*, 1411.
- <sup>85</sup> Boddien, A.; Loges, B.; Gaertner, F.; Torborg, C.; Fumino, K.; Junge, H.; Ludwig, R.; Beller, M. *J. Am. Chem. Soc.* **2010**, *132*, 8924.
- <sup>86</sup> Boddien, A.; Gaertner, F.; Jackstell, R.; Junge, H.; Spannenberg, A.; Baumann, W.; Ludwig, R.; Beller, M. *Angew. Chem., Int. Ed.* **2010**, *49*, 8993.
- <sup>87</sup> Boddien, A.; Mellmann, D.; Gaertner, F.; Jackstell, R.; Junge, H.; Dyson, P. J.; Laurency, G.; Ludwig, R.; Beller, M. *Science* **2011**, *333*, 1733.
- <sup>88</sup> Zell, T.; Butschke, B.; Ben-David, Y.; Milstein, D. *Chem. Eur. J* **2013**, *19*, 8068.
- <sup>89</sup> Langer, R.; Diskin-Posner, Y.; Leitus, G.; Shimon, L. J. W.; Ben-David, Y.; Milstein, D. *Angew. Chem. Int. Ed.* **2011**, *50*, 9948.
- <sup>90</sup> Bielinski, E.A.; Lagaditis, P.O.; Zhang, Y.; Mercado, B.Q.; Würtele, C.; Bernskoetter, W.H.; Hazari, N.; Schneider, S. *J. Am. Chem. Soc.* **2014**, *136*, 10234.



# Chapter 2

## Formic acid dehydrogenation catalysed by ruthenium complexes bearing the tripodal ligands triphos and NP<sub>3</sub>

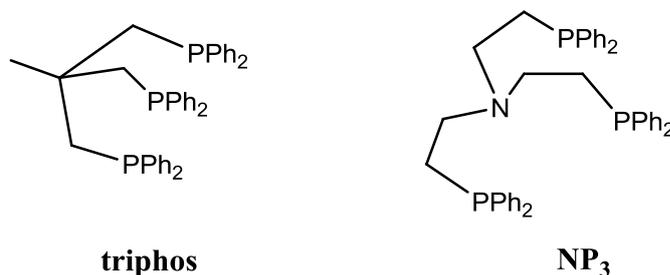
### 2.1 Overview

This Chapter opens with a brief summary of literature data on selected ruthenium triphos and NP<sub>3</sub> complexes, and their important applications in catalysis. Then, the synthesis of complexes [Ru( $\kappa^3$ -triphos)(MeCN)<sub>3</sub>](OTf)<sub>2</sub> (**1**), [Ru( $\kappa^4$ -NP<sub>3</sub>)Cl<sub>2</sub>] (**2**) and *cis*-[Ru( $\kappa^3$ -triphos)(CO)(H)<sub>2</sub>] (**3**) used as catalysts in formic acid dehydrogenation reaction is reported, followed by the detailed description of results of catalytic tests. These studies were carried out in collaboration with the group of Prof. M. Beller at LIKAT, Rostock (Germany). In the second part of this Chapter, mechanistic studies by VT NMR spectroscopy and DFT calculations, which gave information on the nature of some of the species formed during the reaction of the catalysts with formate and formic acid/ amine adduct, are described. In the last part of the Chapter, the experimental section summarizes details of the catalytic tests, VT NMR experiments and DFT methodologies.

## 2.2 Introduction

Ruthenium polydentate phosphine-based systems have received much attention due to their potential catalytic activities in a wide variety of reactions.

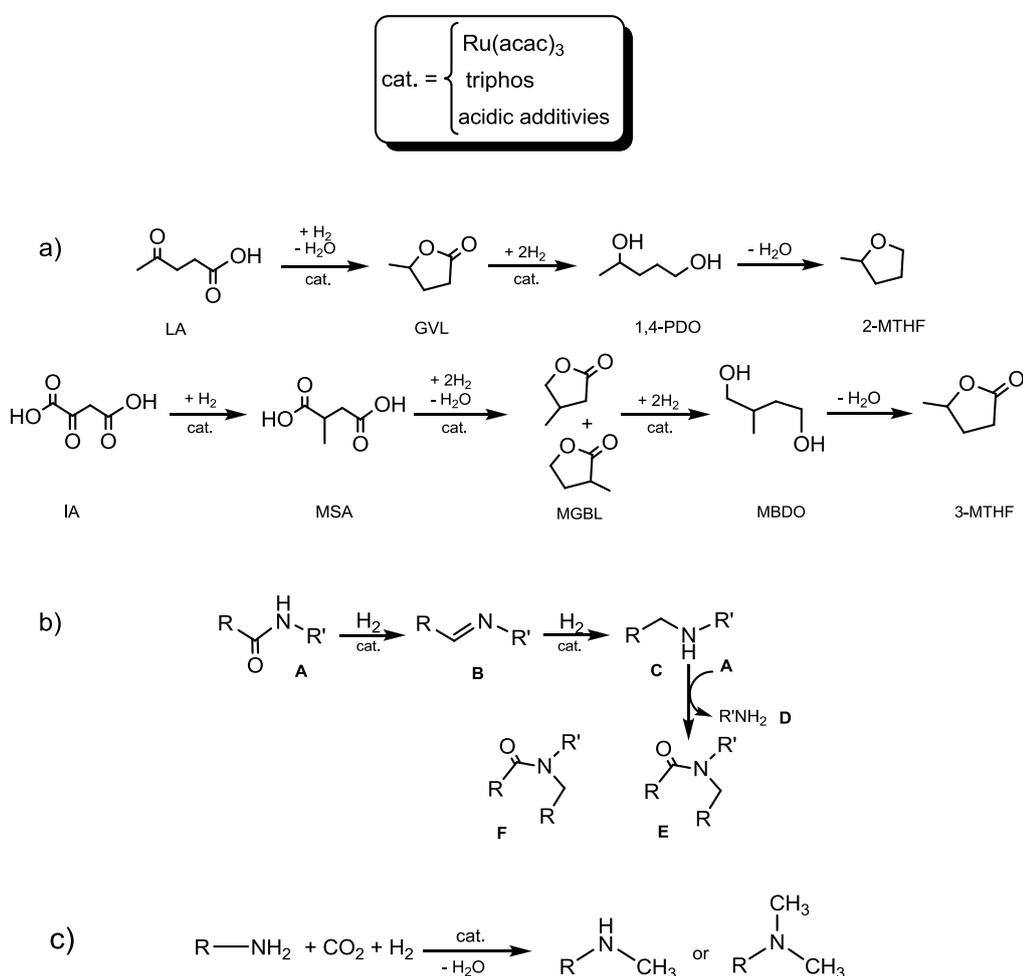
Among these ligands, the facially capping tridentate 1,1,1-tris(diphenylphosphinomethyl)ethane (triphos) and tetradentate ligand tris(2-diphenylphosphinoethyl) amine (NP<sub>3</sub>) (Scheme 2.1) have found interesting applications which are here briefly summarized.



**Scheme 2.1.** Polydentate ligands triphos and NP<sub>3</sub>.

Triphos and its derivatives are the most extensively investigated for coordination to transition metal complexes, many of which have found applications in catalysis.<sup>1,2</sup> Bianchini and co-workers pioneered the use of this ligand in homogeneous catalysis using platinum group metals for a number of processes, including hydrogenation and hydroformylation of alkenes,<sup>3</sup> hydrogenation of N-heterocycles,<sup>4</sup> hydrogenation, hydrogenolysis, and hydrodesulfurization of thiophene<sup>5</sup> and oxidation of catechols.<sup>6</sup> In particular, the reactivity of ruthenium(II)-triphos complexes toward various substrates in hydrogenation reactions<sup>7,8</sup> were studied extensively by NMR and IR spectroscopies.<sup>9</sup> The increased stability provided by the tripodal nature of the triphos ligand was found to be crucial to obtain highly active catalysts for the hydrogenation of esters, amides, and even carboxylic acids.<sup>10</sup> In recent years the use of molecularly defined ruthenium-triphos complexes as well as catalytic systems obtained *in situ*, by mixing an adequate Ru precursor with triphos, were employed in reactions such as the selective catalytic conversion of biomass feedstock<sup>10c, 11</sup> and CO<sub>2</sub> utilization for the production of fuels and chemicals.<sup>12</sup>

Leitner and co-workers reported the use of the multifunctional catalyst systems composed of the ruthenium precursor  $\text{Ru}(\text{acac})_3$ , the ligand triphos and acidic additives for the conversion of levulinic acid (LA) and itaconic acid (IA) to a set of isomeric lactones, diols and cyclic esters via hydrogenation and dehydration sequences (Scheme 2.2a). In the presence of a  $\text{Ru}(\text{acac})_3$ :triphos = 1:2 ratio, levulinic acid (LA) and itaconic acid (IA) were converted into the desired products with high yields, at 160 °C under a hydrogen pressure (100 bar).<sup>13</sup> Hydrogenation of N-aryl substituted amides<sup>14</sup> and methylation of amines<sup>15</sup> has also been achieved under similar conditions (Scheme 2.2b,c).



**Scheme 2.2.** Reactions catalyzed by *in situ*  $\text{Ru}(\text{acac})_3/\text{triphos}$  system.<sup>13,14,15</sup>

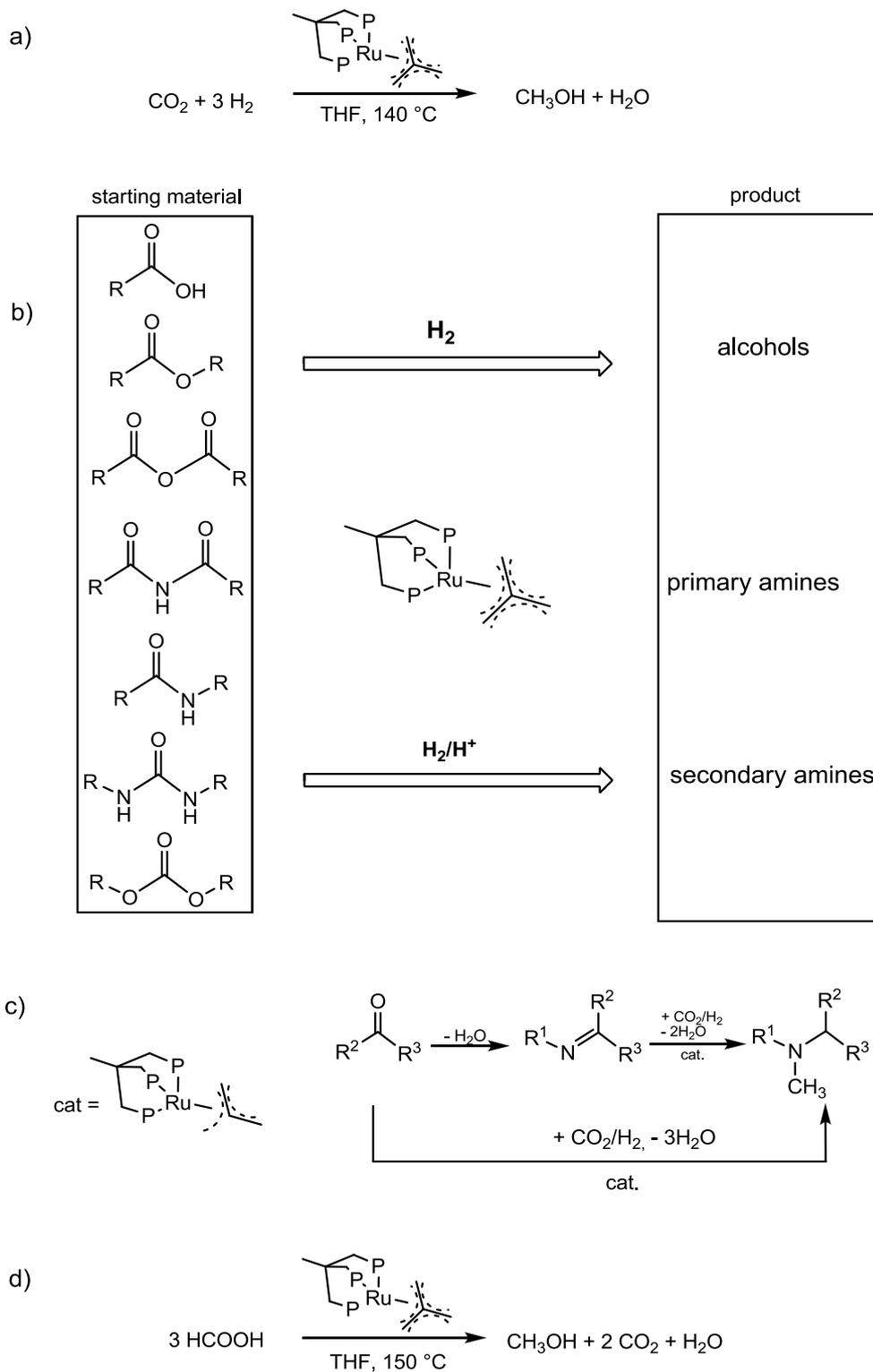
More recently, the same authors showed that the *in situ* generated  $\text{Ru}(\text{acac})_3/\text{triphos}$  system and the ruthenium complex  $[\text{Ru}(\text{triphos})(\text{TMM})]$  (TMM =

trimethylenemethane) are active in the homogeneous hydrogenation of CO<sub>2</sub> to methanol, at 140 °C under a carbon dioxide and hydrogen pressure of 20 and 60 bar, respectively (Scheme 2.3a).<sup>16, 17</sup> Mechanistic studies obtained from NMR experiments and DFT calculations demonstrated that the cationic formate complex [Ru(triphos)(η<sup>2</sup>-O<sub>2</sub>CH)(S)]<sup>+</sup> (S = solvent) is the catalytically active species. This complex could be synthesized from various catalyst precursors in presence or absence of acidic co-catalysts.<sup>16</sup> Moreover, the ruthenium complexes [Ru(triphos)(TMM)] was found to be an efficient catalyst in the hydrogenation of a broad range of challenging unsaturated functional groups including carboxylic esters, amides, carboxylic acids, carbonates, and urea derivatives as well as in the methylation of imines (Scheme 2.3b,c).<sup>18</sup>

Cantat and co-workers reported the efficient disproportionation of formic acid to methanol using [Ru(triphos)(TMM)]. The reaction was carried out in THF at 150 °C in the presence of methanesulfonic acid reaching methanol yields of up to 50.2 % (Scheme 2.3d).<sup>19</sup>

Another interesting polydentate phosphine is the tetradentate tris(2-diphenylphosphinoethyl)amine (NP<sub>3</sub>). The presence of the amine N donor and of ethylene spacer separating the P donors from the bridgehead atom makes NP<sub>3</sub> more sterically and coordinatively flexible than other polyphosphines, and increases the overall basicity at the metal center. These peculiarities impart particular coordinative properties and sometimes an unexpected chemical behavior.<sup>20</sup>

Differently from triphos, there are few examples of ruthenium complexes bearing NP<sub>3</sub>. Romero *et al.* reported the dehydration of propargyl alcohol derivatives with [Ru(NP<sub>3</sub>)Cl<sub>2</sub>] to give allenylidene- and alkenyl-allenylidene-Ru(NP<sub>3</sub>) complexes.<sup>21</sup> Dahlenburg *et al.* showed that the ruthenium complex [Ru(NP<sub>3</sub>)H(Ph)] was an active catalyst for the dimerization of 1-alkynes, RC≡CH (R = Ph, Bu, CMe<sub>3</sub>) yielding 1,4-disubstituted 1-en-3-yne, RCH=CHC≡CR, with varying E/Z stereoselectivities. In particular, good results were obtained for the dimerization of n-BuC≡CH to give (Z)-(n-Bu)CH=CHC≡C(n-Bu) with a selectivity >95%.<sup>22</sup>



**Scheme 2.3.** Reactions catalyzed by [Ru(triphos)(TMM)].<sup>16,18,19</sup>

Jia *et al.* also studied the alkyne dimerization in organic and aqueous media using complex  $[\text{Ru}(\text{NP}_3)\text{H}(\text{CH}_3\text{CN})]\text{OTf}$  obtaining the selective dimerization of both aliphatic and aromatic alkynes to give (*Z*)-enynes.<sup>23</sup>

Recently, Rossin *et al.* reported the synthesis and characterization of  $\text{NP}_3$  ruthenium hydrides,  $[\text{Ru}(\text{NP}_3)(\text{H})_2]$  and  $[\text{Ru}(\text{NP}_3)\text{H}(\text{H}_2)]\text{BAr}^{\text{Cl}}_4$  and showed that both complexes are active homogeneous catalysts for ammonia borane dehydrogenation at room temperature. A combination of experimental data (VT NMR spectroscopy, kinetic rate measurements, kinetic isotope effect determination) and DFT calculations demonstrated two different reaction mechanisms for the two catalysts due to the coordination flexibility of  $\text{NP}_3$  that plays a crucial role in tuning the catalytic performance of the related transition-metal complexes.<sup>24</sup>

### 2.3 Synthesis of Ru complexes bearing triphos and $\text{NP}_3$

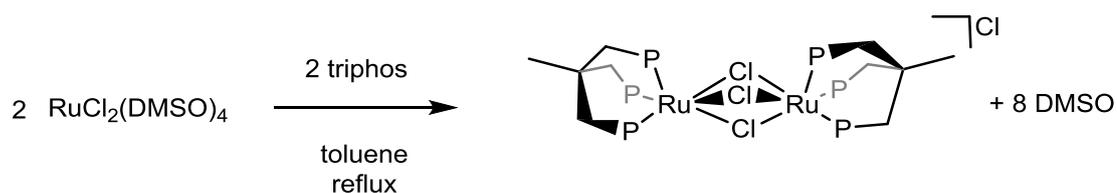
Although a variety of metal complexes with multidentate phosphine ligands have been shown to be efficient catalysts for  $\text{HCOOH}$  dehydrogenation and  $\text{CO}_2$  hydrogenation (see Chapter 1), to the best of our knowledge neither triphos nor  $\text{NP}_3$  ligands had been reported in combination with Ru precursors for the former reaction. Thus, we decided to investigate the behaviour of such complexes and ligands for  $\text{HCOOH}$  dehydrogenation. In particular, we selected the known complexes  $[\text{Ru}(\kappa^3\text{-triphos})(\text{MeCN})_3](\text{OTf})_2$  (**1**),  $[\text{Ru}(\kappa^4\text{-NP}_3)\text{Cl}_2]$  (**2**) and *cis*- $[\text{Ru}(\kappa^3\text{-triphos})(\text{CO})(\text{H})_2]$  (**3**). The synthesis of such complexes was carried out in our laboratories and is here described.

#### ***Synthesis of $[\text{Ru}(\kappa^3\text{-triphos})(\text{MeCN})_3](\text{OTf})_2$ (1)***

The synthesis of  $[\text{Ru}(\text{triphos})(\text{MeCN})_3]^{2+}$  complex was initially reported by Venanzi *et al.*<sup>25</sup> using the method outlined by Crabtree and Pearman<sup>26</sup> for the synthesis of the cationic complexes  $[\text{Ru}(\text{MeCN})\text{L}_3]^{2+}$  (L =  $\text{PMe}_2\text{Ph}$ ,  $\text{PMePh}_2$ ) through halogen abstraction from  $[\text{L}_3\text{Ru}(\mu\text{-Cl})_3\text{RuL}_3]^+$  in acetonitrile. Chatt *et al.*<sup>27</sup> obtained these binuclear complexes by refluxing  $\text{RuCl}_3 \cdot n\text{H}_2\text{O}$  with an excess of phosphine in 2-methoxyethanol. However, when triphos was used in this reaction, only moderate yields (ca. 40%) of the yellow product  $[\text{Ru}_2(\mu\text{-Cl}_3)(\text{triphos})_2\text{Cl}_3]\text{Cl}$  were obtained.

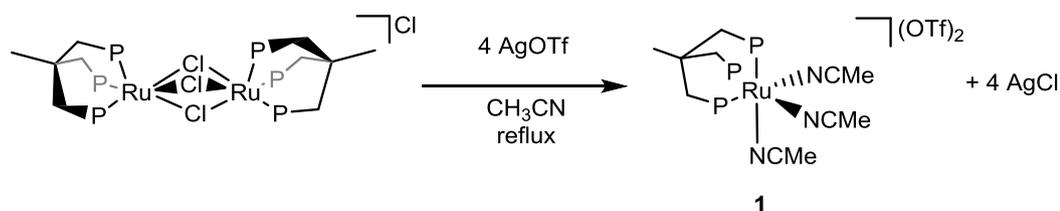
The yields of  $[\text{Ru}_2(\mu\text{-Cl}_3)(\text{triphos})_2\text{Cl}_3]\text{Cl}$  were increased to ca. 60% by reacting ruthenium “blue solutions” in methanol with only 1 molar equivalent of triphos in 2-methoxyethanol.<sup>28</sup>

A further yield increase (ca. 80%) of  $[\text{Ru}_2(\mu\text{-Cl}_3)(\text{triphos})_2\text{Cl}_3]\text{Cl}$  was obtained by refluxing  $[\text{RuCl}_2(\text{DMSO})_4]$  with triphos in toluene<sup>29</sup> (Scheme 2.4). The  $^{31}\text{P}$  NMR spectrum of  $[\text{Ru}_2(\mu\text{-Cl}_3)(\text{triphos})_2\text{Cl}_3]\text{Cl}$  showed a singlet at 36.0 ppm, consistent with a face-sharing bioctahedral structure with bridging chlorides.



**Scheme 2.4.** Synthesis of  $[\text{Ru}_2(\mu\text{-Cl}_3)(\text{triphos})_2\text{Cl}_3]\text{Cl}$ .<sup>29</sup>

The reaction of  $[\text{Ru}_2(\mu\text{-Cl}_3)(\text{triphos})_2\text{Cl}_3]\text{Cl}$  with 4.1 equiv of AgOTf in refluxing acetonitrile gave, after workup, colorless crystals of  $[\text{Ru}(\kappa^3\text{-triphos})(\text{MeCN})_3](\text{OTf})_2$  in high yields (Scheme 2.5).<sup>25</sup>



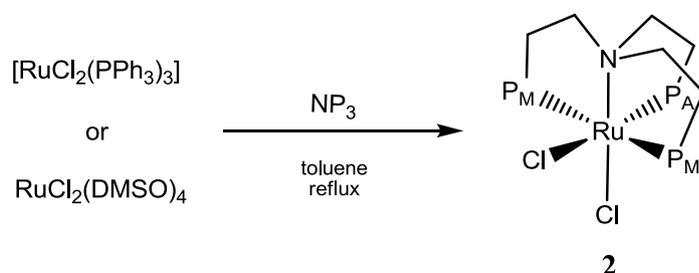
**Scheme 2.5.** Synthesis of  $[\text{Ru}(\kappa^3\text{-triphos})(\text{MeCN})_3](\text{OTf})_2$  (**1**).<sup>25</sup>

The corresponding  $^{31}\text{P}\{^1\text{H}\}$  NMR spectrum showed a singlet at 26.6 ppm, while the  $^1\text{H}$  NMR spectrum exhibited a singlet at 2.34 ppm (9 H) as expected for a tris(acetonitrile) complex.

**Synthesis of  $[\text{Ru}(\kappa^4\text{-NP}_3)\text{Cl}_2](\mathbf{2})$** 

The synthesis of  $[\text{Ru}(\kappa^4\text{-NP}_3)\text{Cl}_2]$  was reported by Dahlenburg *et al.* By refluxing  $[\text{RuCl}_2(\text{PPh}_3)_3]$  with  $\text{NP}_3$  in toluene, the complex precipitated as a yellow solid by addition of  $\text{Et}_2\text{O}$  (Scheme 2.6).<sup>22</sup>

The same reaction was carried out using  $[\text{RuCl}_2(\text{DMSO})_4]$  as ruthenium precursor. In this case the product was obtained as a microcrystalline precipitate from the reaction mixture and collected by filtration in high yields (Scheme 2.6). The corresponding  $^{31}\text{P}\{^1\text{H}\}$  NMR spectrum showed the expected  $\text{AM}_2$  spin system with the  $\text{P}_\text{A}$  triplet at 45.7 ppm ( $^2J_{\text{PP}} = 30$  Hz) and the  $\text{P}_\text{M}$  doublet at 26.6 ppm ( $^2J_{\text{PP}} = 30$  Hz).

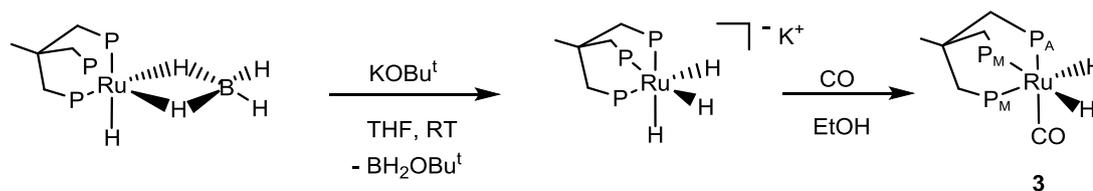


**Scheme 2.6.** Synthesis of  $[\text{Ru}(\kappa^4\text{-NP}_3)\text{Cl}_2]$  (**2**).<sup>22</sup>

**Synthesis of  $[\text{Ru}(\kappa^3\text{-triphos})(\text{CO})(\text{H})_2](\mathbf{3})$** 

The Ru carbonyl dihydride complex  $[\text{Ru}(\kappa^3\text{-triphos})(\text{CO})(\text{H})_2]$  was synthesized and characterized for the first time by Peruzzini *et al.*<sup>30</sup> The reaction of (tetrahydroborate)hydride complex  $[\text{Ru}(\text{triphos})\text{H}(\eta^2\text{-BH}_4)]$  with a slight excess of  $\text{KOBu}^\text{t}$  in anhydrous THF at room temperature gave a yellow-orange solution of  $\text{K}[\text{Ru}(\kappa^3\text{-triphos})\text{H}_3]$ .

The  $[\text{Ru}(\kappa^3\text{-triphos})(\text{CO})(\text{H})_2]$  complex **3** was obtained by adding ethanol saturated with CO to a THF solution of  $\text{K}[\text{Ru}(\kappa^3\text{-triphos})\text{H}_3]$  (Scheme 2.7), and characterized in the solid state by X-ray diffraction methods (Figure 2.1).



**Scheme 2.7.** Synthesis of  $[\text{Ru}(\kappa^3\text{-triphos})(\text{CO})(\text{H})_2]$  (**3**).<sup>30</sup>

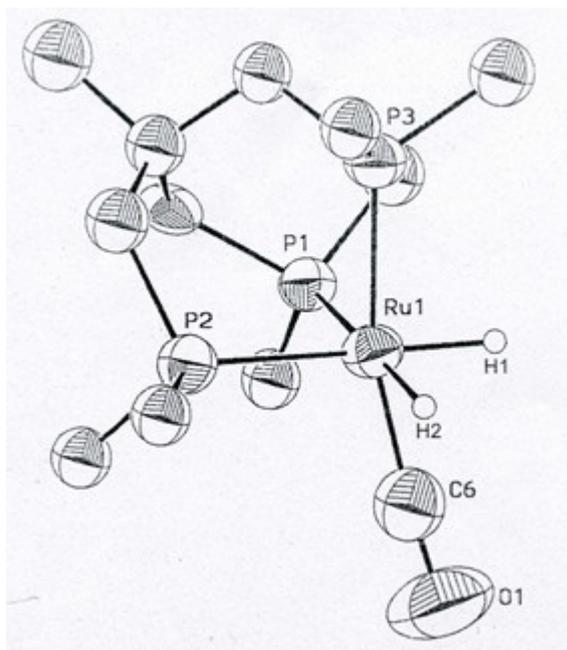
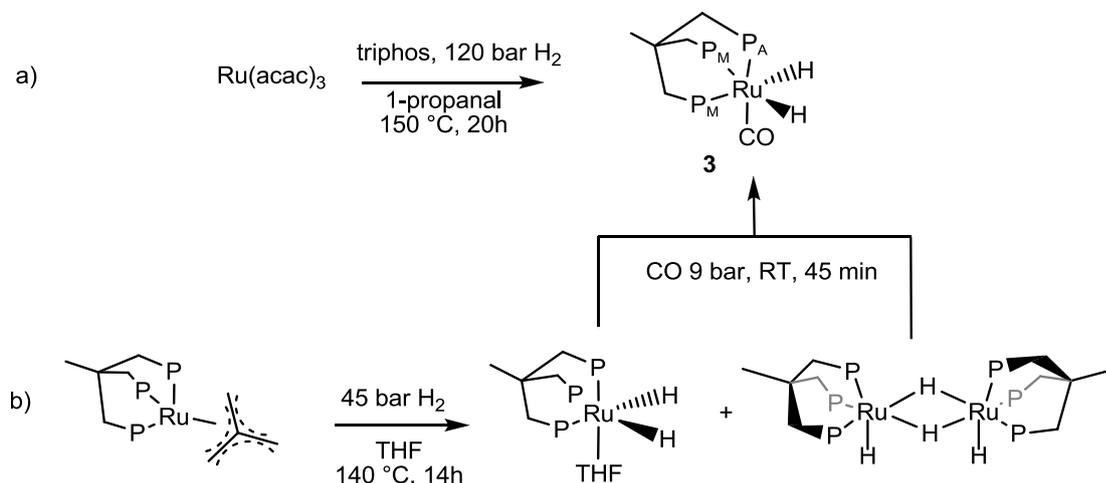


**Figure 2.1.** Molecular structure of  $[\text{Ru}(\kappa^3\text{-triphos})(\text{CO})(\text{H})_2]$ .<sup>30</sup>

The  $^{31}\text{P}\{^1\text{H}\}$  NMR spectrum of **3** showed two phosphorus signals expected for a  $\text{AM}_2$  spin system, the first as a phosphorus triplet at 34.6 ppm ( $\text{P}_\text{A}$ ) and the second as a doublet at 27.0 ppm ( $\text{P}_\text{M}$ ), with a mutual  $^2J_{\text{PP}}$  coupling constant of 30 Hz. The  $^1\text{H}$  NMR spectrum showed a signal at -7.32 ppm integrating as to two protons, in the chemical shift range expected for Ru-coordinated classical hydride ligands. The  $^{13}\text{C}\{^1\text{H}, ^{31}\text{P}\}$  NMR spectrum displayed a resonance associated with the carbonyl carbon atom at 209.9 ppm.

Recently, Leitner and co-workers reported two new useful procedures for the synthesis of **3**. In the first reaction (Scheme 2.8a), a solution of  $\text{Ru}(\text{acac})_3$  and triphos in propanal was stirred for 20 h at 150 °C under a pressure of 120 bar of hydrogen. The complex was precipitated and isolated with addition of ethanol in 84% yield.<sup>13</sup>

In the second case (Scheme 2.8b), a solution of  $[\text{Ru}(\kappa^3\text{-triphos})(\text{TMM})]$  in THF under 45 bar of hydrogen at 140 °C gave a neutral dihydride complex  $[\text{Ru}(\kappa^3\text{-triphos})(\text{THF})(\text{H})_2]$  and the dimer  $[\text{Ru}_2(\mu\text{-H})_2(\text{triphos})_2(\text{H})_2]$ . In the presence of CO, this species were converted into **3** which could be recovered after workup.<sup>18</sup>



**Scheme 2.8.** New synthetic procedures for  $[\text{Ru}(\kappa^3\text{-triphos})(\text{CO})(\text{H})_2]$  (**3**).<sup>13,18</sup>

## 2.4 Catalytic formic acid (FA) dehydrogenation tests

We have tested five variations on the catalytic system obtained by combination of Ru(II) and triphos and  $\text{NP}_3$  in the  $\text{HCOOH}$  dehydrogenation reaction to  $\text{CO}_2$  and  $\text{H}_2$ , namely (i)  $\text{Ru}(\text{acac})_3$  + triphos (1:1); (ii)  $\text{Ru}(\text{acac})_3$  +  $\text{NP}_3$  (1:1); (iii)  $[\text{Ru}(\kappa^3\text{-triphos})(\text{MeCN})_3](\text{OTf})_2$  (**1**); (iv)  $[\text{Ru}(\kappa^4\text{-NP}_3)\text{Cl}_2]$  (**2**);  $[\text{Ru}(\kappa^3\text{-triphos})(\text{CO})(\text{H})_2]$  (**3**), running the tests under atmospheric pressure, measuring the development of gas with either an automatic<sup>31</sup> or a manual gas-burette. Aliquots of the gas mixtures produced were analyzed off-line either by GC or FT-IR methods. The effect of the temperature on the productivity of the catalytic systems was also investigated, running the tests both at 40 °C and 80 °C, using either the commercial azeotropic mixture  $\text{HCOOH}/\text{NET}_3$  (5:2) or the combination  $\text{HCOOH}/\text{OctNMe}_2$  (11:10,  $\text{OctNMe}_2$  = *n*-octyldimethylamine, DMOA), respectively.<sup>32</sup>

At 40 °C using  $\text{HCOOH}/\text{NET}_3$  (5:2), the reaction proceeded with moderate TOFs using both molecular complexes **1** and **2** (see Table 2.1). GC analysis of the gas

mixtures showed the presence of a 1:1 mixture of CO<sub>2</sub> and H<sub>2</sub>, hence complete selectivity for HCOOH dehydrogenation *vs.* decarbonylation is obtained as no signal corresponding to CO was detected, implying a quantity lower than 10 ppm which is the sensitivity limit for this technique. For a maximum expected gas volume of ca. 2.91 L, under these conditions (FA:catalyst = ca. 3000), **1** produced ca. 454 mL after 18 h, whereas **2** gave ca. 564 mL after 45 h, corresponding to final TONs of 487 and 604, respectively. Disappointingly, using the *in situ* generated catalysts prepared according to methods (i)–(ii), the reactions did not show any significant activity under the conditions described in Table 2.1.

**Table 2.1.** Formic acid dehydrogenation catalyzed by complexes **1** and **2** in the presence of NEt<sub>3</sub> at 40 °C.

Entry	Catalyst	Vol (mL) after 180 min	TON after 180 min	MaxVol (mL) [t(h)]	Final TON	Final Conversion (%)
<b>1</b>	1	65	69	454 [18]	487	16
<b>2</b>	2	20	21	564 [45]	604	19

*Reaction conditions:* catalyst, 19.1 mmol; HCOOH/NEt<sub>3</sub> (5:2), 5 mL; HCOOH : catalyst = 3117, 40 °C; gas measured via automatic gas-burette and analyzed by GC (H<sub>2</sub>:CO<sub>2</sub> = 1:1).

This suggests that under such mild conditions the metal cannot be efficiently reduced from Ru(III) to the active Ru(II) form and/or be stabilized by the ancillary ligand to form catalytically active species. Improved catalytic performances were observed running the HCOOH dehydrogenation tests at 80 °C, in the presence of *n*-octyldimethylamine (Table 2.2), using HCOOH : Ru = 1000 and HCOOH : Ru = 10000 ratios. In all cases the gas volume expected for complete conversion (630 mL) was obtained at different reaction times depending on the catalytic system used. From Table 2.2, it can be concluded that the best catalytic system under the conditions applied was complex **1**, as would be expected for a Ru(II) species bearing a strongly coordinating tripodal polyphosphine and three labile solvent ligands, able in principle to make up to three coordination sites available for substrate coordination and activation. In contrast to the results reported by Leitner and co-workers for the Ru(triphos)-catalysed CO<sub>2</sub> hydrogenation to methanol under acidic conditions, which were however run at higher temperature (140 °C),<sup>16</sup> the system

based on *in situ* formation of the putative active catalyst (Table 2.2, entry 1) did not perform as efficiently as complex **1**. Complete conversion of HCOOH was reached only after 3 h instead of 1 h as for the molecular Ru-triphos complex **1**. In the case of the NP<sub>3</sub>-based system, both methods gave more sluggish conversions than triphos (Table 2.2, entries 2 and 5). Both complexes **1** and **2** were active at higher substrate to catalyst ratios, reaching final TONs of 10000 after 320 and 420 min, respectively.

**Table 2.2.** Formic acid dehydrogenation catalyzed by Ru/L (L = triphos, NP<sub>3</sub>) and **1-3** in the presence of OctNMe<sub>2</sub> at 80 °C.

Entry	Catalyst	Vol (mL) after 60 min	TON after 60 min	Max Vol (mL) [t (min)]	Final TON
1	i <sup>a</sup>	210	314	630 [180]	1000
2	ii <sup>a</sup>	70	105	630 [490]	1000
3	<b>1</b> <sup>b</sup>	630	1000	630 [60]	1000
4	<b>1</b> <sup>c</sup>	100	1504	630 [320]	10000
5	<b>2</b> <sup>b</sup>	130	204	630 [230]	1000
6	<b>2</b> <sup>c</sup>	60	902	630 [420]	10000
7	<b>3</b> <sup>b</sup>	250	373	630 [220]	1000

*Reaction conditions:* <sup>a</sup> Ru(acac)<sub>3</sub>, 12.9 μmol; ligand 12.9 μmol; HCOOH/OctNMe<sub>2</sub> (11:10), 2.73 mL (density at 25 °C = 0.894 mg mL<sup>-1</sup>); HCOOH : catalyst = 1000; 80 °C. Gas measured via manual gas burette and analyzed via FT-IR spectroscopy. <sup>b</sup> As above, preformed catalyst 12.9 μmol. <sup>c</sup> As above, preformed catalyst 1.29 μmol (HCOOH : catalyst = 10000).

Interestingly, a few nicely shaped crystals formed at the end of a catalytic experiment using Ru(acac)<sub>3</sub> and triphos. <sup>31</sup>P{<sup>1</sup>H} and <sup>1</sup>H NMR spectra of the crystals dissolved in CDCl<sub>3</sub> showed unequivocally that the complex formed under these conditions was the known [Ru(κ<sup>3</sup>-triphos)(CO)(H)<sub>2</sub>] (**3**).<sup>30</sup> Thus, we thought it could be of interest to test **3** as preformed catalyst for HCOOH dehydrogenation under the same conditions. Indeed, also this complex was endowed with catalytic activity that closely resembles that observed for an *in situ* generated Ru-triphos system (runs 1 and 7, Table 2.2). This observation may in turn suggest that either **3** is formed under the conditions applied in run 1 or that both Ru(acac)<sub>3</sub>/triphos and **3** evolve toward the same (or at least very similar) catalytically active species, perhaps [Ru(κ<sup>3</sup>-triphos)(H)(η<sup>2</sup>-H<sub>2</sub>)]<sup>+</sup> upon loss of CO and protonation of one hydrido ligand. This species has already

been proposed in the literature as an active catalyst for hydrogenation reactions.<sup>13</sup> However, **3** was neither observed to be formed during the HCOOH dehydrogenation tests when complex **1** was used as a pre-catalyst, nor during NMR mechanistic studies starting from an analogue of **1** as a ruthenium source (*vide infra*).

Recycling experiments using the best catalyst found in this study, i.e. complex **1**, were also carried out. After evolution of the gas volume expected in the first run (630 mL), neat HCOOH (1000 equiv. to Ru originally used) was added to the thermostated reaction vessel kept at 80 °C and the next run was started. In this way, it was possible to recycle the mixture containing the catalyst and the amine for up to eight consecutive runs (Table 2.3, Fig. 2.2 for reaction profile). As can be seen from Table 2.3, complete conversion of the substrate was invariably reached after each recycle, albeit with a decrease of TOFs already noticeable after 1 h.

**Table 2.3.** Recycling test for formic acid dehydrogenation catalyzed by **1** in the presence of OctNMe<sub>2</sub> at 80 °C.

Cycle	Vol (mL) after	TOF (h <sup>-1</sup> ) after	MaxVol (mL)	Final TOF
	60 min	60 min	[t(min)]	(h <sup>-1</sup> )
<b>I</b>	630	1000	630 [60]	1000
<b>II</b>	600	944	630 [65]	923
<b>III</b>	430	676	630 [90]	666
<b>IV</b>	350	550	630 [110]	545
<b>V</b>	340	535	630 [120]	500
<b>VI</b>	330	519	630 [130]	461
<b>VII</b>	300	472	630 [140]	428
<b>VIII</b>	240	377	630 [150]	400

*Reaction conditions:* complex **1**, 12.9 μmol; HCOOH/OctNMe<sub>2</sub> (11:10), 2.73 mL (density at 25 °C = 0.894 mg mL<sup>-1</sup>); HCOOH : catalyst = 1000; 80 °C; from run 2, 12.9 mmol of neat HCOOH were added by microsyringe for each run. Gas measured via manual gas burette and analyzed via FT-IR spectroscopy.

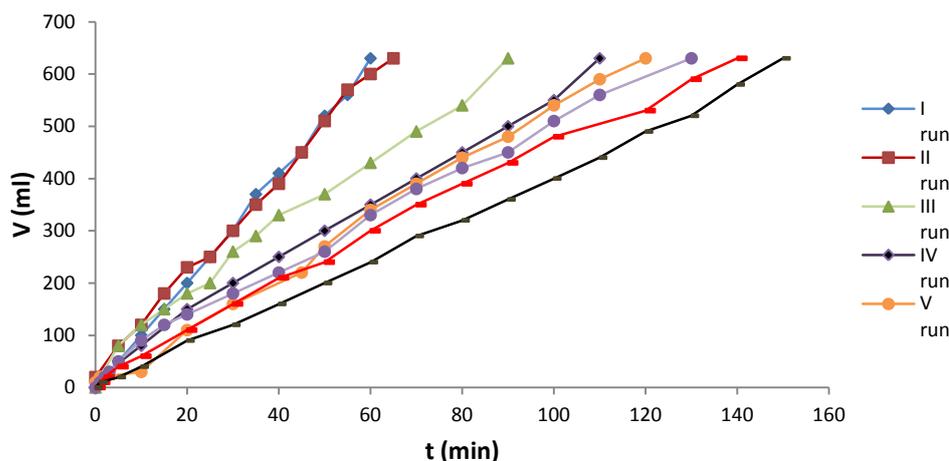
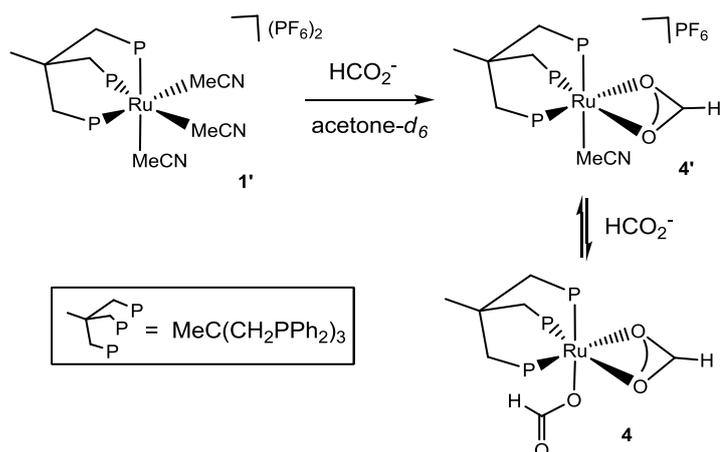


**Figure 2.2.** Reaction profiles of catalytic runs using complex **1** in the recycling experiment. Reaction conditions: catalyst 12.9  $\mu\text{mol}$ ;  $\text{HCOOH}/\text{OctNMe}_2$  (11:10), 2.73 ml;  $\text{HCOOH}$  : catalyst = 1000; 80  $^\circ\text{C}$ . Gas measured via manual gas burette and analyzed via FT-IR spectroscopy. 0.49 ml of neat  $\text{HCOOH}$  were added to the reaction vessel after the each run.

## 2.5 VT-NMR mechanistic studies

To gain a better insight into the mechanism of substrate activation and pre-catalyst modifications during the catalytic cycle, the reactivity of complexes **1** and **2** with formate and formic acid/amine were tested. At first, the behavior of complex **1** was studied. Prior to the mechanistic studies, anion metathesis on **1** was carried out to exchange the potentially coordinating triflate with hexafluorophosphate, obtaining the new complex  $[\text{Ru}(\kappa^3\text{-triphos})(\text{MeCN})_3](\text{PF}_6)_2$  (**1'**). A series of variable temperature (VT) NMR experiments involving **1'** was carried out as follows. In the first experiment, 2.58 mg of  $\text{HCOONHET}_3$  (0.1 mL of a solution of 25.8 mg of reagent dissolved in 1.0 mL of acetone- $d_6$ ), freshly prepared by the reaction of  $\text{HCOOH}$  and  $\text{NET}_3$  in a 1 : 1 ratio, were added under nitrogen to a solution of **1'** (20 mg,  $1.76 \times 10^{-2}$  mmol) in 0.6 mL of acetone- $d_6$  at 233 K. The first  $^{31}\text{P}\{^1\text{H}\}$  NMR spectrum recorded at this temperature immediately after mixing the reagents showed that the original singlet due to **1'** at 27.2 ppm was now accompanied (ca. 1:1 ratio) by a new  $\text{AM}_2$  system at 42.7 ppm (d,  $^2J_{\text{PP}} = 42$  Hz) and 29.5 ppm (t), which we assigned to the diformate complex  $[\text{Ru}(\kappa^3\text{-triphos})(\eta^1\text{-OOCH})(\eta^2\text{-OOCH})]$  (**4**) (Scheme 2.9).



**Scheme 2.9.** Proposed reaction pathway leading from **1'** to **4** based on VT NMR studies.

In keeping with formate coordination, the corresponding <sup>1</sup>H NMR spectrum showed a broad resonance at 8.34 ppm, at chemical shift values expected for Ru-coordinated formate.<sup>33</sup> The appearance of a new singlet at 2.18 ppm confirms that MeCN has been partially released in solution. Complex **4** may arise from stepwise ligand substitution from putative species such as [Ru(κ<sup>3</sup>-triphos)(MeCN)(η<sup>2</sup>-OOCH)] (**4'**) depending on the Ru/formate stoichiometry. In keeping with this hypothesis, addition of 1 equiv. of neat HCOOH at 233 K caused the complete disappearance of the signal due to **1'**, while maintaining the pattern due to **4**. The VT NMR experiment was continued by raising gradually the temperature up to 313 K, and a broadening of the signals corresponding to **4** was observed, to eventually collapse at 313 K. A close inspection of the corresponding <sup>1</sup>H NMR spectra showed that no hydride species were formed throughout the heating sequence. In a second experiment, **1'** was mixed with 2 equiv. of HCOONHET<sub>3</sub> at 233 K before starting the VT NMR sequence. The initial <sup>31</sup>P{<sup>1</sup>H} NMR spectrum measured upon mixing of the reagents gave the same picture observed for experiment 1, except that **1'** was much less abundant (ca. 8% left), supporting the hypothesis discussed above. The addition of HCOOH caused the complete disappearance of **1'** accompanied by release of MeCN in solution as observed in the <sup>1</sup>H NMR spectra. By increasing the temperature, at 273 K two singlets at 42.3 ppm and 42.0 ppm appeared, reaching a maximum concentration at 293 K. The situation at 313 K showed that the pattern due to **4** was still present, together with a broad hump at ca. 41.0 ppm. This behaviour again suggests a rapid formate exchange at higher temperatures.

$^{13}\text{C}\{^1\text{H}\}$  NMR spectra in acetone- $d_6$  of a mixture of **1'** with 2 equiv. of  $\text{HCOONHEt}_3$  and 1 equiv. of  $\text{HCOOH}$ , taken at 233 K, showed a small singlet at 178.7 ppm, at values expected for coordinated formate.<sup>33a</sup> Finally, FT-IR spectra of the final solution at room temperature showed  $\nu_{\text{CO}}$  formate stretching modes at 1697 and 1546  $\text{cm}^{-1}$ , in the range expected for  $\eta^1\text{-O(O)CH}$  and  $\eta^2\text{-O(O)CH}$  coordination, respectively.<sup>33,34</sup> These spectroscopic investigations suggest the presence of Ru-coordinated formate species equilibrating between  $\eta^2$ - to  $\eta^1$ -fashion in this system. Attempts to isolate **4** by carrying out the reactions at preparative scale have unfortunately failed in our hands due to decomposition of the complex during workup. During all experiments, no  $^{31}\text{P}\{^1\text{H}\}$  signals at negative chemical shift values attributable to triphos partial de-chelation (i.e.  $\kappa^3$ - to  $\kappa^2$ -coordination switch), proposed by some authors to occur during reactions,<sup>23,35</sup> were visible throughout the experiments. Moreover, complex **3** was never observed to be formed during the VT NMR experiments (Figure 2.3).

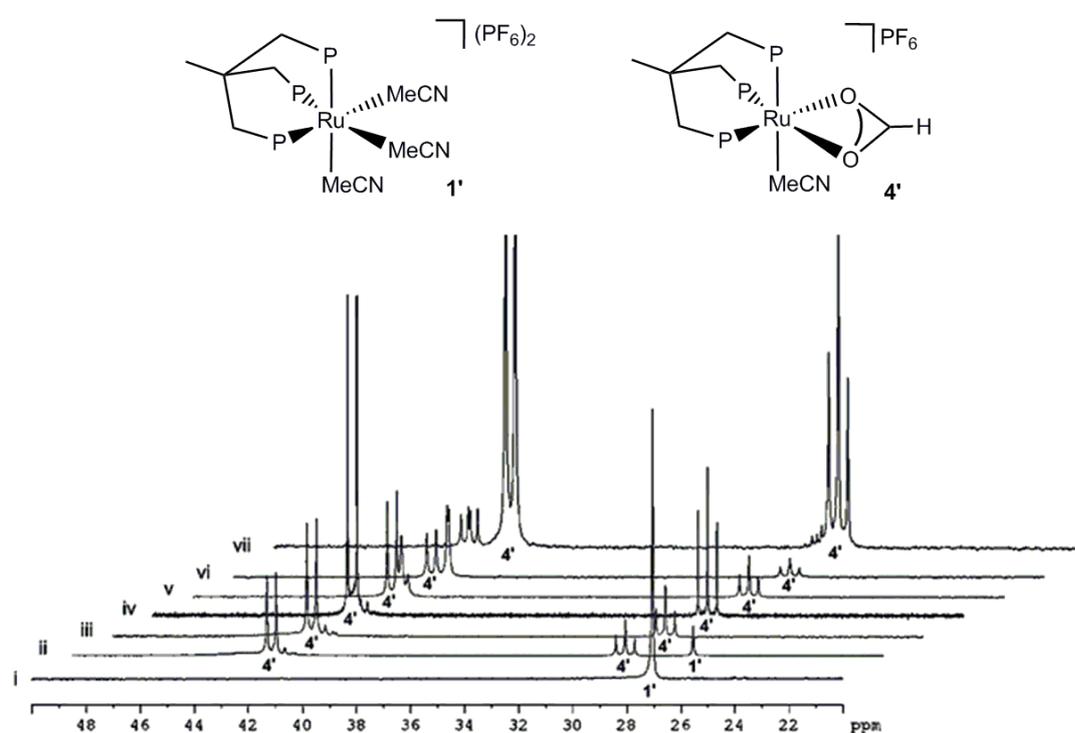


**Figure 2.3.** Variable temperature  $^{31}\text{P}\{^1\text{H}\}$  NMR spectra of the reaction between **1** and  $\text{HCO}_2\text{NHEt}_3$ , overlay view of the experiment. i) **1**, 233 K; ii) **1** + 2 equiv.  $\text{HCO}_2\text{NHEt}_3$ , 233 K; iii) addition of 1 equiv.  $\text{HCO}_2\text{H}$ , 233 K; (iv) as iii, 253 K; v) as iii, 273 K; vi) as iii, 293 K; vii) as iii after heating to 313K, 233 K.

We could safely rule out the presence of Ru carbonyl species such as  $[\text{Ru}(\kappa^3\text{-triphos})(\text{MeCN})_x(\text{CO})_y]^{2+}$  ( $x = 0\text{--}2$ ;  $y = 1\text{--}3$ ;  $x + y = 3$ ) by comparison with NMR spectra obtained by saturating an acetone- $d_6$  solution of **1'** with CO gas (1 bar, see Experimental section 2.7.3). On the basis of all the evidence obtained it can be concluded that for these systems triphos behaves as a  $\kappa^3\text{-P}$  facial ligand, and that any metal-hydrido species which may form are quickly converted on an NMR timescale in the temperature range 233–313 K using **1'** as a starting complex.

A VT-NMR study was also carried out starting from complex **2**. By dissolving **2** in  $\text{CD}_2\text{Cl}_2$ , chosen for solubility reasons, a first  $^{31}\text{P}\{^1\text{H}\}$  NMR spectrum showed the expected  $\text{AM}_2$  spin system with the  $\text{P}_A$  triplet at 45.7 ppm ( $^2J_{\text{PP}} = 30$  Hz) and the  $\text{P}_M$  doublet at 26.6 ppm. To this solution,  $\text{HCOONHET}_3$  (1 equiv.) was added under nitrogen at 233 K. The corresponding  $^{31}\text{P}\{^1\text{H}\}$  NMR spectrum showed the appearance of a new set of signals at 47.8 ppm (t,  $^2J_{\text{PP}} = 29$  Hz,  $\text{P}_A$ ) and 25.8 ppm (d,  $\text{P}_M$ ). The corresponding  $^1\text{H}$  NMR spectrum showed a new singlet at 8.41 ppm which can be attributed to coordinated formate. Based on chemical shift and coupling constant values, we propose for the new species the tentative formula  $[\text{Ru}(\kappa^4\text{-NP}_3)\text{Cl}(\eta^1\text{-OOCH})]$  (**5**). This species reached a 1 : 1 ratio with **2** at 253 K. At 273 K a new  $\text{AM}_2$  system, showing a doublet at 42.4 ppm ( $^2J_{\text{PP}} = 18$  Hz) and a triplet at 29.3 ppm, slowly increased at the expense of **5**. This species was identified by comparison with literature data<sup>23</sup> as the hydrochloride complex  $[\text{Ru}(\kappa^4\text{-NP}_3)\text{Cl}(\text{H})]$  (**6**), as confirmed by the presence of the Ru–H resonance at  $-6.56$  ppm (dt,  $J_{\text{HP}(\text{trans})} = 97$  Hz;  $J_{\text{HP}(\text{cis})} = 26$  Hz, 1H, RuH) in the corresponding  $^1\text{H}$  NMR spectrum. At 283 K the ratio between **2**, **5** and **6** reached 7 : 3 : 1, while at 273 K a further decrease in the concentration of **5** was accompanied by an increase of **6** (ratio **2** : **5** : **6** = 3 : 1.5 : 1). At 273 K a new octahedral species characterized by a doublet at 56.4 ppm (d,  $^2J_{\text{PP}} = 16$  Hz, 2P,  $\text{P}_M$ ) and a triplet at 51.6 ppm ( $\text{P}_A$ ) slowly increased. A broad singlet at  $-9.99$  ppm appeared in the corresponding  $^1\text{H}$  NMR spectrum. This new species was identified as the highly fluxional complex  $[\text{Ru}(\kappa^4\text{-NP}_3)(\eta^2\text{-H}_2)(\text{H})]^+$  (**7**) by comparison with previous data obtained in our laboratories.<sup>24</sup> At this point, a second equivalent of  $\text{HCOONHET}_3$  was added. As expected, this caused an increase in the concentration of **5** and a decrease of **2**. Raising the temperature to 293 K a further increase of **6** and **7** was observed, together with a decrease of **2** and **5**. The probe was

then cooled to 233 K and 1 equiv. of HCOOH was added. This in turn caused the complete disappearance of **2** and **5**, leaving **7** and a new AM<sub>2</sub> set of signals with a P<sub>A</sub> triplet at 50.0 ppm (<sup>2</sup>J<sub>PP</sub> = 33 Hz) and a P<sub>M</sub> doublet at 25.5 ppm. At 293 K the latter (**8**) was the main species present in the <sup>31</sup>P{<sup>1</sup>H} NMR spectrum, with only a small residue of **7**. The broad singlet at -9.99 ppm in the <sup>1</sup>H NMR spectrum, typical of Ru(η<sup>2</sup>-H<sub>2</sub>) moiety, increased in intensity.

The <sup>31</sup>P{<sup>1</sup>H} and <sup>1</sup>H NMR variable temperature experiments were repeated reacting **1'** and **2** with the azeotrope HCOOH/NEt<sub>3</sub> (5 : 2) which was used for the catalytic tests, using a 5 : 1 ratio to the complexes, and the observations previously described were consistent with these experiments.

In order to assign the signals due to **8**, a close inspection of the VT NMR experiment sequence (Fig. 2.4 and Appendix) suggested that species such as **2** and **5**, having Cl<sup>-</sup> trans to apical P, were characterized by <sup>31</sup>P NMR patterns bearing the triplet at lower (i.e. more deshielded) and the doublet at higher fields, whereas this order reverts in the case of **6** and **7**. As the former pattern (deshielded triplet) was observed also for **8**, we reasoned that this species could be structurally related to **2** and **5**. For this reason, compound **6** was prepared and isolated as described in the literature,<sup>24</sup> and reacted at 233 K with HCOOH on an NMR tube scale using CD<sub>2</sub>Cl<sub>2</sub> as a solvent. The corresponding <sup>31</sup>P{<sup>1</sup>H} NMR and <sup>1</sup>H NMR spectra showed unequivocally the formation of **8**, to which we assign the formula [Ru(κ<sup>4</sup>-NP<sub>3</sub>)Cl(η<sup>2</sup>-H<sub>2</sub>)]<sup>+</sup>, as a major product. Interestingly, by leaving the NMR tube at room temperature and collecting another set of spectra after 1 h at 293 K, formation of **2** was observed to form at the expense of **8**. From these experiments it can be proposed that the stable complex **6** may follow two different activation pathways, shown in Scheme 2.10. In path A, chloride exchange with formate in **6** leads to an (unobserved) hydrido-formate species [Ru(κ<sup>4</sup>-NP<sub>3</sub>)H(η<sup>1</sup>-OOCH)] which rapidly evolves upon protonation to **7**, which then regenerates **6** by hydrogen release and chloride coordination, in line with the mechanism reported for the Fe/PP<sub>3</sub> system.<sup>36</sup>

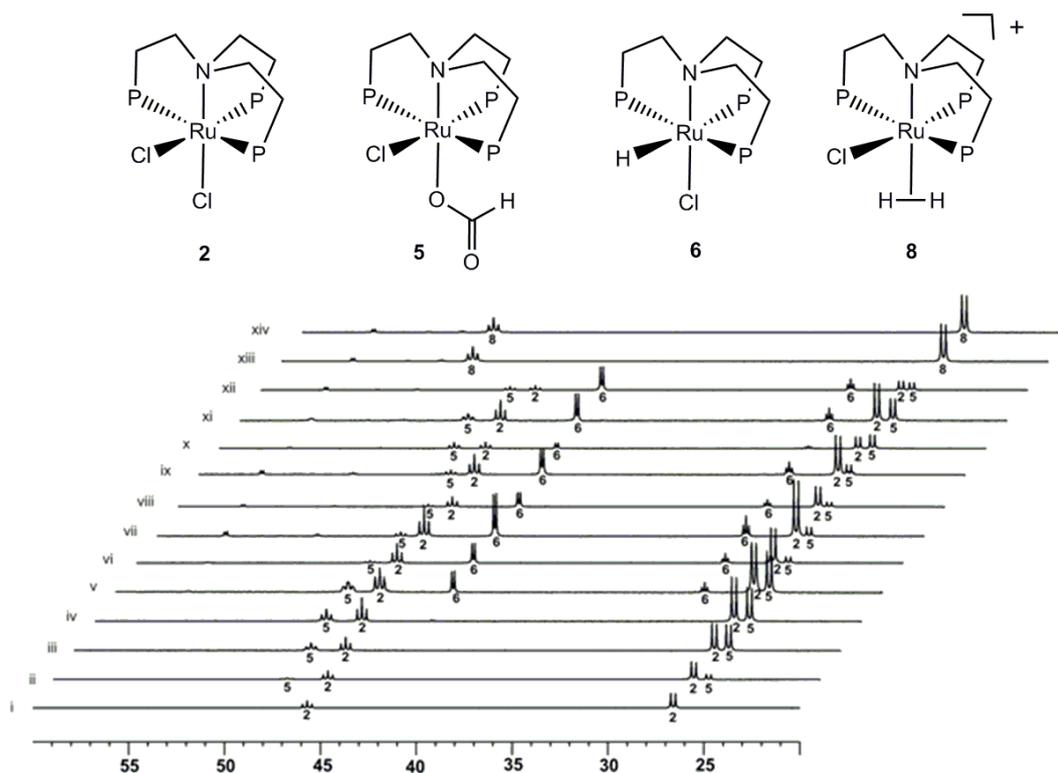
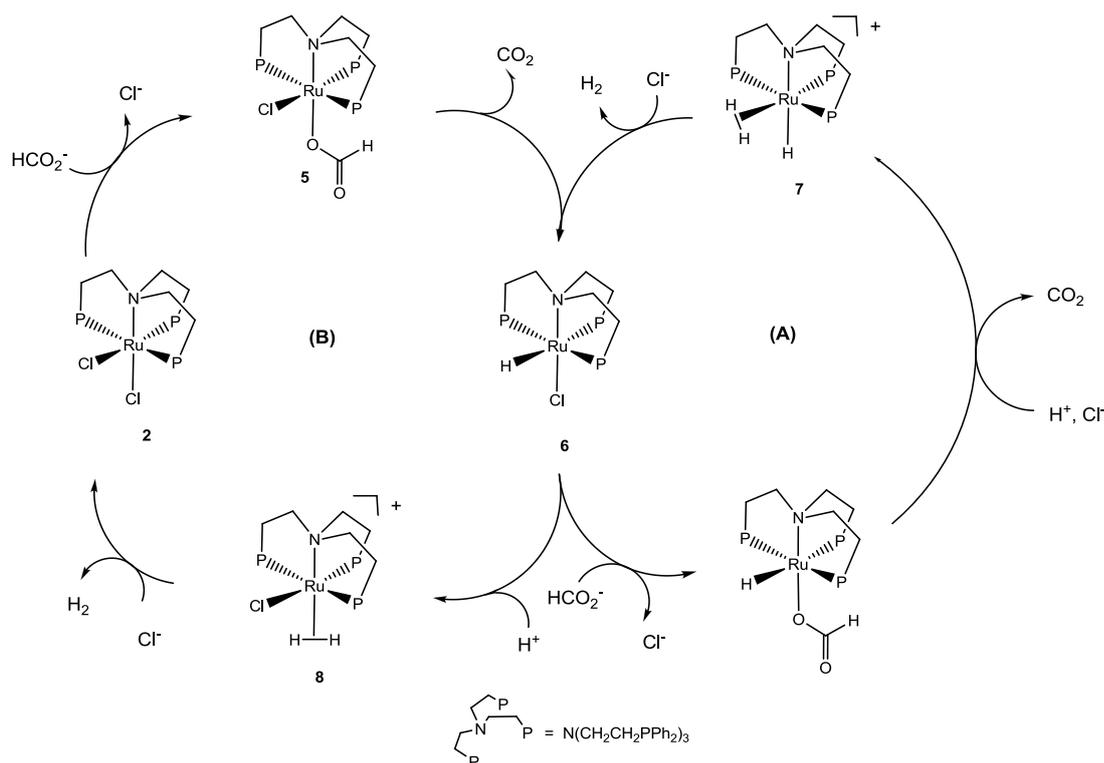


**Figure 2.4.** Variable temperature  $^{31}\text{P}\{^1\text{H}\}$  NMR spectra of the reaction between **2** and  $\text{HCO}_2\text{NHET}_3$ , overlay view of the experiment. i) **2**, 233 K; ii) **2** + 1 equiv.  $\text{HCO}_2\text{NHET}_3$ , 233 K; iii) as ii, 253 K; (iv) as ii, 273 K; v) as ii, 283 K; vi) as ii, 293 K; vii) as ii, 273 K; viii) as ii, 233 K; ix) as ii, 213 K; x) addition of 1 equiv.  $\text{HCO}_2\text{NHET}_3$ , 233 K; xi) as x, 293 K; xii) as x, 233 K; xiii) addition of 5equiv.  $\text{HCO}_2\text{H}$ , 233 K; xiv) as xiii, 293 K.

In path B, protonation of **6** leads to **8**, which then gives back **2** releasing hydrogen. The coexistence of these two pathways may have an implication in the lower activity of **2** compared to **1** observed in formic acid dehydrogenation tests.



**Scheme 2.10.** Proposed catalytic cycles for HCOOH dehydrogenation in the presence of **2** based on VT NMR studies.

## 2.6 DFT calculations

### 2.6.1 The Mechanism of Formic Acid Dehydrogenation Catalyzed by $[\text{Ru}(\kappa^3\text{-triphos})(\text{MeCN})_3]^{2+}$ (**1**).

The computational investigation started by modeling the cationic species  $[\text{Ru}(\kappa^3\text{-triphos})(\text{MeCN})_3]^{2+}$  (**1**) where the peripheral phenyl rings were substituted by simpler methyl substituents ( $\text{triphos}^{\text{Me}}$ ). The corresponding structure **1m**<sup>2+</sup> was optimized in acetone solution, the same solvent used for the VT NMR experiments. The structure, shown in Figure 2.5, although with some slight overestimation due to the pseudo-potential usage for Ru,<sup>37</sup> could be reasonably compared with that of  $[\text{Ru}(\kappa^3\text{-sulphos})(\text{MeCN})_3]^{2+}$ , (see Cambridge Structural Database<sup>38</sup> refcode WIBKOH)<sup>39</sup> where the sulphos ligand differs from triphos for the presence of a  $\text{CH}_2(\text{C}_6\text{H}_4\text{SO}_3^-)$  moiety replacing the bridgehead methyl group. The optimized structure shows three identical Ru-P distances of *ca.* 2.336 Å (average 2.3118(18) Å in the experimental one) while the Ru-N bond lengths are in the range from 2.115 to

2.120 Å (average 2.099(6) Å in the experimental one), with the Ru-coordinated acetonitrile N≡C stretching frequency estimated at 2383.3 cm<sup>-1</sup>.

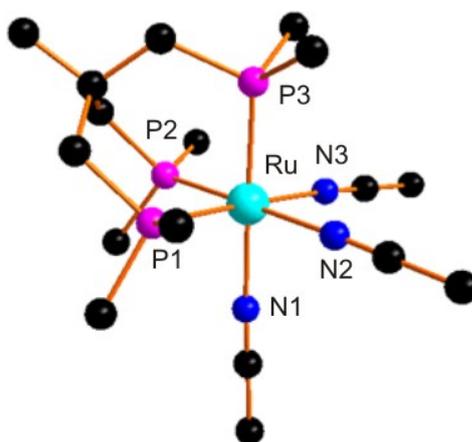


**Figure 2.5.** Optimized structure of compound **1m**<sup>2+</sup>. Main bond lengths (Å): Ru-N = 2.117 (average) and Ru-P = 2.336 (average).

In this system, the three labile solvento-ligands are all potentially prone to substitution with an incoming formate, which can in principle bind Ru in both  $\eta^2$ - and  $\eta^1$ -modes. A useful tool to assess the matching between calculations and experimental results is the comparison between the calculated and the experimental IR spectra. In particular, upon sequential substitution of one or more MeCN ligands in **1m**<sup>2+</sup> with formate, the intensity of the corresponding C≡N stretching bands was expected to decrease, associated with the appearance of CO carboxylate stretching bands in the range 1546 to 1697 cm<sup>-1</sup>, due to  $\eta^2$ - and  $\eta^1$ -formate coordination to Ru. Five octahedral structures were therefore optimized taking in account the possible substitution degrees and coordination modes, namely [Ru( $\kappa^3$ -triphos<sup>Me</sup>)(MeCN)( $\eta^2$ -OOCH)]<sup>+</sup> (**4'm**<sup>+</sup>), [Ru( $\kappa^3$ -triphos<sup>Me</sup>)( $\eta^1$ -OOCH)( $\eta^2$ -OOCH)] (**4m**), [Ru( $\kappa^3$ -triphos<sup>Me</sup>)(MeCN)<sub>2</sub>( $\eta^1$ -OOCH)]<sup>+</sup> (**9m**<sup>+</sup>), [Ru( $\kappa^3$ -triphos<sup>Me</sup>)(MeCN)( $\eta^1$ -OCH)<sub>2</sub>] (**10m**) and [Ru( $\kappa^3$ -triphos<sup>Me</sup>)( $\eta^1$ -OOCH)<sub>3</sub>]<sup>-</sup> (**11m**<sup>-</sup>), shown in Figure 2.6, Table 2.4 summarizes the calculated bond lengths associated with these species.

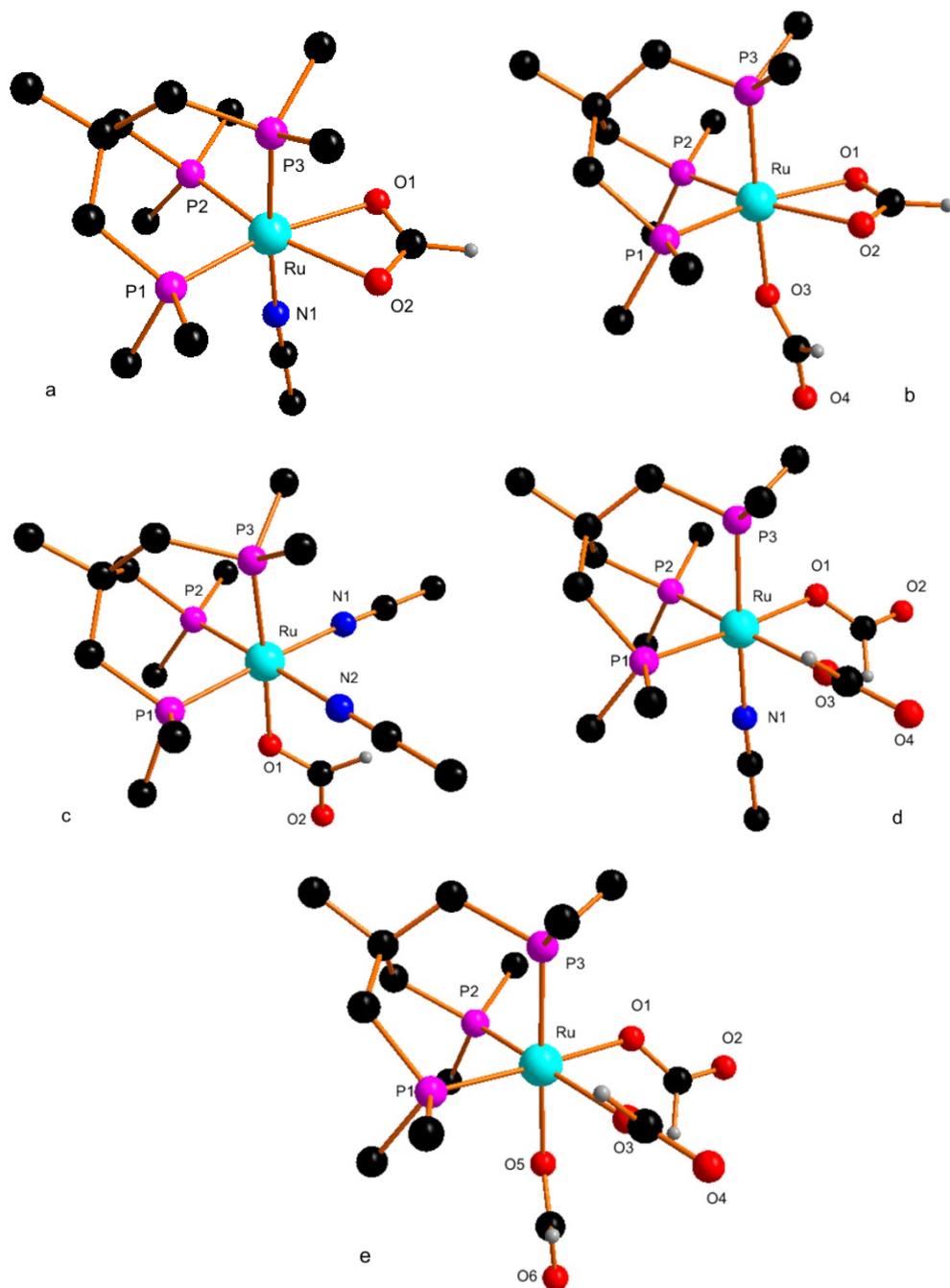


**Figure 2.6.** Optimized structures for: a)  $[\text{Ru}(\kappa^3\text{-triphos}^{\text{Me}})(\text{MeCN})(\eta^2\text{-OOCH})]^+$  (**4m**<sup>+</sup>); b)  $[\text{Ru}(\kappa^3\text{-triphos}^{\text{Me}})(\eta^1\text{-HCO}_2)(\eta^2\text{-OOCH})]$  (**4m**); c)  $[\text{Ru}(\kappa^3\text{-triphos}^{\text{Me}})(\text{MeCN})_2(\eta^1\text{-OOCH})]^+$  (**9m**<sup>+</sup>); d)  $[\text{Ru}(\kappa^3\text{-triphos}^{\text{Me}})(\text{MeCN})(\eta^1\text{-OOCH})_2]$  (**10m**) and e)  $[\text{Ru}(\kappa^3\text{-triphos}^{\text{Me}})(\eta^2\text{-OOCH})_3]^-$  (**11m**<sup>-</sup>).

**Table 2.4.** Main calculated structural and spectroscopic features for  $4'm^+$ ,  $4m$ ,  $9m^+$ ,  $10m$  and  $11m^-$ .

	$4'm^+$	$4m$	$9m^+$	$10m$	$11m^-$
Bond lengths (Å)					
Ru-P1	2.285	2.275	2.324	2.302	2.298
Ru-P2	2.288	2.276	2.330	2.309	2.294
Ru-P3	2.322	2.299	2.313	2.325	2.293
Ru-N1	2.101	-	2.113	2.105	-
Ru-N2	-	-	2.109	-	-
Ru-O1	2.273	2.278	2.195	2.202	2.204
Ru-O2	2.272	2.272	-	2.197	2.198
Ru-O3	-	2.181	-	-	2.198
C-O	1.269	1.267-1.282	1.283	1.279	1.277
C=O	-	1.248	1.246	1.250	1.251
C-H	1.100	1.101-1.108	1.108	1.106	1.107
Computed IR stretching frequencies ( $cm^{-1}$ )					
$\nu_{C=O}$	1583.2	1588.3 1629.7	1635.0	1617.0 1634.2	1608.2 1618.7 1640.3
$\nu_{C-H}$	3053.1	2949.1 3040.2	2952.2	2964.8 2991.0	2955.4 2959.3 3005.1
$\nu_{C\equiv N}$	2372.4	-	2377.5	2373.5	-

Being triphos a symmetrical ligand, no *trans*-influence arising from different donor atoms coordinating the metal center should be considered, as for  $1m$  and derivatives, simplifying the overall modeling. In structure  $9m^+$  (Figure 2.6c) two Ru-coordinated acetonitrile ligands are maintained and one is replaced by a  $\eta^1$ -coordinate formate anion. The formation of compound  $9m^+$  from  $1m^{2+}$  was calculated to be exoergic by  $-7.4 \text{ kcal mol}^{-1}$ . The second isomer,  $4'm^+$ , (Figure 2.6a) showed a coordinated  $CH_3CN$  molecule and the formate binding the metal in  $\eta^2$ -mode. The reaction from

$\mathbf{1m}^{2+}$  to  $\mathbf{4m}^+$  was favored by  $-11.5 \text{ kcal mol}^{-1}$ . In the presence of a 3:1 excess of formate, the formation of a neutral compound  $\mathbf{4m}$  bearing both  $\eta^1$ -OOCH and  $\eta^2$ -OOCH (Figure 2.6b) would also be plausible. The calculated Ru-O distances were in the range between 2.181 (for  $\eta^1$ -OOCH) and 2.278 Å (for  $\eta^2$ -OOCH), thus two CO stretching frequencies should be present, differing by *ca.*  $50 \text{ cm}^{-1}$  ( $1630$  and  $1584 \text{ cm}^{-1}$  for  $\eta^1$ -OOCH and  $\eta^2$ -OOCH, respectively). The free energy associated with the formation  $\mathbf{4m}$  from  $\mathbf{1m}^{2+}$  was calculated as  $-16.5 \text{ kcal mol}^{-1}$ . The other possible structures obtained by further MeCN substitution, namely  $\mathbf{10m}$  (Figure 2.6d) and  $\mathbf{11m}$ , (Figure 2.6e) should be less relevant, in view of their higher free energies of formation, at  $-8.01$  and  $-8.02 \text{ kcal mol}^{-1}$ , respectively.

The computational results described above confirm the experimental VT NMR tests involving  $\mathbf{1}'$ , carried out in acetone- $d_6$  solution at different Ru:formate ratios of 1:1, 1:2 and 1:3, respectively.<sup>40</sup> In the first experiment, an initial mixture of  $\mathbf{1}'$  and  $\mathbf{4}$  was observed, to give exclusively  $\mathbf{4}$  upon further addition of formate (second and third experiment) at 233 K. Upon heating and after addition of HCOOH, hydrogen gas was evolved as shown by the appearance of a singlet at 4.6 ppm in the  $^1\text{H}$  NMR spectra.

The mechanism involved in hydrogen release from species such as  $\mathbf{4}'\text{m}^+$ ,  $\mathbf{4m}$  and  $\mathbf{9m}^+$  was therefore studied. At this stage,<sup>41</sup> the computational analysis of the mechanism associated with formic acid dehydrogenation in the presence of  $\mathbf{1}'$  made us propose that an outer sphere mechanism involving release of  $\text{H}_2$  and  $\text{CO}_2$  from the formate ligands without the need for any Ru-hydrido species was plausible and favored by  $-23.8 \text{ kcal mol}^{-1}$  starting from  $\mathbf{1m}^{2+}$  and having  $\mathbf{4m}$  as pivotal species.

This hypothesized mechanism involves as key-step the cleavage of the C-H bond of coordinated formate in  $\mathbf{4m}$  followed by hydrogen abstraction by direct interaction with acidic protons present in solution. In this approach, through the interaction with the ammonium cation, one oxygen of the  $\eta^2$ -formate ligand in  $\mathbf{4m}$  undergoes protonation, opens the chelate ring changing from  $\eta^2$ - to  $\eta^1$ -coordination,<sup>42</sup> completing the coordination geometry with a formic acid molecule. Thus, structure  $[\text{Ru}(\kappa^3\text{-triphos}^{\text{Me}})(\eta^1\text{-OC(OH)H})(\eta^1\text{-OOCH})_2]$  ( $\mathbf{12m}$ ) was achieved, with a free energy cost of  $+10.5 \text{ kcal mol}^{-1}$  (Figure 2.7).

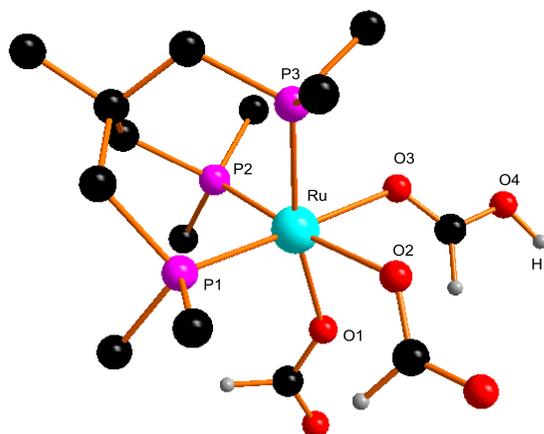


**Figure 2.7.** Optimized structure for  $[\text{Ru}(\kappa^3\text{-triphos}^{\text{Me}})(\eta^1\text{-OC(OH)H})(\eta^1\text{-OOCH})_2]$  (**12m**). Main bond lengths (Å) : Ru-O1 = 2.183, Ru-O2 = 2.187, Ru-O3 = 2.263, O4-H1 = 0.972, Ru-P1 = 2.285, Ru-P2 = 2.297 and Ru-P3 = 2.300.

From structure **12m**, the transition state **12m<sub>TS</sub>** (Figure 2.8) was calculated, where the acidic proton (H1) of the  $\eta^1\text{-OC(OH)H}$  group interacts with the hydrogen of the coordinated formate ligand ( $\text{H1}\cdots\text{H2} = 0.871$  Å).

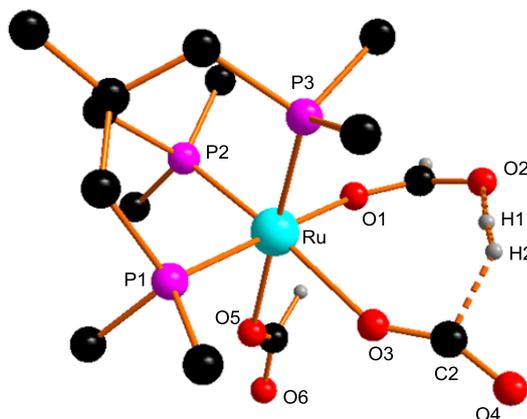
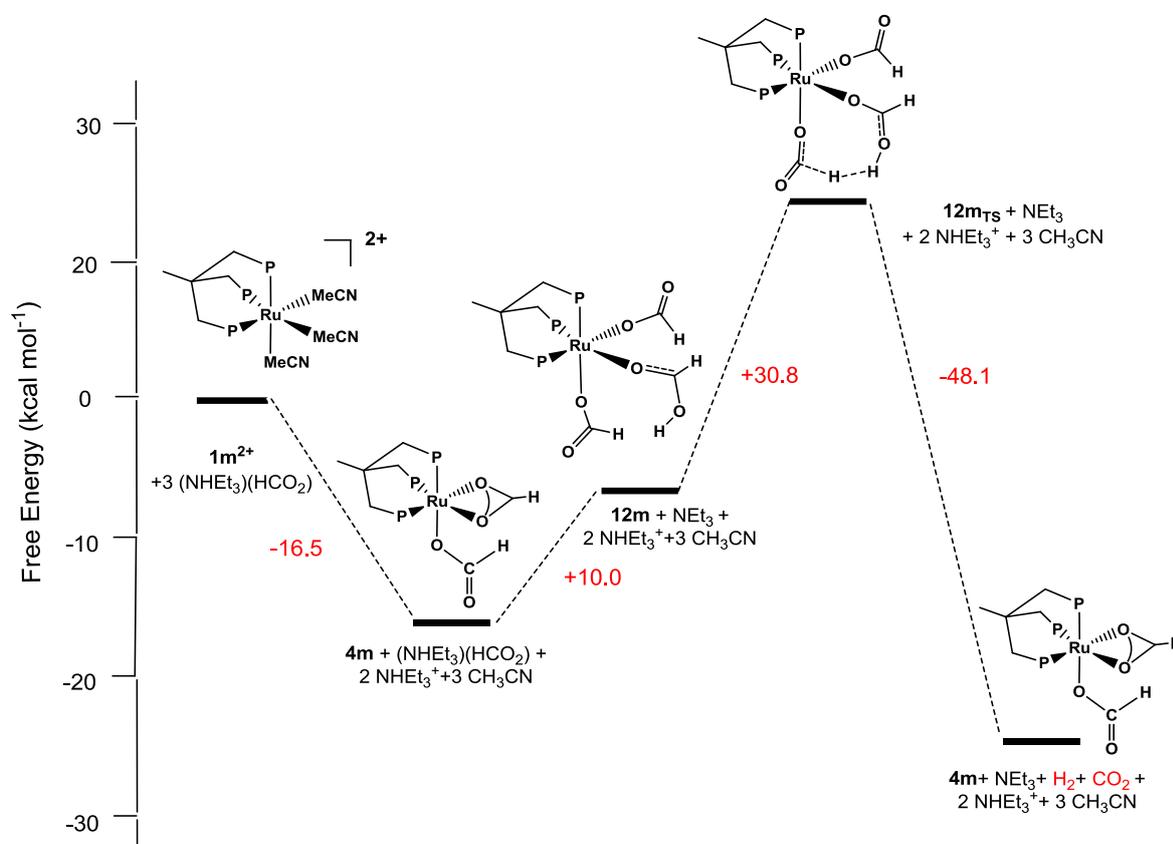


**Figure 2.8.** Optimized structure for Transition State **12m<sub>TS</sub>**. Main bond lengths (Å) : Ru-O1 = 2.22, O2-H1 = 1.407, H1-H2 = 0.871, C2-H2 = 1.582, Ru-O3 = 2.317, C2-O3 = 1.201 and C2-O4 = 1.190.

Such an interaction causes a marked weakening of the O2-H1 and C2-H2 bonds, with distances of 1.407 and 1.582 Å, respectively, and a consequent widening of the O3-C2-O4 angle of about 26°. An energy barrier of +30.8 kcal mol<sup>-1</sup> was calculated, however it is expected to decrease by replacing Me groups with “real” phenyl rings in the simplified calculated model triphos<sup>Me</sup>. The next step, accounting for the release

of both H<sub>2</sub> and CO<sub>2</sub> and regeneration of **8m**, was found to be exoergonic by -48.1 kcal mol<sup>-1</sup> (Scheme 2.11).



**Scheme 2.11.** Free Energy reaction pathway associated with the release of H<sub>2</sub> and CO<sub>2</sub> from **4m** following a proposed *outer-sphere*, ligand-centered mechanism.

After the publication of this study, Cantat and co-workers reconsidered the mechanistic details associated to FA disproportionation to methanol starting from **4**, showing that the implication of the ruthenium(II) hydrido formate complex [Ru( $\kappa^3$ -triphos)(H)( $\eta^2$ -OCHO)] in the first step of the reaction, i.e. FA dehydrogenation, was likely under pressure conditions.<sup>19</sup>

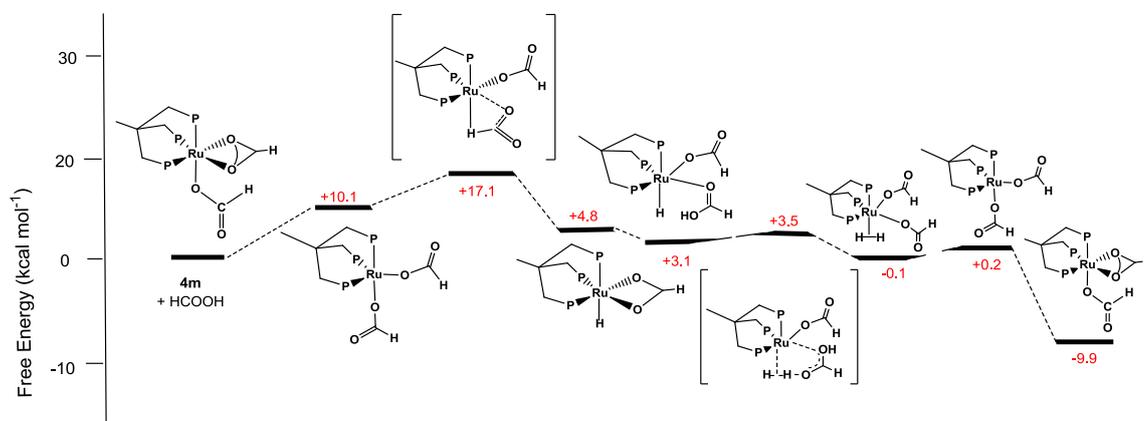
By reacting the precursor [Ru(cod)(2-allylmethyl)<sub>2</sub>], 1 equiv of triphos and two equivalents of HCOOH in THF, the ruthenium(II) bis-formate complex [Ru( $\kappa^3$ -triphos)( $\eta^1$ -OCHO)( $\eta^2$ -OCHO)] (**4**) was collected and characterized by X-ray diffraction and NMR spectroscopy. In the <sup>1</sup>H and <sup>13</sup>C NMR spectra, the singlets at 8.49 ppm and 172.3 ppm respectively, corresponding to C-H bond of the two formate, revealed the presence of a fluxional behavior at room temperature.

From decarboxylation of **4** a new complex was obtained and identified on the basis of  $^1\text{H}$ ,  $^{13}\text{C}$ , and  $^{31}\text{P}$  NMR and ESI-MS data as the ruthenium(II) hydrido formate complex  $[\text{Ru}(\kappa^3\text{-triphos})(\text{H})(\eta^2\text{-OCHO})]$ . In the  $^1\text{H}$  NMR spectra were present a typical Ru-H signal at -2.42 (dt,  $^2J_{\text{PcisH}}=20$  Hz,  $^2J_{\text{PtransH}}=124$  Hz) and a Ru-OCOH singlet at 8.24 ppm.

DFT calculations were carried out to investigate the competition between the dehydrogenation of formic acid and its disproportionation to MeOH, replacing the peripheral phenyl rings with simpler methyl substituents (triphos<sup>Me</sup>). The decoordination of one  $\eta^2\text{-OCHO}$  formate ligand and decarboxylation of the unsaturated  $[\text{Ru}(\kappa^3\text{-triphos}^{\text{Me}})(\eta^2\text{-OCHO})_2]$  intermediate was implicated in both reactions for the generation of  $[\text{Ru}(\kappa^3\text{-triphos}^{\text{Me}})(\text{H})(\eta^2\text{-OCHO})]$  from **4m**, with an activation energy of  $\Delta G^\ddagger = 17.1$  kcal mol<sup>-1</sup> (TS<sub>1</sub>).

Coordination of FA followed through two intermediates evolving along different pathways, leading to dehydrogenation vs. disproportionation.

The incoming molecule of FA in  $[\text{Ru}(\kappa^3\text{-triphos}^{\text{Me}})(\text{H})(\eta^2\text{-OCHO})]$  opens the chelate ring changing from  $\eta^2$ -to  $\eta^1$ -coordination and completing the coordination sphere, giving  $[\text{Ru}(\kappa^3\text{-triphos}^{\text{Me}})(\text{H})(\eta^1\text{-OCHO})_2]$ . Then, the interaction between the acidic proton of the  $\eta^1\text{-OC(OH)H}$  group and the coordinated hydride generated the transition state TS<sub>2</sub> with a low energy barrier of +3.5 kcal mol<sup>-1</sup>. The next step, accounting for the release of both H<sub>2</sub> and CO<sub>2</sub> and regeneration of  $[\text{Ru}(\kappa^3\text{-triphos}^{\text{Me}})(\text{H})(\eta^2\text{-OCHO})]$ , was found to be exoergonic by -9.9 kcal mol<sup>-1</sup> (Scheme 2.12).



**Scheme 2.12.** Free Energy reaction pathway associated with the release of H<sub>2</sub> and CO<sub>2</sub> from **4m** following a proposed mechanism by Cantat and co-workers.<sup>19</sup>

### 2.6.2 The mechanism of Formic Acid dehydrogenation catalyzed by $[\text{Ru}(\kappa^4\text{-NP}_3)\text{Cl}_2]$ (**2**)

The DFT computational analysis was started from structure optimization of **2**. In this compound, the Ru atom is located at the center of an octahedron, with four vertices occupied by one nitrogen and three phosphorus atoms of the tetrapodal  $\text{NP}_3$  ligand and two remaining positions filled by two chloride atoms in *cis* position. A model structure **2m** (Figure 2.9) was used in place of **2**, with methyl substituents on phosphorus atoms instead of the more bulky phenyl ones, in order to decrease significantly the computational time. Steric effects due to phenyl groups could be in this way underestimated, however **2m** was compared with an available X-ray structure of **2** found on CCDC database<sup>38</sup> (refcode IFEZUO).<sup>43</sup> A good agreement between the calculated structure **2m** and the X-ray structure of **2** was observed, with Ru-N distances of 2.224 Å (**2m**) vs. 2.188(7) Å (**2**); Ru-Cl1 2.607 (**2m**) vs. 2.479(2) Å (**2**); Ru-Cl2 2.510 (**2m**) vs. 2.447(2) Å (**2**); Ru-P2 2.275 (**2m**) vs. 2.254(2) Å (**2**). In the calculated structure **2m** the Ru-P1 and Ru-P3 distances were *ca.* 0.11 Å longer than Ru-P2. Interestingly, the different *trans*-influence<sup>44</sup> expected for the phosphorus and nitrogen donor atoms shows well from the comparison of Ru-Cl distances in **2m**, with Ru-Cl1 (Cl *trans* to P) *ca.* 0.1 Å longer than the Ru-Cl2 bondlength (Cl *trans* to N).

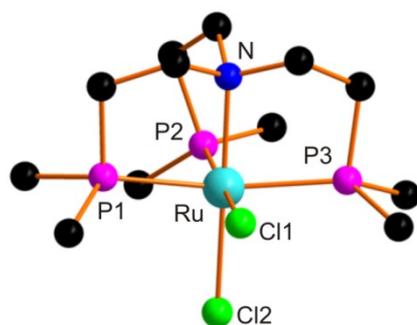


**Figure 2.9.** Optimized structure for **2m**. Hydrogen atoms on the capping ligand omitted for clarity. Main bond lengths (Å): Ru-N = 2.224, Ru-P2 = 2.275, Ru-Cl1 = 2.607, Ru-Cl2 = 2.510, Ru-P1 = 2.377 and Ru-P3 = 2.400.

The first step in the proposed catalytic cycle (Scheme 2.10) is the substitution of one chloride with a formate ligand. At 233 K, using a Ru:formate 1:1 ratio, the putative formate complex **5** observed by NMR was formed in 1:1 ratio to **2**. In principle, two different coordination modes for formate are possible: a chelating mode  $\eta^2\text{-5m}^+$  (Figure 2.10a), implying the dissociation of a second chloride ligand, and a monohapto coordination  $\eta^1\text{-5m}$ , for which two configurational isomers are possible, namely with the formate substituent *trans* to N, modeled as  $\eta^1\text{-5m}_\text{N}$  (Figure 2.10b) or *trans* to phosphorus,  $\eta^1\text{-5m}_\text{P}$  (Figure 2.10c). The main structural features of the three structures are summarized in Table 2.5.

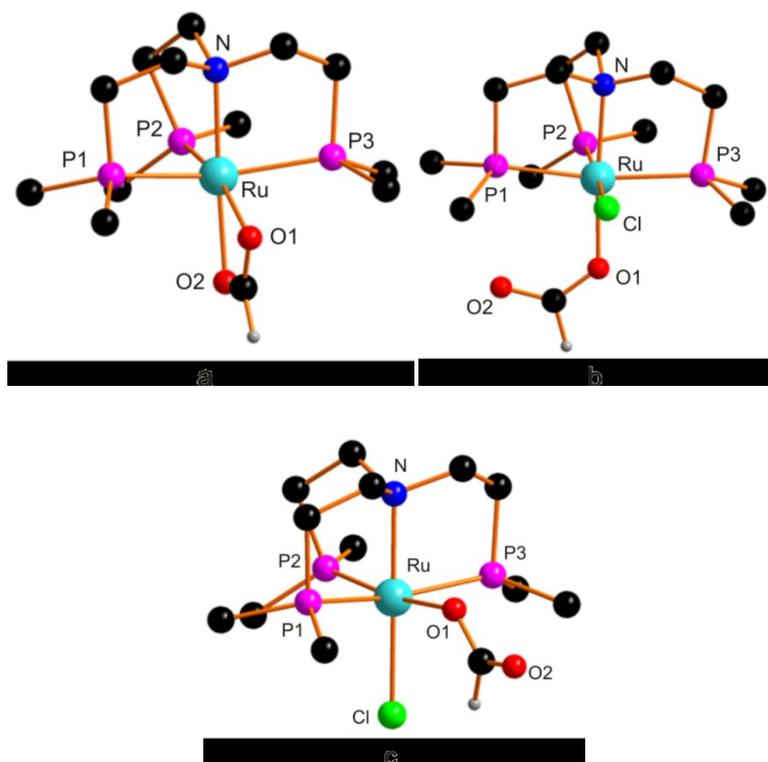


**Figure 2.10.** Optimized structures for  $\eta^2\text{-5m}^+$  (a),  $\eta^1\text{-5m}_\text{N}$  (b) and  $\eta^1\text{-5m}_\text{P}$  (c).

**Table 2.5.** Main calculated structural features for  $\eta^2\text{-5m}^+$ ,  $\eta^1\text{-5m}_\text{N}$  and  $\eta^1\text{-5m}_\text{P}$ .

	$\eta^2\text{-5m}^+$	$\eta^1\text{-5m}_\text{N}$	$\eta^1\text{-5m}_\text{P}$
Bond lengths (Å)			
Ru-P2	2.272	2.275	2.278
Ru-P1	2.375	2.383	2.363
Ru-P3	2.402	2.400	2.395
Ru-N	2.231	2.228	2.222
Ru-O1	2.309	2.142	2.219
Ru-O2	2.185	-	-
Ru-Cl	-	2.604	2.513
C-O	1.265	1.282	1.283
	1.272	-	-
C=O	-	1.245	1.247
C-H	1.099	1.111	1.105

To identify the nature of the most abundant product in solution, the free energy contributions at 298 K ( $\Delta G_{298}$ , kcal mol<sup>-1</sup>) to generate the formate derivatives have been calculated. Therefore, in spite of the small energy differences among the three species **5m** ( $\Delta G_{298}$  for  $\eta^2\text{-5m}^+$ ,  $\eta^1\text{-5m}_\text{N}$  and  $\eta^1\text{-5m}_\text{P}$  were calculated as +1.13, -0.81 and -2.73 kcal mol<sup>-1</sup>, respectively), it can be safely assumed that the most stable species is  $\eta^1\text{-5m}_\text{P}$ . The stronger *trans* influence of phosphorus compared to nitrogen justifies the formation of  $\eta^1\text{-5m}_\text{P}$  associated to a significant elongation (0.77 Å) of the Ru-O bond compared to isomer  $\eta^1\text{-5m}_\text{N}$ .

During the described NMR experiment, upon heating to 273 K, <sup>31</sup>P{<sup>1</sup>H}NMR and <sup>1</sup>H NMR measurements showed unequivocally the formation of the hydrido-chloride derivative **6**. Again, two different isomers can form, in which alternatively the hydride lies opposite to the phosphorus or nitrogen atoms, and these structures were optimized as **6m<sub>P</sub>** and **6m<sub>N</sub>** (Figures 2.11a and 2.11b, respectively). The former resulted slightly more stabilized ( $\Delta G_{298} = -0.71$  kcal mol<sup>-1</sup>). Such a result is not unexpected since the incoming hydride ligand should bind *trans* to the donor atom with the highest *trans*-influence.<sup>44</sup> Although the calculated energy differences are not

particularly high, the structural details match the previously reported NMR data. The Ru-P2 bond (*trans* to H) in **6m<sub>P</sub>** was *ca.* 0.1 Å more elongated than in **6m<sub>N</sub>**.

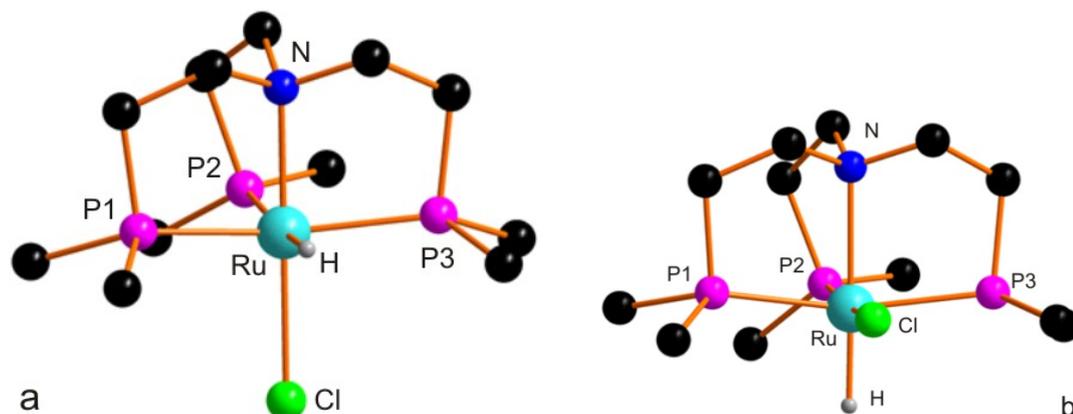


**Figure 2.11.** Optimized structures for **6m<sub>P</sub>** (a) and **6m<sub>N</sub>** (b). Main bond lengths (Å) for **6m<sub>P</sub>**: Ru-H = 1.645, Ru-Cl = 2.562, Ru-P2 = 2.379 and Ru-N = 2.222. Main bond lengths (Å) for **6m<sub>N</sub>**: Ru-H = 1.618, Ru-Cl = 2.616, Ru-P2 = 2.258 and Ru-N = 2.350.

The energies for the reaction pathway leading from  $\eta^1$ -**5m<sub>P</sub>** to **6m<sub>P</sub>** were then calculated. Since a hydride ligand must be formed in the coordination sphere of ruthenium, a possible mechanism may involve an interaction between the terminal hydrogen of the formate and the metal, followed by CO<sub>2</sub> elimination.<sup>36,45</sup> We could rule out an associative mechanism for this step as all efforts in optimizing an hepta-coordinated Ru intermediate were unsuccessful. In order to obtain the formation of a Ru-H bond, as in the experimentally observed complex **6**, a dissociative mechanism involving a penta-coordinated intermediate, derived from prior dissociation of a second chloride ligand, namely  $[\text{Ru}(\kappa^4\text{-NP}_3)(\eta^1\text{-OOCH})]^+$ , was thus considered. This step was found to be endoergic by only 6.46 kcal mol<sup>-1</sup>, with a long separation between the metal center and the formate hydrogen (4.042 Å). The process resulted to be endothermic ( $\Delta H = +15.2$  kcal mol<sup>-1</sup>) and the entropic contribution ( $-T\Delta S = -8.7$  kcal mol<sup>-1</sup>) only partially lowers such an energy, with a net free energy cost of +6.46 kcal mol<sup>-1</sup>. The dissociation of the chloride ligand might be favored in the real system by the presence of the triethylammonium cation in solution, to form the corresponding salt, poorly soluble in CD<sub>2</sub>Cl<sub>2</sub>, and contribute to the driving force for this step.

In the calculations, a transition state  $\mathbf{5m}_{\text{TS}}^+$ , shown in Figure 2.12, was isolated and validated by the presence of an imaginary frequency at  $-89.9 \text{ cm}^{-1}$ , which is indicative of the formation of the Ru-H bond. This TS exhibits an agostic Ru-H interaction with a distance of  $2.154 \text{ \AA}$  accompanied by a significant elongation of the formate C-H bond ( $1.162 \text{ \AA}$ ). The energy barrier for the process was estimated as  $15.0 \text{ kcal mol}^{-1}$ . Such a TS exhibits the Ru---H interaction *trans* to nitrogen, and all the efforts to isolate a TS with H *trans* to P failed.

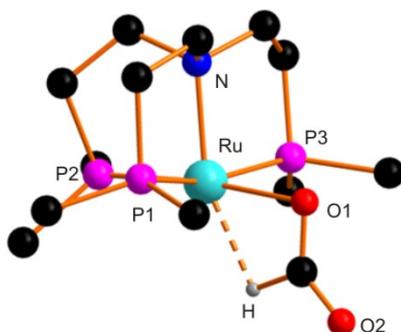
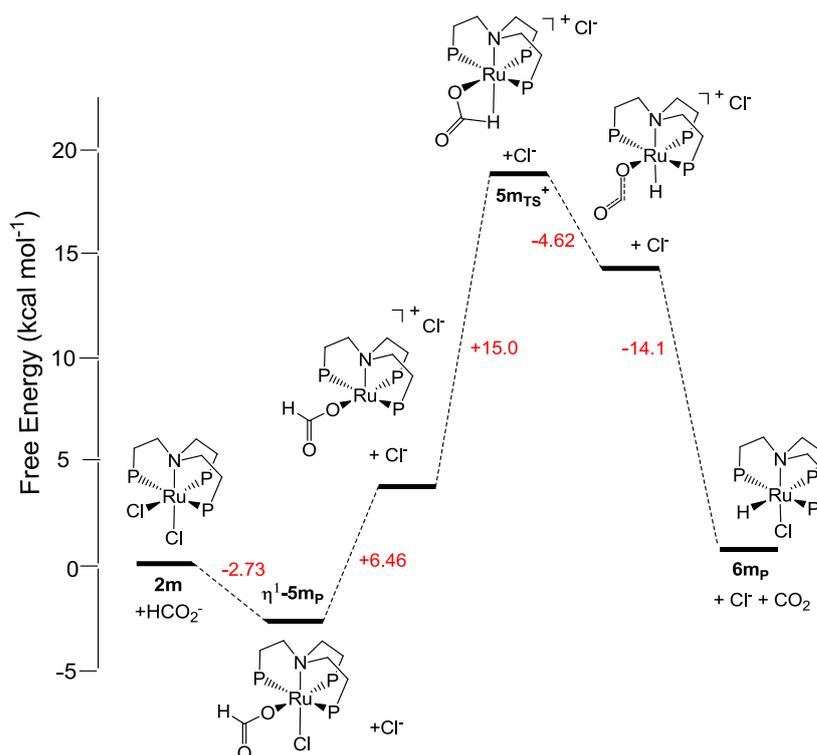


**Figure 2.12.** Optimized structure of  $\mathbf{5m}_{\text{TS}}^+$ . Main bond lengths ( $\text{\AA}$ ): Ru-H =  $2.154$ , Ru-O1 =  $2.209$ , Ru-P2 =  $2.295$  and Ru-N =  $2.174$ .

The following step would involve the formation of a hexa-coordinated complex with a Ru-bound hydride and a slightly interacting bent CO<sub>2</sub> ligand. This reaction is favored by  $-4.62 \text{ kcal mol}^{-1}$  with a significant elongation of Ru-O1 bond of about  $0.1 \text{ \AA}$ . Elimination of CO<sub>2</sub> further stabilizes the system by  $-14.1 \text{ kcal mol}^{-1}$ , to give  $\mathbf{6m}_{\text{P}}$  by coordinating back the chloride ligand, in agreement with the experimental data. The overall reaction pathway is shown in Scheme 2.13.



**Scheme 2.13.** Free energy reaction pathway leading from **2m** to **5m<sub>P</sub>**.

As described above, further addition of formic acid (5 equivalents) at 233 K to the reaction mixture in the NMR tube<sup>40</sup> yielded as main product the new complex identified as  $[\text{Ru}(\kappa^4\text{-NP}_3)(\eta^2\text{-H}_2)\text{Cl}]$  (**8**), from which hydrogen was released together with regeneration of **2** by increasing the temperature. In order to establish the pathway responsible for the formation of **8**, different possibilities were postulated. Firstly, the formic acid proton has two potential attack sites on complex **6m**, namely the hydride and the chloride ligands. The experimental results showed however the exclusive formation of the  $\text{Ru}(\eta^2\text{-H}_2)$  derivative, from protonation of the hydrido ligand, which was thus modeled as structure **8m<sup>+</sup>**, where the Ru octahedral geometry features a  $\kappa^4\text{-NP}_3$  ligand, a chloride and a  $\eta^2\text{-H}_2$  non classical molecular hydrogen ligand. Also in this case two isomers could form in principle, namely with  $\eta^2\text{-H}_2$  *trans* to N (**8m<sub>N</sub><sup>+</sup>**, Figure 2.13a) and *trans* to P (**8m<sub>P</sub><sup>+</sup>**, Figure 2.13b) therefore both structures were optimized and their relative energies compared. Structure **8m<sub>N</sub><sup>+</sup>** is estimated to be  $-3.88 \text{ kcal mol}^{-1}$  more stable than **8m<sub>P</sub><sup>+</sup>**, as expected from the better *trans*-effect of P compared to N. Ru-( $\eta^2\text{-H}_2$ ) distances were calculated as  $1.702 \text{ \AA}$  (**8m<sub>N</sub><sup>+</sup>**) vs.  $1.778 \text{ \AA}$  (**8m<sub>P</sub><sup>+</sup>**), whereas H-H distances of  $0.872 \text{ \AA}$  and  $0.819 \text{ \AA}$  were

obtained, respectively. This bond length difference should involve a blue shift of the associated H-H stretching frequencies. As expected, the corresponding calculated IR frequencies (2745.9 for  $\mathbf{8m}_N^+$  vs. 3293.2  $\text{cm}^{-1}$  for  $\mathbf{8m}_P^+$ ), follow this trend and suggest a decreased back donation from Ru( $d\pi$ ) to ( $\text{H}_2$ ) $\sigma^*$  orbital.

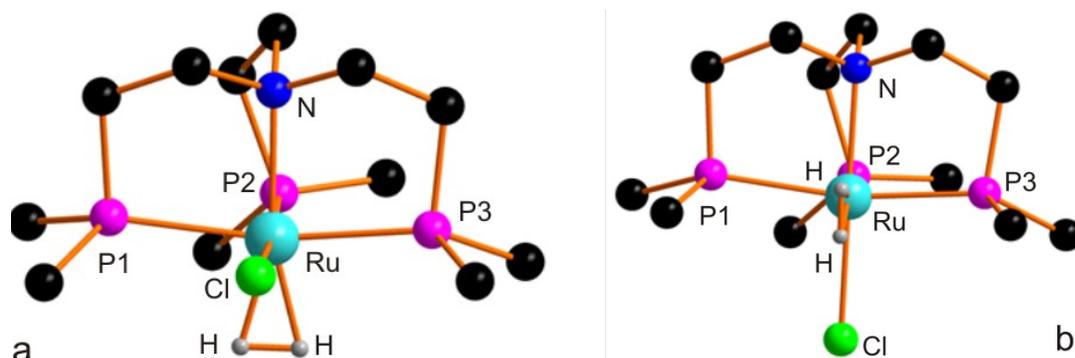


**Figure 2.13** Optimized structures of  $\mathbf{8m}_N^+$  (a) and  $\mathbf{8m}_P^+$  (b). Main bond lengths ( $\text{\AA}$ ) for  $\mathbf{8m}_N^+$ : Ru-( $\eta^2$ -H<sub>2</sub>) = 1.702, H-H = 0.872, Ru-Cl = 2.543, Ru-P2 = 2.304 and Ru-N = 2.236. Main bond lengths ( $\text{\AA}$ ) for  $\mathbf{8m}_P^+$ : Ru-( $\eta^2$ -H<sub>2</sub>) = 1.778, H-H = 0.819, Ru-Cl = 2.491, Ru-P2 = 2.325 and Ru-N = 2.229.

In passing from  $\mathbf{6m}_P$  to  $\mathbf{8m}_N^+$ , an accessible transition state  $\mathbf{6m}_{TS}$  was optimized for the approach of formic acid to  $\mathbf{6m}_P$ . The resulted structure of  $\mathbf{6m}_{TS}$ , shown in Figure 2.14, exhibited a relatively short H1-H2 distance of 1.944  $\text{\AA}$ , indicative of an interaction between the two ligands. The Cl $\cdots$ H2 separation (2.445  $\text{\AA}$ ) appeared too elongated to account for chloride protonation, confirming the initial hypothesis for the choice of protonation site. A similar TS was calculated for the water-assisted dihydrogen elimination from a Ru(PNN)<sup>46a</sup> and a series<sup>46b</sup> of Group 6 hydrido complexes. An imaginary frequency at -93.1  $\text{cm}^{-1}$ , relative to the shift of formic acid proton toward the hydride ligand, validates the nature of the TS. The energy barrier for accessing such transition state was estimated as +7.46  $\text{kcal mol}^{-1}$ .

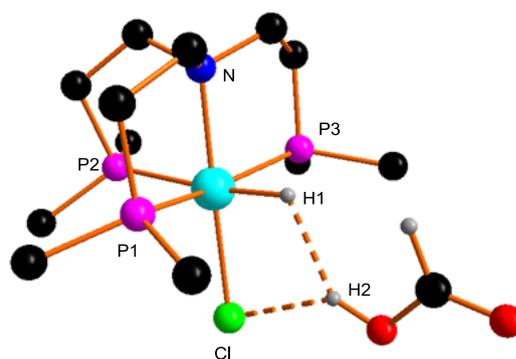
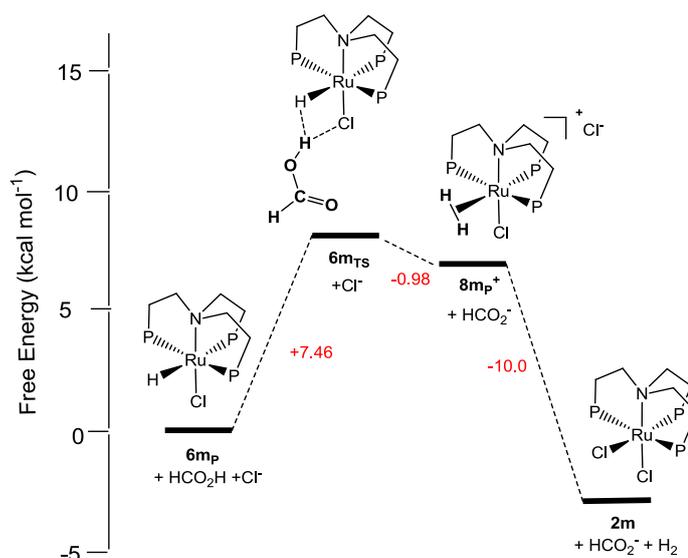


**Figure 2.14.** Optimized structure of transition state  $6m_{TS}$ , obtained by interaction of  $6m_P$  with a formic acid molecule. Main bond lengths (Å) : Ru-H1 = 1.652, Ru-Cl = 2.540, H1-H2 = 1.944, Cl-H2 = 2.445, Ru-P2 = 2.379 and Ru-N = 2.230.

The step from  $6m_{TS}$  to  $8m_P^+$  gave a calculated energy gain of  $-0.98$  kcal mol $^{-1}$ . Elimination of H $_2$  and coordination of chloride restores the initial complex  $2m$  with a free energy gain of  $-10.0$  kcal mol $^{-1}$  (Scheme 2.14).



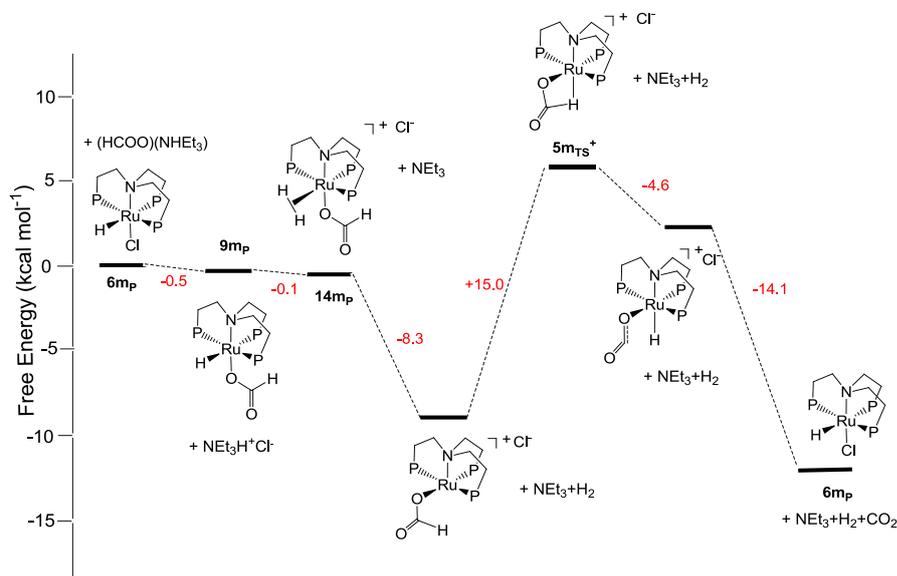
**Scheme 2.14.** Reaction pathway leading from  $6m_P$  to  $2m$ .

The mechanism described in Scheme 2.10 (cycle A) was reconsidered and an additional VT NMR study was carried out (see Experimental Section 2.7.6 for details). Complex **6** was synthesized following literature procedures<sup>23</sup> and dissolved in CD $_2$ Cl $_2$ . The corresponding  $^{31}\text{P}\{^1\text{H}\}$  NMR spectrum collected at 233 K showed the known AM $_2$  spin system composed by a P $_M$  doublet at 41.7 ppm ( $^2J_{PP} = 18$  Hz)

and a  $P_A$  triplet at 27.4 ppm. To this solution,  $(HCOO)(NHEt_3)$  (1 equiv.) was added under nitrogen at 233 K. The corresponding  $^{31}P\{^1H\}$  NMR spectrum showed the appearance of a new set of signals, at 44.8 ppm (t,  $^2J_{PP} = 29$  Hz,  $P_A$ ) and 23.8 ppm (d,  $P_M$ ), which was attributed to  $[Ru(\kappa^4-NP_3)H(\eta^1-OOCH)]$  (**13**) and formed in a 1:2 ratio with **6**. Complex **7** characterized by signals at 55.2 ppm (t,  $^2J_{PP} = 17.4$  Hz,  $P_M$ ) and 50.2 ppm (t,  $P_A$ ) formed in traces under these conditions. By increasing the temperature, the ratio between **6** and **13** gradually changed in favor of **13** while the concentration of **7** remained almost unchanged. In details, at 253 K the **13**:**6** ratio was calculated as 2.5:1, reaching the value 5.6:1 after 30 min. At 273 K, the signals due to **13** began slowly to decrease. At 293 K the **13**:**6** ratio was 1:2, and after 1h became 1:4. At this point, the tube was cooled again to 233 K and a second equivalent of  $(HCOO)(NHEt_3)$  was added. The reactivity previously described was again observed, and again **7** increased only in small quantities. Finally, addition of  $HCOOH$  (1 equiv to initial **6**) was added at 233 K. This caused the complete conversion of **6** to **13**, without affecting significantly the concentration of **7**. No other changes were observed by raising the temperature to 293 K. After one night at room temperature, the NMR spectrum showed almost only **6** to have formed again as major species.

Resorting again to DFT calculations, the reaction pathway involving release of  $H_2$  and  $CO_2$  from **6m<sub>P</sub>** by reaction with formate and formic acid was then modeled. The first step would involve chloride substitution in **6m<sub>P</sub>** by formate anion to generate **13m<sub>P</sub>**, as observed experimentally. This process was calculated to be favored by  $-0.53$  kcal mol<sup>-1</sup> at 233 K. Then, a protonation step could occur leading to  $[Ru(\kappa^4-NP_3)(\eta^2-H_2)(\eta^1-OOCH)]$  (**14m<sub>P</sub>**). The acidity source in solution is likely to stem from the alkyl ammonium  $NHEt_3^+$  and/or traces of undissociated  $HCOOH$ . The  $\eta^2-H_2$  ligand should be *trans* to P rather than to N, due to better trans influence. Upon temperature increase,  $H_2$  should be easily displaced giving the ruthenium penta-coordinated intermediate  $[Ru(\kappa^4-NP_3)(\eta^1-OOCH)]$  (free energy gain of  $-8.3$  kcal mol<sup>-1</sup>). The free coordination site may be then available for a  $\beta$ -elimination step through the transition state **5m<sub>Ts</sub>**<sup>+</sup> ( $\Delta G = +15.0$  kcal mol<sup>-1</sup>) to form a Ru-H bond and eliminate  $CO_2$  ( $\Delta G = -4.6$  kcal mol<sup>-1</sup>). Finally, coordination of chloride ( $\Delta G = -3.9$

kcal mol<sup>-1</sup>) could give back compound **6m<sub>P</sub>**. The free energy reaction pathway associated to this mechanism is shown in Scheme 2.15.



**Scheme 2.15.** Free energy reaction pathway for the production of CO<sub>2</sub> and H<sub>2</sub> from **6m<sub>P</sub>**.

The possible involvement of **7** in cycle A was finally reconsidered. This species was modeled by DFT calculations and two structural isomers **7m<sub>P</sub><sup>+</sup>** and **7m<sub>N</sub><sup>+</sup>** (Figure 2.15) emerged, having the hydride ligand either *trans* to P or *trans* to N, respectively. Structure **7m<sub>P</sub><sup>+</sup>** was estimated to be more stable by -3.63 kcal mol<sup>-1</sup>, in view of the more pronounced *trans*-effect of phosphorus, as pointed out by comparison of the optimized Ru-P bonds, with Ru-P2 (*trans* to hydride) being more elongated than the other two (2.398 vs 2.350 Å).

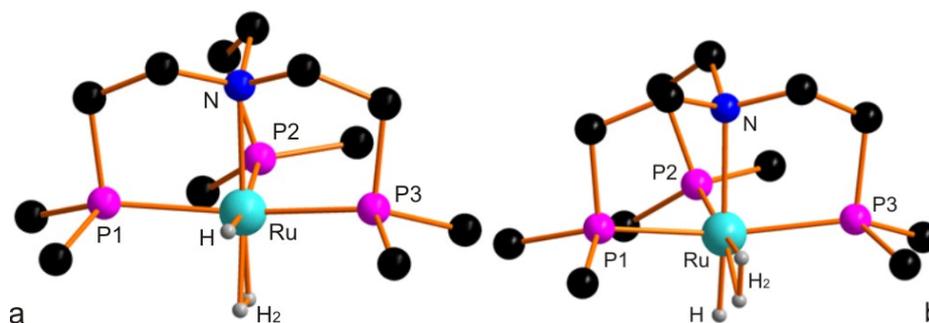
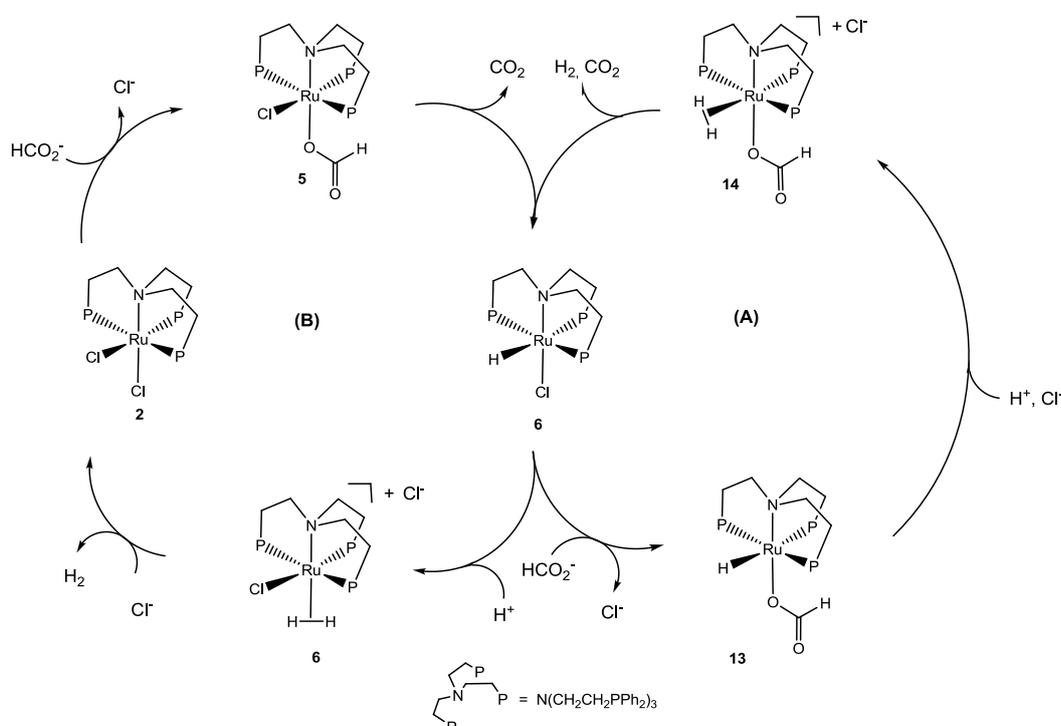


**Figure 2.15.** Optimized structures of **7m<sub>P</sub><sup>+</sup>** (a) and **7m<sub>N</sub><sup>+</sup>** (b). Main bond lengths (Å) for **7m<sub>P</sub><sup>+</sup>**: Ru-H = 1.603, Ru-H<sub>2</sub> = 1.672, H-H = 0.920, Ru-P2 = 2.39 and Ru-N = 2.246. Main bond lengths (Å) for **7m<sub>N</sub><sup>+</sup>**: Ru-H = 1.609, Ru-H<sub>2</sub> = 1.707, H-H = 0.897, Ru-P2 = 2.333 and Ru-N = 2.340.

Many different mechanisms generating  $7\mathbf{m}_N^+$  from  $6\mathbf{m}_P$  were considered. The most likely should involve the release of  $\text{CO}_2$  and formation of a Ru-H bond from  $[\text{Ru}(\kappa^4\text{-NP}_3)(\eta^2\text{-H}_2)(\eta^1\text{-OOCH})]$  ( $14\mathbf{m}_P$ ). However, this pathway provided too high barriers ( $+35.0 \text{ kcal mol}^{-1}$ ) to explain the formation of compound  $7\mathbf{m}_N^+$  even at low temperature (233 K). All the computational efforts to localize a transition state leading to  $7\mathbf{m}_N^+$  failed. On the basis of NMR and DFT data, it can be concluded that  $7$  may not be associated to the catalytic cycle of HCOOH dehydrogenation based on the Ru-NP<sub>3</sub> system, but rather form as a stable side-product under the reaction conditions applied in the NMR experiments. Consequently, Scheme 2.10 should be more correctly redrawn as below (Scheme 2.16).



**Scheme 2.16.** Catalytic cycles for HCOOH dehydrogenation in the presence of **2** based on VT NMR and DFT studies.

## 2.7 Conclusions

The activity of Ru(II) complexes containing the tripodal phosphine triphos and the amino(tris)phosphine NP<sub>3</sub> in the selective catalytic dehydrogenation of formic acid to carbon dioxide and hydrogen has been assessed under different conditions. The complex  $[\text{Ru}(\kappa^3\text{-triphos})(\text{MeCN})_3](\text{OTf})_2$  (**1**) showed superior performances with a

TON of 10000 after 6 h using 0.01 mol% of the catalyst and allowed for recycling up to eight times (0.1 mol% catalyst) giving a total TON of 8000 after ca. 14 h of continuous reaction at 80 °C in the presence of OctNMe<sub>2</sub>.

From the combination of DFT calculations and VT-NMR experiments, it was shown that complex [Ru( $\kappa^4$ -NP<sub>3</sub>)Cl<sub>2</sub>] (**2**) promoted an inner-sphere activation of HCOOH centered on the hydrochloride derivative [Ru( $\kappa^4$ -NP<sub>3</sub>)(H)Cl] (**6**), and recent results have shown that formic acid disproportionation occurs under pressure conditions through the coordination of formate ligand to the metal and its decarboxylation produces a reactive Ru hydride species representing the rate-determining step of the reaction.

This study highlights the importance of the choice of type and denticity of the stabilizing polydentate phosphines, i.e. 1,1,1-tris-(diphenylphosphinomethyl)ethane (triphos) vs. tris-[2-(diphenylphosphino)ethyl]amine (NP<sub>3</sub>), and of the nature, lability and number of ancillary ligands (Cl vs. MeCN), decisive for the formation of the active catalytic species.

## 2.8 Experimental section

### 2.8.1 General methods and materials

Complexes **1**, **2**, **3** and **6** were prepared according to literature procedures.<sup>25,22,30,23</sup> Formic acid and N,N-dimethyloctylamine were distilled in vacuum prior to use and stored under nitrogen. The formic acid to amine ratio was determined by <sup>1</sup>H NMR spectroscopy on a Bruker Avance 400 spectrometer. Ru(acac)<sub>3</sub> and the HCOOH/NEt<sub>3</sub> (5:2) mixture were purchased from commercial suppliers and used without further purification. Deuterated solvents for NMR measurements were purchased from commercial suppliers and stored onto activated 4A molecular sieves under N<sub>2</sub> before use. The variable temperature <sup>1</sup>H and <sup>31</sup>P{<sup>1</sup>H} NMR spectra were recorded on a Bruker Avance 400 spectrometer (operating at 400.13 and 100.61 MHz, respectively). Peak positions are relative to tetramethylsilane and were calibrated against the residual solvent resonance (<sup>1</sup>H) or the deuterated solvent multiplet (<sup>13</sup>C). <sup>31</sup>P{<sup>1</sup>H} NMR were referenced to 85% H<sub>3</sub>PO<sub>4</sub>, with the downfield shift taken as positive.

### 2.8.2 Synthesis of [Ru( $\kappa^3$ -triphos)(MeCN)<sub>3</sub>](PF<sub>6</sub>)<sub>2</sub> (**1'**)

Complex **1** (1.0 mmol, 1.15 g) was dissolved under nitrogen in warm MeCN (20 mL), to which a solution of NH<sub>4</sub>PF<sub>6</sub> (2.3 mmol, 0.38 g) in warm EtOH (20 mL) was added. After 15 min stirring at room temperature, the mixture was concentrated under vacuum and cold EtOH was added to induce precipitation. The desired complex was obtained in almost quantitative yield, recrystallised from MeCN/EtOH (1:1) giving a white microcrystalline product (1.06 g, 0.93 mmol).

### 2.8.3 Reaction of [Ru( $\kappa^3$ -triphos)(MeCN)<sub>3</sub>](PF<sub>6</sub>)<sub>2</sub> (**1'**) with CO (1 atm)

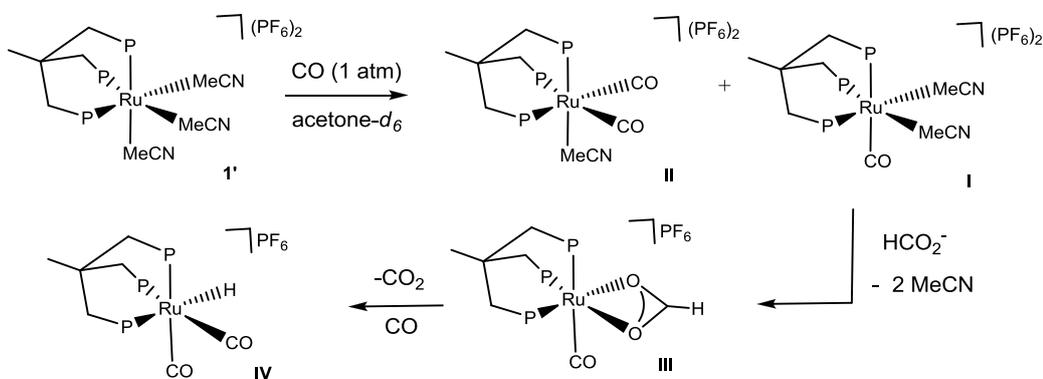
A solution of **1'** (20 mg, 1,176 x 10<sup>-2</sup> mmol) was dissolved in 0.6 mL of acetone-*d*<sub>6</sub> under nitrogen into a screw-cap NMR tube. The tube was placed in a ice bath and CO (1 atm) was bubbled into the solution for 15 min. The tube was then allowed to warm up to room temperature and a set of <sup>31</sup>P{<sup>1</sup>H} and <sup>1</sup>H NMR spectra were collected. The initial <sup>31</sup>P{<sup>1</sup>H} singlet at 27.0 ppm due to **1'** disappeared leaving two AM<sub>2</sub> sets of signals composed (**I**) of a doublet at 23.8 ppm (<sup>2</sup>J<sub>PP</sub> = 40 Hz) and a triplet at 2.0 ppm and (**II**) of a triplet at 19.2 ppm (<sup>2</sup>J<sub>PP</sub> = 32 Hz) and a doublet at 4.2 ppm, in *ca.* 8:1 ratio. In the corresponding <sup>1</sup>H NMR spectrum both signals of coordinated (2.49 ppm) and free MeCN (2.18 ppm) were visible. The tube was removed from the NMR probehead and warmed to 40 °C in a water bath for 2h, after which another set of NMR spectra were collected. In the <sup>31</sup>P{<sup>1</sup>H} spectrum it could be observed that the ratio **I:II** changed to *ca.* 1:10, while no other sets of signals appeared. In parallel the <sup>1</sup>H NMR signal due to free MeCN increased in intensity while the signal due to Ru-coordinated MeCN decreased.

On the basis of these observations and literature data,<sup>25,47</sup> we attribute the signals due to **I** to [Ru( $\kappa^3$ -triphos)(MeCN)<sub>2</sub>(CO)]<sup>2+</sup> and those due to **II** to [Ru( $\kappa^3$ -triphos)(MeCN)(CO)<sub>2</sub>]<sup>2+</sup>.

At this point HCO<sub>2</sub>NHEt<sub>3</sub> (1 equiv) was added to the mixture at room temperature. It was possible to observe complete disappearance of the signals due to **I**, the presence of **II** and formation of two new AM<sub>2</sub> species, (**III**) characterised by a triplet at 24.8 ppm (<sup>2</sup>J<sub>PP</sub> = 34 Hz) and a doublet at 0.2 ppm, and (**IV**) showing a doublet at 18.3 ppm (<sup>2</sup>J<sub>PP</sub> = 36 Hz) and a triplet at 8.5 ppm. In the corresponding <sup>1</sup>H NMR spectrum,

signals due to coordinated formate (8.28 ppm) and a weak high field doublet of triplets centred at -6.2 (dt,  ${}^2J_{\text{HP}(\text{trans})} = 81$ ,  ${}^2J_{\text{HP}(\text{cis})} = 15$  Hz, RuH) were present. Finally, neat HCOOH (1 equiv) was added at room temperature, apparently causing no further changes. The solution was dried under vacuum. The FT-IR spectrum of the solid in nujol mull showed the presence of  $\nu_{\text{CO}}$  stretching bands at 2103, 2078 and 2043  $\text{cm}^{-1}$ .

Thus, we propose the attribution of the signals due to **III** to  $[\text{Ru}(\kappa^3\text{-triphos})(\eta^2\text{-OOCH})(\text{CO})]^+$  and of the signals due to **IV** to  $[\text{Ru}(\kappa^3\text{-triphos})(\text{H})(\text{CO})_2]^+$ . The proposed reaction pathway can be visualised in Scheme 2.17 below.



**Scheme 2.17.** Reaction of  $[\text{Ru}(\kappa^3\text{-triphos})(\text{MeCN})_3](\text{PF}_6)_2$  (**1'**) with CO (1 atm).

#### 2.8.4 Catalytic tests

All catalytic experiments were carried out under an inert argon or nitrogen atmosphere in a flask heated either by oil bath or by external heating liquid circulation. The flask was connected to a reflux condenser, which was connected either to a setup of two manual burettes or to an automatic burette to measure the amounts of gas generated. The mixture of gas produced during the catalytic runs was either analyzed by FTIR on aATR Shimadzu IRAffinity-1 spectrophotometer with a gas cell (KBr windows, path length 10 cm) or by GC using a gas chromatograph HP 6890N (permanent gases: Carboxen 1000, TCD, external calibration; amines: HP Plot Q, 30 m, FID) and a hydrogen sensor (Hach Ultra Analytics GmbH). Typical procedure for the HCOOH dehydrogenation tests: A solution of HCOOH/amine (2.5 mL) was pre-warmed to 80 °C (HCOOH/OctNMe<sub>2</sub> 11:10) in a three-necked round

bottomed flask with a thermostated oil bath. The flask was purged with argon or nitrogen before the starting reaction by addition of the solid catalyst. In the case of experiments run at 40 °C (using the mixture HCOOH/NEt<sub>3</sub> 5:2), the automatic burette setup previously described was used.<sup>31</sup>

Typical procedure for recycling experiments at 80 °C: As soon as the gas volume evolution reached the theoretical value expected for 100% HCOOH conversion, the apparatus was flushed with nitrogen to remove any traces of hydrogen and carbon dioxide. The remaining reaction mixture containing the catalyst and the amine, kept at 80 °C, was reutilized as such for the following run by addition of neat HCOOH (0.49 mL, 12.9 mmol) through a syringe.

### 2.8.5 Variable temperature NMR experiments

Typically, the NMR tube samples were prepared at 233 K (acetone–liquid nitrogen bath) under nitrogen by dissolving 20 mg of the Ru complex in 0.70 mL of deuterated solvent and adding either 1 to 2 equiv. of HCO<sub>2</sub>NHEt<sub>3</sub>, followed by 1 equiv. of neat HCOOH, or 5 equiv. of HCOOH/NEt<sub>3</sub> (5:2). The NMR spectra were collected in the temperature range 233–313 K in the case of **2** (CD<sub>2</sub>Cl<sub>2</sub>) or 233–323 K in the case of **1** (acetone-d<sub>6</sub>).

### 2.8.6 Reactivity of [Ru(κ<sup>4</sup>-NP<sub>3</sub>)(H)Cl] with HCO<sub>2</sub>NHEt<sub>3</sub>

Complex [Ru(κ<sup>4</sup>-NP<sub>3</sub>)(H)Cl] (**4**, 20 mg, 2.53 x 10<sup>-2</sup> mmol) was dissolved in CD<sub>2</sub>Cl<sub>2</sub> (0.6 mL) under nitrogen at 233 K (acetone-liquid nitrogen bath). HCO<sub>2</sub>NHEt<sub>3</sub> (4.0 μL, ca. 1 equiv.) was then syringed into the tube, which was then inserted into the NMR probehead pre-cooled at 233 K. Subsequently, the probe was warmed slowly to room temperature in steps of 20 K each, and new sets of <sup>31</sup>P {<sup>1</sup>H} and <sup>1</sup>H NMR data were collected at each step. The probe was cooled at 233 K and a second equiv. of HCO<sub>2</sub>NHEt<sub>3</sub> was added, then the same heating sequence and NMR recording was applied. Finally, neat HCOOH (1.0 μL, ca. 1 equiv.) was added at 233 K, applying again the same heating sequence and NMR recording.

### 2.8.7 Computational methodology

The model systems reported herein were optimized at the hybrid density functional theory (DFT) level using the B3LYP functional.<sup>48</sup> All the DFT calculations were carried out using the Gaussian 09 package.<sup>49</sup> The nature of stationary point (minima or transition state) was confirmed for all of the fully optimized structures through vibrational frequencies calculations. The pseudo-potential Stuttgart-Dresden<sup>50</sup> was used for the Ru center while the 6-31G basis set with the important addition of the polarization functions (d, p) for all atoms including hydrogens. All the structures were optimized in solution using the Conductor-Like Polarizable Continuum Model (CPCM)<sup>51</sup> as implemented in the Gaussian 09 package,<sup>49</sup> and in particular in dichloromethane solution for **2** and in acetone for **1'**.

## 2.9 References

- <sup>1</sup> Sevillano, P.; Habtemariam, A.; Castiñeiras, A. M.; Garcia, E.; Sadler, P. J. *Polyhedron*, **1999**, *18*, 383.
- <sup>2</sup> Chaplin, A. B.; Dyson, P. J. *Inorg. Chem.*, **2008**, *47*, 381.
- <sup>3</sup> Bianchini, C. Meli, A.; Peruzzini, M.; Vizza, F.; Frediani, P. *Organometallics*, **1990**, *9*, 226.
- <sup>4</sup> Barbaro, P.; Bianchini, C.; Meli, A.; Moreno, M.; Vizza, F. *Organometallics*, **2002**, *21*, 1430.
- <sup>5</sup> (a) C. Bianchini, A. Meli, F. Vizza, *J. Organomet. Chem.*, **2004**, *689*, 4277; (b) C. Bianchini, A. Meli, S. Moneti, F. Vizza, *Organometallics*, **1998**, *17*, 2636; (c) C. Bianchini, D. Masi, A. Meli, M. Peruzzini, F. Vizza, F. Zanobini, *Organometallics*, **1998**, *17*, 2495.
- <sup>6</sup> Barbaro, P.; Bianchini, C.; Frediani, P.; Meli, A.; Vizza, F.; *Inorg. Chem.*, **1992**, *31*, 1523.
- <sup>7</sup> Bianchini, C.; Meli, A.; Moneti, S.; Oberhauser, W.; Vizza, F.; Herrera, V.; Fuentes, A.; Sanchez-Delgado, R. A. *J. Am. Chem. Soc.* **1999**, *121*, 7071.
- <sup>8</sup> Bianchini, C.; Meli, A.; Peruzzini, M.; Vizza, F.; Zanobini, F. *Coord. Chem. Rev.* **1992**, *120*, 193.
- <sup>9</sup> Belkova, N. V.; Bakhmutova, E. V.; Shubina, E. S.; Bianchini, C.; Peruzzini, M.; Bakhmutov, V. I.; Epstein, L. M. *Eur. J. Inorg. Chem.* **2000**, 2163.
- <sup>10</sup> (a) Geilen, F. M. A.; Engendahl, B.; Harwardt, A.; Marquardt, W.; Klankermayer, J.; Leitner, W. *Angew. Chem., Int. Ed.* **2010**, *49*, 5510; (b) Van Engelen, M. C.; Teunissen, H. T.; de Vries, J. G.; Elsevier, C. J. *J. Mol. Catal. A: Chem.* **2003**, *206*, 185; (c) Mehdi, H.; Fábos, V.; Tuba, R.; Bodor, A.; Mika, L. T.; Horvath, I. T. *Top. Catal.* **2008**, *48*, 49; (d) Ohkuma, T.; Noyori, R. In *Handbook of Homogeneous Hydrogenation*; de Vries, J. G., Elsevier, C. J., Eds.; Wiley-VCH: Weinheim, Germany, **2007**; *Vol. 4*, p 1105; (e) Teunissen, H. T.; Elsevier, C. J. *Chem. Commun.* **1997**, 667; (f) Teunissen, H. T.; Elsevier, C. J. *Chem. Commun.* **1998**, 1367; (g) , A. A.; Eastham, G. R.; Cole-Hamilton, D. J. *Chem. Commun.* **2007**, 3154; (h) Rosi, L.; Frediani, M.; Frediani, P. *J. Organomet. Chem.* **2010**, *695*, 1314.

- <sup>11</sup> (a) Corma, A.; Iborra, S.; Velty, A. *Chem. Rev.* **2007**, *107*, 2411; (b) Shiramizu, M.; Toste, F. D. *Angew. Chem., Int. Ed.* **2012**, *51*, 8082; (c) Geilen, F. M. A.; vom Stein, T.; Engendahl, B.; Winterle, S.; Liauw, M. A.; Klankermayer, J.; Leitner, W. *Angew. Chem., Int. Ed.* **2011**, *50*, 6831.
- <sup>12</sup> (a) Cokoja, M.; Bruckmeier, C.; Rieger, B.; Herrmann, W. A.; Kühn, F. E. *Angew. Chem., Int. Ed.* **2011**, *50*, 8510; (b) Peters, M.; Köhler, B.; Kuckshinrichs, W.; Leitner, W.; Markewitz, P.; Müller, T. E. *ChemSusChem.* **2011**, *4*, 1216.
- <sup>13</sup> Geilen, F. M. A.; Engendahl, B.; Hölscher, M.; Klankermayer, J.; Leitner, W. *J. Am. Chem. Soc.* **2011**, *133*, 14349.
- <sup>14</sup> (a) Núñez Magro, A. A.; Eastham, G. R.; Cole-Hamilton, D. J. *Chem. Commun.* **2007**, 3154; (b) Coetzee, J.; Dodds, D. L.; Klankermayer, J.; Brosinski, S.; Leitner, W.; Slawin, A. M. Z.; Cole-Hamilton, D. J. *Chem. Eur. J.* **2013**, *19*, 11039; (c) Beydoun, K.; vom Stein, T.; Klankermayer, J.; Leitner, W. *Angew. Chem., Int. Ed.* **2013**, *52*, 9554.
- <sup>15</sup> (a) Beydoun, K.; vom Stein, T.; Klankermayer, J.; Leitner, W. *Angew. Chem. Int. Ed.* **2013**, *52*, 9554; (b) Li, Y.; Sorribes, I.; Yan, T.; Junge, K.; Beller, M. *Angew. Chem. Int. Ed.* **2013**, *52*, 12156.
- <sup>16</sup> Wesselbaum, S.; vom Stein, T.; Klankermayer, J.; Leitner, W. *Angew. Chem., Int. Ed.* **2012**, *51*, 7449.
- <sup>17</sup> Wesselbaum, S.; Moha, V.; Meuresch, M.; Brosinski, S.; Thenert, K. M.; Kothe, J.; vom Stein, T.; Englert, U.; Hölscher, M.; Klankermayer, J.; Leitner, W. *Chem. Sci.* **2014**, DOI: 10.1039/c4sc02087a
- <sup>18</sup> vom Stein, T.; Meuresch, M.; Limper, D.; Schmitz, M.; Hölscher, M.; Coetzee, J.; Cole-Hamilton, D. J.; Klankermayer, J.; Leitner, W. *J. Am. Chem. Soc.* **2014**, *136*, 13217.
- <sup>19</sup> Savourey, S.; Lefèvre, G.; Berthet, J-C.; Thuéry, P.; Genre, C.; Cantat, T. W. *Angew. Chem., Int. Ed.* **2013**, *52*, 9554.
- <sup>20</sup> (a) Sacconi, L. *Coord. Chem. Rev.* **1972**, *8*, 351; (b) Morassi, I.; Bertini, I.; Sacconi, L. *Coord. Chem. Rev.* **1973**, *11*, 343; (c) Sacconi, L.; Ghilardi, C. A.; Mealli, C.; Zanobini, F. *Inorg. Chem.* **1975**, *14*, 6, 1380; (d) Bianchini, C.; Masi, D.; Meli, A.; Peruzzini, M.; Zanobini, F. *J. Am. Chem. Soc.* **1988**, *110*, 6411; (e) Mealli, C.; Ghilardi, C.A.; Orlandini, A. *Coord. Chem. Rev.* **1992**, *120*, 361; (f) Bertolasi, V.; Marchi, A.; Marvelli, L.; Rossi, R.; Bianchini, C.; de los Rios, I.; Peruzzini, M. *Inorg. Chim. Acta* **2002**, *327*, 140; (g) Rossin, A.; Gutsul, E. I.; Belkova, N. V.; Epstein, L. M.; Gonsalvi, L.; Lledós, A.; Lyssenko, K.; Peruzzini, M.; Shubina, E. S.; Zanobini, F. *Inorg. Chem.* **2010**, *49*, 4343.
- <sup>21</sup> Wolinska, A.; Touchard, D.; Dixneuf, P. H.; Romero, A. *J. Organomet. Chem.* **1991**, *420*, 217.
- <sup>22</sup> Dahlenburg, L.; Frosin, K. M.; Kerstan, S.; Werner, D. *J. Organomet. Chem.* **1991**, *407*, 115.
- <sup>23</sup> Chen, X.; Xue, P.; Sung, H. H. Y.; Williams, I. D.; Peruzzini, M.; Bianchini, C.; Jia, G. *Organometallics* **2005**, *24*, 4330.
- <sup>24</sup> Rossi, A.; Zanobini, F.; Rossin, A.; Peruzzini, M. *ChemPlusChem.* **2014**, *79*, 1316.
- <sup>25</sup> Rhodes L. F.; Sorato, C.; Venanzi, L. M.; Bachechi, F. *Inorg. Chem.* **1988**, *27*, 604.
- <sup>26</sup> Crabtree, R. H.; Pearman, A. J. *J. Organomet. Chem.* **1978**, *257*, 335.
- <sup>27</sup> Chatt, J.; Shaw, B. L.; Field, A. E. *J. Chem. Soc.* **1964**, 3466.
- <sup>28</sup> Rose, D.; Wilkinson, G. *J. Chem. Soc. A* **1970**, 1791.
- <sup>29</sup> James, B. R.; Ochiai, E.; Rempel, G. I. *Inorg. Nucl. Chem. Lett.* **1971**, *7*, 781.
- <sup>30</sup> Bakhmutov, V. I.; Bakhmutov, E. V.; Belkova, N. V.; Bianchini, C.; Epstein, L. M.; Masi, D.; Peruzzini, M.; Shubina, E. S.; Vorontsov, E. V.; Zanobini, F. *Can. J. Chem.* **2001**, *79*, 479.
- <sup>31</sup> Boddien, A.; Loges, B.; Junge, H.; Beller, M. *ChemSusChem.* **2008**, *1*, 751.
- <sup>32</sup> (a) Junge, H.; Boddien, A.; Capitta, F.; Loges, B.; Noyes, J. R.; Gladiali, S.; Beller, M. *Tetrahedron Lett.*, **2009**, *50*, 1603; (b) Majeovski, A.; Morris, D. J.; Kendall, K.; Wills, M. *ChemSusChem*, **2010**, *3*, 431.

- <sup>33</sup> (a) Whittlesey, M. K.; Perutz, R. N.; Moore, M. H. *Organometallics* **1996**, *15*, 5166; (b) Allen, O. R.; Dalgarno, S. J.; Field, L. D.; Jensen, P.; Willis, A. C. *Organometallics* **2009**, *28*, 2385.
- <sup>34</sup> (a) I. S. Kolomnikov, A I. Gusev, G. G. Aleksandrov, T. S. Lobeeva, Yu. T. Struchkov and M. Fi. Vol'pin *J. Organomet. Chem.* **1973**, *59*, 359.
- <sup>35</sup> (a) Sarmah, B. J.; Dutta, D. K. *J. Organomet. Chem.* **2010**, *695*, 781; (b) Chaplin A. B.; Dyson, P. J. *Eur. J. Inorg. Chem.* **2007**, 4973; (c) Landgrafe, C.; Sheldrick, W. S.; Südfeld, M. *Eur. J. Inorg. Chem.* **2007**, 4973.
- <sup>36</sup> Boddien, A.; Mellmann, D.; Gärtner, F.; Jackstell, R.; Junge, H.; Dyson, P. J.; Laurency, G.; Ludwig, R.; Beller, M. *Science* **2011**, *333*, 1733.
- <sup>37</sup> (a) Hirva, P.; Haukka, M.; Jakonen, M.; Moreno, M. A. *J. Mol. Mod.* **2008**, *17*, 171. (b) Lombardi, J. R.; Davis, B. *Chem. Rev.* **2002**, *102*, 2431. (c) Barden, C. J.; Rienstra-Kiracofe, J. C.; Schaefer, H. F., *J. Chem. Phys.* **2000**, *113*, 690. (d) Yanagisawa, S.; Tsuneda, T.; Hirao, K. *J. Chem. Phys.* **2000**, *112*, 545.
- <sup>38</sup> Cambridge Structural Database System, Cambridge Crystallographic Data Centre, Cambridge, UK Version 5.32.
- <sup>39</sup> Bianchini, C.; Dal Santo, V.; Meli, A.; Oberhauser, W.; Psaro, R.; Vizza, F. *Organometallics* **2000**, *19*, 2433.
- <sup>40</sup> Mellone, I.; Peruzzini, M.; Rosi, L.; Mellmann, D.; Junge, H.; Beller, M.; Gonsalvi, L. *Dalton Trans.* **2013**, *42*, 2495.
- <sup>41</sup> Manca, G.; Mellone, I.; Bertini, F.; Peruzzini, M.; Rosi, L.; Mellmann, D.; Junge, H.; Beller, M.; Ienco, A.; Gonsalvi, L. *Organometallics* **2013**, *32*, 7053.
- <sup>42</sup> Morris, D. J.; Clarkson, C. J.; Wills, M. *Organometallics* **2009**, *28*, 4133.
- <sup>43</sup> Anzellotti, A.; Briceno, A.; Delgado, G.; Diaz de Delgado, G.; Fontal, B. *Acta Crystallogr., Sect. C: Cryst. Struct. Commun.* **2002**, *58*, 355.
- <sup>44</sup> (a) Hartley, F. R. *Chem. Soc. Rev.* **1973**, *2*, 163. (b) Sajith, P. K.; Suresh, C. H. *Dalton Trans.* **2010**, *39*, 815. (c) Sajith, P. K.; Suresh, C. H. *J. Organomet. Chem.* **2011**, 696, 2086. (d) See, R. F.; Kozina, D. *J. Coord. Chem.* **2013**, *66*, 490.
- <sup>45</sup> Ziebart, C.; Federsel, C.; Anbarasan, P.; Jackstell, R.; Baumann, W.; Spannenberg, A.; Beller, M. *J. Am. Chem. Soc.* **2012**, *134*, 20701.
- <sup>46</sup> (a) Sandhya, K. S.; Suresh, C. H. *Organometallics* **2011**, *30*, 3888; (b) Sandhya, K. S.; Suresh, C. H. *Dalton Trans.* **2012**, *41*, 11018.
- <sup>47</sup> Michos, D.; Luo, X.-L.; Crabtree, R. H. *Inorg. Chem.* **1992**, *31*, 4245.
- <sup>48</sup> Becke, A. D. *J. Chem. Phys.* **1993**, *98*, 5648.
- <sup>49</sup> Frisch, M. J.; Trucks, G. W.; Schlegel, H. B.; Scuseria, G. E.; Robb, M. A.; Cheeseman, J.R.; Scalmani, G.; Barone, V.; Mennucci, B.; Petersson, G. A.; Nakatsuji, H.; Caricato, M.; Li, X.; Hratchian, H. P.; Izmaylov, A. F.; Bloino, J.; Zheng, G.; Sonnenberg, J. L.; Hada, M.; Ehara, M.; Toyota, K.; Fukuda, R.; Hasegawa, J.; Ishida, M.; Nakajima, T.; Honda, Y.; Kitao, O.; Nakai, H.; Vreven, T.; Montgomery, J. J. A.; Peralta, J. E.; Ogliaro, F.; Bearpark, M.; Heyd, J. J.; Brothers, E.; Kudin, K. N.; Staroverov, V. N.; Keith, T.; Kobayashi, R.; Normand, J.; Raghavachari, K.; Rendell, A.; Burant, J. C.; Iyengar, S. S.; Tomasi, J.; Cossi, M.; Rega, N.; Millam, J. M.; Klene, M.; Knox, J. E.; Cross, J. B.; Bakken, V.; Adamo, C.; Jaramillo, J.; Gomperts, R.; Stratmann, R. E.; Yazyev, O.; Austin, A. J.; Cammi, R.; Pomelli, C.; Ochterski, J. W.; Martin, R. L.; Morokuma, K.; Zakrzewski, V. G.; Voth, G. A.; Salvador, P.; Dannenberg, J. J.; Dapprich, S.; Daniels, A. D.; Farkas, O.; Foresman, J. B.; Ortiz, J. V.; Cioslowski, J.; Fox, D. J. *Gaussian 0.9, Revision B.01* ed., Gaussian, Inc., Wallingford CT, **2010**.
- <sup>50</sup> Dolg, M.; Stoll, H.; Preuss, H.; Pitzer, R. M. *J. Phys. Chem.* **1993**, *97*, 5852.
- <sup>51</sup> (a) Barone, V.; Cossi, M. *J. Phys. Chem. A* **1998**, *102*, 1995. (b) Cossi, M.; Rega, N.; Scalmani, G.; Barone, V. *J. Comput. Chem.* **2003**, *24*, 669.



## Chapter 3

### **Hydrogen Storage and Release by HCOOH Dehydrogenation and NaHCO<sub>3</sub> Hydrogenation Catalyzed by Ru(II) Complexes Bearing Bulky Polydentate Phosphines**

#### **3.1 Overview**

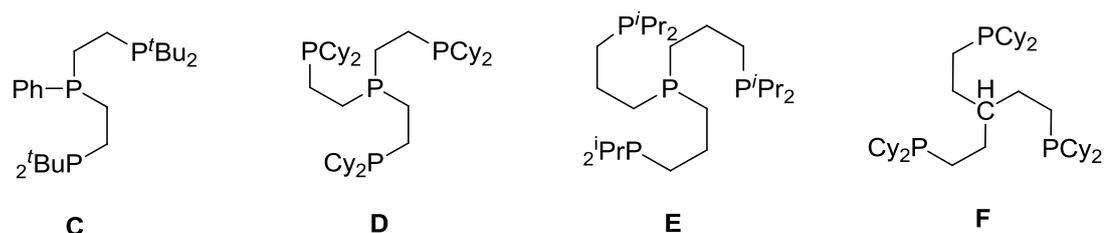
In this chapter, the use of iron and ruthenium complexes bearing PP<sub>3</sub> and CP<sub>3</sub>-type ligands as catalysts for formic acid dehydrogenation and sodium bicarbonate hydrogenation is reported. After an introduction section summarizing literature data on the synthesis of some of the complexes, supplied to our laboratories by Field and coworkers at UNSW Sydney, Australia, as part of a collaboration project involving also colleagues at LIKAT Rostock, Germany, the chapter follows with the description of the catalytic results and ends with the experimental section related to the methodology used for the catalytic tests.

## 3.2 Introduction

Polydentate phosphine ligands have become an important class of ligands, since they provide a strong coordination environment and allow to control stereochemistry at the metal centre. In particular,  $PP_3$ -type ligands of the form  $P[(CH_2)_nPR_2]_3$  ( $n= 2,3$ ;  $R = Ph, Me, Cy, iPr$ ) are able to coordinate to a metal with four donor phosphorus atoms, and form metal complexes which have found a wide range of applications, especially with iron and ruthenium.<sup>1</sup> These organometallic reactivities of these complexes include the formation of stable dinitrogen complexes, C–H activation derivatives and stabilization of  $\eta^2$ -dihydrogen complexes.<sup>2</sup> Geometries ranging from octahedral, trigonal bipyramidal, and square-pyramidal are possible with  $PP_3$ -type ligands. Moreover, when coordinated to a metal centre, they can leave two available *cis*-coordination sites, a crucial requisite for a number of catalytic transformations.

The encapsulating nature of  $PP_3$  ligands and the presence of sterically encumbered bulky groups on the terminal phosphines of  $PP_3$  ligands can be used to restrict access to the metal center and enhance chemical reactivity and selectivity.

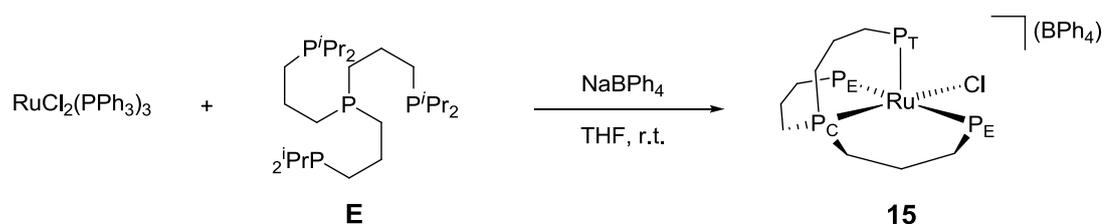
Since the progenitor of this class of ligands,  $P[(CH_2CH_2)PPh_2]_3$  ( $PP_3$ ) was successfully applied in the Fe-catalysed dehydrogenation of formic acid<sup>3</sup> as well as in the bicarbonate or  $CO_2$  hydrogenation to sodium formate, methyl formate and formamides,<sup>4</sup> we decided to investigate the behaviour of iron and ruthenium complexes of other  $PP_3$  type ligands, in particular those of  $P^2P_3^{Cy}$  and  $P^3P_3^{iPr}$ , and by comparison that of the related tridentate ligand  $PhP^2P_2^{tBu}$  (**C-E**, Scheme 3.1).<sup>5,6,7</sup> Finally, a ruthenium complex bearing the podand ligand  $^H C^2P_3^{Cy}$  (**F**, Scheme 3.1)<sup>8</sup> was also studied. Podand ligands provide rigid coordination geometries, which can impart chemical properties and reactivity similar to those of *pincer* complexes.<sup>9</sup> Furthermore, the interest for carbon-centered podands comes from studies of the active site of the nitrogenase enzyme, used in nature to achieve nitrogen fixation. Recently, a growing number of reports on the carbon-centered podand ligand were reported.<sup>10</sup>

Scheme 3.1.  $PP_3$  and  $CP_3$ -type ligands.

### 3.3 Synthesis of Ru and Fe complexes bearing $P^2P_3^{Cy}$ , $P^3P_3^{iPr}$ , $PhP^2P_2^{tBu}$ and $HC^2P_3^{Cy}$

A series of Fe and Ru complexes bearing the abovementioned ligands were synthesised by Field and coworkers<sup>5b,6,7,8</sup> and were supplied to our laboratories for testing as potential catalysts for FA dehydrogenation and  $NaHCO_3$  hydrogenation. Hereby are reported the main synthetic and characterization details for completeness. These complexes are characterized by different bulkiness and donor abilities (**C-F**, Scheme 3.1). In particular, we selected the complexes  $[Ru(P^3P_3^{iPr})Cl][BPh_4]$  (**15**),  $[Ru(P^3P_3^{iPr})(H)_2]$  (**16**),  $[Ru(PhP^2P_2^{tBu})Cl_2]$  (**17**),  $[Ru(P^2P_3^{Cy})H(N_2)][BF_4]$  (**18**),  $[Ru(HC^2P_3^{Cy})H(CO)]$  (**19**),  $[Fe(P^2P_3^{Cy})(N_2)]$  (**20**),  $[Fe(P^2P_3^{Cy})(N_2)][BPh_4]$  (**21**),  $[Fe(P^2P_3^{Cy})(H)_2]$  (**22**),  $[Fe(P^2P_3^{Cy})H(N_2)][BF_4]$  (**23**).

For the synthesis of  $[Ru(P^3P_3^{iPr})Cl][BPh_4]$  (**15**),<sup>6</sup> after addition of sodium tetraphenylborate to a THF solution of  $P^3P_3^{iPr}$  (**E**) and  $RuCl_2(PPh_3)_3$ ,  $[Ru(P^3P_3^{iPr})Cl][BPh_4]$  (**15**) precipitated as a pink solid (Scheme 3.2). Crystals suitable for structural analysis were grown from a THF/pentane solution of **15** (Figure 3.1).

Scheme 3.2. Synthesis of  $[Ru(P^3P_3^{iPr})Cl][BPh_4]$  (**15**).<sup>6</sup>

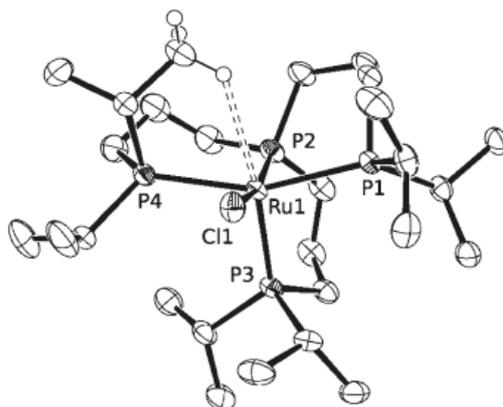
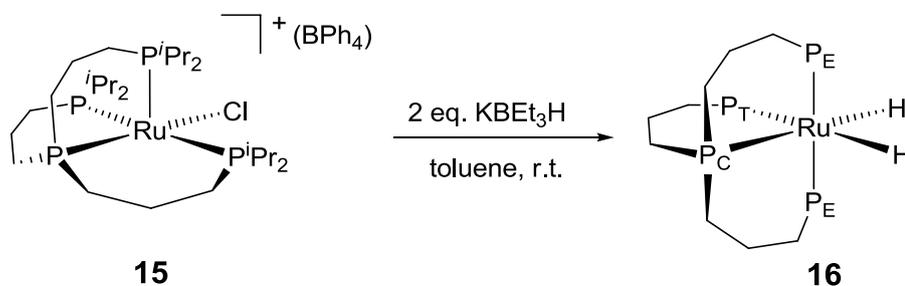


**Figure 3.1.** X-ray crystal structure of  $[\text{Ru}(\text{P}^3\text{P}_3^{\text{iPr}})\text{Cl}][\text{BPh}_4]$  (**15**).<sup>6</sup>

The  $^{31}\text{P}\{^1\text{H}\}$  NMR spectrum of **15** exhibited at room temperature a very broad resonance at 25.7 ppm and a sharp quartet at 14.2 ppm ( $^2J_{\text{PCPE/T}} = 36.4$  Hz) corresponding to the three terminal phosphines  $\text{P}_\text{E}/\text{P}_\text{T}$  and the central phosphines  $\text{P}_\text{C}$ , respectively.

At 220 K, the single broad resonance for the terminal phosphines separated into three distinct resonances for the non-equivalent terminal phosphorus atoms, giving four distinct resonances representing the four different phosphine.

For the synthesis of  $[\text{Ru}(\text{P}^3\text{P}_3^{\text{iPr}})(\text{H})_2]$  (**16**),<sup>6</sup> potassium triethylborohydride was added to a toluene solution of  $[\text{Ru}(\text{P}^3\text{P}_3^{\text{iPr}})\text{Cl}][\text{BPh}_4]$  (**15**) and the resulting mixture was stirred overnight at room temperature. After solvent evaporation **16** was collected as a white crystalline powder (Scheme 3.3). Crystals suitable for X-ray diffraction were grown by slow evaporation of a THF solution of **16** under an atmosphere of nitrogen (Figure 3.2).



**Scheme 3.3.** Synthesis of  $\text{Ru}(\text{P}^3\text{P}_3^{\text{iPr}})(\text{H})_2$  (**16**).<sup>6</sup>

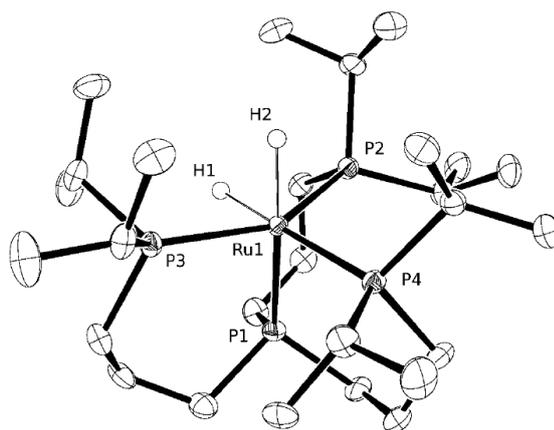
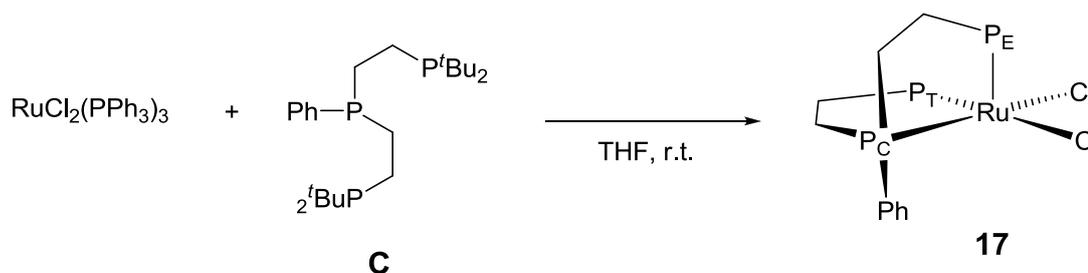


**Figure 3.2.** X-ray crystal structure of  $[\text{Ru}(\text{P}^3\text{P}_3^{\text{iPr}})(\text{H})_2]$  (**16**).<sup>6</sup>

The  $^{31}\text{P}\{^1\text{H}\}$  NMR spectrum showed a doublet of doublets at 49.2 ppm ( $^2J_{\text{PEPC}} = 28.5$  Hz,  $^2J_{\text{PEPT}} = 18.5$  Hz) and a doublet of triplets at 28.5 ppm ( $^2J_{\text{PTPC}} = 28.5$  Hz) corresponding to the two equivalent terminal phosphines  $\text{P}_\text{E}$  and the terminal phosphine  $\text{P}_\text{T}$ , respectively. The central phosphine  $\text{P}_\text{C}$  signal appears as a doublet of triplets at 0.4 ppm.

In the corresponding  $^1\text{H}$  NMR spectrum, resonances for the two hydrido ligands of **16** both appear as doublets of triplets of doublets of doublets at -9.43 ( $^2J_{\text{HH}} = 6.2$  Hz,  $^2J_{\text{HP}} = 59.6$  Hz, 24.2 Hz and 18.8 Hz) and -12.50 ppm ( $^2J_{\text{HH}} = 6.2$  Hz,  $^2J_{\text{HP}} = 63.2$  Hz, 34.0 Hz and 15.0 Hz).

For the synthesis of  $[\text{Ru}(\text{PhP}^2\text{P}_2^{\text{tBu}})\text{Cl}_2]$  (**17**),<sup>7</sup> addition of a THF solution of  $\text{RuCl}_2(\text{PPh}_3)_3$  to a THF solution of  $\text{PhP}^2\text{P}_2^{\text{tBu}}$  (**C**), followed by overnight stirring and addition of hexane, afforded **17** as a yellow solid (Scheme 3.4). Crystals suitable for structural analysis were grown by slow diffusion of pentane into a dichloromethane solution of **17** (Figure 3.3).



**Scheme 3.4.** Synthesis of  $[\text{Ru}(\text{PhP}^2\text{P}_2^{\text{tBu}})\text{Cl}_2]$  (**17**).<sup>7</sup>

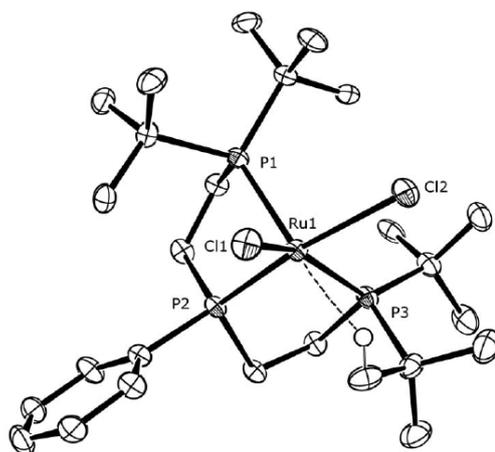
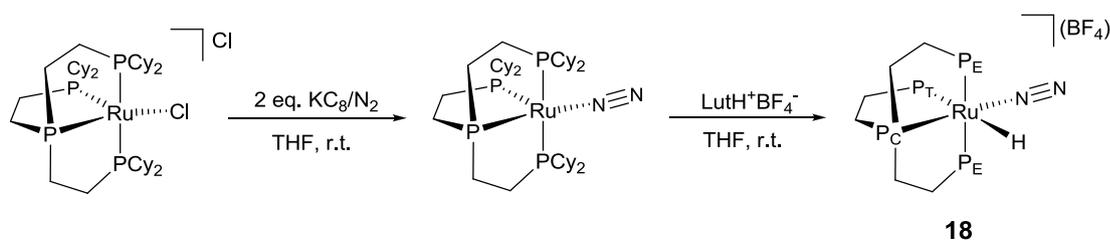


**Figure 3.3.** X-ray crystal structure of  $[\text{Ru}(\text{PhP}^2\text{P}_2^{\text{tBu}})\text{Cl}_2]$  (**17**).<sup>7</sup>

The  $^{31}\text{P}\{^1\text{H}\}$  NMR spectrum of **17** showed, at room temperature, a very broad resonance at 92.3 ppm corresponding to the two bound terminal phosphines  $\text{P}_\text{E}/\text{P}_\text{T}$ . The central phosphine  $\text{P}_\text{C}$  appears as a triplet at 94.4 ppm ( $^2J_{\text{PP}} = 12.6$  Hz). By decreasing temperatures to about  $-90$  °C the  $\text{P}_\text{E}/\text{P}_\text{T}$  resonance broadened into the baseline before resolving into two separate resonances at 128 and 52 ppm. The NMR data is consistent with a fluxional 5-coordinate complex with fast exchange at room temperature of the resonances for  $\text{P}_\text{E}$  and  $\text{P}_\text{T}$ .

Complex  $[\text{Ru}(\text{P}^2\text{P}_3^{\text{Cy}})\text{H}(\text{N}_2)][\text{BF}_4]$  (**18**) was synthesised<sup>5b</sup> by treatment of a THF solution of  $[\text{Ru}(\text{P}^2\text{P}_3^{\text{Cy}})(\text{N}_2)]$  with 1 equivalent of 2,6-lutidinium tetrafluoroborate. A pale orange solid was obtained and collected by filtration to afford  $[\text{Ru}(\text{P}^2\text{P}_3^{\text{Cy}})\text{H}(\text{N}_2)][\text{BF}_4]$  (**18**) (Scheme 3.5). Crystals of **18** suitable for X-ray diffraction analysis were grown by vapour diffusion of pentane into THF solutions of **18** (Figure 3.4).



**Scheme 3.5.** Synthesis of  $[\text{Ru}(\text{P}^2\text{P}_3^{\text{Cy}})\text{H}(\text{N}_2)][\text{BF}_4]$  (**18**).<sup>5b</sup>

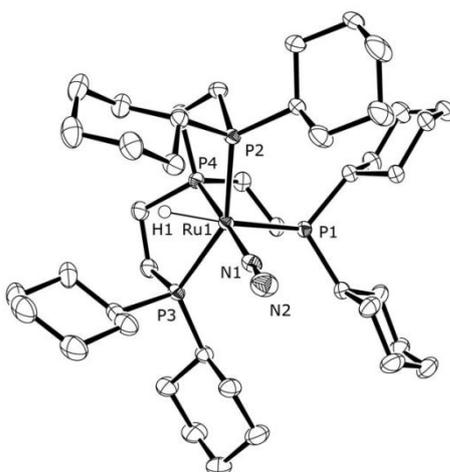
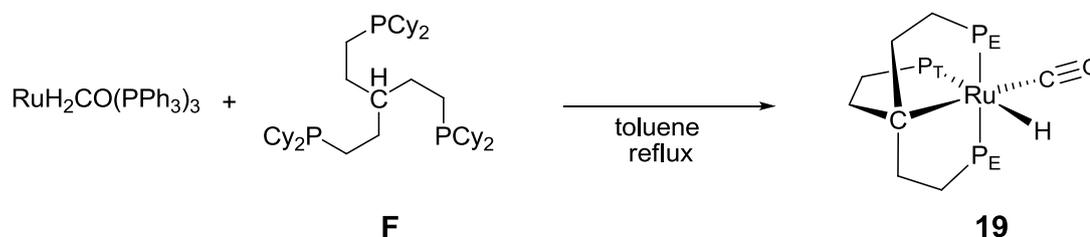


**Figure 3.4.** X-ray crystal structure of  $[\text{Ru}(\text{P}^2\text{P}_3^{\text{Cy}})\text{H}(\text{N}_2)][\text{BF}_4]$  (**18**).<sup>5b</sup>

The  $^{31}\text{P}\{^1\text{H}\}$  NMR spectrum of **18** showed two doublets of triplets at 140.7 ( $^2J_{\text{PP}} = 11$  Hz,  $^2J_{\text{PP}} = 11$  Hz) and 51.4 ppm ( $^2J_{\text{PP}} = 11$  Hz,  $^2J_{\text{PP}} = 11$  Hz), corresponding to the  $\text{P}_{\text{C}}$  and  $\text{P}_{\text{T}}$  atoms, respectively. The two equivalent terminal phosphorus atoms  $\text{P}_{\text{E}}$  appear as a single resonance at 63.8 ppm ( $^2J_{\text{PP}} = 11$  Hz,  $^2J_{\text{PP}} = 11$  Hz) which is observed as a doublet of doublets and has twice the intensity of the signals for  $\text{P}_{\text{C}}$  and  $\text{P}_{\text{T}}$ . In the corresponding  $^1\text{H}$  NMR spectrum, the hydride ligand appears as a doublet of triplets of doublets at -11.26 ppm ( $^2J_{\text{HPT}} = 72$  Hz,  $^2J_{\text{HPE}} = 26$  Hz,  $^2J_{\text{HPC}} = 23$  Hz).

For the synthesis of  $[\text{Ru}(\text{H}^{\text{C}}\text{P}_3^{\text{Cy}})\text{H}(\text{CO})]$  (**19**),<sup>8</sup> reaction of  $[\text{Ru}(\text{PPh}_3)_3(\text{CO})(\text{H})_2]$  with  $\text{H}^{\text{C}}\text{P}_3^{\text{Cy}}$  (**F**) in refluxing toluene gave, after workup, the desired complex as a white solid (Scheme 3.6). Crystals of **19** suitable for structural analysis were grown by slow evaporation of a toluene solution under nitrogen (Figure 3.5).



**Scheme 3.6.** Synthesis of  $[\text{Ru}(\text{H}^{\text{C}}\text{P}_3^{\text{Cy}})\text{H}(\text{CO})]$  (**19**).<sup>8</sup>

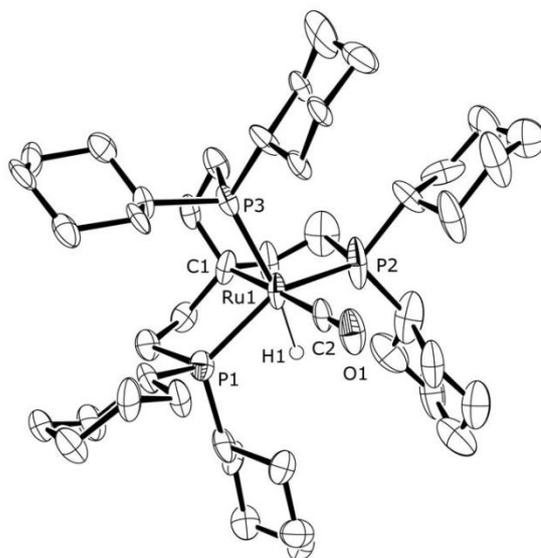
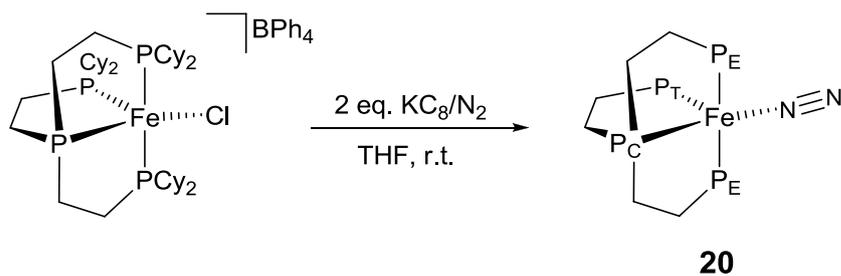


**Figure 3.5.** X-ray crystal structure of  $[\text{Ru}(\text{H}^{\text{C}^2\text{P}_3^{\text{Cy}}})\text{H}(\text{CO})]$  (**19**).<sup>8</sup>

The  $^{31}\text{P}\{^1\text{H}\}$  NMR spectrum of **19** showed two phosphorus signals, the first as a phosphorus doublet at 69.4 ppm corresponding to the two equivalent terminal  $\text{P}_\text{E}$  atoms and the second as a triplet at 56.1 ppm corresponding to  $\text{P}_\text{T}$ , with a mutual  $^2J_{\text{PP}}$  coupling constant of 17 Hz. In the corresponding  $^1\text{H}$  NMR spectrum, the metal-bound hydride appeared as a doublet of triplets at -10.31 ppm ( $^2J_{\text{PPT}} = 77$  Hz,  $^2J_{\text{PPE}} = 28$  Hz).

The  $^{13}\text{C}\{^1\text{H}, ^{31}\text{P}\}$  NMR spectrum displayed resonances associated with the carbonyl carbon atom and the  $\text{CP}_3$  ligand central carbon at 203.4 ppm and 66.3 ppm, respectively.

Complex  $[\text{Fe}(\text{P}^2\text{P}_3^{\text{Cy}})(\text{N}_2)]$  (**20**) was synthesized<sup>5b</sup> by treatment of a THF solution of  $[\text{Fe}(\text{P}^2\text{P}_3^{\text{Cy}})\text{Cl}][\text{BPh}_4]$  with two equivalents of potassium graphite under an atmosphere of nitrogen (Scheme 3.7). After workup, the product was obtained as an orange/red solid. Crystals of  $[\text{Fe}(\text{P}^2\text{P}_3^{\text{Cy}})(\text{N}_2)]$  (**20**) suitable for analysis by X-ray diffraction were grown by evaporation of a benzene solution of **20** (Figure 3.6).



**Scheme 3.7.** Synthesis of  $[\text{Fe}(\text{P}^2\text{P}_3^{\text{Cy}})(\text{N}_2)]$  (**20**).<sup>5b</sup>

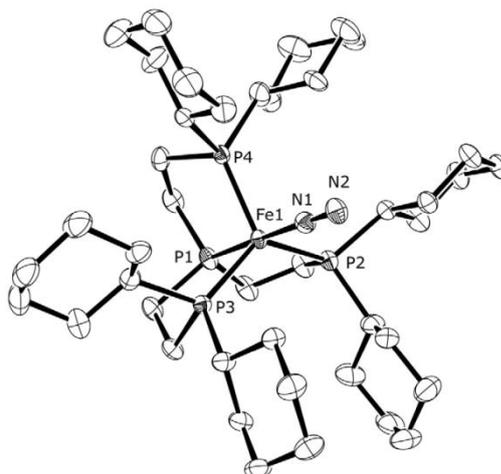
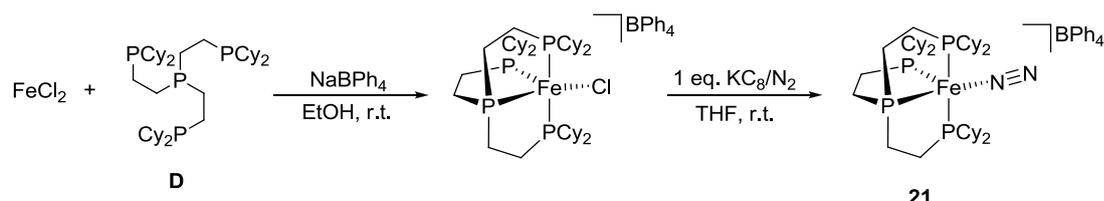


**Figure 3.6.** X-ray crystal structure of  $\text{Fe}(\text{P}^2\text{P}_3^{\text{Cy}})(\text{N}_2)$  (**20**).<sup>5b</sup>

In the  $^{31}\text{P}\{^1\text{H}\}$  NMR spectrum of **20** two phosphorus signals appeared, the first as a quartet at 175.3 ppm ( $\text{P}_\text{C}$ ) and the second as a doublet at 84.2 ppm ( $\text{P}_\text{E}$ ), with a mutual  $^2J_{\text{PP}}$  coupling constant of 36 Hz.

For the synthesis of  $[\text{Fe}(\text{P}^2\text{P}_3^{\text{Cy}})(\text{N}_2)][\text{BPh}_4]$  (**21**), one equivalent of potassium graphite was added to a THF solution of  $[\text{Fe}(\text{P}^2\text{P}_3^{\text{Cy}})\text{Cl}][\text{BPh}_4]$  under an atmosphere of nitrogen to afford  $[\text{Fe}(\text{P}^2\text{P}_3^{\text{Cy}})(\text{N}_2)][\text{BPh}_4]$  (**21**) (Scheme 3.8). After workup, **21** was obtained as a deep red solid. Crystals of  $[\text{Fe}(\text{P}^2\text{P}_3^{\text{Cy}})(\text{N}_2)][\text{BPh}_4]$  (**21**) suitable for structural analysis were grown by vapour diffusion of pentane into a THF solution of **21** (Figure 3.7).



**Scheme 3.8.** Synthesis of  $[\text{Fe}(\text{P}^2\text{P}_3^{\text{Cy}})(\text{N}_2)][\text{BPh}_4]$  (**21**).<sup>5b</sup>

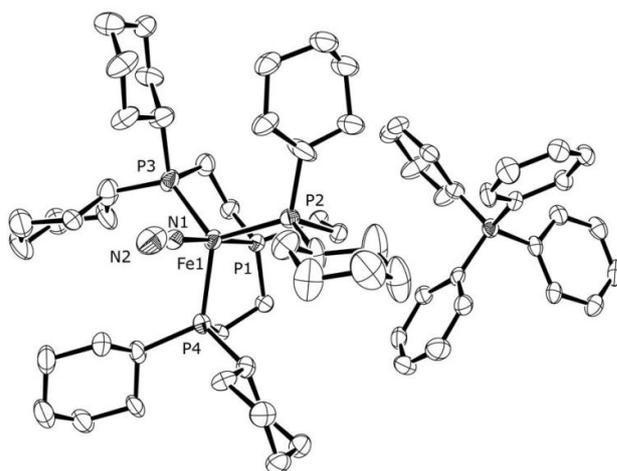
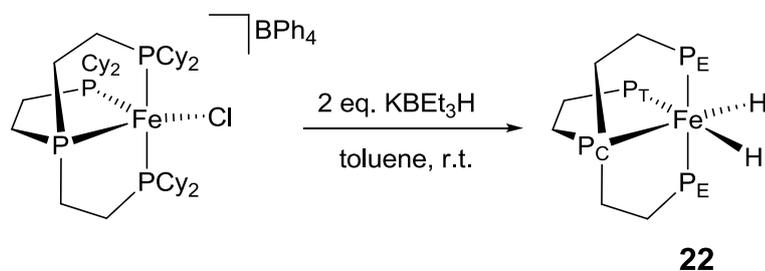


**Figure 3.7.** X-ray crystal structure of  $[\text{Fe}(\text{P}^2\text{P}_3^{\text{Cy}})(\text{N}_2)][\text{BPh}_4]$  (**21**).<sup>5b</sup>

The infrared spectrum of **21** shows a sharp absorbance at  $2059\text{ cm}^{-1}$  assigned to the nitrogen-nitrogen triple bond stretching mode  $\nu(\text{N}\equiv\text{N})$ .

For the synthesis of  $[\text{Fe}(\text{P}^2\text{P}_3^{\text{Cy}})(\text{H})_2]$  (**22**),<sup>5b</sup> potassium triethylborohydride ( $\text{KBEt}_3\text{H}$ ) was reacted with  $[\text{Fe}(\text{P}^2\text{P}_3^{\text{Cy}})\text{Cl}][\text{BPh}_4]$  in toluene to give  $[\text{Fe}(\text{P}^2\text{P}_3^{\text{Cy}})(\text{H})_2]$  (**22**) (Scheme 3.9). Crystals suitable for structural analysis were grown by evaporation of a toluene solution of complex **22** (Figure 3.8).



**Scheme 3.9.** Synthesis of  $[\text{Fe}(\text{P}^2\text{P}_3^{\text{Cy}})(\text{H})_2]$  (**22**).<sup>5b</sup>

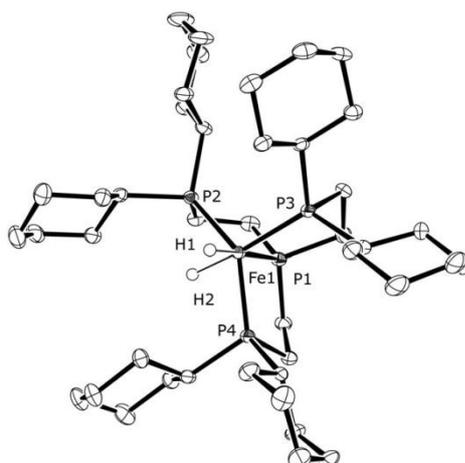
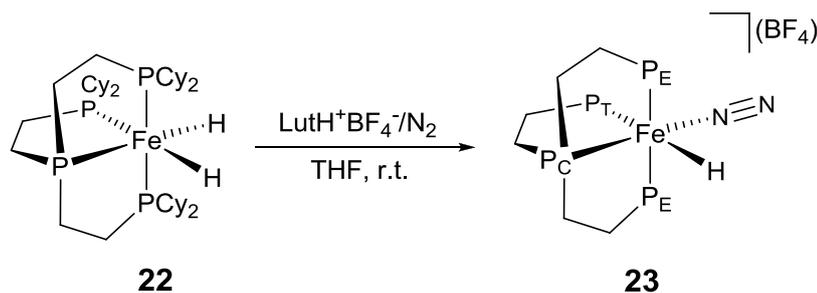


**Figure 3.8.** X-ray crystal structure of  $[\text{Fe}(\text{P}^2\text{P}_3^{\text{Cy}})(\text{H})_2]$  (**22**).<sup>5b</sup>

The  $^{31}\text{P}\{^1\text{H}\}$  NMR spectrum of **22** showed two sharp resonances, a quartet at 174.4 ppm ( $^2J_{\text{PP}} = 18$  Hz) assigned to the central  $\text{P}_{\text{C}}$  and a doublet at 102.3 ppm ( $^2J_{\text{PP}} = 18$  Hz) assigned to the terminal  $\text{P}_{\text{E}}/\text{P}_{\text{T}}$  in a 1:3 ratio. The spectrum is consistent with fast exchange occurring between the terminal phosphorus atoms,  $\text{P}_{\text{E}}$  and  $\text{P}_{\text{T}}$ . At low temperature (190 K), two distinct broad resonances appeared at 96.8 and 113.7 ppm for the two  $\text{P}_{\text{E}}$  and one  $\text{P}_{\text{T}}$  atoms, respectively.

The corresponding  $^1\text{H}$  NMR spectrum of **22** showed also a single sharp resonance at  $-12.84$  ppm, corresponding to a fast exchange with the two hydride signals at 285 K. At 210 K two broad resonances appeared at  $-7.95$  and  $-17.71$  ppm, with these resonances becoming significantly sharper at 190 K.

For the synthesis of  $[\text{Fe}(\text{P}^2\text{P}_3^{\text{Cy}})(\text{H})(\text{N}_2)][\text{BF}_4]$  (**23**),<sup>5b</sup> treatment of  $[\text{Fe}(\text{P}^2\text{P}_3^{\text{Cy}})(\text{N}_2)][\text{BPh}_4]$  (**21**) with one equivalent of 2,6-lutidinium tetrafluoroborate, slowly gave  $[\text{Fe}(\text{P}^2\text{P}_3^{\text{Cy}})(\text{H})(\text{N}_2)][\text{BF}_4]$  (**23**) by acid-assisted disproportionation (Scheme 3.10). Crystals of  $[\text{Fe}(\text{P}^2\text{P}_3^{\text{Cy}})(\text{H})(\text{N}_2)][\text{BF}_4]$  (**23**) suitable for structural analysis were grown by vapour diffusion of pentane into THF solutions of **23** (Figure 3.9).



**Scheme 3.10.** Synthesis of  $[\text{Fe}(\text{P}^2\text{P}_3^{\text{Cy}})(\text{H})(\text{N}_2)][\text{BF}_4]$  (**23**).<sup>5b</sup>

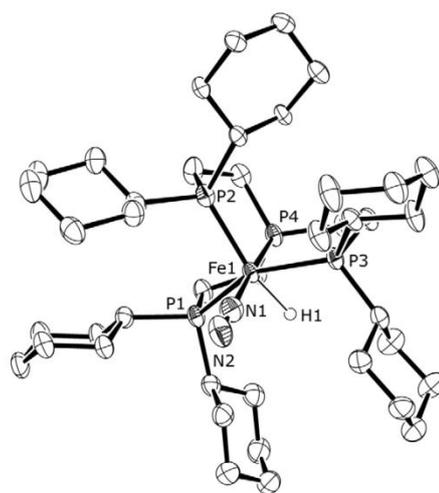


**Figure 3.9.** X-ray crystal structure of  $[\text{Fe}(\text{P}^2\text{P}_3^{\text{Cy}})(\text{H})(\text{N}_2)][\text{BF}_4]$  (**23**).<sup>5b</sup>

The  $^{31}\text{P}\{^1\text{H}\}$  NMR spectrum of **23** showed two doublets of triplets at 160.7 ( $^2J_{\text{PCPT}} = 28$  Hz,  $^2J_{\text{PCPE}} = 24$  Hz) and 70.3 ppm ( $^2J_{\text{PTPC}} = 28$  Hz,  $^2J_{\text{PTPE}} = 11$  Hz), corresponding to the  $\text{P}_\text{C}$  and  $\text{P}_\text{T}$  atoms, respectively. The two equivalent terminal  $\text{P}_\text{E}$  atoms appear as a resonance at 79.8 ppm ( $^2J_{\text{PEPC}} = 24$  Hz,  $^2J_{\text{PEPT}} = 11$  Hz) which is observed as a doublet of doublets and has twice the intensity of the signals for  $\text{P}_\text{C}$  and  $\text{P}_\text{T}$ . In the corresponding  $^1\text{H}$  NMR spectrum, the hydride appears as a doublet of triplets of doublets at -14.62 ppm ( $^2J_{\text{HPT}} = 69$  Hz,  $^2J_{\text{HPE}} = 53$  Hz,  $^2J_{\text{HPC}} = 25$  Hz).

### 3.4 Catalytic formic acid and formic acid/amine dehydrogenation.

The iron and ruthenium complexes **15-23** were tested as catalysts for the  $\text{HCOOH}$  dehydrogenation to  $\text{CO}_2$  and  $\text{H}_2$ . In addition, we have also tested Fe-based catalytic

systems prepared *in situ* from the iron(II) source  $\text{Fe}(\text{BF}_4)_2 \cdot 6\text{H}_2\text{O}$  and free ligands **C-F**.

The catalytic tests were performed in glass reactors under isobaric conditions (1 atm) measuring the development of gas during the reaction with manual gas-burettes. The gas mixtures were analyzed off-line by GC and FT-IR spectroscopy, showing absence of CO for all tests (detection limit 3 ppm). The HCOOH dehydrogenation to  $\text{H}_2/\text{CO}_2$  gas mixtures was tested at 60 °C using either formic acid (2 mL) in the presence of the inert solvent propylene carbonate (PC) (5 mL) or formic acid/amine adducts. The chosen amine was dimethyloctylamine (DMOA), with FA/Amine = 11:10 (total volume 5 mL).

Disappointingly, none of the well defined iron complexes **20-23**, nor the complexes formed *in situ* from  $\text{Fe}(\text{BF}_4)_2 \cdot 6\text{H}_2\text{O}$  and ligands **C-F** (1:2 ratio), showed any significant catalytic activity neither in the dehydrogenation of formic acid in propylene carbonate at 60 °C, nor in the dehydrogenation of formic acid/amine adducts. Preliminary NMR experiments showed that both complex  $[\text{Fe}(\text{P}^2\text{P}_3^{\text{Cy}})(\text{H})(\text{N}_2)][\text{BF}_4]$  (**23**) and free ligand  $\text{P}^2\text{P}_3^{\text{Cy}}$  are rapidly decomposed and protonated by addition of an excess of HCOOH.

Ruthenium complexes **15-19** were at first tested for the base-free catalytic dehydrogenation of HCOOH in the inert solvent propylene carbonate (PC) at 60 °C at a catalyst to substrate ratio of 1:10000 (5.3  $\mu\text{mol}$  catalyst). Among the tested metal complexes, only  $[\text{Ru}(\text{P}^3\text{P}_3^{\text{iPr}})(\text{H})_2]$  (**16**) ( $\text{TON}_{2\text{h}} = 46$ ,  $\text{TON}_{3\text{h}} = 46$ ),  $[\text{Ru}(\text{P}^2\text{P}_3^{\text{Cy}})(\text{H})(\text{N}_2)][\text{BF}_4]$  (**18**) ( $\text{TON}_{2\text{h}} = 257$ ,  $\text{TON}_{3\text{h}} = 357$ ) and  $[\text{Ru}(\text{H}^{\text{C}2}\text{P}_3^{\text{Cy}})(\text{H})(\text{CO})]$  (**19**) ( $\text{TON}_{2\text{h}} = 12$ ,  $\text{TON}_{3\text{h}} = 50$ ) exhibited a modest catalytic activity giving a 1:1  $\text{H}_2/\text{CO}_2$  mixture ( $\text{CO} < 3$  ppm) (Table 3.1). The activity of **16** dropped after 2 hours (entry 2), whereas that of **18** (entry 4) decreased only slightly after six hours ( $\text{TON}_{6\text{h}} = 583$ ) giving a  $\text{TOF}_{2\text{h}} = 129 \text{ h}^{-1}$  and  $\text{TOF}_{6\text{h}} = 95 \text{ h}^{-1}$ .

**Table 3.1.** FA dehydrogenation catalyzed by ruthenium complexes **15** – **18** in the absence of an added base at 60 °C.

Entry <sup>[a]</sup>	catalyst	Cat/sub	V <sub>2h</sub> [mL]	TON <sub>2h</sub>	V <sub>3h</sub> [mL]	TON <sub>3h</sub>	V <sub>6h</sub> [mL]	TON <sub>6h</sub>
1	<b>15</b>	1:10000	0	0	0	0	0	0
2	<b>16</b>	1:10000	15	46	15	46	15	46
3	<b>17</b>	1:10000	0	0	0	0	0	0
4	<b>18</b>	1:10000	70	257	96	357	151	583
5	<b>19</b>	1:10000	6	12	16	50	22	85

[a] Reaction conditions: catalyst, 5.3 μmol; PC, 5 mL; HCOOH, 2 mL; catalyst:FA = 1:10000, 60 °C. Gas volume measured via manual gas burette and analyzed via GC.

In the presence of N,N-dimethyloctylamine (HCOOH/OctNMe<sub>2</sub> 11:10), the catalytic activity was observed to increase for all complexes (Table 3.2). The ruthenium (II) complex **18** bearing the tetradentate ligand P<sup>2</sup>P<sub>3</sub><sup>Cy</sup> was found to be the most active catalyst for the dehydrogenation of formic acid both in the absence (Table 3.2; entry 4) and in the presence of DMOA as amine (DMOA = OctNMe<sub>2</sub>) (Table 3.2; entry 7). Full conversion of HCOOH to H<sub>2</sub>/CO<sub>2</sub> (1:1) was achieved within approximately 3 hours. Addition of solvent (PC) did not influence the catalytic performance (entry 8). Only catalyst **16** was slightly more active than **18** in the presence of HCOOH/OctNMe<sub>2</sub> (11:10).

At the same catalyst/substrate ratio (1:4122), also the ruthenium chloride complex **17** bearing the tridentate ligand PhP<sup>2</sup>P<sub>2</sub><sup>tBu</sup> gave complete formic acid dehydrogenation within 5 hours (TOF<sub>5h</sub> = 797 h<sup>-1</sup>, entry 3), whereas complex **15** dehydrogenated FA at a slower rate (TOF<sub>8h</sub> = 190 h<sup>-1</sup>, entry 5). Oddly, increasing the catalyst/substrate ratio (1:1000) had a detrimental effect in the case of **17** (entry 4). In contrast, **15** showed increased activity at cat/sub = 1:1000 ratio (TOF<sub>3h</sub> = 302 h<sup>-1</sup>, entry 6) compared to standard conditions (TOF<sub>3h</sub> = 218 h<sup>-1</sup>, entry 5). As in the absence of amine, the ruthenium carbonyl complex [Ru(<sup>H</sup>C<sup>2</sup>P<sub>3</sub><sup>Cy</sup>)H(CO)] (**19**) showed very little activity also in the presence of DMOA (entry 9). The various reaction profiles obtained at catalyst : substrate = 1:4200 are shown in Figure 3.10.

**Table 3.2.** Formic Acid/amine dehydrogenation in the presence of catalysts **15-19**.

Entry <sup>[a]</sup>	Cat.	Cat/sub	V <sub>2h</sub> [mL]	TON <sub>2h</sub>	V <sub>3h</sub> [mL]	TON <sub>3h</sub>	V <sub>max</sub> [mL] (time, h)	TON <sub>max</sub>
1	<b>15</b>	1:4200	125	440	177	655	391 (7.8)	1378
2	<b>15</b>	1:1000	675	620	920	905	1140 (5.5)	986
3	<b>16</b>	1:4200	595	1956	1060	3485	1145 (3.3)	3765
4	<b>16</b>	1:1000	1100	952	1150	1000	1150 (2.6)	1000
5	<b>17</b>	1:4200	381	1436	660	2496	1115 (5.3)	3666
6	<b>17</b>	1:1000	888	867	1113	1087	1163 (5.6)	1000
7	<b>18</b>	1:4200	972	3196	1072	3525	1122 (3.4)	3689
8 <sup>b</sup>	<b>18</b>	1:4200	925	3042	1110	3650	1110 (2.7)	3650
9	<b>19</b>	1:4200	3	10	5	17	10 (6)	33

Reaction Conditions: HCO<sub>2</sub>H/OctNMe<sub>2</sub> (11:10), 5 mL; FA:catalyst = 1:4200 or 1:1000; 60 °C. Gas measured via manual gas-burette and analyzed via GC.<sup>b</sup> In presence of 2 mL of PC.

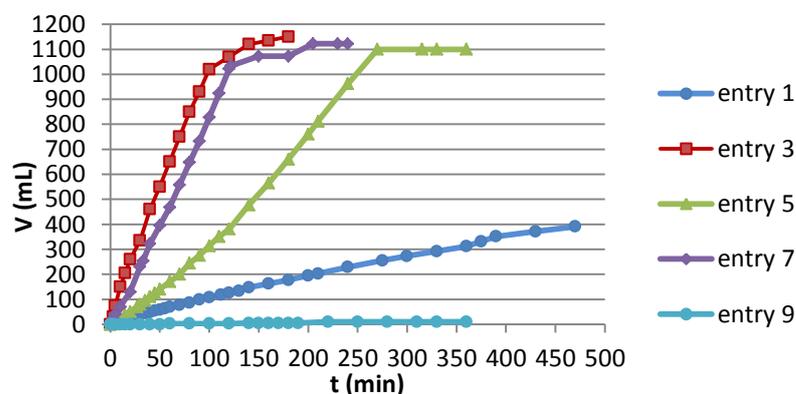


**Figure 3.10.** Reaction profile of catalytic runs using complexes **15-19**. Reaction conditions: catalyst 5.3  $\mu$ mol; HCO<sub>2</sub>H/OctNMe<sub>2</sub> (11:10), 5 mL; catalyst:substrate = 1:3800; 60 °C. Gas measured via manual gas-burette and analyzed via GC. For legenda, see Table 3.2.

### 3.5 Catalytic bicarbonate hydrogenation

Ruthenium complexes **15-19** were tested for the hydrogenation of sodium bicarbonate to sodium formate in MeOH. The initial catalyst screening was performed at 80 °C under 60 bar H<sub>2</sub> pressure, with a catalyst:substrate ratio of 1:1000, at a 0.5 mM catalyst concentration. The results are summarized in Table 3.3. The ruthenium dihydride complex **16** showed no catalytic activity (entry 1), while in the presence of the hydrido carbonyl complex [Ru(<sup>H</sup>C<sup>2</sup>P<sub>3</sub><sup>Cy</sup>)H(CO)] (**19**), only minor amounts of formate were obtained (entry 2). The dark colour of the catalytic mixture observed after the catalytic test using **16** under these conditions suggested complex decomposition.

Catalysts **17** and **18** gave the best performances, affording sodium formate in nearly quantitative yields with TONs in the range 801–895 (entries 6 and 9), whereas a lower catalytic activity was observed for **15** (TON = 485, entry 3).

Catalysts **15**, **17** and **18** were further tested at intermediate (2000 - 3000) and higher (10000) substrate/catalyst ratios, by either reducing the catalyst loading or increasing the substrate loading.

When the substrate loading was trebled (30 mmol NaHCO<sub>3</sub>; 0.01 mmol catalyst; 20 mL MeOH), a significant increase in TON was observed for catalysts **15** (TON<sub>1000</sub> = 485 vs TON<sub>3000</sub> = 832, entries 3 and 4) and **17** (TON<sub>1000</sub> = 878 vs TON<sub>3000</sub> = 2222, entries 6 and 7). In the presence of 0.001 mmol catalyst (vs. 10 mmol NaHCO<sub>3</sub>; substrate / catalyst = 10000; [catalyst] = 0.05 mM), **15** gave TONs similar to that obtained at substrate / catalyst = 1000 (entry 5), while **17** gave TON<sub>10000</sub> = 2511 (entry 8), which is a small improvement respect to TON<sub>3000</sub> = 2222, albeit formate was obtained in a significantly lower yield (Y<sub>10000</sub> = 27 vs Y<sub>3000</sub> = 74%). The highest TON<sub>10000</sub> = 4588 was observed in the case of **18**.

**Table 3.3.** Hydrogenation of sodium bicarbonate catalyzed by ruthenium complexes.<sup>a</sup>

Entry	catalyst	mmol catalyst	mmol NaHCO <sub>3</sub>	Cat/sub	T (°C)	pH <sub>2</sub> (bar)	TON <sup>b,d</sup>	Yield(%) <sup>c,d</sup>
1	<b>16</b>	0.01	10	1000	70	60	0	0
2	<b>19</b>	0.01	10	1000	80	60	22	2
3	<b>15</b>	0.01	10	1000	70	60	485	49
4	<b>15</b>	0.01	30	3000	80	60	832	28
5	<b>15</b>	0.001	10	10000	80	60	406	14
6	<b>17</b>	0.01	10	1000	80	60	878	88
7	<b>17</b>	0.01	30	3000	80	60	2222	74
8	<b>17</b>	0.001	10	10000	80	60	2511	25
9	<b>18</b>	0.01	10	1000	80	60	895	89
10	<b>18</b>	0.005	10	2000	80	60	1583	79
11	<b>18</b>	0.01	30	3000	80	60	nd	nd
12	<b>18</b>	0.001	10	10000	80	60	4588	46
13	<b>18</b>	0.001	10	10000	80	30	2384	24

<sup>a</sup> General reaction conditions: catalyst; NaHCO<sub>3</sub>; MeOH (20 mL); H<sub>2</sub> pressure, 24 h. <sup>b</sup> TON = mmoles of sodium formate per mmoles of catalyst. <sup>c</sup> Yields calculated from the integration of <sup>1</sup>H NMR signals due to HCO<sub>2</sub>Na, using THF as internal standard. <sup>d</sup> Yields and TONs were calculated as averages from the analysis of 2-4 samples, the largest deviations are reported in brackets; selected experiments were repeated to ensure reproducibility

### 3.6 Conclusions

In this Chapter, it was shown that a series of Ru complexes bearing different polydentate phosphine ligands are active catalysts for the FA/DMOA dehydrogenation and sodium bicarbonate hydrogenation. In particular, complexes **16-18** gave interesting TON values for FA dehydrogenation using a substrate to catalyst ratio of ca. 4000 at 60 °C, reaching a maximum TON = 3765 for **16**, whereas complex **18** showed the best activity (TON = 4588) for sodium bicarbonate hydrogenation using 0.01 mol% of catalyst at 80 °C under a pressure of 30 bar of H<sub>2</sub>. Mechanistic studies are under way to correlate the catalytic results to the different denticities, bulkiness and basicities of the various stabilizing ligands. In the case of Fe complexes, the lack of activity in formic acid dehydrogenation can be likely due to the poor stability of such pre-catalysts under reaction conditions, leading to deactivation.

## 3.7 Experimental section

### 3.7.1 General methods and materials

Complexes **15-23** were prepared according to literature procedures.<sup>5b,6,7,8</sup> Formic acid and N,N-dimethyloctylamine were distilled under reduced pressure prior to use and stored under nitrogen. The formic acid to amine ratio was determined by <sup>1</sup>H NMR spectroscopy on a Bruker Avance 400 spectrometer.

### 3.7.2 Formic acid dehydrogenation procedures

All catalytic experiments were carried out under an inert argon or nitrogen atmosphere in a flask heated either by oil bath or by external heating liquid circulation. The flask was connected to a reflux condenser, which was connected either to a setup of two manual burettes to measure the amounts of gas generated. The mixture of gas produced during the catalytic runs was either analyzed by FTIR on a Perkin-Elmer Spectrum BXII spectrophotometer with a gas cell (KBr windows, path length 10 cm) or by GC using a gas chromatograph HP 6890N (permanent gases: Carboxen 1000, TCD, external calibration; amines: HP Plot Q, 30 m, FID) and a hydrogen sensor (Hach Ultra Analytics GmbH).

Typical procedure for the HCOOH dehydrogenation tests: a solution of HCOOH/amine (5 mL) was pre-warmed to 60 °C (HCOOH/OctNMe<sub>2</sub> 11:10) in a three-necked round bottomed flask with a thermostated oil bath. The flask was purged with argon or nitrogen before starting the reaction by addition of the solid catalyst. In the case of experiments run using HCOOH, a solution of catalyst (typically 5.3 mmol) in propylene carbonate (5 mL) is placed under an argon atmosphere in a magnetically stirred glass reaction vessel thermostated by external liquid circulation and connected to a reflux condenser and gas-burette. After heating to 60 °C, HCOOH (2.0 mL) is added and the experiment started.

### 3.7.3 Sodium bicarbonate hydrogenation procedures

In a typical experiment, a 40 mL magnetically stirred stainless steel autoclave built at CNR-ICCOM is charged under inert atmosphere (glovebox) with NaHCO<sub>3</sub> (typically 840 mg, 10 mmol) and the catalyst (0.01–0.001 mmol as solid or stock solution in

THF). The autoclave is then closed and thoroughly purged through several vacuum/argon cycles. MeOH (20 mL) is then added to the autoclave by suction. Finally the autoclave is pressurized with H<sub>2</sub> gas at the desired pressure. The autoclave is then placed into an oil bath pre-heated to the desired temperature and left stirring for the set reaction time. After the run, the autoclave is cooled in an ice/water bath, de-pressurized, and the catalytic mixture is transferred to a flask and concentrated under vacuum at room temperature. The formate content is determined by analyzing aliquots (ca. 30 mg) of the solid mixtures dissolved in D<sub>2</sub>O (0.5 mL) by <sup>1</sup>H NMR, using dry THF (20 μL) as internal standard with a relaxation delay of 20 seconds.

### 3.8 References

- 
- <sup>1</sup> Mayer, H. A.; Kaska, W. C. *Chem. Rev.* **1994**, *94*, 1239.
  - <sup>2</sup> (a) Antberg, M.; Frosin, K. M.; Dahlenburg, L. *J. Organomet. Chem.* **1988**, *338*, 319; (b) Antberg, M.; Prengel, C.; Dahlenburg, L. *Inorg. Chem.* **1984**, *23*, 4170; (c) Bampos, N.; Field, L. D. *Inorg. Chem.* **1990**, *29*, 587; (d) Bampos, N.; Field, L. D.; Messerle, B. A. *Organometallics* **1993**, *12*, 2529; (e) Field, L. D.; Bampos, N.; Messerle, B. A. *Magn. Reson. Chem.* **1991**, *29*, 36; (f) Bemi, L.; Clark, H. C.; Davies, J. A.; Drexler, D.; Fyfe, C. A.; Wasylishen, R. *J. Organomet. Chem.* **1982**, *224*, C5; (g) Bhadbhade, M. M.; Field, L. D.; Gilbert-Wilson, R.; Guest, R. W.; Jensen, P. *Inorg. Chem.* **2011**, *50*, 6220; (h) Field, L. D.; Guest, R. W.; Vuong, K. Q.; Dalgarno, S. J.; Jensen, P. *Inorg. Chem.* **2009**, *48*, 2246; (i) Osman, R.; Pattison, D. I.; Perutz, R. N.; Bianchini, C.; Casares, J. A.; Peruzzini, M. *J. Am. Chem. Soc.* **1997**, *119*, 8459; (j) Bianchini, C.; Perez, P. J.; Peruzzini, M.; Zanobini, F.; Vacca, A. *Inorg. Chem.* **1991**, *30*, 279.
  - <sup>3</sup> Boddien, A.; Mellmann, D.; Gaertner, F.; Jackstell, R.; Junge, H.; Dyson, P. J.; Laurenczy, G.; Ludwig, R.; Beller, M. *Science* **2011**, *333*, 1733.
  - <sup>4</sup> Boddien, A.; Gaertner, F.; Jackstell, R.; Junge, H.; Spannenberg, A.; Baumann, W.; Ludwig, R.; Beller, M. *Angew. Chem., Int. Ed.* **2010**, *49*, 8993.
  - <sup>5</sup> (a) Jia, G.; Drouin, S. D.; Jessop, P. G.; Lough, A. J.; Morris, R. H. *Organometallics* **1993**, *12*, 906; (b) Gilbert-Wilson, R.; Field, L. D.; Colbran, S. B.; Bhadbhade, M. M. *Inorg. Chem.* **2013**, *52*, 3043.
  - <sup>6</sup> Bhadbhade, M. M.; Field, L. D.; Gilbert-Wilson, R.; Guest, R. W.; Jensen, P. *Inorg. Chem.* **2011**, *50*, 6220.
  - <sup>7</sup> Gilbert-Wilson, R.; Field, L. D.; Bhadbhade, M. M. *Inorg. Chem.* **2012**, *51*, 3239.
  - <sup>8</sup> Gilbert-Wilson, R. Ph.D Thesis, University of New South Wales, **2011**.
  - <sup>9</sup> Kuzu, I.; Krummenacher, I.; Meyer, J.; Armbruster, F.; Breher, F. *Dalton Trans.* **2008**, 5836-5865.
  - <sup>10</sup> a) Ciclosi, M.; Lloret, J.; Estevan, F.; Lahuerta, P.; Sanau, M.; Perez-Prieto, J., *Angew. Chem. Int. Ed.* **2006**, *45*, 6741; b) Allen, O. R.; Field, L. D.; Magill, A. M.; Vuong, K. Q.; Bhadbhade, M. M.; Dalgarno, S. J. *Organometallics* **2011**, *30*, 6433.



# Chapter 4

## **Iron(II) Complexes of the Linear *rac*-tetraphos-1 Ligand as Homogeneous Catalysts for Sodium Bicarbonate Hydrogenation and Formic Acid Dehydrogenation**

### **4.1 Overview**

In this chapter, the synthesis of novel Fe(II) complexes bearing *rac*-P4, their reactivity toward H<sub>2</sub> and CO<sub>2</sub>, and their application as efficient catalysts for formic acid dehydrogenation and sodium bicarbonate hydrogenation to sodium formate are described. The catalytic data are complemented by mechanistic details obtained by model stoichiometric reactions and *in operando* high pressure HPNMR experiments. The Chapter ends with the experimental section reporting the characterization of all the new Fe compounds including X-ray crystal structure determinations and details of the catalytic tests.

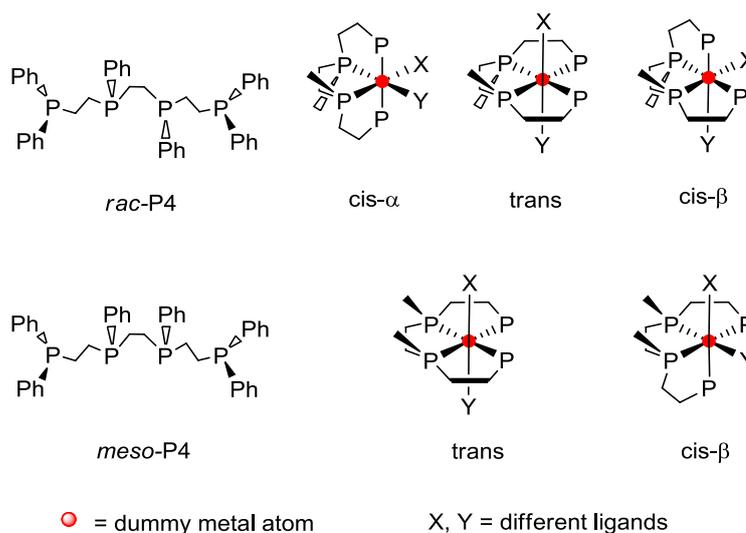
## 4.2 Introduction

The most active additive-free Fe-based catalyst system for formic acid (FA) dehydrogenation under mild temperature conditions (40 °C) reported to date was obtained by combining the iron(II) salt  $\text{Fe}(\text{BF}_4)_2 \cdot 6\text{H}_2\text{O}$  with the tetraphosphine ligand  $\text{P}(\text{CH}_2\text{CH}_2\text{PPh}_2)_3$  ( $\text{PP}_3$ ).<sup>1,2</sup> Although the nature of the initial complex formed in this reaction has not been fully ascertained, mechanistic studies indicated that under catalytic conditions (FA in propylene carbonate, PC) complexes  $[\text{Fe}(\text{PP}_3)\text{H}]^+$  and  $[\text{Fe}(\text{PP}_3)\text{H}(\eta^2\text{-H}_2)]^+$  are formed.<sup>1</sup> This catalytic system was also successfully applied to bicarbonate hydrogenation to formates and carbon dioxide valorization to alkyl formates and formamides.<sup>3</sup> In continuation of this work, efficient iron-catalyzed hydrogenation of carbon dioxide and bicarbonates was achieved using  $\text{Fe}(\text{BF}_4)_2 \cdot 6\text{H}_2\text{O}$  and  $\text{P}^{\text{Ph}}\text{P}_3$  [ $\text{P}^{\text{Ph}}\text{P}_3 = \text{tris}(2\text{-(diphenylphosphino)phenylphosphine}]$ . In this case, metal complexation afforded the well-defined complex  $[\text{Fe}(\text{P}^{\text{Ph}}\text{P}_3)\text{F}]^+$  via  $\text{F-BF}_3$  activation. Mechanistic studies established that this complex reacts with  $\text{H}_2$  to give  $[\text{Fe}(\text{P}^{\text{Ph}}\text{P}_3)\text{H}(\eta^2\text{-H}_2)]^+$ . High pressure HPNMR  $\text{CO}_2$  hydrogenation experiments in the presence of  $\text{NEt}_3$  suggested the formation of the dihydride complex  $[\text{Fe}(\text{P}^{\text{Ph}}\text{P}_3)(\text{H})_2]$  as active intermediate.<sup>4,5</sup>

In recent years, our group has been interested in FA dehydrogenation and  $\text{CO}_2$  hydrogenation, so far using  $\text{Ru}$ <sup>6</sup> and  $\text{Ir}$ <sup>7</sup> homogeneous catalysts. In an effort to develop novel, non-noble metal-based catalysts for such transformations, we became eager to explore the potential of Fe(II) complexes of other tetradentate phosphines.

The linear tetradentate phosphine ligand 1,1,4,7,10,10-hexaphenyl-1,4,7,10-tetraphosphadecane (tetraphos-1, P4) exists as a mixture of *racemic* (*S,S*; *R,R*) and *meso* (*S,R*) diastereoisomers (hereafter *rac*-P4 and *meso*-P4, respectively), which can be separated by fractional crystallization.<sup>8,9</sup> Despite the existence of these stereoisomers was recognized as early as in 1974,<sup>10</sup> the importance of this isomerism was not fully appreciated until the work of Brown and Canning.<sup>8</sup> The configurations that these diastereoisomers can adopt in an octahedral complex are denoted as *cis- $\alpha$* , *cis- $\beta$*  and *trans* (Scheme 4.1). While the *meso* isomer can adopt only a *trans* or *cis- $\beta$*  configuration, all three configurations are physically possible for the *rac* isomer. Nevertheless, the *rac* isomer is known for its propensity to form *cis- $\alpha$*  complexes.<sup>8,11</sup> Since the original preparation of tetraphos-1 by King and co-workers,<sup>12</sup> there have

been a number of reports on its coordination behavior.<sup>8-13</sup> By a close perusal of available literature, we noticed that the chemistry of the *meso* isomer is far more developed than that of the *rac* isomer. Only complexes  $[\text{Fe}(\text{P4})\text{Br}][\text{BPh}_4]^{13\text{d}}$  and *trans*- $[\text{Fe}(\text{P4})\text{H}(\text{N}_2)]^{13\text{c}}$  were characterized crystallographically and in both the ligand exhibits a *meso* configuration. This was probably due to the fact that the authors used commercial tetraphos-1 which is richer in the *meso* isomer. The syntheses of  $[\text{Fe}(\text{P4})\text{H}]\text{X}$ ,  $[\text{Fe}(\text{P4})(\text{NCS})_2]$ ,  $[\text{Fe}(\text{P4})\text{H}(\text{NCS})]\text{X}$ , and  $[\text{Fe}(\text{P4})\text{H}(\text{CO})]$  ( $\text{X} = \text{Br}, \text{I}$ ) were also described, but no indications on the configuration of the P4 ligand was provided.<sup>13\text{e}}</sup> Morris and co-workers reported on the hydrogen exchange between  $\eta^2\text{-H}_2$  and hydride ligands in *trans*- $[\text{Fe}(\text{meso-P4})\text{H}(\eta^2\text{-H}_2)]\text{BF}_4$ , obtained by protonation of the corresponding dihydride complex *trans*- $[\text{Fe}(\text{meso-P4})(\text{H})_2]$ .<sup>9,11</sup> To the best of our knowledge, the full exploration of the coordination chemistry of *rac*-P4 to Fe(II) and the reactivity of the complexes so obtained has never been reported.

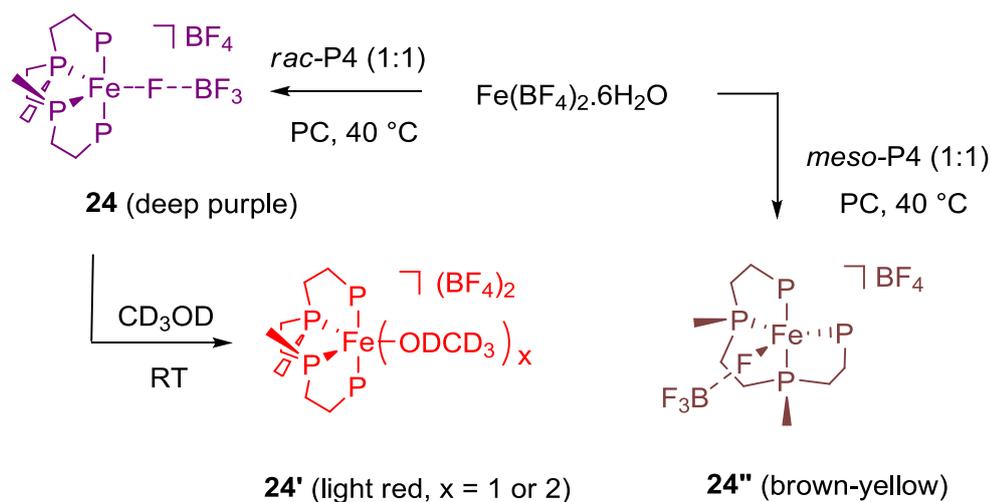


**Scheme 4.1.** The *rac* and *meso* isomers of tetraphos-1 (P4) and allowed configurations for their octahedral complexes.

### 4.3 Synthesis and characterization of new Fe(II) complexes

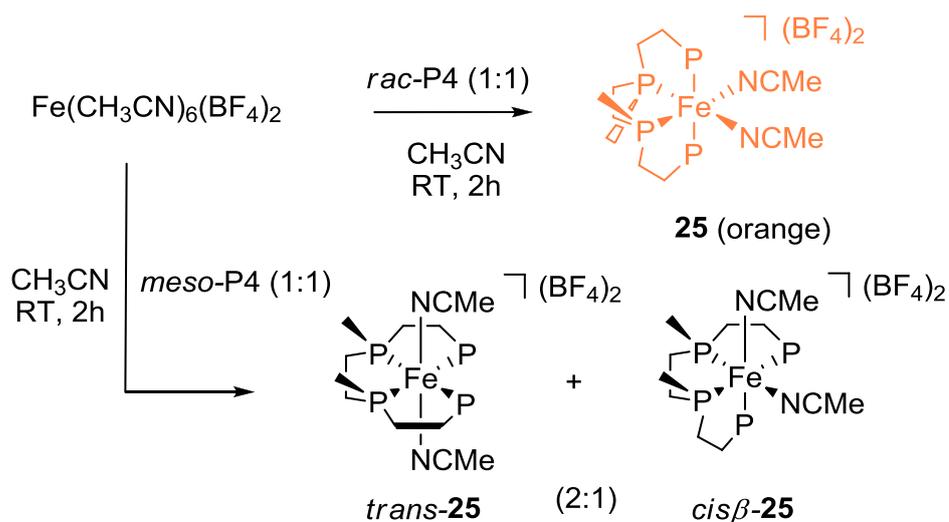
The synthesis of novel Fe(II) complexes bearing *rac*-P4, their reactivity toward  $\text{H}_2$  and  $\text{CO}_2$  are described. At first, *rac*-P4 and *meso*-P4 were obtained in pure isomeric form from the commercial ligand P4, containing a *rac:meso* = 1:3 ratio, by fractional

crystallization as described in the literature.<sup>11</sup> In order to test the coordination abilities of the two isomers with suitable iron(II) sources, the commercially available salt  $\text{Fe}(\text{BF}_4)_2 \cdot 6\text{H}_2\text{O}$  and the easily accessible complex<sup>14</sup>  $[\text{Fe}(\text{CH}_3\text{CN})_6](\text{BF}_4)_2$  were used as metal precursors. The reaction of  $\text{Fe}(\text{BF}_4)_2 \cdot 6\text{H}_2\text{O}$  with *rac*-P4 (1:1) resulted rather sluggish in a variety of common solvents, whereas it proceeded smoothly in propylene carbonate (PC), affording a deep purple solution. The  $^{31}\text{P}\{^1\text{H}\}$  NMR spectrum of such solution ( $\text{C}_6\text{D}_6$  insert) showed two broad signals at 99.9 and 60.9 ppm, indicative of Fe(II) complexation by the ligand.  $^{19}\text{F}\{^1\text{H}\}$  NMR analysis at room temperature showed only a single, sharp peak for the  $\text{BF}_4$  anion, suggesting that complex  $[\text{FeF}(\text{rac-P4})](\text{BF}_4)$ , expected to arise upon F– $\text{BF}_3$  bond activation,<sup>4</sup> had not formed. Due to the known propensity of Fe(P4) complexes to adopt a pentacoordinate geometry, often completed by halide ligands,<sup>13c,d,f</sup> we propose that under these conditions complex  $[\text{Fe}(\text{rac-P4})(\eta^1\text{-FBF}_3)](\text{BF}_4)$  (**24**) has formed, where one of the  $\text{BF}_4$  counterions acts as a weakly coordinating ligand (Scheme 4.2).<sup>15</sup> This complex is likely to be fluxional in solution, and the loosely bound  $\text{BF}_4$  can be easily replaced by a coordinating solvent X (X =  $\text{H}_2\text{O}$ ,  $\text{MeOH}$ ),<sup>16</sup> giving complexes such as *cis- $\alpha$* - $[\text{Fe}(\text{rac-P4})\text{X}_2](\text{BF}_4)_2$ . This was proven by addition of  $\text{CD}_3\text{OD}$  to a solution of **24** in PC, where a new species formed, showing a  $^{31}\text{P}\{^1\text{H}\}$  NMR pattern composed of two triplets at  $\delta_{\text{p}}$  107.6 and 73.8 ( $^2J_{\text{pp}} = 29.9$  Hz), that we attribute to the solvento-species *cis- $\alpha$* - $[\text{Fe}(\text{rac-P4})(\text{CD}_3\text{OD})_x](\text{BF}_4)_2$  (**24'**, x = 1 or 2). To date, all our attempts to obtain crystals of either **24** or **24'** failed. A similar reactivity was observed upon reacting  $\text{Fe}(\text{BF}_4)_2 \cdot 6\text{H}_2\text{O}$  with *meso*-P4, which resulted in the formation of a brown solution containing the putative complex  $[\text{Fe}(\text{meso-P4})(\eta^1\text{-FBF}_3)](\text{BF}_4)$  (**24''**) also characterized by two broad signals in the  $^{31}\text{P}\{^1\text{H}\}$  NMR at 104.8 and 70.8 ppm.



**Scheme 4.2.** Reactivity of  $\text{Fe}(\text{BF}_4)_2 \cdot 6\text{H}_2\text{O}$  with *rac*-P4 and *meso*-P4 to give **24**, **24'** and **24''**.

In contrast, the reaction of *rac*-P4 with  $[\text{Fe}(\text{CH}_3\text{CN})_6](\text{BF}_4)_2$  resulted in the quantitative formation of the well-defined complex *cis*- $\alpha$ - $[\text{Fe}(\text{rac-P4})(\text{CH}_3\text{CN})_2](\text{BF}_4)_2$  (**25**) as the sole product (Scheme 4.3). The  $^{31}\text{P}\{^1\text{H}\}$  NMR spectrum exhibits two triplets at 100.7 and 65.6 ppm in  $\text{CD}_3\text{CN}$ , which reflect an AA'XX' coupling pattern with equivalent *cis*-P,P coupling constants ( $^2J_{\text{PP}} = 31.7$  Hz). These values are in close analogy with those attributed by Habeck *et al.* to *cis*- $\alpha$ - $[\text{Fe}(\text{rac-P}^t\text{P4})(\text{NCS})_2]$  (*rac*- $\text{P}^t\text{P4} = 1,1,4,8,11,11$ -hexaphenyl-1,4,8,11-tetraphosphaundecane).<sup>17</sup> Crystals suitable for X-ray diffraction analysis were grown by adding *n*-pentane to a solution of **25** in acetonitrile/methanol (Figure 4.1). Complex **25** crystallizes in the C2/c space group and has an octahedral coordination geometry at the Fe(II) center, with the Fe–P<sub>ax</sub> distances (Fe1–P1 = 2.2868(13) Å and Fe1–P4 = 2.2982(13) Å) that are longer than the Fe–P<sub>eq</sub> distances (Fe1–P2 2.2138(13) and Fe1–P3 2.2247(12) Å). Notably, complex **25** resulted air stable as a solid and solutions in acetonitrile/methanol could be stored under nitrogen for over a month without any appreciable decomposition. In contrast, reaction of *meso*-P4 with  $[\text{Fe}(\text{CH}_3\text{CN})_6](\text{BF}_4)_2$  was not selective, and afforded a mixture of two products in approximately 2:1 ratio, which were identified on the basis of characteristic  $^{31}\text{P}\{^1\text{H}\}$  NMR resonances,<sup>9,17</sup> as the *trans*- and *cis*- $\beta$  isomers of  $[\text{Fe}(\text{meso-P4})(\text{CH}_3\text{CN})_2](\text{BF}_4)_2$ , respectively.



**Scheme 4.3.** Synthesis of *rac*-P4 and *meso*-P4 complexes starting from  $[\text{Fe}(\text{CH}_3\text{CN})_6](\text{BF}_4)_2$ .

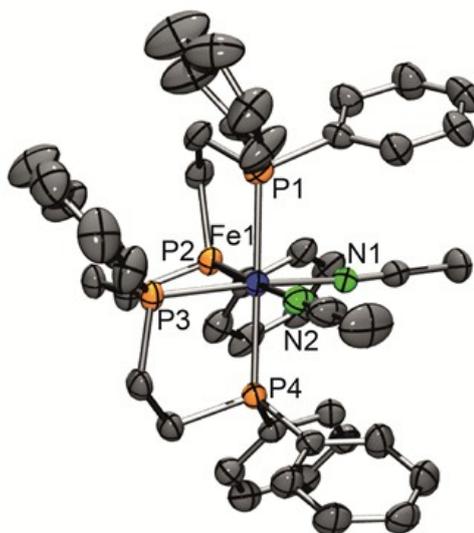


**Figure 4.1.** Molecular structure for the cationic portion of **25**. Ellipsoids are set at 50% probability. Hydrogen atoms are omitted for clarity. Selected bond lengths (Å) and bond angles (°): Fe1–N1 1.943(3); Fe1–N2 1.955(4); Fe1–P1 2.2869(13); Fe1–P2 2.2137(12); Fe1–P3 2.2246(12); Fe1–P4 2.2981(13); N1–Fe1–N2 88.70(15); N1–Fe1–P1 90.36(11); N1–Fe1–P2 92.50(11); N1–Fe1–P3 174.50(12); N1–Fe1–P4 90.06(11); N2–Fe1–P1 91.57(12); N2–Fe1–P2 117.12(12); N2–Fe1–P3 93.76(11); N2–Fe1–P4 88.25(12).

### *Syntheses of Fe(rac-P4) hydrido-complexes*

Due to the relevance of Fe-hydrido complexes to FA dehydrogenation and bicarbonate hydrogenation reactions, we targeted the syntheses of the unknown mono- and dihydride iron complexes of *rac*-P4. The analogues of the *meso* isomer

have been previously reported.<sup>9,13e</sup> The monohydrido complex  $[\text{Fe}(\text{rac-P4})\text{H}][\text{BPh}_4]$  (**26**·BPh<sub>4</sub>) was obtained upon reacting *rac*-P4, anhydrous FeCl<sub>2</sub>, NaBPh<sub>4</sub> and NaBH<sub>4</sub> in stoichiometric amounts in THF/MeOH, and was characterized by NMR and X-ray diffraction studies upon growing suitable crystals from these solutions. The <sup>31</sup>P{<sup>1</sup>H} NMR spectrum of **26**·BPh<sub>4</sub> in *d*<sub>8</sub>-THF showed two triplets at 119.4 and 99.4 ppm, reflecting an AA'XX' coupling pattern with an observed splitting of 24,56 Hz, while in the corresponding <sup>1</sup>H NMR spectrum, the hydride signal appears as a broad triplet at -9.16 ppm (<sup>2</sup>J<sub>HP</sub> = 24.0 Hz). The crystal structure of **26**·BPh<sub>4</sub> displays a pseudo-octahedral geometry, with the hydride ligand occupying two sites in the crystal, i.e. alternatively one or the other *cis* positions in 50% occupancy (Figure 4.2). The distortion from the ideal octahedral geometry is evident from the P1–Fe1–P4 angle (170.4°), which is significantly bent compared to the analogous P1–Fe1–P4 angle in **25** (179.5°), whereas the P2–Fe1–P3 angle is comparable in **25** and **26** (85.3° vs. 85.7°).

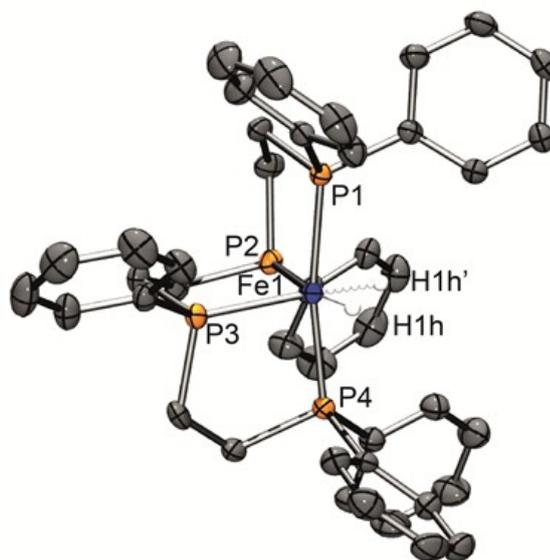


**Figure 4.2.** Molecular structure for the cationic portion of **26**·BPh<sub>4</sub>. Ellipsoids are set at 50% probability. Hydrogen atoms are omitted for clarity except the hydrido ligand. Selected bond lengths (Å) and bond angles (°): Fe1–P1 2.2189(7); Fe1–P2 2.1961(7); Fe1–P3 2.2207(7); Fe1–P4 2.1993(8); Fe1–H1h 1.61(5); Fe1–H1h' 1.41(5); H1h–Fe1–H1h' 90(3); P1–Fe1–P2 85.38(3); P1–Fe1–P3 102.58(3); P1–Fe1–P4 170.41(3); P2–Fe1–P3 85.74(3); P2–Fe1–P4 96.87(3); P3–Fe1–P4 86.91(3); H1h–Fe1–P1 89.0(2); H1h–Fe1–P2 172.4(18); H1h–Fe1–P3 100.6(18); H1h–Fe1–P4 87.(2); H1h'–Fe1–P1 83.(2); H1h'–Fe1–P2 83.(2); H1h'–Fe1–P3 168(2); H1h'–Fe1–P4 87 (2).

The neutral dihydrido complex *cis-α*-[Fe(*rac*-P4)(H)<sub>2</sub>] (**27**) was synthesised from *rac*-P4, anhydrous FeCl<sub>2</sub> and excess NaBH<sub>4</sub> under reflux conditions in a THF/EtOH mixture. The <sup>31</sup>P{<sup>1</sup>H} NMR spectrum of **27** in *d*<sub>8</sub>-THF displayed two triplets at 123.8 and 113.1 ppm with a <sup>2</sup>J<sub>PP</sub> = 13.5 Hz due to *cis*-P,P coupling, whereas the two hydride ligands gave a complex multiplet centered at -11.7 ppm (apparent double septuplet). Crystals of **27** suitable for X-ray analysis were grown by diffusion of MeOH into the solution which resulted from the reaction mixture, after filtration and partial evaporation of the solvent. The solid state molecular structure of **27** displays a significantly distorted octahedral coordination geometry at the Fe(II) center with the *rac*-P4 ligand adopting a *cis-α* configuration (Figure 4.3). The P1–Fe1–P4 angle in **27** (159.6 °) is significantly more distorted than in **26**·BPh<sub>4</sub> (170.4°). Furthermore, all Fe–P bond distances are significantly shorter (all < 2.17 Å) respect to those observed in **25** (2.19 – 2.22 Å) and **26**·BPh<sub>4</sub> (2.21 – 2.30 Å).

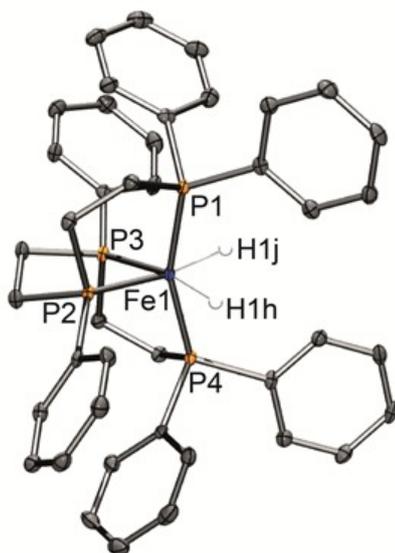


**Figure 4.3.** Molecular structure of **27**. Ellipsoids are set at 50% probability. Hydrogen atoms are omitted for clarity except hydrido ligands. Selected bond lengths (Å) and bond angles (°): Fe1–P1 2.1249(7); Fe1–P2 2.1510(7); Fe1–P3 2.1654(7); Fe1–P4 2.1303(7); Fe1–H1h 1.55(3); Fe1–H1j 1.57(2); H1h–Fe1–H1j 90.6(13); P1–Fe1–P2 89.00(3); P1–Fe1–P3 106.14(3); P1–Fe1–P4 159.62(3); P2–Fe1–P3 86.05(2); P2–Fe1–P4 106.21(3); P3–Fe1–P4 88.71(3); H1h–Fe1–P1 85.0(9); H1h–Fe1–P2 91.8(9); H1h–Fe1–P3 168.6(9); H1h–Fe1–P4 81.1(9); H1j–Fe1–P1 82.3(9); H1j–Fe1–P2 93.3(9); H1j–Fe1–P3 171.8(9); H1j–Fe1–P4 83.0(9).

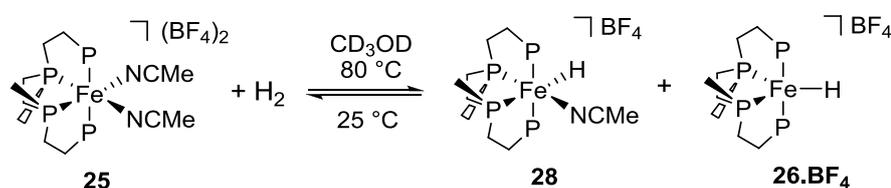
#### 4.4 Reactivity of Fe(II) complexes toward H<sub>2</sub>

To verify the potential of **24** and **25** as hydrogenation catalyst precursors, we investigated at first their reactivity towards molecular H<sub>2</sub> in model reactions under HPNMR conditions. A solution of Fe(BF<sub>4</sub>)<sub>2</sub>·6H<sub>2</sub>O and rac-P4 in PC (1.5 mL, 0.01M) was initially transferred in a 10 mm medium-pressure HPNMR sapphire tube. <sup>31</sup>P{<sup>1</sup>H} NMR analysis at room temperature under Ar atmosphere showed, as expected, the broad signals due to **24**.

Upon addition of CD<sub>3</sub>OD for deuterium lock (0.5 mL), the <sup>31</sup>P{<sup>1</sup>H} NMR pattern due to **24'** appeared, while no hydride signals were observed in the corresponding <sup>1</sup>H NMR spectrum. The tube was then pressurized at RT with 30 bar H<sub>2</sub>, which resulted in the quantitative conversion of **24** and **24'** into a new species, that we identified as **26**·BF<sub>4</sub> based on the identical <sup>31</sup>P{<sup>1</sup>H} NMR pattern of the isolated monohydride **26**·BPh<sub>4</sub>.<sup>18</sup> Due to HPNMR conditions and possible H/D exchange, the Fe–H hydrido ligand appeared as a broad signal centred at ca. -9.16 ppm. In the temperature range 233–353 K, no changes in the spectra were observed, suggesting that a putative hydrido-dihydrogen complex such as [FeH(η<sup>2</sup>-H<sub>2</sub>)(rac-P4)]<sup>+</sup> does not form under these conditions, in analogy to what previously described for [FeH(meso-P4)]<sup>+</sup>.<sup>11</sup> This was further verified by repeating the experiment using a 0.025 M solution of **24** in PC/CD<sub>3</sub>OH (3:1, total volume 2.0 mL) and measuring the longitudinal relaxation time (*T*<sub>1</sub>) at 293 and 273 K, respectively, obtaining values of ca. 900 ms with good exponential fitting of the data, in line with values expected for a classical hydride.

Complex **25** resulted remarkably less reactive towards H<sub>2</sub> than **24**. Complex **25** was dissolved in CD<sub>3</sub>OD and reacted with H<sub>2</sub> (30 bar) under HPNMR conditions (see Appendix). At room temperature, besides the peaks of unreacted **25**, four distinct <sup>31</sup>P{<sup>1</sup>H} NMR resonances were observed to appear at δ<sub>P</sub> 121.7 (br.s), 104.0 (br.d), 101.2 (br.d), 96.3 (br.s). The corresponding <sup>1</sup>H NMR spectrum showed an apparent doublet of quartets centered at δ<sub>H</sub> -8.5 ppm (dq, <sup>2</sup>J<sub>HPtrans</sub> = 36.7 Hz, <sup>2</sup>J<sub>HPcis,eq</sub> = 51.3 Hz, <sup>2</sup>J<sub>HPcis,ax1</sub> = <sup>2</sup>J<sub>HPcis,ax2</sub> = 51.1 Hz). This pattern, indicative of unequivalent phosphorus atoms typical of an octahedral Fe complex, was attributed to the formation of cis-α-[FeH(NCMe)(rac-P4)](BF<sub>4</sub>) (**28**). The resonances due to **26**·BF<sub>4</sub> appeared at 313 K. The temperature was then further increased to 333 and 353 K. The signals due to **26**·BF<sub>4</sub> and **28** were observed to increase, reaching almost

complete conversion of **25** with ca. a final 1:3 ratio between **26**·BF<sub>4</sub> and **28**. The reaction is reversible, as cooling to 293 K gave back the same pattern initially observed (Scheme 4.4 and Appendix). The experiment was repeated in the presence of an added base (NEt<sub>3</sub>), affording at first a mixture of **26**·BF<sub>4</sub> and **28** upon heating, and then **28** as the only product after 20 h standing at 293 K. Addition of Et<sub>2</sub>O/pentane to the reaction mixture resulted in the precipitation of yellow crystals of **28**. The corresponding (X-ray crystal structure, albeit highly disordered, was however useful to confirm the proposed formula (see Appendix).

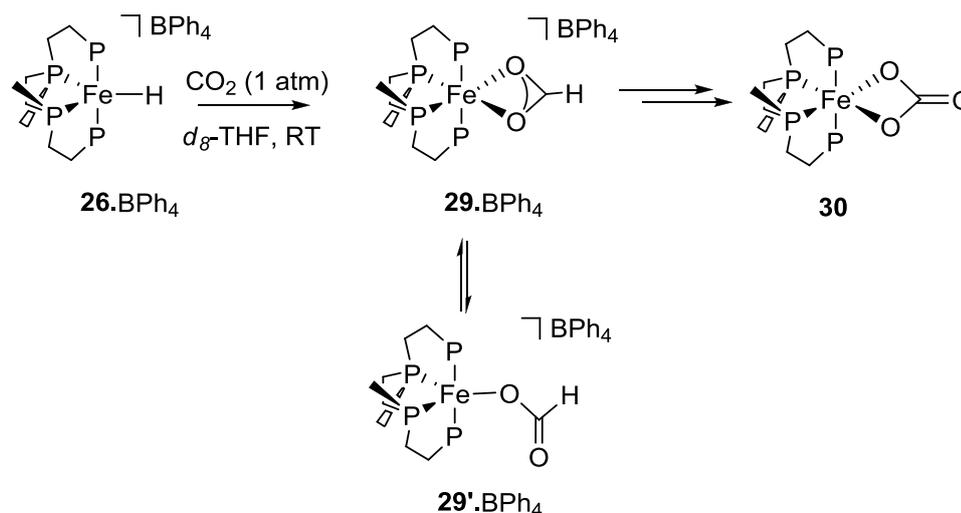


**Scheme 4.4.** Conversion of **25** to **26**·BF<sub>4</sub> via intermediate **28**.

#### 4.5 Reactivity of Fe(II) hydride complexes toward CO<sub>2</sub>

In the next step, we explored the reactivity of the mono- and dihydrides **26**·BPh<sub>4</sub> and **27** toward CO<sub>2</sub>. Beller *et al.* showed that insertion of CO<sub>2</sub> into the Fe–H bond of complex [Fe(PP<sub>3</sub>)H]<sup>+</sup> could be achieved under 10 atm of gas pressure giving the corresponding formate complex.<sup>3</sup> In an NMR-scale experiment, we reacted the monohydride **26**·BPh<sub>4</sub> with CO<sub>2</sub> (1 atm) in *d*<sub>8</sub>-THF, obtaining as expected, the formate complex *cis*- $\alpha$ -[Fe(*rac*-P4)( $\eta^2$ -O<sub>2</sub>CH)](BPh<sub>4</sub>) (**29**·BPh<sub>4</sub>, Scheme 4.5), having <sup>31</sup>P{<sup>1</sup>H} NMR signals at 106.8 (t) and 77.4 (t, <sup>2</sup>J<sub>PP</sub> = 29.5 Hz). In the corresponding <sup>13</sup>C{<sup>1</sup>H} NMR spectrum, apart from the signal at 162.4 ppm due to BPh<sub>4</sub><sup>-</sup>, a broad singlet at 171.9 ppm, compatible with a coordinated formate anion, was observed. By repeating the test using **26**·BF<sub>4</sub> and <sup>13</sup>CO<sub>2</sub>, the singlet at 174.5 ppm turned as expected into a doublet with <sup>1</sup>J<sub>CH</sub> = 208.8 Hz in the corresponding proton-coupled <sup>13</sup>C NMR spectrum (see Appendix).<sup>3a,19</sup> Unfortunately, the <sup>1</sup>H NMR signal expected in the range 8.2–8.5 ppm for the formate ligand, diagnostic for  $\eta^1$  vs.  $\eta^2$ -coordination, was lying under the ligand aromatic protons multiplet. After 24 h, the <sup>31</sup>P{<sup>1</sup>H} NMR spectrum showed signals of a new complex with triplets at  $\delta_p$  106.6 and 73.2 ppm

( $^2J_{\text{PP}} = 30.4$  Hz), which we assigned to the neutral carbonate complex *cis-α*-[Fe( $\eta^2$ -O<sub>2</sub>CO)(*rac*-P4)] (**30**). The corresponding  $^{13}\text{C}\{^1\text{H}\}$  NMR signal was determined from the experiment run using  $^{13}\text{CO}_2$ , giving a singlet at 158.1 ppm. The attribution was confirmed by independent synthesis of **30** by reaction of **24** with an excess of  $\text{K}_2\text{CO}_3$  in PC. In addition, the formation of complex **30** was observed also in HPNMR experiments upon reacting either **24** or **25** with  $\text{NaHCO}_3$  (*vide infra*).



**Scheme 4.5.** Reactivity of complex **26**·BPh<sub>4</sub> with H<sub>2</sub> to give **29**·BPh<sub>4</sub> and **30**.

MeOH diffusion into the *d*<sub>8</sub>-THF solution recovered after the NMR experiment described above afforded few purple crystals which were found to be suitable for X-ray diffraction data collection. Quite surprisingly, the solid-state structure revealed a trimetallic unit in which a central [Fe(MeOH)<sub>4</sub>]<sup>2+</sup> moiety, bridges two [Fe(*rac*-P4)(O<sub>2</sub>CO)] moieties via the two carbonate ligands by  $\eta^1$ -O coordination, as shown in Figure 4.4. Despite the fact that the formation of complex  $\{\mu^2$ -[Fe(MeOH)<sub>4</sub>]-*k*<sup>1</sup>-O-[Fe( $\eta^2$ -O<sub>2</sub>CO)(*rac*-P4)]<sub>2</sub>\}(BPh<sub>4</sub>)<sub>2</sub> (**30'**) may be accidental, its solid-state structure confirmed the presence of CO<sub>3</sub><sup>2-</sup> ligands. Carbonate is likely to form by reductive disproportionation of CO<sub>2</sub> into CO<sub>3</sub><sup>2-</sup> and CO, promoted by **26**·BPh<sub>4</sub>.<sup>20</sup> This reaction, occurring via a formate intermediate, has been previously described with Fe(II) hydrido-complexes such as *trans*-[Fe(dppe)<sub>2</sub>(H)<sub>2</sub>] and [Fe(PP<sub>3</sub>)(H)<sub>2</sub>].<sup>20,21</sup>

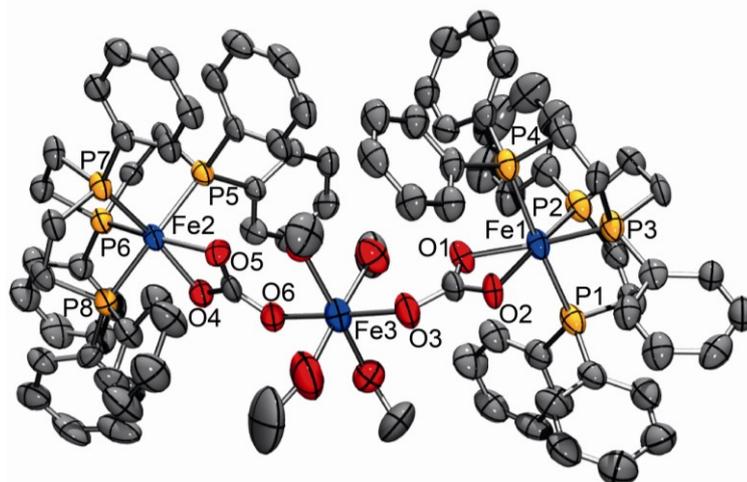


**Figure 4.4.** Molecular structure for the cationic part of  $\{\mu^2\text{-}[\text{Fe}(\text{MeOH})_4]\kappa^1\text{-O-}[\text{Fe}(\eta^2\text{-O}_2\text{CO})(\text{rac-P4})]_2\}(\text{BPh}_4)_2$  (**30'**). Ellipsoids are set at 50% probability. Hydrogen atoms are omitted for clarity. Selected bond lengths (Å) and bond angles (°): Fe1–O1 2.035(5); Fe1–O2 2.027(5); Fe1–P1 2.286(3); Fe1–P2 2.205(3); Fe1–P3 2.197(2); Fe1–P4 2.297(3); Fe2–O4 2.032(5); Fe2–O5 2.046(5); Fe2–P5 2.282(2); Fe2–P6 2.217(3); Fe2–P7 2.204(2); Fe2–P8 2.260(2); Fe3–O3 2.133(6); Fe3–O6 2.076(6); O1–Fe1–O2 65.0(2); O1–Fe1–P1 96.25(17); O1–Fe1–P2 106.26(19); O1–Fe1–P3 165.40(18); O1–Fe1–P4 86.72(17); O2–Fe1–P1 87.63(17); O2–Fe1–P2 167.59(17); O2–Fe1–P3 104.43(18); O2–Fe1–P4 94.20(17); O4–Fe2–O5 64.8(2); O4–Fe2–P5 93.80(16); O4–Fe2–P6 104.65(17); O4–Fe2–P7 166.98(19); O4–Fe2–P8 86.48(16); O5–Fe2–P5 85.36(16); O5–Fe2–P6 164.85(16); O5–Fe2–P7 107.37(16); O5–Fe2–P8 92.69(17); O3–Fe3–O6 178.2(2).

Complex **27** was also tested for reactivity with  $\text{CO}_2$ , to check for the possible formation of Fe-hydrido formate complexes, similarly to what proposed by Beller *et al.* for  $[\text{Fe}(\text{P}^{\text{Ph}}\text{P}_3)(\text{H})_2]$ .<sup>4</sup> No reaction was observed under the conditions described above (*i.e.* 1 atm  $\text{CO}_2$  in  $d_8$ -THF, RT). The experiment was repeated under moderate pressure of  $\text{CO}_2$  (7 bar) under HPNMR conditions, but again no reaction occurred.

## 4.6 Fe-Catalyzed Formic Acid Dehydrogenation

FA dehydrogenation to  $\text{H}_2/\text{CO}_2$  gas mixtures was tested in the presence of the in situ and pre-formed catalysts described above, using an inert solvent (PC) under isobaric conditions (1 atm) and in absence of added base, measuring the development of gas during the reaction with a manual gas-burette. The gas mixtures were analyzed off-line by FT-IR spectroscopy, showing absence of CO for all tests (detection limit 0.02%).<sup>22</sup> Much to our surprise, the well-defined catalyst precursor **25** (0.1 %mol) resulted inactive in the dehydrogenation of FA in PC at 40 °C. Thus, we targeted the

use of in situ catalysts formed using *rac*- and *meso*-P4. Initially, we checked the activity of commercial P4 (0.1 %mol, *meso*/*rac* = ca. 3) under the same conditions described above, and observed a FA conversion of 4% after 6 h, corresponding to a TON = 444 (entry 1, Table 4.1). When pure *rac*-P4 was used, generating in situ catalyst **24** (0.1%mol) FA dehydrogenation proceeded with good conversions, reaching TON = 604 after 8 h at 40 °C (entry 2). As reported for the  $\text{PP}_3/\text{Fe}(\text{BF}_4)_2 \cdot 6\text{H}_2\text{O}$  catalyst system,<sup>1</sup> higher ligand/Fe ratios are beneficial to reach high reaction turnovers. Using a Fe/*rac*-P4 = 1/2 ratio, as expected<sup>1</sup> the catalyst performance improved significantly, affording full conversion of FA in ca. 6 h (TON = 1000; entry 3). Using a catalyst/substrate ratio = 1:10000 at 40 °C, low conversions (11%) were obtained after 6 h, with TON = 1081 (entry 5). Using the same catalyst/substrate ratio at 60 °C, gave a higher TON = 3088 after 6 h (entry 6). Using a higher Fe /ligand = 1:4 ratio, at 60 °C considerably enhanced catalytic activity was achieved (TON = 6061, 6h; entry 9). In contrast, pre-catalysts obtained from  $\text{Fe}(\text{BF}_4)_2 \cdot 6\text{H}_2\text{O}$  and *meso*-P4 showed worse catalytic activities (generally ca. 33% lower) compared to *rac*-P4 (entries 4, 7,8 and 10). Also in this case, the exclusive *cis*-geometry forced by *rac*-P4 is the most suitable to convey a catalytically active species, compared to *meso*-P4 for which different geometrical isomers are possible. Selected results are summarized in Table 4.1. Selected reaction profiles (volumes vs. time) of catalytic runs obtained at catalyst/substrate = 1:10000 ratio, at various Fe/ligand ratios and temperatures, are shown in Figure 4.5. Disappointingly, recycling experiments at catalyst / substrate = 1:1000, Fe/ligand = 1:2, 40 °C showed a severe drop in activity from the first to the third cycle, namely from TON = 1000 to 295 after 6 h.

**Table 4.1.** Formic Acid Dehydrogenation catalyzed using *in situ* Fe(II) pre-catalysts.

Entry	L	sub/cat	Fe/L	T(°C)	V <sub>1h</sub> (mL) <sup>d</sup>	TON <sub>1h</sub> <sup>e</sup>	TOF <sub>10min</sub> <sup>f</sup>	V <sub>final</sub> (mL) <sup>d</sup>	TON <sub>final</sub> <sup>e</sup>	Total Conv. (%)
<b>1<sup>a</sup></b>	P4 <sup>c</sup>	10000	1:2	40	25	97	232	115	444 (6h)	4
<b>2<sup>a</sup></b>	<i>rac</i> - P4	1000	1:1	40	220	85	35	1560	604 (8h)	60
<b>3<sup>a</sup></b>	<i>rac</i> - P4	1000	1:2	40	345	133	139	2570	1000 (6h)	100
<b>4<sup>a</sup></b>	<i>meso</i> - P4	1000	1:2	40	165	64	151	810	313 (8h)	31
<b>5<sup>b</sup></b>	<i>rac</i> - P4	10000	1:2	40	45	174	347	280	1081 (6h)	11
<b>6<sup>b</sup></b>	<i>rac</i> - P4	10000	1:2	60	215	830	1853	800	3088 (6h)	31
<b>7<sup>b</sup></b>	<i>meso</i> - P4	10000	1:2	40	15	58	116	90	348 (6h)	3
<b>8<sup>b</sup></b>	<i>meso</i> - P4	10000	1:2	60	70	270	579	260	1003 (6h)	10
<b>9<sup>b</sup></b>	<i>rac</i> - P4	10000	1:4	60	400	1544	1737	1570	6061 (6h)	61
<b>10<sup>b</sup></b>	<i>meso</i> - P4	10000	1:4	60	140	540	579	590	2278 (8h)	23

Reaction conditions: <sup>a</sup> Fe(BF<sub>4</sub>)<sub>2</sub>·6H<sub>2</sub>O, 5.3 mmol; ligand (1 to 4 equiv. to Fe); HCOOH, 5.3 mol (2 mL); PC, 5 mL. <sup>b</sup> As above, Fe(BF<sub>4</sub>)<sub>2</sub>·6H<sub>2</sub>O, 5.3 μmol. <sup>c</sup> Commercial tetraphos-1 (P4) ligand, *meso*-P4/*rac*-P4 = 3. <sup>d</sup> Gas evolution measured by manual gas burette, based on 2-4 tests, error ± 10%. Gas mixture analyzed off-line by FTIR spectroscopy. <sup>e</sup> Defined as mmol<sub>gas produced</sub> / mmol<sub>catalyst</sub>. <sup>f</sup> Defined as mmol<sub>gas produced</sub> / mmol<sub>catalyst</sub> × h<sup>-1</sup>, calculated at conversions observed after 10 min.

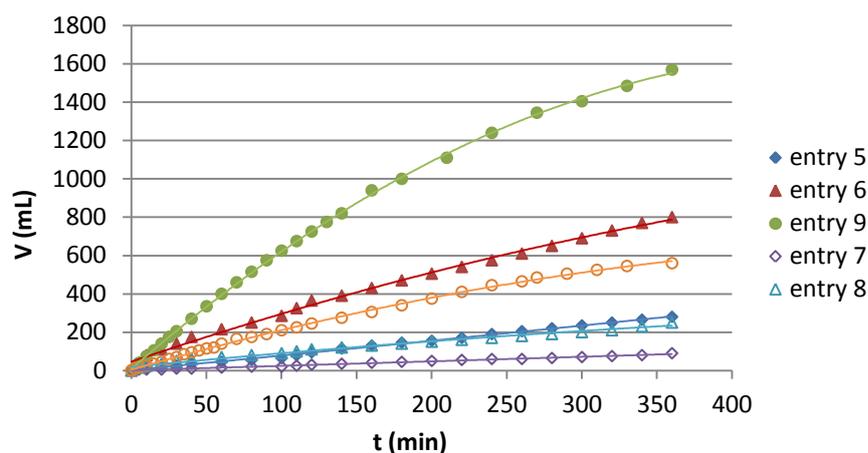


**Figure 4.5.** Reaction profiles of selected FA dehydrogenation catalytic runs using catalyst/substrate = 1:10000 ratio at different temperatures and Fe:P4 ratios. For legenda and conditions see Table 4.1.

#### 4.7 Fe-Catalyzed Sodium Bicarbonate Hydrogenation

The added base-free hydrogenation of sodium bicarbonate to formate in MeOH was tested in stainless steel autoclaves at different  $H_2$  pressures and temperatures. In a preliminary experiment, we tested the activity of a combination of commercial tetraphos-1 (P4) and  $Fe(BF_4)_2 \cdot 6H_2O$  (0.01 mmol, 1:1 ratio) in the hydrogenation of sodium bicarbonate in MeOH. To our delight, at 80 °C under 30 bar  $H_2$ , sodium formate was formed with TON = 154 (Table 4.2; entry 1). The activity of **24** and **24'** was then tested to check for ligand effects.

The in situ formed pre-catalysts were obtained from stock solutions made from  $Fe(BF_4)_2 \cdot 6H_2O$  and either *rac*-P4 or *meso*-P4 (0.01M in PC). The solutions were analyzed by  $^{31}P\{^1H\}$  NMR before use to confirm the formation of the corresponding Fe(II) complexes **24** and **24''**. Catalyst precursor **24''** gave a rather poor catalytic performance, reaching a TON = 62 after 24 h under 60 bar  $H_2$  and 80 °C using 0.1%mol catalyst (Table 4.2; entry 2). In contrast, **24** resulted rather active in the catalytic hydrogenation of  $NaHCO_3$  in MeOH. Under 60 bar  $H_2$  pressure, using 0.1% mol catalyst, rather good yields (58% and 59%) and TONs (575 and 588) were achieved at 80 °C and 100 °C, respectively (Table 4.2; entries 3 and 4). TON values are in the order of magnitude obtained by Beller *et al.* with the  $Fe(BF_4)_2/PP_3$  system under comparable conditions.<sup>3</sup> At 60 °C (entry 5) the TON decreased to 186 with a

formate yield of 19%. The effect of H<sub>2</sub> pressure on the productivity of the reaction was also tested. TON and yield were not affected at 80 °C in passing from 60 to 30 bar (entry 6), whereas at 10 bar the yield of formate was slightly reduced (entry 7). Using a catalyst/substrate ratio = 1:10000, significantly lower TON and yield were obtained (entry 8). At an intermediate catalyst/substrate ratio (1:3000, obtained by increasing the substrate concentration) good activity was observed with TON = 723 and 24% yield in formate (entry 9). The hydrogenation of NaHCO<sub>3</sub> to NaHCO<sub>2</sub> using the well-defined molecular complex **25** as catalyst precursor (0.1 mol%) proceeded smoothly at 80 °C, affording sodium formate in excellent yields (76 and 71%) and good TONs (762 and 766) under 60 and 30 bar H<sub>2</sub> pressure (entries 10 and 13, respectively). Lowering the catalyst loading to 0.01 mol%, an increased TON = 1229 was measured, albeit with a lower yield in formate (12%) (entry 14). At this catalyst/substrate ratio, **25** performed better than **24** (1.2 mmol sodium formate vs. ca. 0.1 mmol obtained, entries 14 and 8, respectively). Finally, at higher (100 °C) or lower temperatures (60 °C) in the presence of **25** (0.1 mol%), lower yields of formate were obtained (entries 11 and 12). Based on these results, we propose that the better performance of the rac- vs. meso-systems can be related to the preferred cis-conformation of the former, suitable for an inner-sphere mechanism (vide infra). In the case of meso-P4, different isomers can form in solution (Scheme 4.2), hence decreasing the concentration of the likely active form, i.e. cis-β-**25** (Scheme 4.3).

**Table 4.2.** Hydrogenation of sodium bicarbonate using either *in situ* formed or defined molecular Fe(II) pre-catalysts.<sup>a</sup>

Entry	Catalyst precursor	sub/cat	T(°C)	p (H <sub>2</sub> ) (bar)	TON <sup>i,k</sup>	Yield (%) <sup>j,k</sup>
<b>1<sup>b</sup></b>	i	1000	80	60	154(±4)	15(±0)
<b>2<sup>c</sup></b>	24 <sup>''</sup>	1000	80	60	62(±16)	6(±2)
<b>3<sup>d</sup></b>	24	1000	80	60	575(±52)	58(±5)
<b>4<sup>d</sup></b>	24	1000	100	60	588(±74)	59(±7)
<b>5<sup>d</sup></b>	24	1000	60	60	186(±14)	19(±1)
<b>6<sup>d</sup></b>	24	1000	80	30	620(±36)	62(±4)
<b>7<sup>d</sup></b>	24	1000	80	10	398(±14)	40(±1)
<b>8<sup>e</sup></b>	24	10000	80	60	83(±27)	1(±0)
<b>9<sup>d,f</sup></b>	24	3000	80	60	723(±40)	24(±1)
<b>10<sup>g</sup></b>	25	1000	80	60	762(±105)	76(±11)
<b>11<sup>g</sup></b>	25	1000	100	60	555(±15)	55(±1)
<b>12<sup>g</sup></b>	25	1000	60	60	161(±6)	16(±1)
<b>13<sup>g</sup></b>	25	1000	80	30	766(±81)	71(±14)
<b>14<sup>h</sup></b>	25	10000	80	60	1229(±18)	12(±0)

<sup>a</sup> General reaction conditions: catalyst precursor (0.01 mmol); NaHCO<sub>3</sub> (10 mmol); MeOH (20 mL); H<sub>2</sub> pressure, 24 h. <sup>b</sup> Catalyst precursor i: 1 mL of a 0.01M stock solution of commercial P4 and Fe(BF<sub>4</sub>)<sub>2</sub>·6H<sub>2</sub>O (1:1). <sup>c</sup> Catalyst precursor 24<sup>''</sup>: 1 mL of a 0.01M stock solution of 24<sup>''</sup> in PC. <sup>d</sup> Catalyst precursor 1: 1 mL of a 0.01M stock solution of 24 in PC. <sup>e</sup> 0.1 mL of a 0.01M stock solution of 24 in PC. <sup>f</sup> 30.0 mmol NaHCO<sub>3</sub>. <sup>g</sup> Complex 25 (0.01 mmol) was added to the autoclave from a CH<sub>3</sub>CN stock solution, from which the solvent was subsequently removed (0.02 M, 0.5 mL, see Experimental Section for details). <sup>h</sup> Complex 25 (0.001 mmol) was added to the autoclave from a CH<sub>3</sub>CN stock solution, from which the solvent was subsequently removed (0.02 M, 50 μL). <sup>i</sup> TON = mmoles of sodium formate per mmoles of catalyst. <sup>j</sup> Yields calculated from the integration of 1H NMR signals due to NaHCO<sub>2</sub>, using THF as internal standard. <sup>k</sup> Values of yields and TONs were calculated as averages from the analysis of 2-4 samples, the largest deviations are reported in brackets; selected experiments were repeated to ensure reproducibility.

## 4.8 NMR mechanistic studies

The reactivity of the different pre-catalysts with FA was studied by monitoring stoichiometric reactions by NMR and by HPNMR *in operando* conditions. A solution of complex 25 (0.7 mL, 0.012 M in PC, C<sub>6</sub>D<sub>6</sub> insert) was reacted with FA (1

equiv.) for 1h in a NMR tube. No changes in the  $^{31}\text{P}\{^1\text{H}\}$  and  $^1\text{H}$  NMR spectra were observed even after heating to 60 °C, confirming that **25** is not reactive under these conditions, probably due to stable coordination of MeCN ligands to the Fe center.

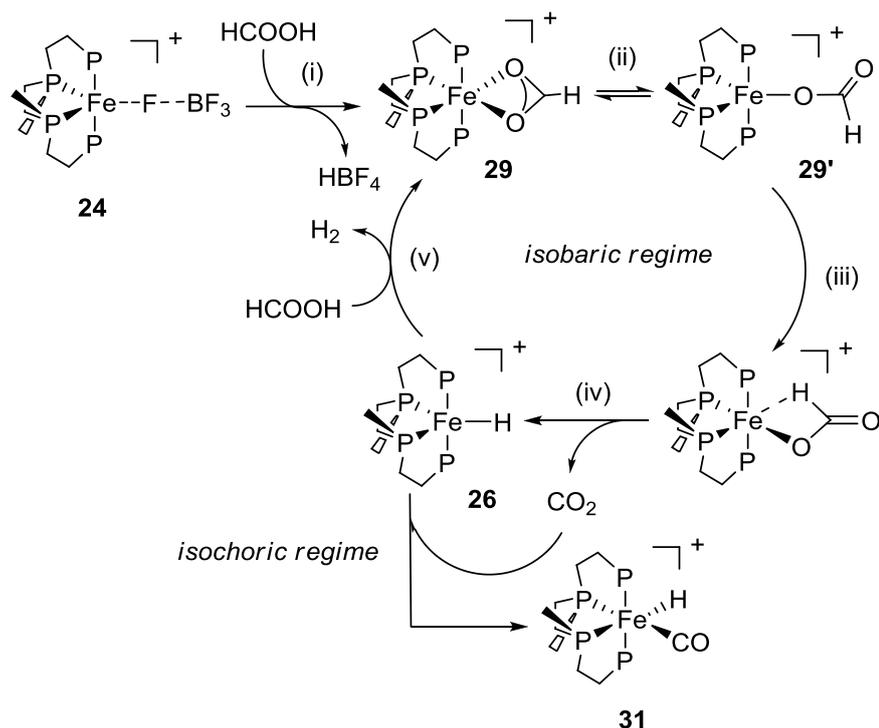
In contrast, addition of 1 equivalent of FA to a solution of **24** in PC in a NMR tube (0.7 mL, 0.042 M,  $\text{C}_6\text{D}_6$  insert) at room temperature, resulted in the formation of the monohydride  $[\text{Fe}(\text{rac-P4})\text{H}](\text{BF}_4)$  (**26**· $\text{BF}_4$ ) and of the formate complex  $[\text{Fe}(\text{rac-P4})(\eta^2\text{-O}_2\text{CH})](\text{BF}_4)$  (**29**· $\text{BF}_4$ ,  $\delta_{\text{P}}$  107.6 (t), 76.0 (t);  $^2J_{\text{PP}} = 29.0, 28.9$  Hz), initially in 6:1 ratio. Heating to 40 °C for 1h then leaving the tube overnight at 25 °C gave almost complete conversion to **26**· $\text{BF}_4$ . The experiment was repeated in the presence of a large excess of FA (100 equiv.) monitoring catalyst evolution by HPNMR spectroscopy. A 10 mm HPNMR sapphire tube was thus charged with a solution of **24** in PC (1.8 mL; 0.012 M), to which  $\text{CD}_3\text{OD}$  (0.4 mL) was added for deuterium lock.

Upon addition of FA at room temperature, complexes **26**· $\text{BF}_4$  and **29**· $\text{BF}_4$  were observed to form in 1:6 ratio. The probehead was then heated to 40 °C. After 1h, the reaction mixture evolved further with formation of a new species (**31**), characterized by four structured signals in the  $^{31}\text{P}\{^1\text{H}\}$  NMR and by a complex high field resonance signal (ddd;  $\delta_{\text{H}}$  -9.55 ppm,  $^2J_{\text{PP}} = 25.5, 46.5, 70.7$  Hz; 1H,  $\text{FeH}$ ) in the corresponding  $^1\text{H}$  NMR spectrum, indicative of the formation of an octahedral  $[\text{Fe}(\text{rac-P4})\text{HL}]$  complex with *cis- $\alpha$*  configuration. Prolonged heating resulted in the complete conversion to **31**, affording a yellow solution. Further multinuclear NMR analysis and ESI-MS spectroscopy data obtained from aliquots of the final solution allowed to identify complex **31** as the Fe-carbonyl hydrido complex *cis- $\alpha$* - $[\text{Fe}(\text{rac-P4})\text{H}(\text{CO})](\text{BF}_4)$  (L = CO).

As CO may result from the a competitive FA decomposition pathway, *i.e.* dehydration to  $\text{H}_2\text{O}$  and CO, we thought it was of interest to investigate further the reaction of **24** with FA. Some hints were given from the experimental data described above. Firstly, CO was never detected in the gas mixtures resulting from the catalytic runs by off-line FTIR measurements.<sup>22</sup> Secondly, complex **31** was never obtained in the NMR experiment carried out using a FA:**24** = 1:1 ratio. Thirdly, **31** was formed under isochoric conditions (HPNMR) in the presence of 100 equiv. of FA. Under these conditions, it is likely that the  $\text{CO}_2$  pressure built up in the HPNMR tube during

the course of the experiment may have undergone partial reductive disproportionation to CO and  $\text{CO}_3^{2-}$  as previously observed upon prolonged reaction of the monohydride  $\mathbf{26}\cdot\text{BPh}_4$  with  $\text{CO}_2$ .

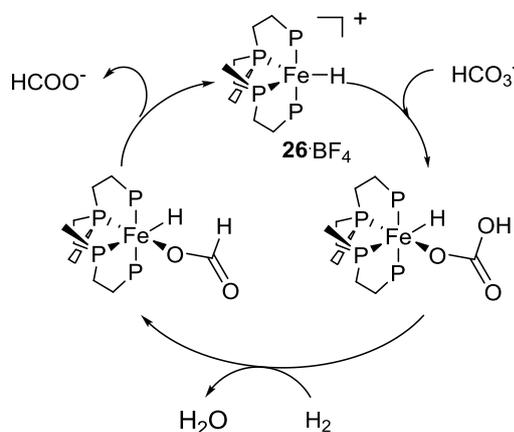
To confirm this hypothesis, we repeated the experiment in the glass reactor (isobaric conditions) normally used for the catalytic runs. Under the same conditions applied for the HPNMR experiment, gas evolution was complete after 20 min and again no CO was detected in the gas mixture. Furthermore, the mixture color remained purple throughout the run, whereas a bright yellow color should be expected upon formation of  $\mathbf{31}$  in high concentrations. As further confirmation, NMR analysis of the catalytic mixture at the end of the run showed the typical  $^{31}\text{P}\{^1\text{H}\}$  NMR resonances of  $\mathbf{26}\cdot\text{BF}_4$  and  $\mathbf{29}\cdot\text{BF}_4$  in 1:1 ratio, while the signals due to  $\mathbf{31}$  were not observed. Based on these observations, although we cannot rule out that at low catalyst concentrations (0.01 %mol) catalyst deactivation may occur by formation of  $\mathbf{31}$  due to a higher concentration of CO in the gas mixture, we propose that in closed (isochoric) vessels Fe-catalyzed  $\text{CO}_2$  reductive disproportionation becomes a competing pathway, and CO coordination to  $\mathbf{26}\cdot\text{BF}_4$  gives the stable (and catalytically inactive) octahedral  $\mathbf{31}$ . Based on our experimental observations, we propose the following pathway for the base-free FA catalytic dehydrogenation reaction (Scheme 4.6). In step (i), the catalyst precursor  $\mathbf{24}$ , formed *in situ* from  $\text{Fe}(\text{BF}_4)_2\cdot 6\text{H}_2\text{O}$  and *rac*-P4, reacts with FA to give  $\text{HBF}_4$  and the formate complex  $[\text{Fe}(\eta^2\text{-O}_2\text{CH})(\text{rac-P4})](\text{BF}_4)$  ( $\mathbf{29}\cdot\text{BF}_4$ ). Through  $\eta^2 \rightarrow \eta^1$  coordination shift from  $\mathbf{29}$  to  $\mathbf{29}'$  (ii) and ligand rearrangement (iii),  $\beta$ -hydride elimination from  $\mathbf{29}\cdot\text{BF}_4$  gives the monohydride  $\mathbf{26}\cdot\text{BF}_4$  and liberation of  $\text{CO}_2$  (iv). Protonation of  $\mathbf{26}\cdot\text{BF}_4$  by FA results in the fast elimination of  $\text{H}_2$  and regeneration of the formate complex  $\mathbf{29}\cdot\text{BF}_4$  (v). Although we cannot exclude in principle an alternative pathway, suggested for the Fe/ $\text{PP}_3$  system,<sup>1</sup> involving in step (v) coordination of  $\text{HCOO}^-$  to  $\mathbf{26}\cdot\text{BF}_4$  to form a putative and short-lived intermediate  $[\text{Fe}(\text{rac-P4})\text{H}(\eta^1\text{-O}_2\text{CH})]^+$ , we tend to disfavor this hypothesis as we never observed the formation of such complex during our studies.



**Scheme 4.6.** Proposed mechanism for the catalytic dehydrogenation of FA.

To gain mechanistic insights into the iron-catalysed hydrogenation of NaHCO<sub>3</sub> to sodium formate in the presence of **24** and **25**, we monitored catalyst evolution by HPNMR spectroscopy under *in operando* conditions. In details, a 10 mm HPNMR sapphire tube was initially charged with a 0.01M solution of **24** in PC (1.5 mL), CD<sub>3</sub>OD (0.5 mL) and NaHCO<sub>3</sub> (84 mg; 1.0 mmol, 100 equiv). The <sup>31</sup>P{<sup>1</sup>H} NMR pattern showed the presence of **24** (25%), **24'**(25%) and a new species **32** (50%, percentages are based on integrals), characterized by two triplets at δ<sub>p</sub> 107.1 and 72.9 ppm (<sup>2</sup>J<sub>pp</sub> = 30.3 Hz).<sup>23</sup> Pressurization of the reaction mixture with H<sub>2</sub> (30 bar) resulted in the formation of the monohydride complex **26**·BF<sub>4</sub> (34%) at room temperature. The mixture composition evolved fully to **26**·BF<sub>4</sub> in less than 2h upon slow heating to 60 °C, as confirmed by <sup>31</sup>P{<sup>1</sup>H} NMR spectra. Further heating to 80 °C did not result in further changes of the NMR patterns. A similar experiment was carried out using **25** (0.01 mmol) and NaHCO<sub>3</sub> (100 equiv) in CD<sub>3</sub>OD (2 mL). The initial mixture prepared under Ar atmosphere showed in the corresponding <sup>31</sup>P{<sup>1</sup>H} NMR the presence of unreacted **25** (84%), **24'** (7%) and **30** (9%). Upon standing at room temperature for 75 min, the resonances observed for **24'** and **30** increased

significantly (up to 34% and 27%), by slow reaction of **25** with NaHCO<sub>3</sub>. The slow ligand exchange from CH<sub>3</sub>CN to CO<sub>3</sub><sup>2-</sup> mirrors the reactivity of **25** with H<sub>2</sub> described above. By pressurization of the HPNMR tube with H<sub>2</sub> (30 bar), the resonances due to **28** appeared in the <sup>31</sup>P{<sup>1</sup>H} and <sup>1</sup>H NMR spectra, already at room temperature. At 80 °C, the signals of **25**, **24'** and **30** disappeared, with concomitant formation of **26**·BF<sub>4</sub> and **28** and free sodium formate (broad signals at 8.6-8.9 in the <sup>1</sup>H NMR spectrum).<sup>24</sup> The experimental results clearly indicate in **26**·BF<sub>4</sub> the key intermediate in the catalytic hydrogenation of NaHCO<sub>3</sub> with **24** and **25**, similarly to what described by Beller and co-workers in the case of CO<sub>2</sub> hydrogenation by [Fe(PP<sub>3</sub>)(H)]<sup>+</sup>.<sup>3</sup> Despite the fact that we could not observe other catalytic intermediates besides **26** under HPNMR conditions, an outer sphere mechanism involving intermolecular hydride transfer is unlikely, as it would not account for the different catalytic activities observed for *rac* and *meso* systems. In contrast, we suggest that an inner sphere mechanism requiring two available *cis* positions would be more likely and consistent with the better catalytic activity observed using **24**. A proposed mechanism for NaHCO<sub>3</sub> hydrogenation centred on **26** is shown in Scheme 4.7.



**Scheme 4.7.** Proposed mechanism for the catalytic hydrogenation of NaHCO<sub>3</sub> in the presence of **26**.

## 4.9 Conclusions

In summary, the coordination chemistry of the *rac*- and *meso*-isomers of the linear tetraphosphine 1,1,4,7,10,10-hexaphenyl-1,4,7,10-tetraphosphadecane (tetraphos-1, P<sub>4</sub>) towards Fe(II) was explored in details, obtaining novel complexes which were applied for base-free H<sub>2</sub>/CO<sub>2</sub> generation from formic acid and for the hydrogenation of sodium bicarbonate to formate under mild conditions, showing a higher activity in the case of Fe/*rac*-P<sub>4</sub> systems. Mechanistic studies highlighted the pivotal role of the monohydride [Fe(*rac*-P<sub>4</sub>)H]<sup>+</sup> in both reactions, and that CO<sub>2</sub> reductive disproportionation should not be underestimated as a competing pathway in the case of Fe(II)/polyphosphine systems. A full DFT study of both catalytic reactions promoted by Fe/tetraphos-1 is currently under way.

## 4.10 Experimental section

### 4.10.1 General methods and materials

All synthesis were performed using standard Schlenk techniques under an atmosphere of dry nitrogen or argon. Solvents were freshly distilled over appropriate drying agents, collected over Linde type 3Å or 4Å molecular sieves under nitrogen, and degassed with nitrogen or argon gas. Formic acid and N,N-dimethyloctylamine were distilled in vacuum prior to use and stored under nitrogen. The formic acid to amine ratio was determined by <sup>1</sup>H NMR spectroscopy on a BrukerAvance 400 spectrometer. Ligand 1,1,4,7,10,10-hexaphenyl-1,4,7,10-tetraphosphadecane (tetraphos-1, P<sub>4</sub>) was supplied by Pressure Chemicals Inc., Pittsburgh, PA. [Fe(MeCN)<sub>6</sub>](BF<sub>4</sub>)<sub>2</sub> was synthesized according to literature methods.<sup>14</sup> Anhydrous FeCl<sub>2</sub>, Fe(BF<sub>4</sub>)<sub>2</sub>·6H<sub>2</sub>O, NaBH<sub>4</sub>, NaHCO<sub>3</sub> and propylene carbonate were purchased from commercial suppliers and used without further purification. Deuterated solvents for NMR measurements were purchased from commercial suppliers and stored onto activated 4Å molecular sieves under Ar before use.

The high pressure <sup>1</sup>H and <sup>31</sup>P{<sup>1</sup>H} NMR spectra were recorded on a Bruker Avance II 300 spectrometer (operating at 300.13, 75.47, and 121.50 MHz, respectively). The <sup>1</sup>H, <sup>13</sup>C{<sup>1</sup>H}, and <sup>31</sup>P{<sup>1</sup>H} NMR spectra were recorded on a Bruker Avance II 300

spectrometer (operating at 300.13, 75.47, and 121.50 MHz, respectively) and a Bruker Avance II 400 spectrometer (operating at 400.13, 100.61, and 161.98 MHz, respectively) at room temperature.  $^{19}\text{F}$  spectra were run on Bruker Avance 400 DRX spectrometers (operating at 376.15 MHz). Peak positions are relative to tetramethylsilane and were calibrated against the residual solvent resonance ( $^1\text{H}$ ) or the deuterated solvent multiplet ( $^{13}\text{C}$ ).  $^{19}\text{F}$  and  $^{31}\text{P}\{^1\text{H}\}$  NMR were referenced to external  $\text{CFCl}_3$  and to 85%  $\text{H}_3\text{PO}_4$ , with the downfield shift taken as positive. Electrospray mass spectrometry (ESI-MS) analyses were measured on a LCQ Orbitrap mass spectrometer (ThermoFischer, San Jose, CA, USA) equipped with a conventional ESI source by direct injection of the sample solution and are reported in the form  $m/z$  (intensity relative to base = 100). Infrared spectra of gas mixture were measured on a Perkin-Elmer FT-IR Spectrum BX II instrument with a ICL 10 cm G-2 gas cell with KBr windows and Plain Ending Joints (PTE). CO calibration (0.02-0.3%) within a pure mixture of  $\text{CO}_2/\text{H}_2$  (1:1, Air Liquide) was carried out using Wills' method.<sup>22</sup>

#### 4.10.2 Synthetic procedures

##### Reaction of *rac*-P4 with $\text{Fe}(\text{BF}_4)_2 \cdot 6\text{H}_2\text{O}$

Ligand *rac*-P4 (67 mg, 0.1 mmol) was dissolved in propylene carbonate (PC) (2.0 mL) under gentle heating (40-50 °C) to afford complete dissolution. One equivalent of  $\text{Fe}(\text{BF}_4)_2 \cdot 6\text{H}_2\text{O}$  (34 mg, 0.1 mmol) was added to the colorless solution, which immediately turned deep purple.  $^{31}\text{P}\{^1\text{H}\}$  NMR analysis showed quantitative formation of a single product. The purple product could be precipitated by adding a large amount of  $\text{Et}_2\text{O}$  (at least 8.0 mL). The decanted solid was recovered by removing the colorless solution via cannula, and washed with  $\text{Et}_2\text{O}$  to remove all propylene carbonate yielding analytically pure complex  $[\text{Fe}(\textit{rac}\text{-P4})(\eta^1\text{-FBF}_3)](\text{BF}_4)$  (**24**). Due to the poor stability of **24** as isolated solid, we chose to use stock solutions of **24** in PC for both catalytic and NMR experiments. Yield: 78 mg (94%).  $^{31}\text{P}\{^1\text{H}\}$  NMR (121.49 MHz, PC +  $\text{C}_6\text{D}_6$  capillary): 99.9 ppm (br.s.; 2P, *PPh*), 60.9 ppm (br.s.; 2P, *PPh*<sub>2</sub>).  $^{19}\text{F}\{^1\text{H}\}$  NMR (376.15 MHz, PC +  $\text{C}_6\text{D}_6$  insert): 154 ppm (s.; 4F,  $\text{BF}_4$ ).

**Reaction of *meso*-P4 with Fe(BF<sub>4</sub>)<sub>2</sub>·6H<sub>2</sub>O**

In a 5 mm NMR tube, *rac*-P4 (20 mg, 0.03 mmol) was dissolved in propylene carbonate (PC, 0.7 mL). Gentle heating (40-50 °C) was needed to afford complete dissolution of the ligand. One equivalent of Fe(BF<sub>4</sub>)<sub>2</sub>·6H<sub>2</sub>O (10 mg, 0.03 mmol) was added to the colorless solution, which immediately turned brown and then yellow. <sup>31</sup>P{<sup>1</sup>H} NMR analysis showed formation of [Fe(*meso*-P4)(η<sup>1</sup>-FBF<sub>3</sub>)](BF<sub>4</sub>) (**24''**) as a single product. No attempts were made to isolate the product. <sup>31</sup>P{<sup>1</sup>H} NMR (121.49 MHz, PC + C<sub>6</sub>D<sub>6</sub> capillary): 104.3 ppm (br.s.; 2P, PPh), 70.3 ppm (br.s.; 2P, PPh<sub>2</sub>).

**Synthesis of *cis-α*-[Fe(*rac*-P4)(MeCN)<sub>2</sub>](BF<sub>4</sub>)<sub>2</sub> (**25**)**

Ligand *rac*-P4 (134 mg, 0.2 mmol) was suspended in MeCN (10.0 mL) and the mixture was vigorously stirred until the tetraphosphine turned into a thin powder. One equivalent of [Fe(MeCN)<sub>6</sub>](BF<sub>4</sub>)<sub>2</sub> (95 mg, 0.2 mmol) was added to the white suspension, affording a bright orange solution. The reaction mixture was allowed to stir until a clear solution was obtained, and was subsequently stirred one more hour. The solution was then concentrated under vacuum to remove all volatiles. The resulting orange solid was then dissolved in a minimum volume of acetonitrile (ca. 0.5 mL). Addition of pentane resulted in the precipitation of analytically pure **25** as a crystalline, orange solid. Yield: 170 mg (87%). Crystals of **25** suitable for X-ray diffraction data collection were grown by adding pentane (4.0 mL) to an acetonitrile/methanol solution (0.5 + 1.0 mL) of **25**. <sup>31</sup>P{<sup>1</sup>H} NMR (121.49 MHz, CD<sub>3</sub>CN): 100.7 ppm (t, <sup>2</sup>J<sub>PP</sub> = 31.7 Hz; 2P, PPh), 65.6 ppm (t, <sup>2</sup>J<sub>PP</sub> = 31.7 Hz; 2P, PPh<sub>2</sub>). ESI-MS: calcd. for <sup>12</sup>C<sub>46</sub><sup>1</sup>H<sub>48</sub><sup>14</sup>N<sub>2</sub><sup>56</sup>Fe<sup>31</sup>P<sub>4</sub>, [M]<sup>++</sup>: m/z = 404.10532, found: m/z = 404.10474.

**Reaction of *meso*-P4 with [Fe(MeCN)<sub>6</sub>](BF<sub>4</sub>)<sub>2</sub>**

In an NMR-scale experiment, *meso*-P4 (13 mg, 0.02 mmol) was placed into an NMR tube, to which 0.5 mL of CD<sub>3</sub>CN were added. The NMR tube was shaken vigorously to help dissolution of the ligand and subsequently [Fe(MeCN)<sub>6</sub>](BF<sub>4</sub>)<sub>2</sub> (ca. 10 mg, 0.02 mmol) was added, resulting in immediate color change to red-orange. The reaction mixture was analyzed by <sup>31</sup>P{<sup>1</sup>H} NMR, which showed the formation of

*trans*-[Fe(*meso*-P4)(MeCN)<sub>2</sub>](BF<sub>4</sub>)<sub>2</sub> (*trans*-**25**) and *cis*- $\beta$ -[Fe(*meso*-P4)(MeCN)<sub>2</sub>](BF<sub>4</sub>)<sub>2</sub> (*cis*- $\beta$ -**25**) in approximately 2:1 ratio. <sup>31</sup>P{<sup>1</sup>H} NMR for *trans*-**25**: (121.49 MHz, CD<sub>3</sub>CN): 85.4 ppm (m; 2P, PPh), 75.4 ppm (m; 2P, PPh<sub>2</sub>). <sup>31</sup>P{<sup>1</sup>H} NMR for *cis*- $\beta$ -**25** (121.49 MHz, CD<sub>3</sub>CN): 115.2 ppm (m; 1P), 111.4 ppm (m; 1P), 72.1 ppm (m; 1P), 59.9 ppm (m; 1P).

### Synthesis of [Fe(*rac*-P4)H](BPh<sub>4</sub>) (**26**·BPh<sub>4</sub>)

In a flame-dried Schlenk tube kept under argon, *rac*-P4 (67 mg, 0.1 mmol) was dissolved in 3.0 mL of THF. A stoichiometric amount of anhydrous FeCl<sub>2</sub> (13 mg, 0.1 mmol) was added as a solid, and the resulting deep blue solution was allowed to stir for 5 min. at room temperature. NaBPh<sub>4</sub> (35 mg; 0.01 mmol) and MeOH (1.5 mL) were added to the reaction mixture, which was then stirred vigorously for about 10 min. NaBH<sub>4</sub> (4 mg, 0.1 mmol) was then added to the reaction mixture as a solid, and a vigorous reaction took place, affording an intense red mixture. All volatiles were removed under vacuum and the solid residue was re-dissolved in THF (8.0 mL). The resulting suspension was filtered via cannula into a second Schlenk tube kept under argon, affording a limpid red solution, from which all volatiles were removed under vacuum, affording NMR pure **26**·BPh<sub>4</sub>. Yield: 103 mg (95%). Crystals suitable for X-ray diffraction data collection were obtained by adding MeOH to a THF solution of **26**·BPh<sub>4</sub>. <sup>31</sup>P{<sup>1</sup>H} NMR (*d*<sub>8</sub>-THF, 121.49 MHz): 119.4 ppm (t, <sup>2</sup>J<sub>PP</sub> = 24.5 Hz; 2P, PPh), 99.4 ppm (t, <sup>2</sup>J<sub>PP</sub> = 24.5 Hz; 2P, PPh<sub>2</sub>). <sup>1</sup>H NMR (*d*<sub>8</sub>-THF, 300.13 MHz, negative region): -9.16 ppm (t, <sup>2</sup>J<sub>HP</sub> = 24.0 Hz; 1H, FeH).

### Synthesis of *cis*- $\alpha$ -[Fe(H)<sub>2</sub>(*rac*-P4)] (**27**)

The synthetic procedure described for the synthesis of *trans*-[Fe(*meso*-P4)(H)<sub>2</sub>] was adapted with slight modifications.<sup>11</sup> A three-necked round bottom flask, equipped with reflux condenser was charged under argon with *rac*-P4 (67 mg, 0.1 mmol) and dry THF (2.5 mL). A solution of anhydrous FeCl<sub>2</sub> (13 mg, 0.1 mmol) in THF (2.5 mL) was added via cannula and the resulting mixture was allowed to stir for 10 min. NaBH<sub>4</sub> (20 mg, 0.55 mmol) was added as a solid, and the dark blue reaction mixture obtained was heated to reflux. As no visible changes occurred, additional THF (3.0 mL) was added, followed by another aliquot of NaBH<sub>4</sub> (10 mg, 0.27 mmol) and

absolute EtOH (0.5 mL). As EtOH was added, a vigorous reaction took place and the deep blue mixture turned orange. After gas evolution had ceased, additional NaBH<sub>4</sub> (10 mg, 0.27 mmol) and absolute EtOH (0.5 mL) were added, and again, gas evolution was observed. The orange mixture was refluxed for about 10 min after gas evolution had ceased, after which it was allowed to cool to room temperature and filtered via cannula. The volume of the solution was partly reduced under vacuum and dry methanol was subsequently layered on top of the orange solution, from which bright yellow crystals formed. Yield: 53 mg (72 %). <sup>31</sup>P{<sup>1</sup>H} NMR (*d*<sub>8</sub>-THF, 121.49 MHz): 123.8 ppm (t, <sup>2</sup>J<sub>PP</sub> = 13.5 Hz; 2P, PPh), 113.1 ppm (t, <sup>2</sup>J<sub>PP</sub> = 13.5; 2P, PPh<sub>2</sub>). <sup>1</sup>H NMR (*d*<sub>8</sub>-THF, 300.13 MHz, negative region): -11.7 ppm (m; 2H, Fe(H)<sub>2</sub>). ESI-MS: calcd. for <sup>12</sup>C<sub>42</sub><sup>1</sup>H<sub>43</sub><sup>56</sup>Fe<sup>31</sup>P<sub>4</sub>, [M-H]<sup>+</sup>: m/z = 727.16592, found: m/z = 727.16523.

#### Reaction of 26·BPh<sub>4</sub> with CO<sub>2</sub>

A few crystals of 26·BPh<sub>4</sub> (ca. 10 mg) were placed in an NMR tube under argon and dissolved in *d*<sub>8</sub>-THF (0.5 mL). CO<sub>2</sub> (1 atm) was then bubbled through the solution, whose color turned light purple. NMR analysis revealed quantitative formation of the expected formate complex [Fe(*rac*-P4)(η<sup>2</sup>-OCHO)](BPh<sub>4</sub>) (29·BPh<sub>4</sub>). <sup>31</sup>P{<sup>1</sup>H} NMR for 29·BPh<sub>4</sub> (*d*<sub>8</sub>-THF, 161.99 MHz): 106.0 ppm (t, <sup>2</sup>J<sub>PP</sub> = 28.5 Hz; 2P, PPh), 76.5 ppm (t, <sup>2</sup>J<sub>PP</sub> = 26.1 Hz; 2P, PPh<sub>2</sub>). <sup>13</sup>C{<sup>1</sup>H} NMR for 29·BPh<sub>4</sub> (*d*<sub>8</sub>-THF, 100.6 MHz): 162.4 ppm (dd; <sup>2</sup>J<sub>PP</sub> = 49.4 Hz, <sup>2</sup>J<sub>PP</sub> = 98.7 Hz, BPh<sub>4</sub>), 171.9 ppm [br. s., Fe(O<sub>2</sub>CH)]. After 24h acquisition, the <sup>31</sup>P{<sup>1</sup>H} NMR spectrum revealed the formation of carbonate complex [Fe(η<sup>2</sup>-O<sub>2</sub>CO)(*rac*-P4)] (30). Based on <sup>31</sup>P{<sup>1</sup>H} NMR integration, complexes 28 and 30 resulted in approximately 1:0.6 ratio. <sup>31</sup>P{<sup>1</sup>H} NMR for 30 (*d*<sub>8</sub>-THF, 161.99 MHz): 104.7 ppm (t, <sup>2</sup>J<sub>PP</sub> = 30.4 Hz; 2P, PPh), 71.3 ppm (t, <sup>2</sup>J<sub>PP</sub> = 30.4 Hz; 2P, PPh<sub>2</sub>). No <sup>13</sup>C{<sup>1</sup>H} NMR resonance was observed for the carbonate O<sub>2</sub>CO carbon atom of 30.

The experiment was repeated using 26·BF<sub>4</sub> and <sup>13</sup>CO<sub>2</sub>, showing identical <sup>31</sup>P{<sup>1</sup>H} NMR and <sup>13</sup>C NMR (proton coupled) signals at 174.5 (d, <sup>1</sup>J<sub>CH</sub> = 208.8 Hz) and 158.1 ppm (s) for 29 and 30, respectively.

Few purple crystals suitable for X-ray diffraction data collection were obtained by layering MeOH on top of the *d*<sub>8</sub>-THF solution and standing for 1 day. The X-ray

crystal structure revealed the serendipitous formation of trimetallic complex  $\{\mu^2\text{-}[\text{Fe}(\text{MeOH})]\text{-k}^1\text{-O-}[\text{Fe}(\eta^2\text{-O}_2\text{CO})(\text{rac-P4})]_2\}(\text{BPh}_4)_2$  (**31'**).

### Reaction of **24** with $\text{K}_2\text{CO}_3$

0.5 mL of a 0.01 M stock solution of **24** in PC were placed in a 5 mm NMR tube under argon. Solid  $\text{K}_2\text{CO}_3$  (7.0 mg, 0.05 mmol) was then added. The solution in the NMR tube was stirred with a small stirring bar and the purple solution turned initially bright pink and then bright red.  $d_8$ -toluene (0.2 mL) was added for deuterium lock and the red solution was analyzed by  $^{31}\text{P}\{^1\text{H}\}$  NMR and  $^{13}\text{C}\{^1\text{H}\}$  NMR.  $^{31}\text{P}\{^1\text{H}\}$  NMR analysis showed the quantitative formation of carbonate complex **30**, whereas no  $^{13}\text{C}\{^1\text{H}\}$  NMR resonance was observed for the carboxylic  $\text{O}_2\text{CO}$  carbon of **30**.  $^{31}\text{P}\{^1\text{H}\}$  NMR for **30** (PC +  $d_8$ -toluene, 121.49 MHz): 104.7 ppm (t,  $^2J_{\text{PP}} = 30.4$  Hz; 2P, PPh), 71.3 ppm (t,  $^2J_{\text{PP}} = 30.4$  Hz; 2P, PPh<sub>2</sub>).

### Reaction of **24** with FA under HPNMR conditions and formation of *cis-α*- $[\text{FeH}(\text{CO})(\text{rac-P4})](\text{BF}_4)$ (**31**)

A 10 mm HPNMR sapphire tube was charged with a solution of  $\text{Fe}(\text{BF}_4)_2 \cdot 6\text{H}_2\text{O}$  (14 mg; 0.04 mmol) and *rac*-P4 (28 mg; 0.04 mmol) in propylene carbonate (1.8 mL) under argon.  $\text{CD}_3\text{OD}$  (0.4 mL) was then added for deuterium lock, followed by  $\text{HCOOH}$  (0.15 mL, 4.15 mmol; 100 equiv. to Fe). The tube was closed and placed in the NMR probe. The probehead was gradually heated to 60 °C and the reaction was monitored by  $^{31}\text{P}\{^1\text{H}\}$  NMR (see Appendix). The tube was left at 60 °C overnight, resulting in a yellow solution.  $^{31}\text{P}\{^1\text{H}\}$  and  $^1\text{H}$  NMR analysis revealed the quantitative formation of *cis-α*- $[\text{Fe}(\text{H})(\text{CO})(\text{rac-P4})](\text{BF}_4)$  (**31**).  $^{31}\text{P}\{^1\text{H}\}$  NMR (121.49 MHz,  $\text{CD}_3\text{OD}$ ):  $\delta$  114.6 (dt,  $^2J_{\text{PP}} = 23.5$ ,  $^2J_{\text{PP}} = 38.6$ , 1P), 105.1 (br.dd.,  $^2J_{\text{PP}} = 8.6$ ,  $^2J_{\text{PP}} = 21.9$ ; 1P), 100.9 (ddd,  $^2J_{\text{PP}} = 10.5$ ,  $^2J_{\text{PP}} = 39.3$ ,  $^2J_{\text{PP}} = 68.7$ ; 1P), 92.3 (dd,  $^2J_{\text{PP}} = 37.9$ ,  $^2J_{\text{PP}} = 68.5$ ; 1P).  $^1\text{H}$  NMR (300.13 MHz,  $\text{CD}_3\text{OD}$ , negative region):  $\delta$  -9.6 (ddd,  $^2J_{\text{PP}} = 25.5$ ,  $^2J_{\text{PP}} = 46.5$ ,  $^2J_{\text{PP}} = 70.7$ ; 1H, FeH).  $^{13}\text{C}\{^1\text{H}\}$  NMR (75.47 MHz,  $\text{CD}_3\text{OD}$ , carbonyl region):  $\delta$  162.77 (s; CO). A sharp singlet of higher intensity was also observed at  $\delta$  162.1 ppm for  $\text{HCOOH}$ . ESI-MS: calcd. for  $^{12}\text{C}_{43}^{1}\text{H}_{43}^{56}\text{Fe}^{16}\text{O}^{31}\text{P}_4$  [M]<sup>+</sup>:  $m/z = 753.16550$ , found:  $m/z = 753.16517$ .

### 4.10.3 Catalytic tests

#### Catalytic formic acid dehydrogenation tests

In a typical experiment, a solution of catalyst (typically 5.3 mmol) in propylene carbonate (5 mL) is placed under an argon atmosphere in a magnetically stirred glass reaction vessel thermostated by external liquid circulation and connected to a reflux condenser and gas-burette (2 mL scale). After heating to 40-60 °C, HCOOH (2.0 mL) is added and the experiment started. The gas evolution is monitored throughout the experiment by reading the values reached on the burettes. The gas mixture is analyzed off-line by FTIR spectroscopy using a 10 cm gas-phase cell (KBr windows) to check for CO formation (detection limit 0.02%).

#### Catalytic sodium bicarbonate hydrogenation tests

In a typical experiment, a 40 mL magnetically stirred stainless steel autoclave built CNR-ICCOM is charged under inert atmosphere (glovebox) with NaHCO<sub>3</sub> (typically 840 mg, 10 mmol) and the catalyst (0.01–0.001 mmol as solid or stock solution in PC). The autoclave is then closed and thoroughly purged through several vacuum/argon cycles. MeOH (20.0 mL) is then added to the autoclave by suction. Finally the autoclave is pressurized with H<sub>2</sub> gas at the desired pressure. The autoclave is then placed into an oil bath pre-heated to the desired temperature and left stirring for the set reaction time. After the run, the autoclave is cooled in an ice/water bath, de-pressurized, and the catalytic mixture is transferred to a flask and concentrated under vacuum at room temperature. The formate content is determined by analyzing aliquots (ca. 30 mg) of the solid mixture dissolved in D<sub>2</sub>O (0.5 mL) by <sup>1</sup>H NMR, using dry THF (20 μL) as internal standard with a relaxation delay of 20 seconds.

## 4.11 References

- 
- <sup>1</sup> Boddien, A.; Mellmann, D.; Gärtner, F.; Jackstell, R.; Junge, H.; Dyson, P. J.; Laurenczy, G.; Ludwig, R.; Beller, M. *Science* **2011**, *333*, 1733-1736.
  - <sup>2</sup> The iron catalyzed decomposition of formic acid by [Fe(PP<sub>3</sub>)H(η<sup>2</sup>-H<sub>2</sub>)]BPh<sub>4</sub> was briereported in earlier literature, see: Bianchini, C.; Peruzzini, M.; Polo, A.; Vacca, A.;

- Zanobini, F. *Gazz. Chim. It.* **1991**, 121, 543 – 549. Another highly active Fe-pincer based system, however needing Lewis acids and higher temperatures (80 °C) to reach TON = 106, was reported very recently, see: Bielinski, E. A.; Lagaditis, P. O.; Zhang, Y.; Mercado, B. Q.; Wrtele, C.; Bernskoetter, W. H.; Hazari, N.; Schneider, S. *J. Am. Chem. Soc.* **2014**, 136, 10234–10237.
- <sup>3</sup> Federsel, C.; Boddien, A.; Jackstell, R.; Jennerjahn, R.; Dyson, P. J.; Scopelliti, R.; Laurency, G.; Beller, M. *Angew. Chem. Int. Ed.* **2010**, 49, 9777–9780.
- <sup>4</sup> Ziebart, C.; Federsel, C.; Anbarasan, P.; Jackstell, R.; Baumann, W.; Spannenberg, A.; Beller, M. *J. Am. Chem. Soc.* **2012**, 134, 20701–20704.
- <sup>5</sup> These hydrides were originally described by: Bianchini, C.; Laschi, F.; Peruzzini, M.; Ottaviani, M. F.; Vacca, A.; Zanello, P. *Inorg. Chem.* **1990**, 29, 3394–3402.
- <sup>6</sup> (a) Mellone, I.; Peruzzini, M.; Rosi, L.; Mellmann, D.; Junge, H.; Beller, M.; Gonsalvi, L. *Dalton Trans.* **2013**, 42, 2495–2501; (b) Manca, G.; Mellone, I.; Bertini, F.; Peruzzini, M.; Rosi, L.; Mellmann, D.; Junge, H.; Beller, M.; Ienco, A.; Gonsalvi, L. *Organometallics* **2013**, 32, 7053–7064; (c) Bosquain, S. S.; Dorcier, A.; Dyson, P. J.; Erlandsson, M.; Gonsalvi, L.; Laurency, G.; Peruzzini, M. *Appl. Organomet. Chem.* **2007**, 21, 947–951.
- <sup>7</sup> Erlandsson, M.; Landaeta, V. R.; Gonsalvi, L.; Peruzzini, M.; Phillips, A. D.; Dyson, P. J.; Laurency, G. *Eur. J. Inorg. Chem.* **2008**, 4, 620–627.
- <sup>8</sup> Brown, J. M.; Canning, L. R. *J. Organomet. Chem.* **1984**, 267, 179–190.
- <sup>9</sup> Bautista, M. T.; Earl, K. A.; Maltby, P. A.; Morris, R. H.; Schweitzer, C. T. *Can. J. Chem.* **1994**, 72, 547–560.
- <sup>10</sup> King, R. B.; Heckley, P. R.; Cloyd, J. C. Jr.; *Z. Naturforsch. B.* **1974**, 296, 574–575.
- <sup>11</sup> Bautista, M. T.; Earl, K. A.; Maltby, P. A.; Morris, R. H. *J. Am. Chem. Soc.* **1988**, 110, 4056–4057.
- <sup>12</sup> King, R. B.; Kapoor, P. N. *J. Am. Chem. Soc.* **1969**, 91, 5191.
- <sup>13</sup> (a) King, R. B.; Kapoor, R. N.; Saran, M. S.; Kapoor, P. N. *Inorg. Chem.* **1971**, 10, 1851–1860; (b) King, R. B.; Kapoor, P. N. *J. Am. Chem. Soc.* **1971**, 93, 4112–4119, 4158–4166; (c) Ghilardi, C. A.; Midollini, S.; Stoppioni, P.; Sacconi, L. *Inorg. Chem.* **1973**, 12, 1801–1805; (d) Bacci, M.; Ghilardi, C. A., *Inorg. Chem.* **1974**, 13, 2398–2403; (e) Ghilardi, C. A.; Midollini, S.; Sacconi, L.; Stoppioni, P. *J. Organomet. Chem.* **1981**, 205, 193–202; (f) Bacci, M.; Ghilardi, C. A.; Orlandini, A. *Inorg. Chem.* **1984**, 23, 2798–2802; (g) Brown, J. M.; Canning, L. R. *J. Organomet. Chem.* **1984**, 267, 179–190; (h) Rivera, V. A.; De Gil, E. R.; Fontal, B. *Inorg. Chim. Acta* **1985**, 98, 153–159; (i) Brüggeller, P. *Inorg. Chem.* **1990**, 29, 1742–1750; (j) Goller, H.; Brüggeller, P. *Inorg. Chim. Acta*, **1992**, 197, 75–81; (k) Chen, J.-D.; Cotton, F. A.; Hong, B. *Inorg. Chem.* **1993**, 32, 2343–2353; (l) Cotton, F. A.; Hang, B.; Shang, M.; Stanley, G. G. *Inorg. Chem.* **1993**, 32, 3620–3627; (m) Chen, J.-D.; Cotton, F. A.; Hong, B. *Inorg. Chem.* **1993**, 32, 2343–2353; (n) Jia, G.; Lough, A. J.; Morris, R. H. *J. Organomet. Chem.* **1993**, 461, 147–156; (o) Dillinger, K.; Oberhauser, W.; Bachmann, C.; Brüggeller, P. *Inorg. Chim. Acta* **1994**, 223, 13–20; (p) Airey, A. L.; Swiegers, G. F.; Willis, A. C.; Wild, S. B. *J. Chem. Soc., Chem. Commun.* **1995**, 693–694; (q) Oberhauser, W.; Bachmann, C.; Brüggeller, P. *Polyhedron* **1995**, 14, 787–792; (r) Oberhauser, W.; Bachmann, C.; Brüggeller, P. *Polyhedron* **1996**, 15, 2223–2230.
- <sup>14</sup> (a) Hathaway, B. J.; Holah, D. G.; Underhill, A. E. *J. Chem. Soc.* **1962**, 2444–2448; (b) Heintz, R. A.; Smith, J. A.; Szalav, P. S.; Weisgerber, A.; Dunbar, K. R. *Inorg. Synth.* **2004**, 33, 75–78.
- <sup>15</sup> Beck, W.; Sünkel, K. *Chem. Rev.* **1988**, 88, 1405–1421.
- <sup>16</sup> Mellmann, D.; Barsch, E.; Bauer, M.; Grabow, K.; Boddien, A.; Kammer, A.; Sponholz, P.; Bentrup, U.; Jackstell, R.; Junge, H.; Laurency, G.; Ludwig, R.; Beller, M. *Chem. Eur. J.* **2014**, 20, 13589–13602.

- 
- <sup>17</sup> Habeck, C. M.; Hoberg, C.; Peters, G.; Näther, C.; Tucek, F. *Organometallics* **2004**, *23*, 3252–3258.
- <sup>18</sup> It was shown that heterolytic hydrogen splitting to give metal hydrides can occur even without the need for added base. See for example: (a) Kubas, G. J. *Adv. Inorg. Chem.* **2004**, *56*, 127–178; (b) Schlaf, M.; Lough, A. J.; Maltby, P. A.; Morris, R. H. *Organometallics* **1996**, *15*, 2270–2278.
- <sup>19</sup> Field, D. L.; Lawrence, E. T.; Shaw, W. J.; Turner, P. *Inorg. Chem.* **2000**, *39*, 5632–5638.
- <sup>20</sup> (a) Allen, O. R.; Dalgarno, S. J.; Field, L. D. *Organometallics* **2008**, *27*, 3328–3330; (b) Allen, O. R.; Dalgarno, S. J.; Field, L. D.; Jensen, P.; Willis, A. D. *Organometallics* **2008**, *27*, 2092–2098.
- <sup>21</sup> For other examples on the reductive disproportionation of CO<sub>2</sub> catalyzed by iron complexes, see: (a) Antberg, M.; Frosin, K.-M.; Dahlenburg, L. *J. Organomet. Chem.* **1988**, *338*, 319–327; (b) Sadique, A. R.; Brennessel, W. W.; Holland, P. L. *Inorg. Chem.* **2008**, *47*, 784–786.
- <sup>22</sup> Gas mixtures analyses were carried out by FTIR spectroscopic method described in previous publications. For details see: (a) Morris, D. J.; Clarkson, G. J.; Wills, M. *Organometallics* **2009**, *28*, 4133–4140; (b) Guerriero, A.; Bricout, H.; Sordakis, K.; Peruzzini, M.; Monflier, E. Hapiot, F.; Laurencyzy, G.; Gonsalvi, L. *ACS Catal.* **2014**, *4*, 3002–3012.
- <sup>23</sup> As the <sup>31</sup>P{<sup>1</sup>H}AA'XX' pattern of **8** does not allow to discriminate between Oh and TBP geometries, we tentatively propose that the corresponding signals may be due to the formation of either *cis*-α-[Fe(η<sup>1</sup>-O<sub>2</sub>COH)<sub>2</sub>(rac-P4)] or *cis*-α-[Fe(η<sup>2</sup>-O<sub>2</sub>COH)(rac-P4)]<sup>+</sup>.
- <sup>24</sup> Complex **30** was generated in solution by reaction of **24** with K<sub>2</sub>CO<sub>3</sub> in PC/CD<sub>3</sub>OD (3:1), then reacted with H<sub>2</sub> (30 bar) under HPNMR conditions. Slow conversion to **26**·BF<sub>4</sub> was observed to occur upon heating and standing at 60 °C.

# Appendix

## 1. Appendix to Chapter 2

Variable temperature NMR experiments

## 2. Appendix to Chapter 4

NMR characterization of *cis-α*-[Fe( $\eta^2$ -O<sub>2</sub>CH)(*rac*-P4)](BPh<sub>4</sub>) (**29**·BPh<sub>4</sub>)

HPNMR studies

X-ray Crystal structure determinations

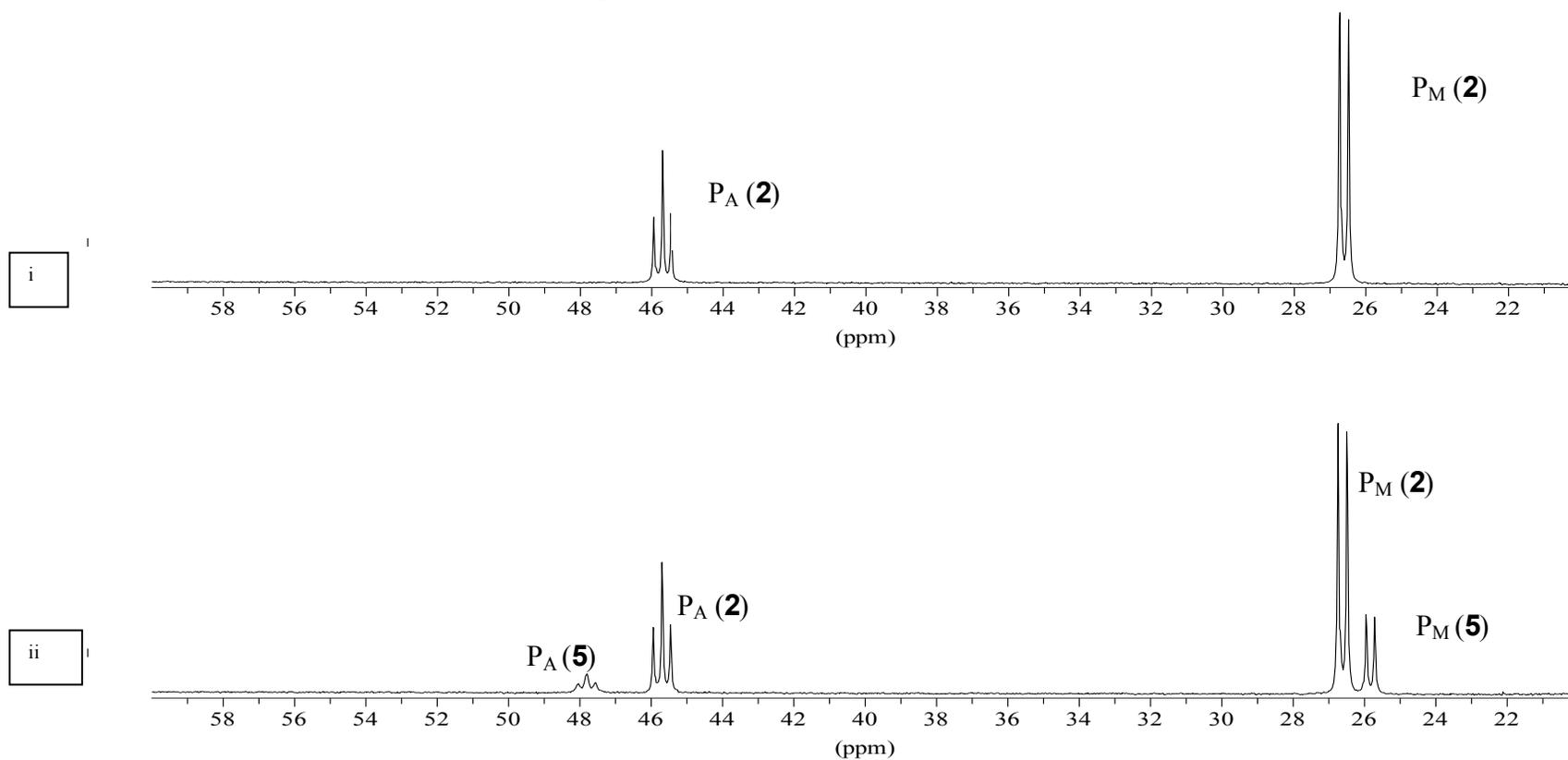
## 3. References



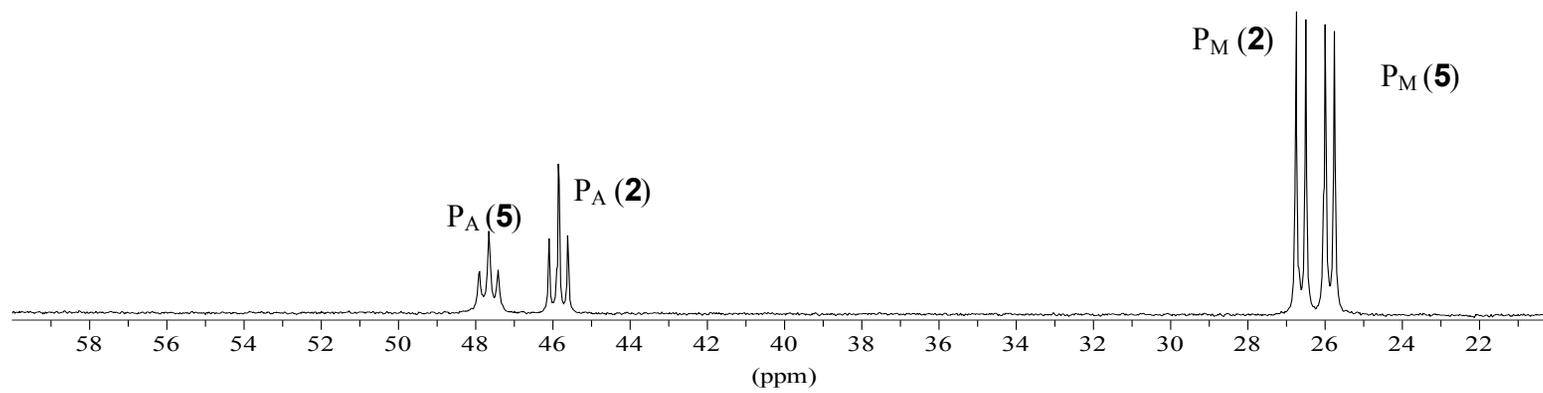
## 1. Appendix to Chapter 2

### Variable temperature NMR experiments

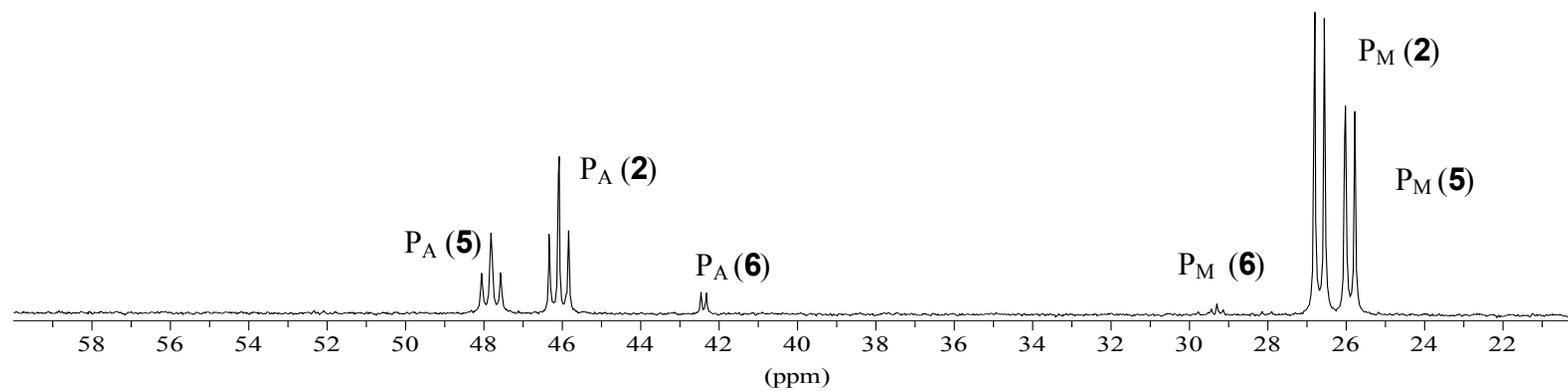
**Figure A1.** Variable temperature  $^{31}\text{P}\{^1\text{H}\}$  NMR spectra of the reaction between **2** and  $\text{HCO}_2\text{NHET}_3$ . All the octahedral  $\text{Ru}(\text{NP}_3)$  complexes exhibit a first order  $\text{AM}_2$  spin system. i) **2**, 233 K; ii) **2** + 1 equiv.  $\text{HCO}_2\text{NHET}_3$ , 233 K; iii) as ii, 253 K; (iv) as ii, 273 K; v) as ii, 283 K; vi) as ii, 293 K; vii) as ii, 273 K; viii) as ii, 233 K; ix) as ii, 213 K; x) addition of 1 equiv.  $\text{HCO}_2\text{NHET}_3$ , 233 K; xi) as x, 293 K; xii) as x, 233 K; xiii) addition of 5 equiv.  $\text{HCO}_2\text{H}$ , 233 K; xiv) as xiii, 293 K.

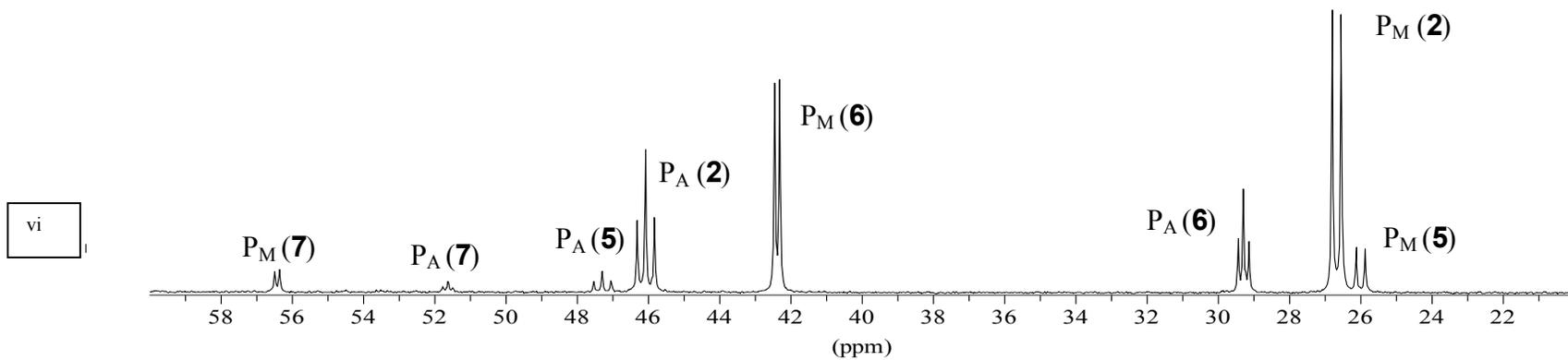
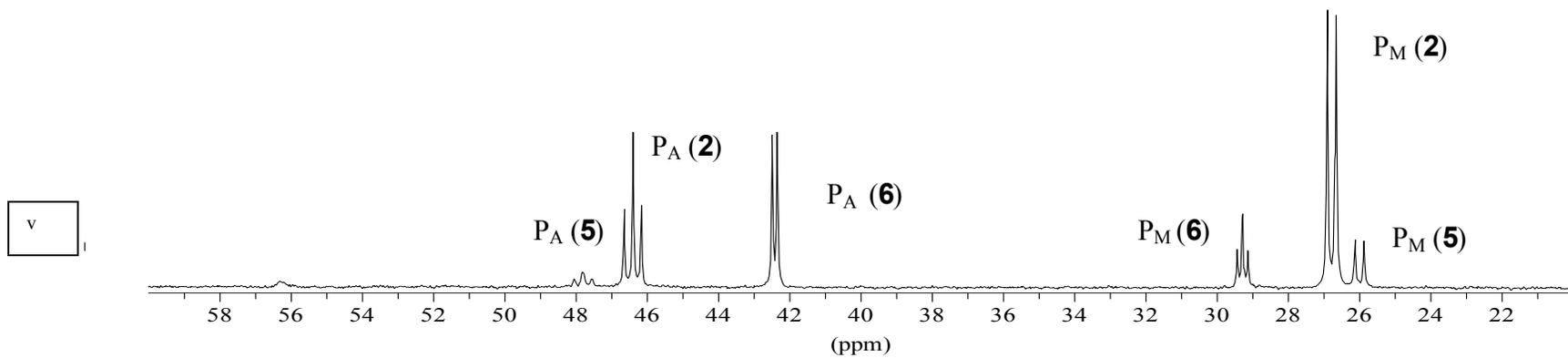


iii

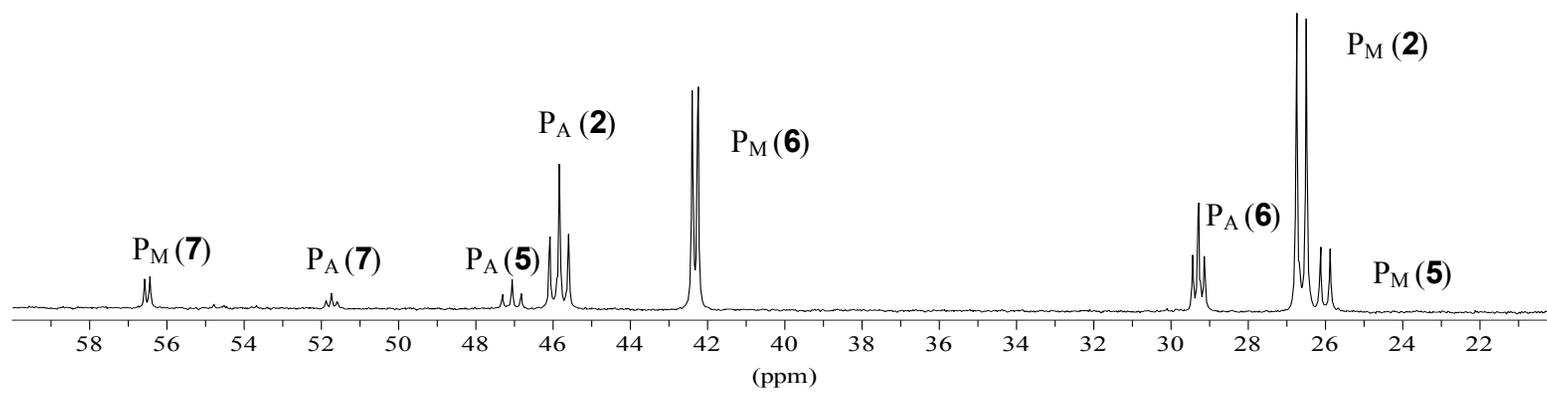


iv

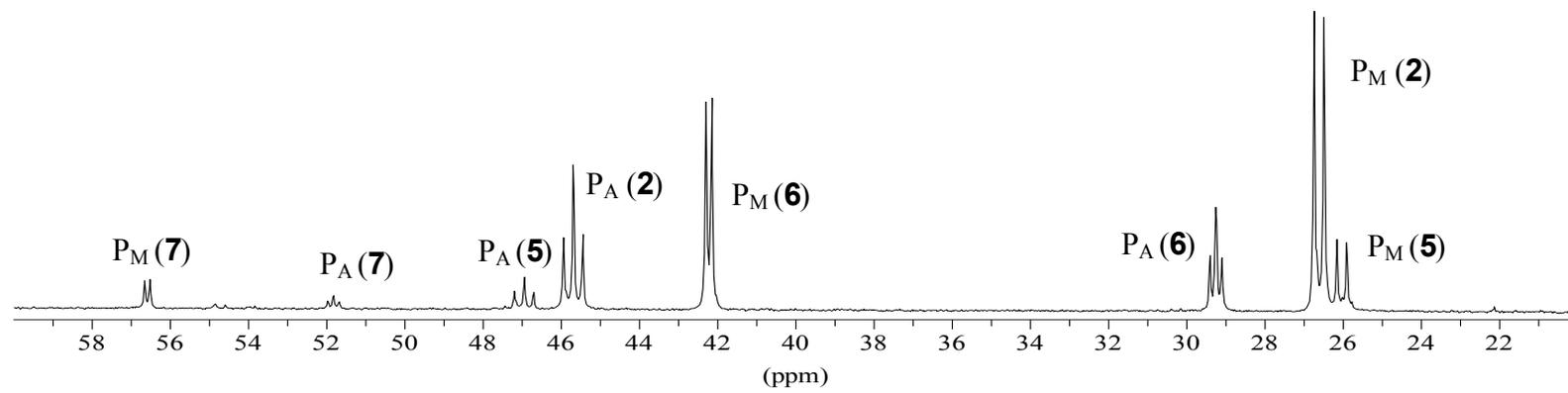




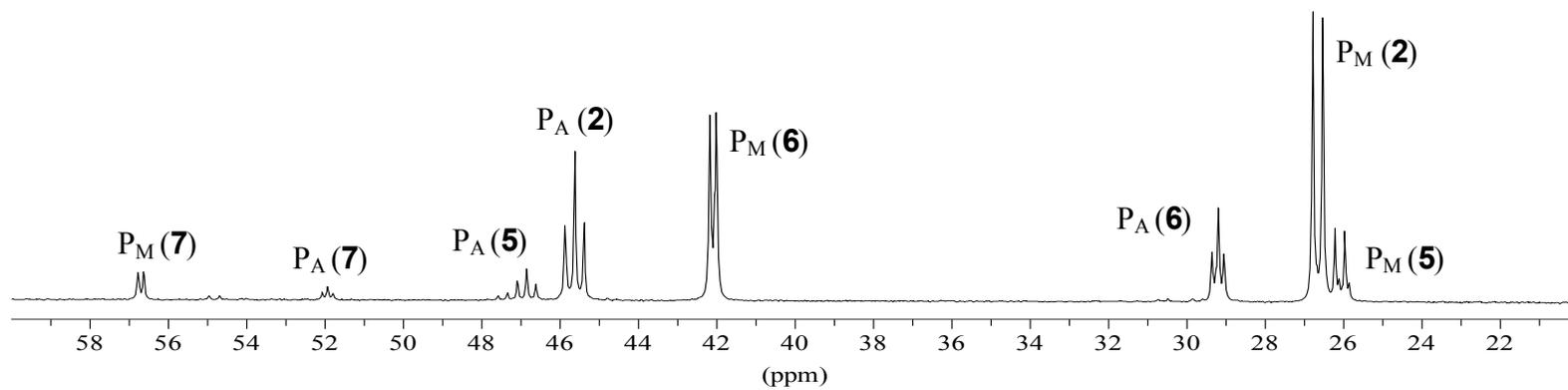
vii



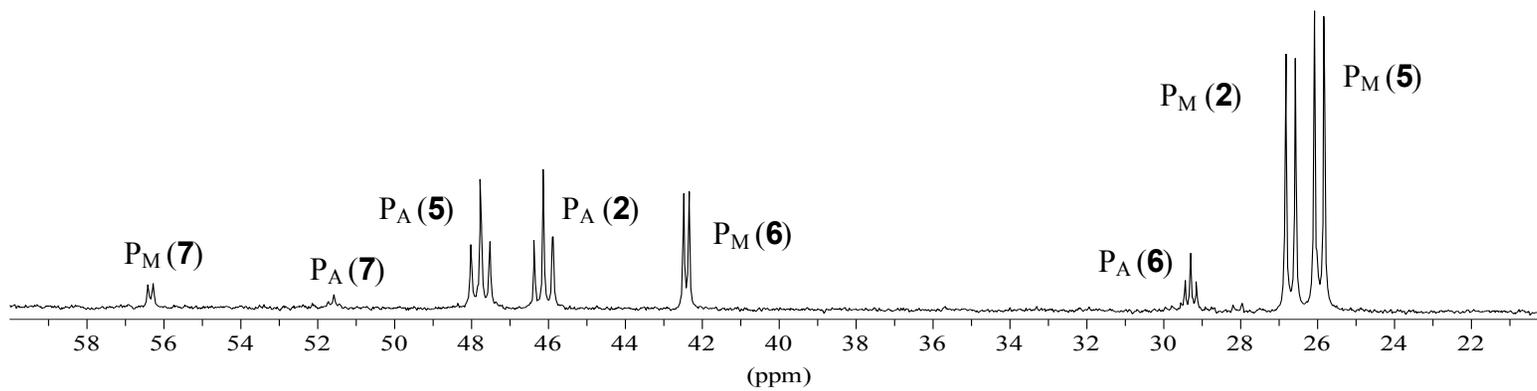
viii



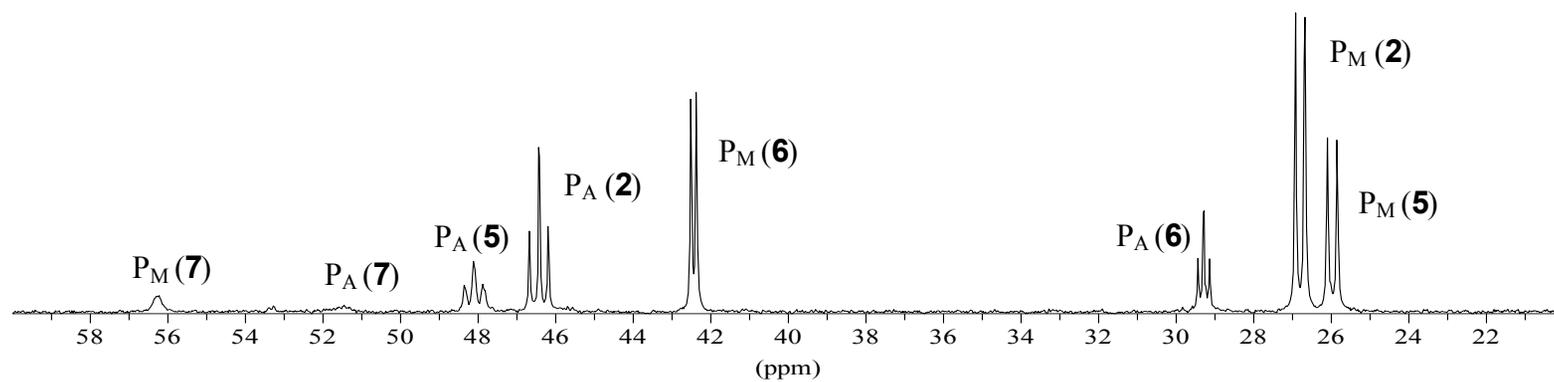
ix



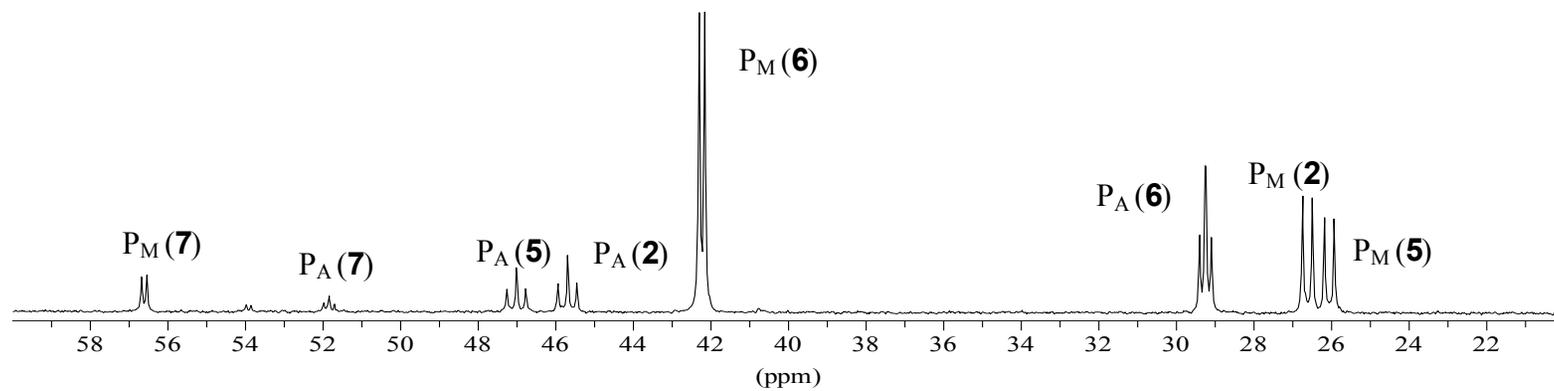
x



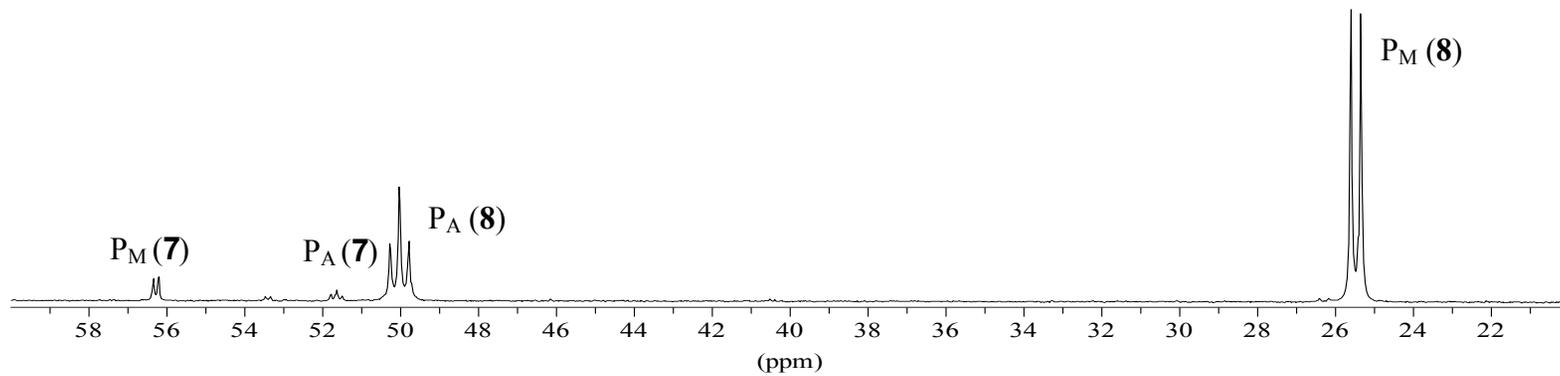
xi



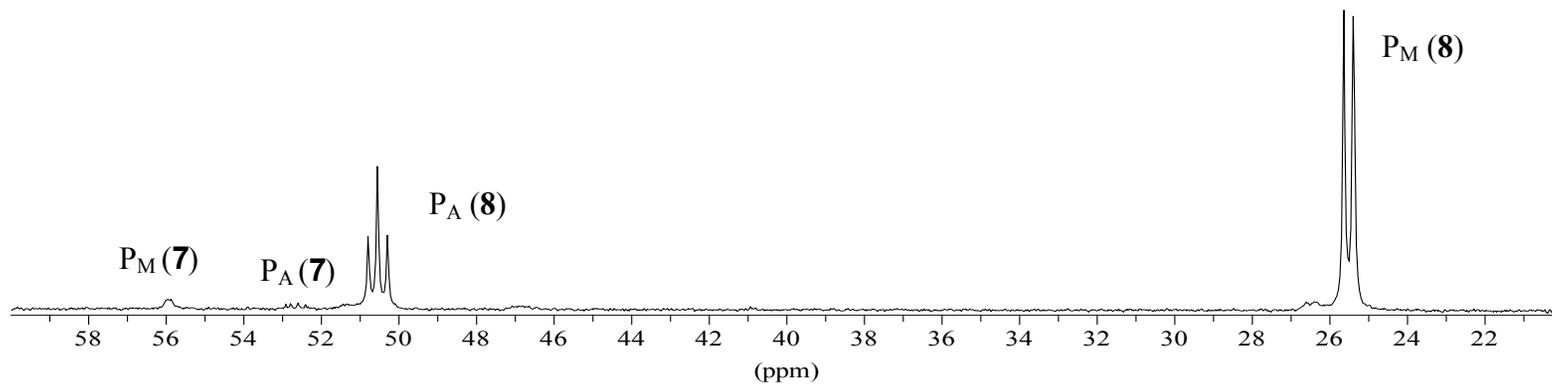
xii



xiii



xiv



## 2. Appendix to Chapter 4

### NMR characterization of *cis-α*-[Fe( $\eta^2$ -O<sub>2</sub>CH)(*rac*-P4)](BPh<sub>4</sub>) (**29**·BPh<sub>4</sub>)

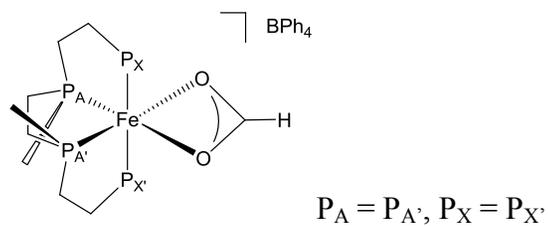


**Figure A2.** <sup>31</sup>P NMR of **29**·BPh<sub>4</sub> obtained from **26**·BPh<sub>4</sub> upon reaction with carbon dioxide (*d*<sub>8</sub>-THF, 75.47 MHz, 298K).

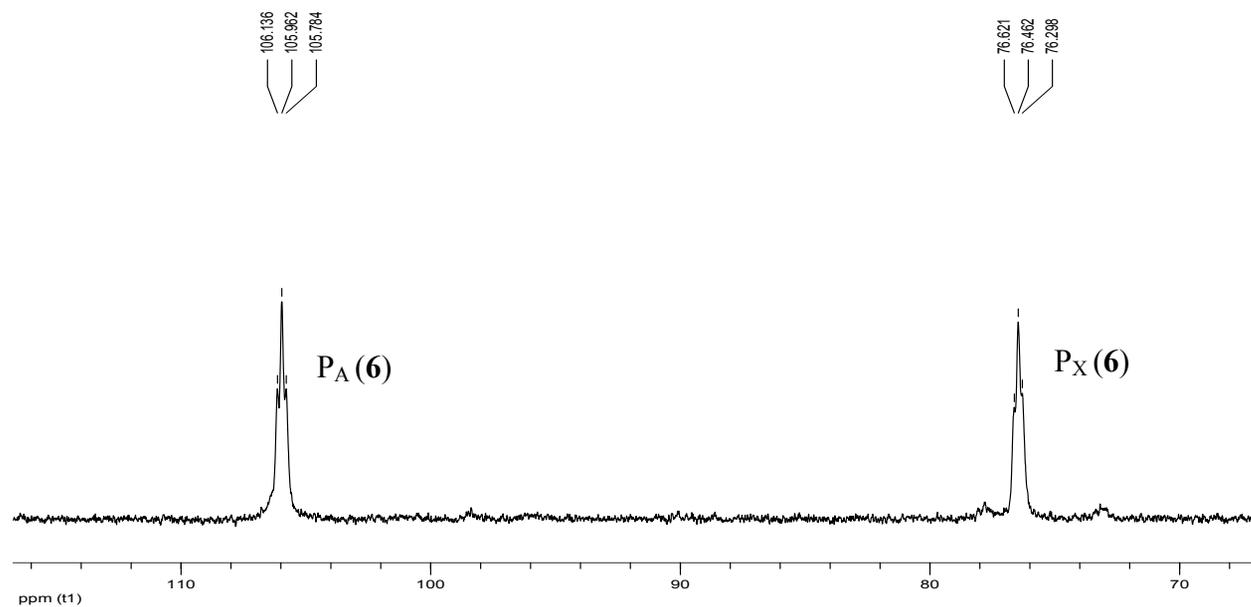


**Figure A3.**  $^{13}\text{C}$  NMR of  $29\cdot\text{BPh}_4$  obtained from  $26\cdot\text{BPh}_4$  upon reaction with carbon dioxide ( $d_8$ -THF, 75.47 MHz, 298K).

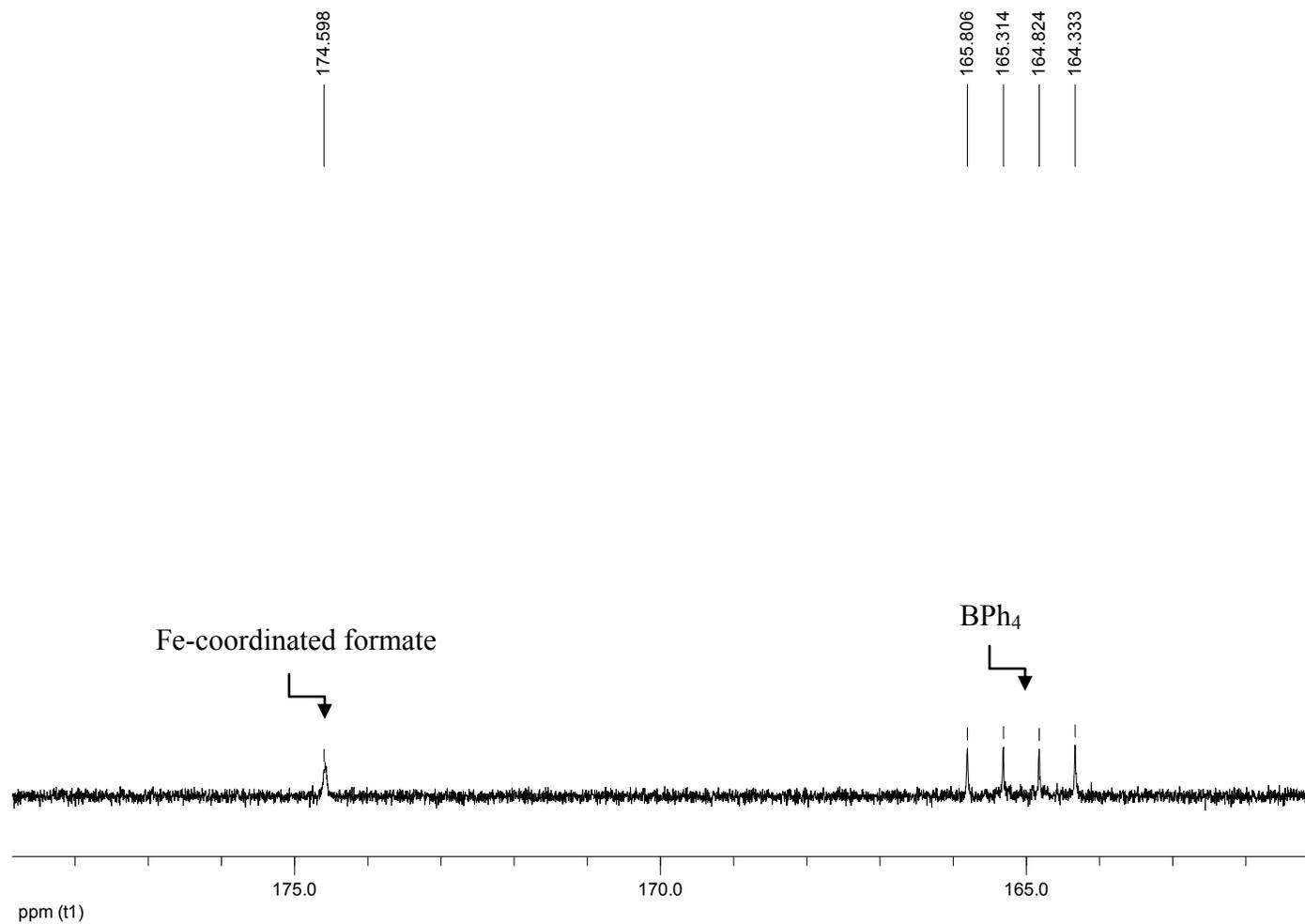


**Figure A4.**  $^{31}\text{P}$  NMR of a mixture of **6**·BPh<sub>4</sub> and **7** obtained from **3**·BPh<sub>4</sub> upon reaction with carbon dioxide after standing for 24h (*d*<sub>8</sub>-THF, 75.47 MHz, 298K).

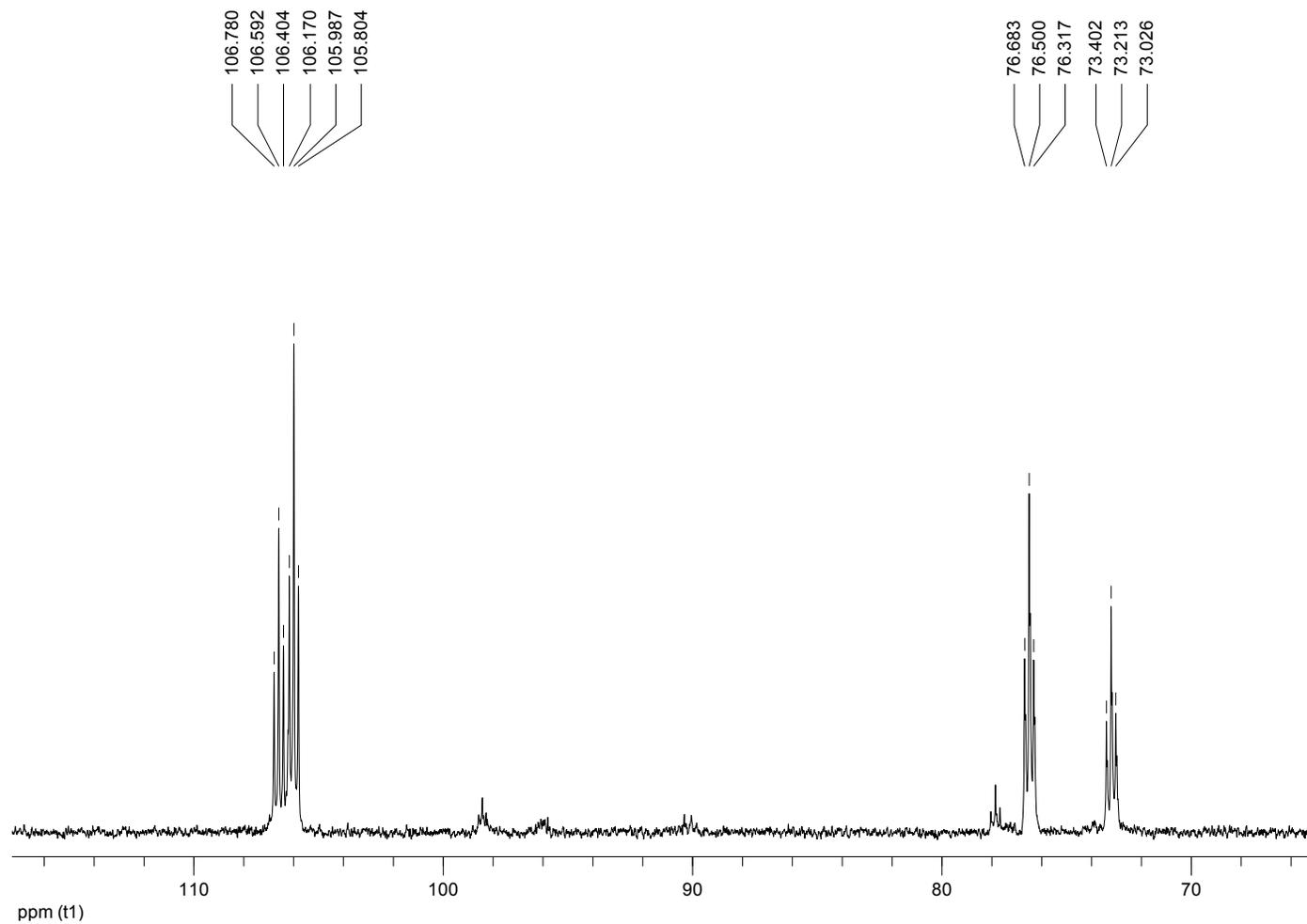
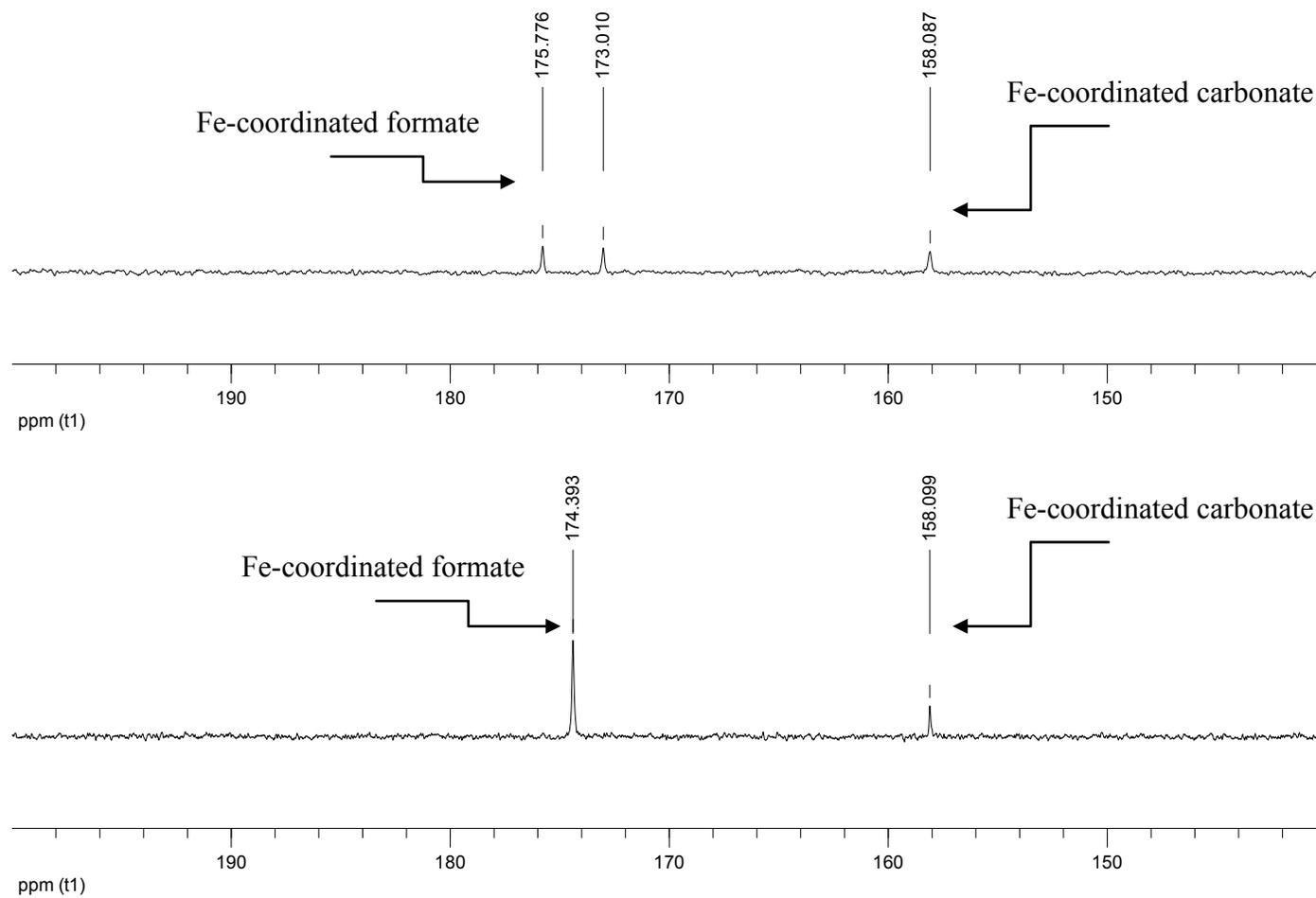


**Figure A5.**  $^{13}\text{C}$  NMR (top) and  $^{13}\text{C}\{^1\text{H}\}$  NMR (bottom) of a mixture of  $6\cdot\text{BF}_4$  and **7** obtained from  $3\cdot\text{BF}_4$  upon reaction with  $^{13}\text{C}$ -labelled carbon dioxide ( $d_8$ -THF, 75.47 MHz, 298K).

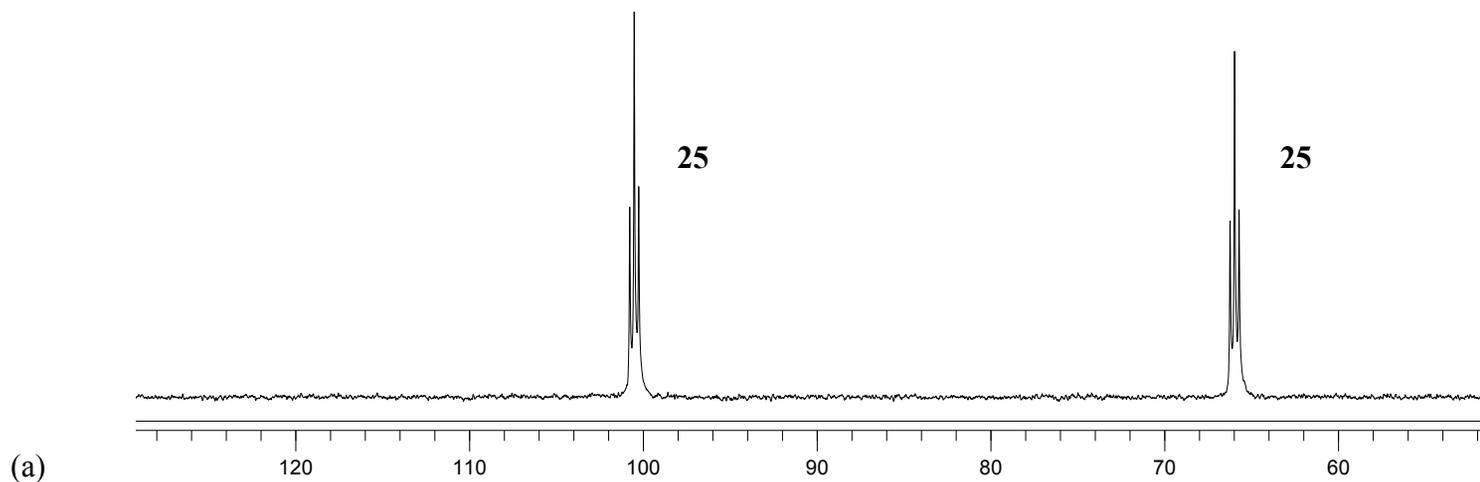


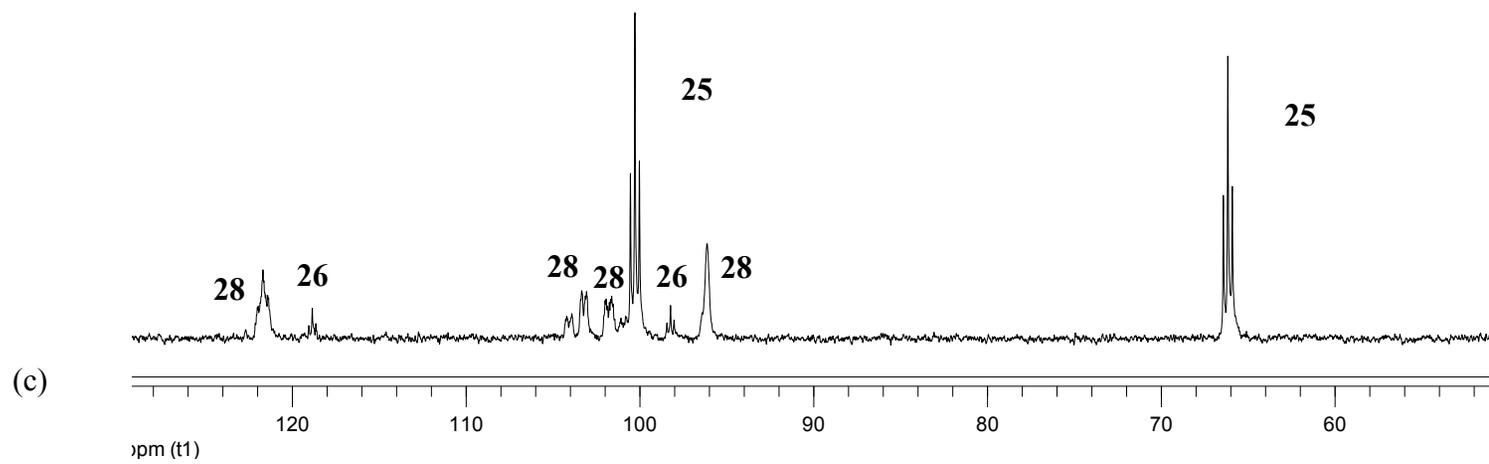
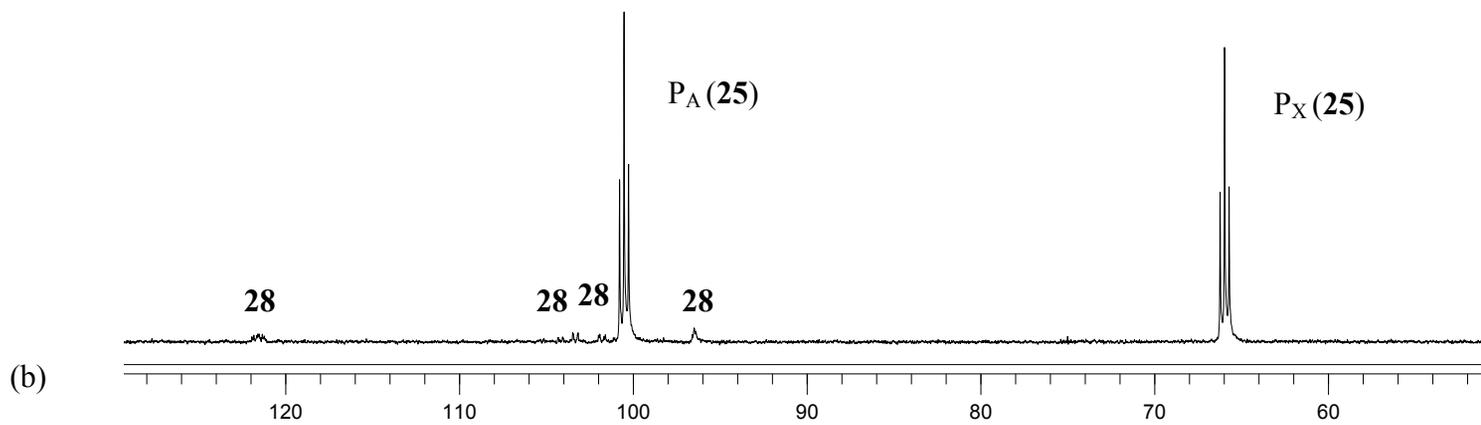
## HPNMR studies

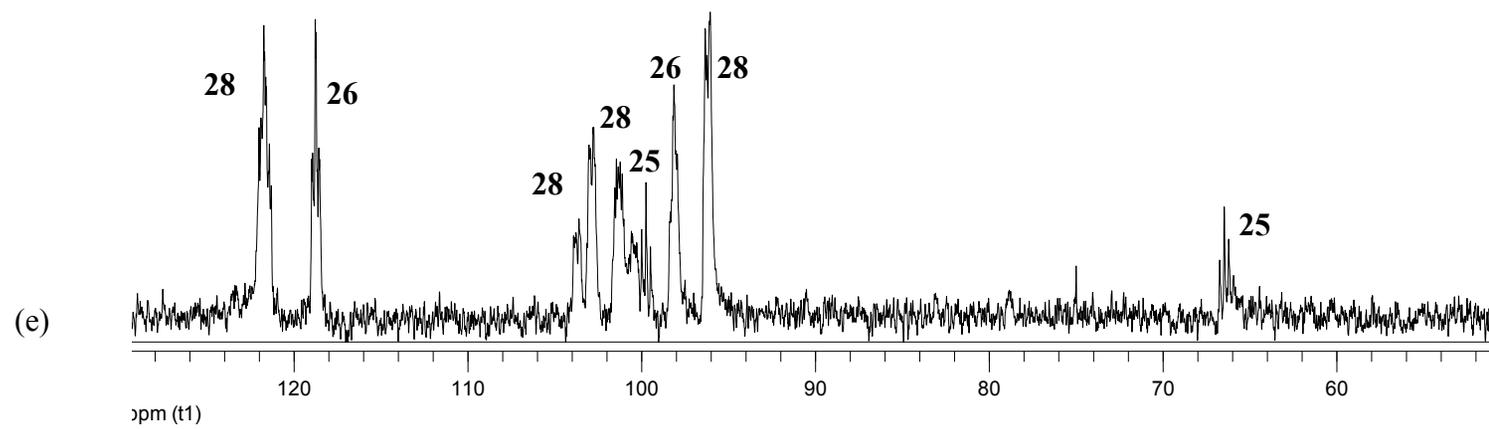
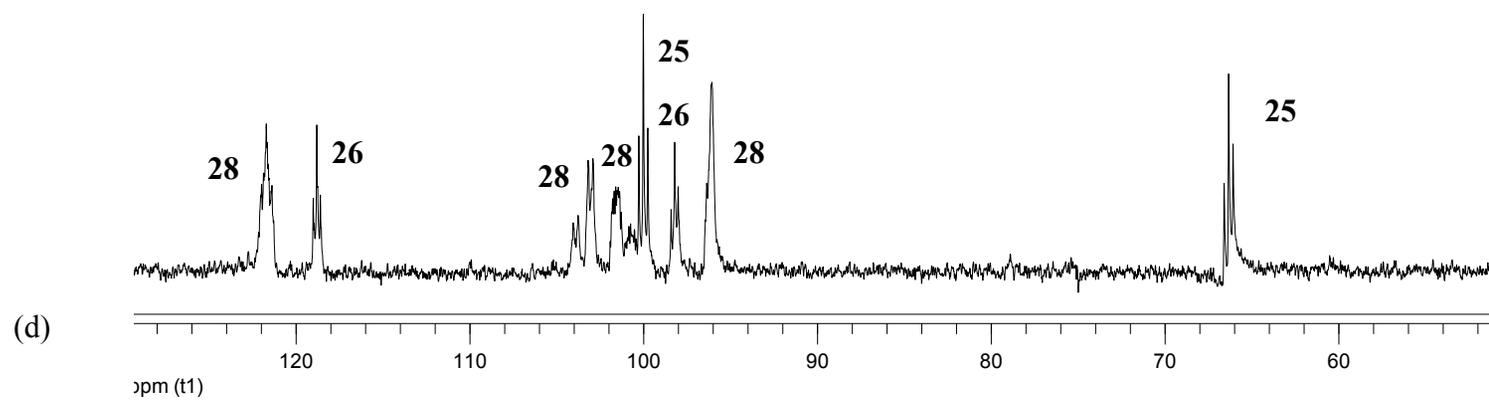
### Reaction of *cis-α*-[Fe(NCMe)<sub>2</sub>(rac-P4)](BF<sub>4</sub>)<sub>2</sub> (**25**) with H<sub>2</sub>

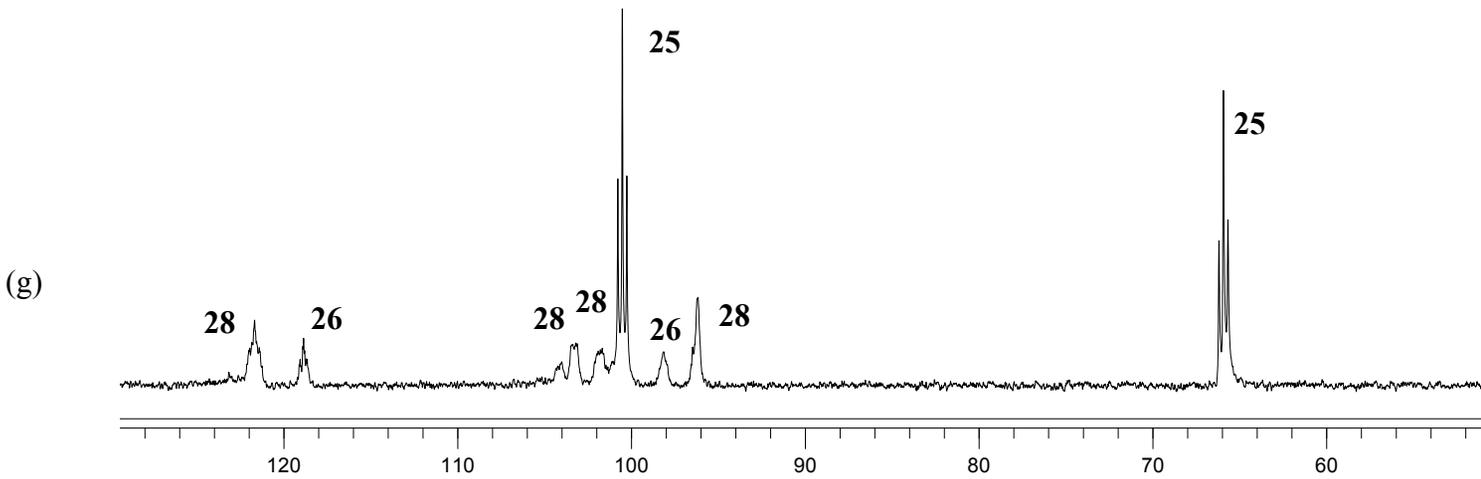
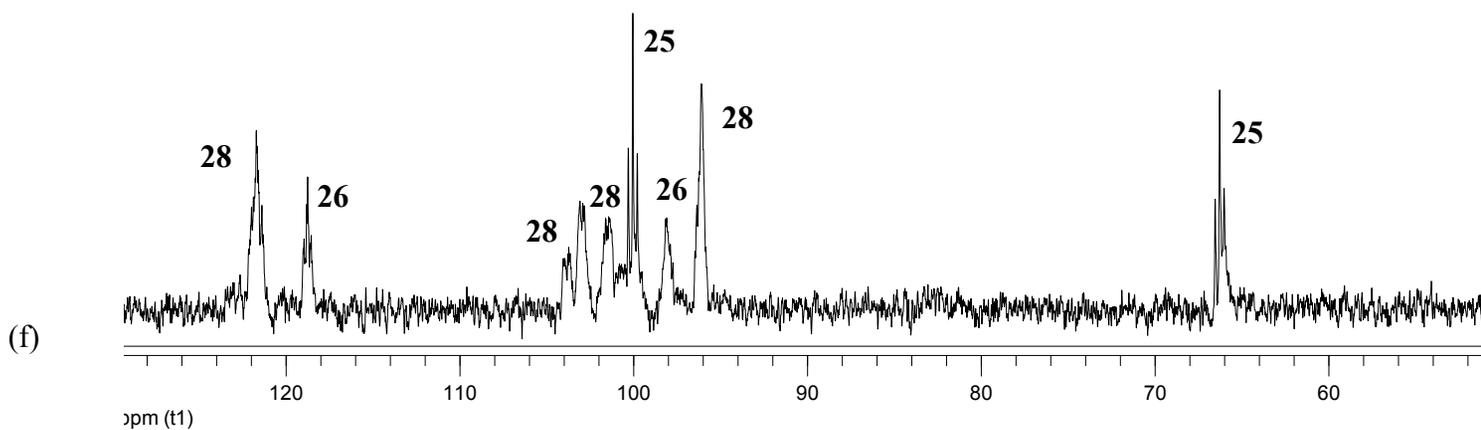
15.0 mg of *cis-α*-[Fe(NCMe)<sub>2</sub>(rac-P4)](BF<sub>4</sub>)<sub>2</sub> (**25**) were dissolved in CD<sub>3</sub>OD (2.5 mL) and the resulting solution was placed into a 10 mm HPNMR sapphire tube. The mixture was then pressurized with 30 bar H<sub>2</sub> and analyzed by multinuclear NMR at 293 K. The temperature was slowly increased to 353 K and the course of the reaction monitored by <sup>31</sup>P{<sup>1</sup>H} NMR and <sup>1</sup>H NMR. Finally, the mixture was cooled to 293 K.

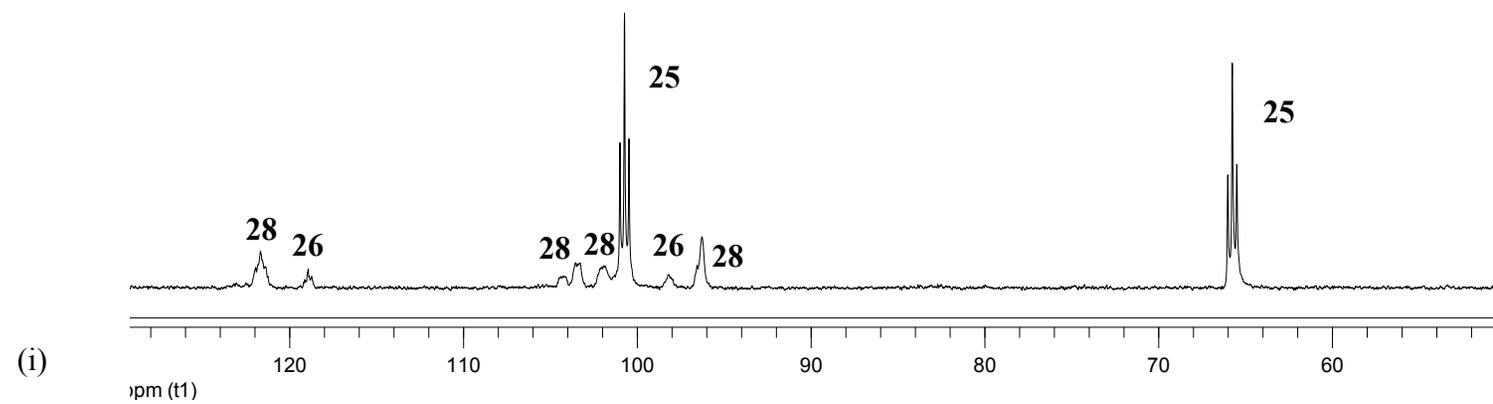
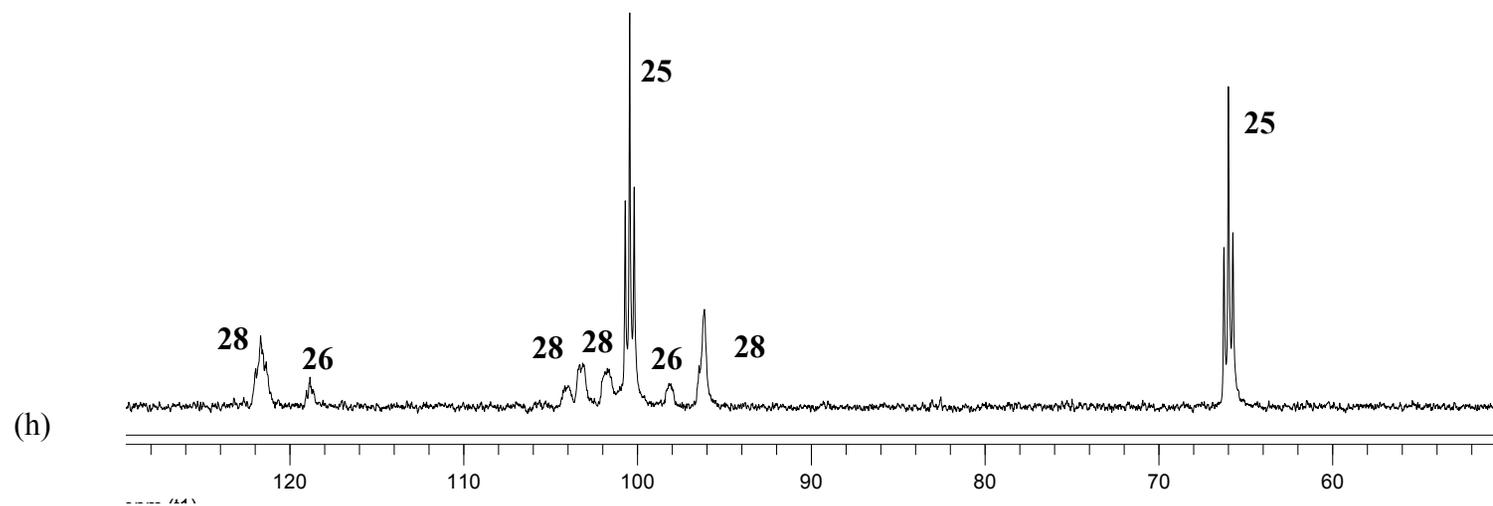
**Figure A6.** <sup>31</sup>P{<sup>1</sup>H} NMR spectra measured during the *in situ* reaction monitoring. (a) Complex **25** (15.0 mg) dissolved in CD<sub>3</sub>OD (2.5 mL) at 293 K. (b) Reaction mixture after pressurization with 30 bar H<sub>2</sub> at 293 K. (c) Reaction mixture heated to 313 K. (d) Reaction mixture heated to 333 K. (e) Reaction mixture heated to 353 K. (f) Reaction mixture cooled to 333 K. (g) Reaction mixture cooled to 293 K. (h) Reaction mixture after standing overnight at room temperature. (i) Reaction mixture after standing overnight at room temperature, analyzed at 273 K.



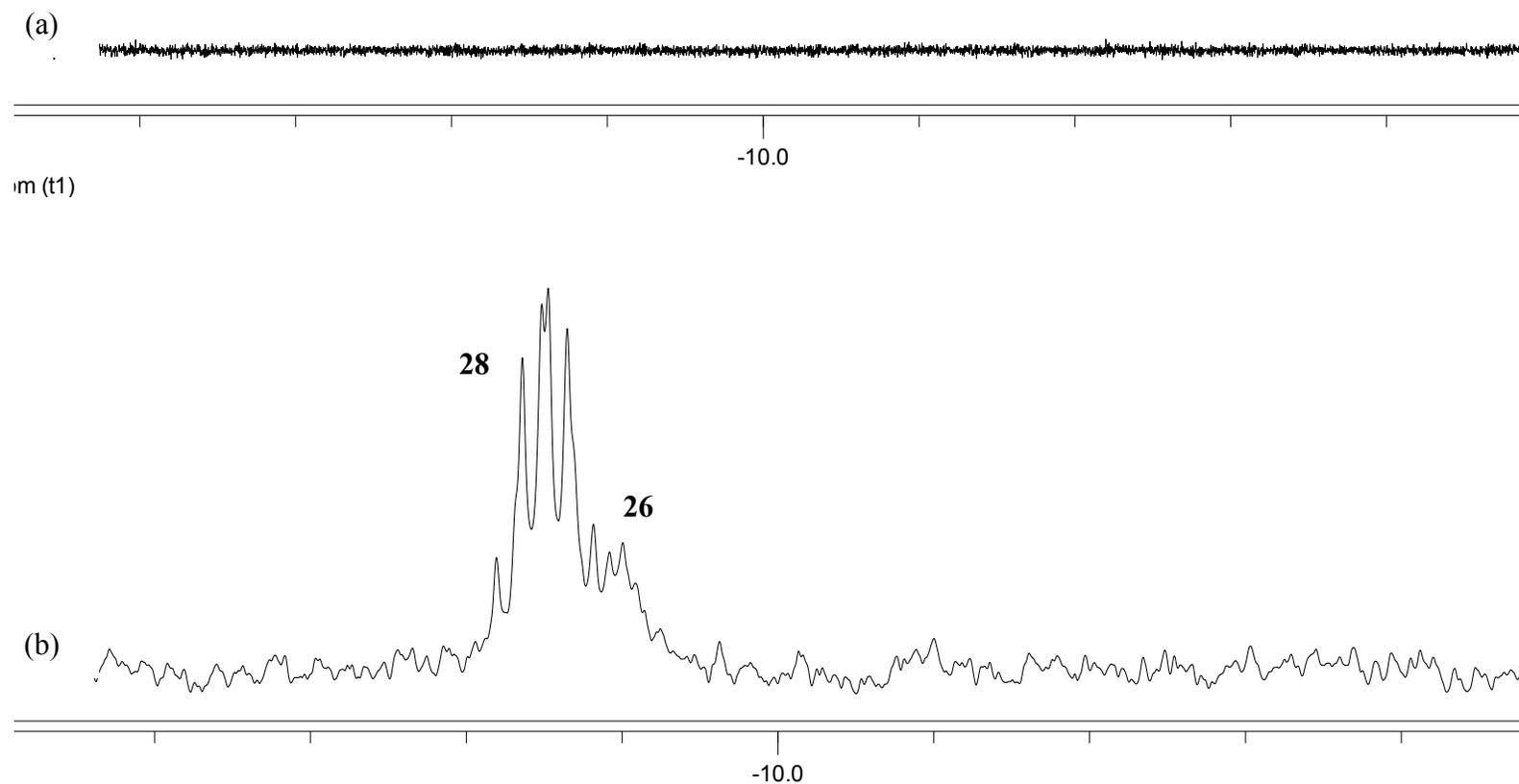


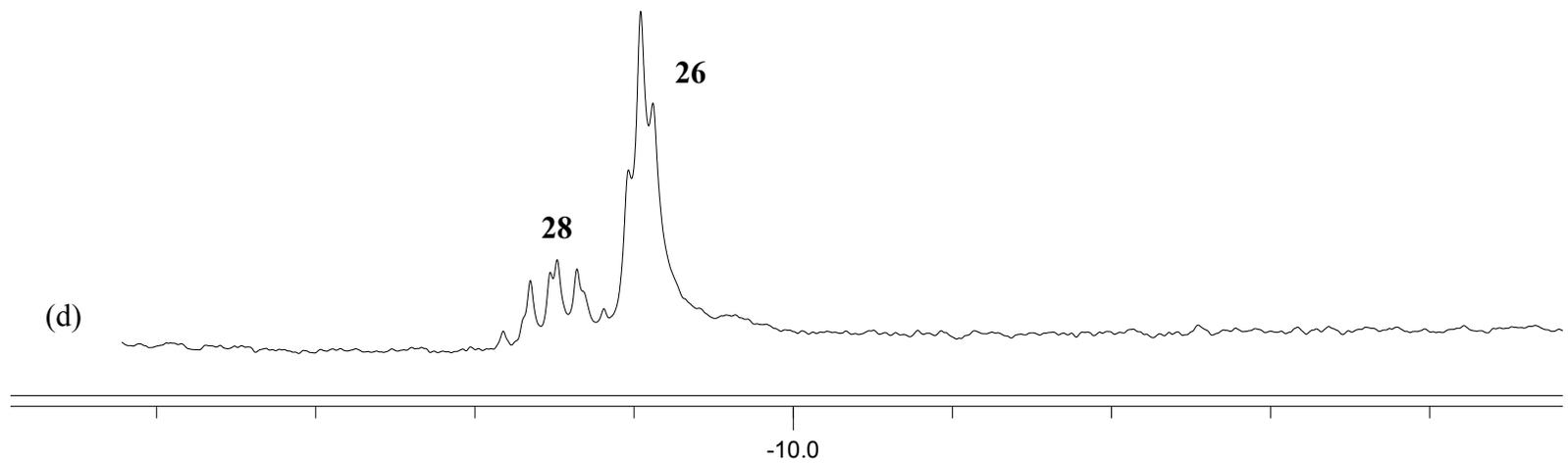
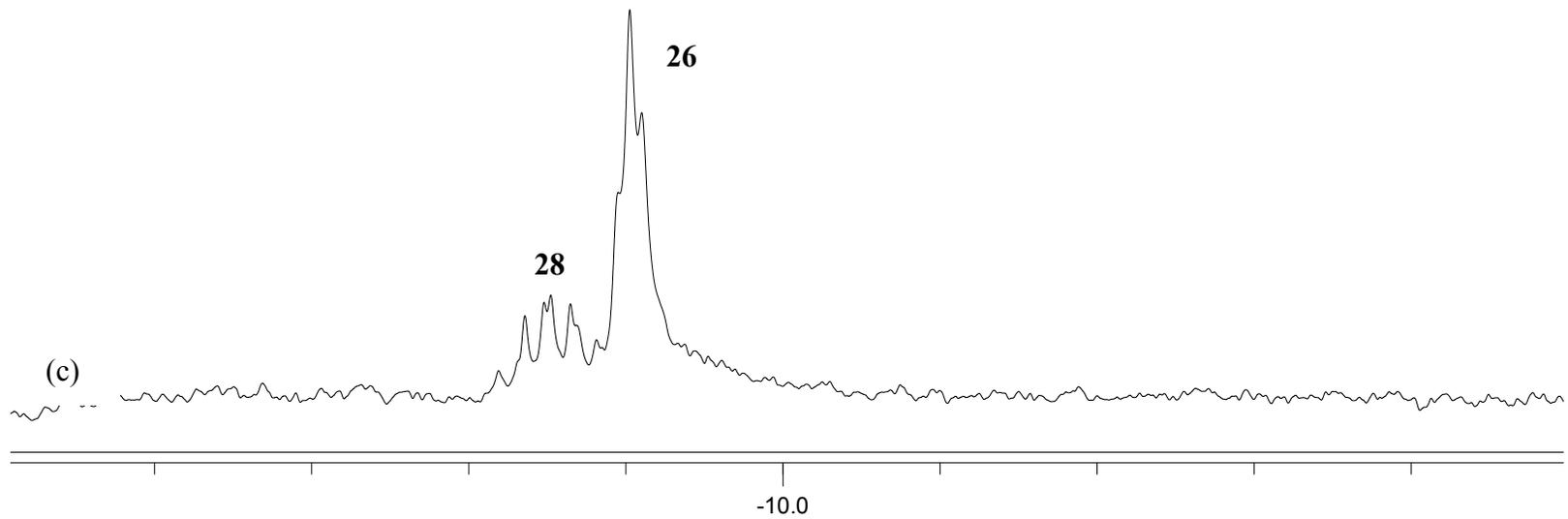


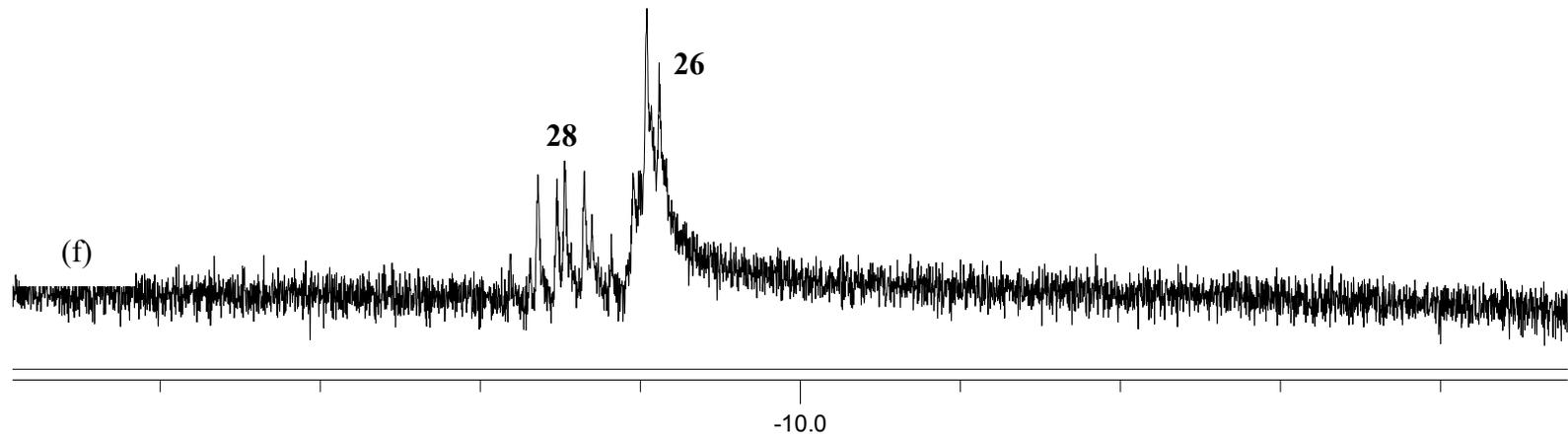
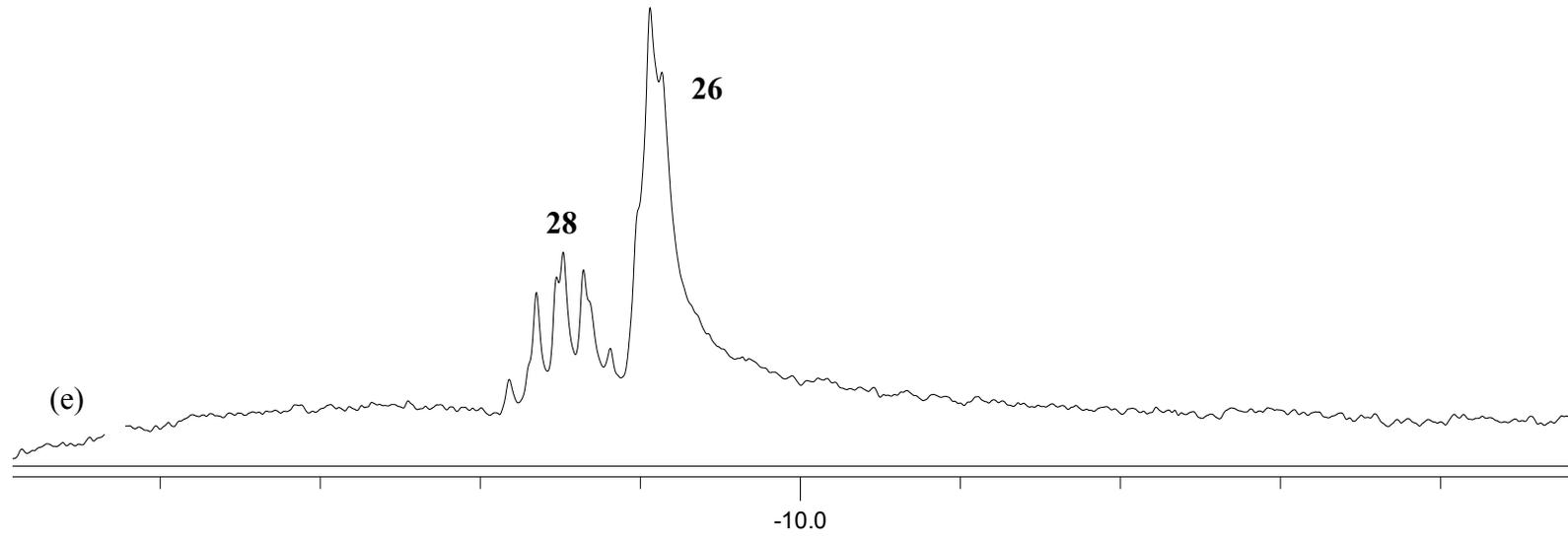


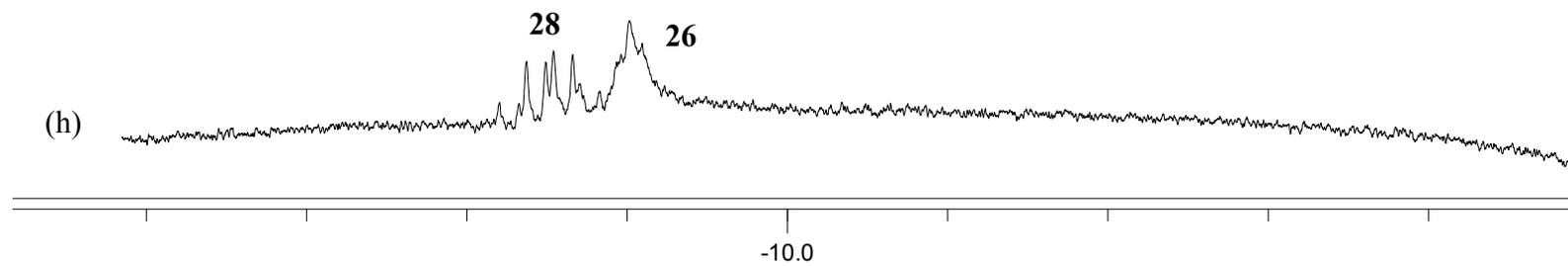
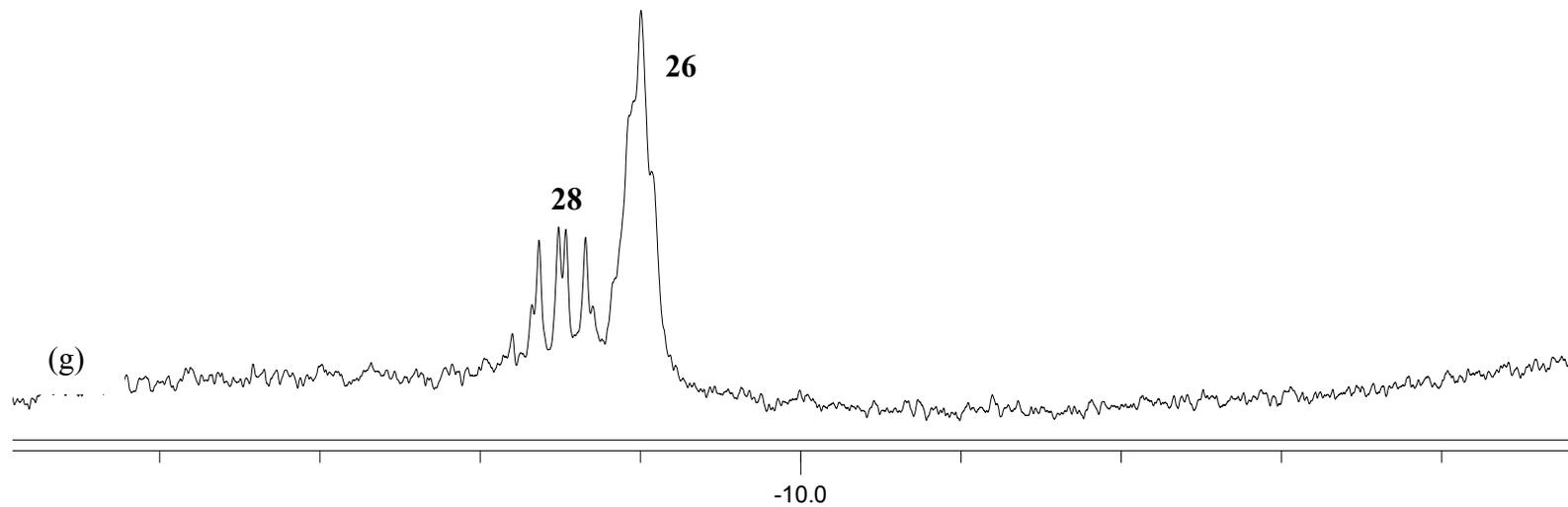


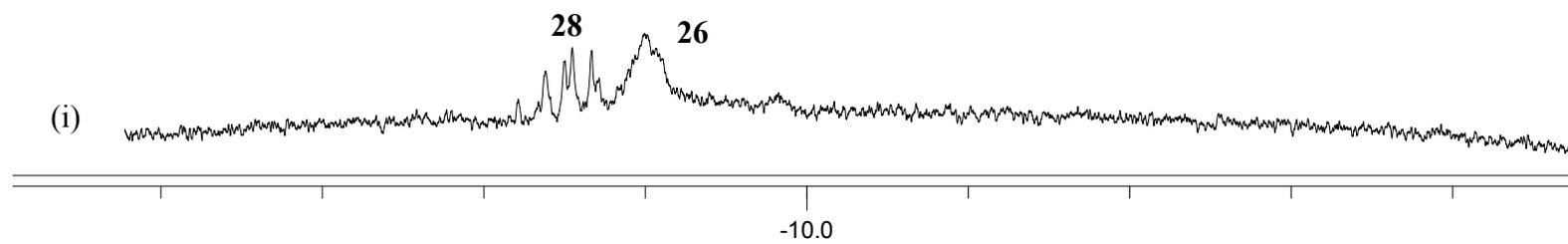
**Figure A7.**  $^1\text{H}$  NMR spectra (negative region only) measured during the *in situ* reaction monitoring. (a) Complex **25** (15.0 mg) dissolved in  $\text{CD}_3\text{OD}$  (2.5 mL) at 293 K. (b) Reaction mixture after pressurization with 30 bar  $\text{H}_2$  at 293 K. (c) Reaction mixture heated to 313 K. (d) Reaction mixture heated to 333 K. (e) Reaction mixture heated to 353 K. (f) Reaction mixture cooled to 333 K. (g) Reaction mixture cooled to 293 K. (h) Reaction mixture after standing overnight at room temperature. (i) Reaction mixture after standing overnight at room temperature, analyzed at 273 K.







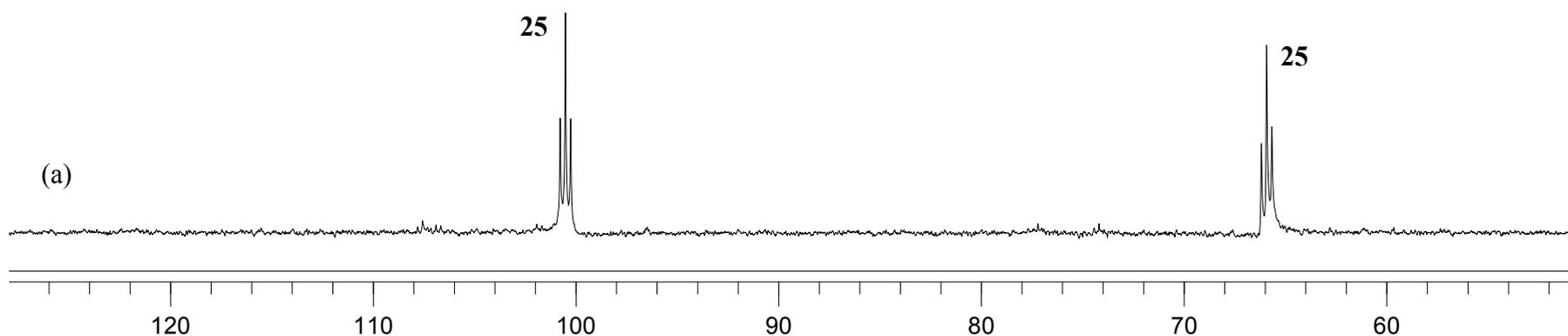


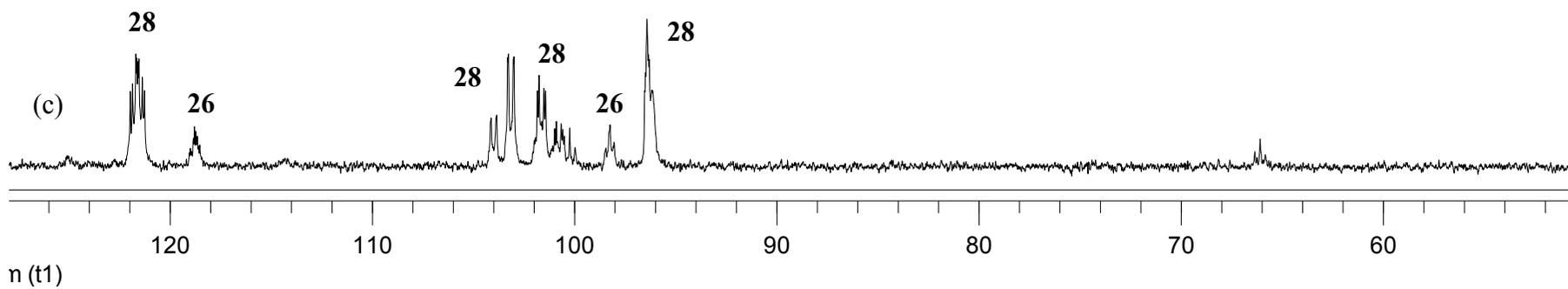
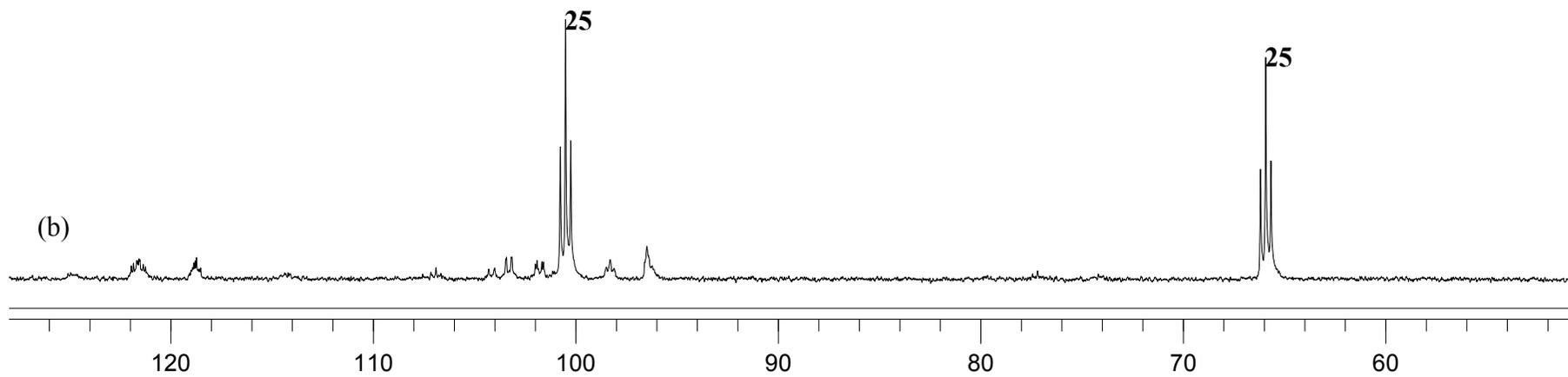


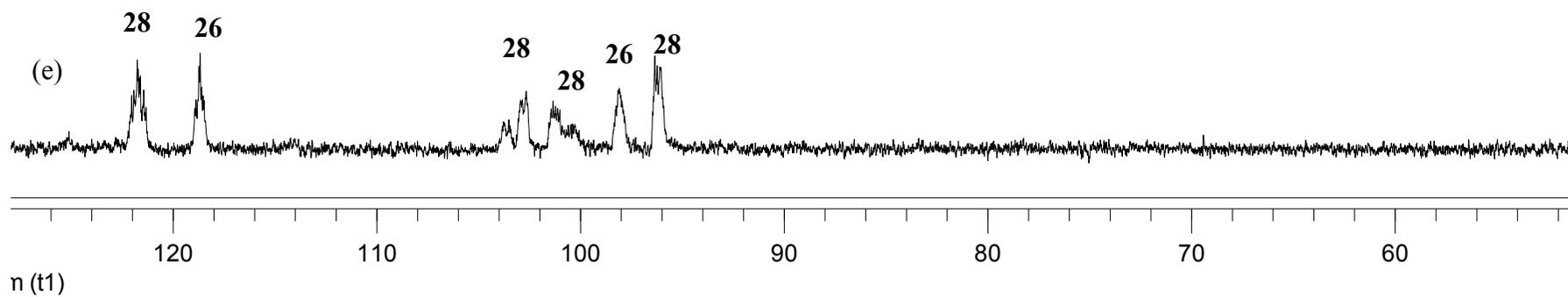
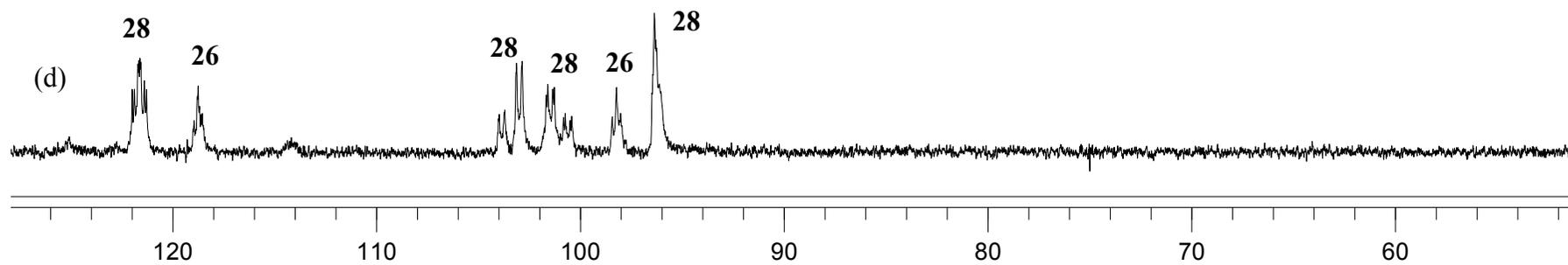
**Reaction of *cis-α*-[Fe(NCMe)<sub>2</sub>(*rac*-P4)](BF<sub>4</sub>)<sub>2</sub> (**25**) towards H<sub>2</sub> in the presence of NEt<sub>3</sub>**

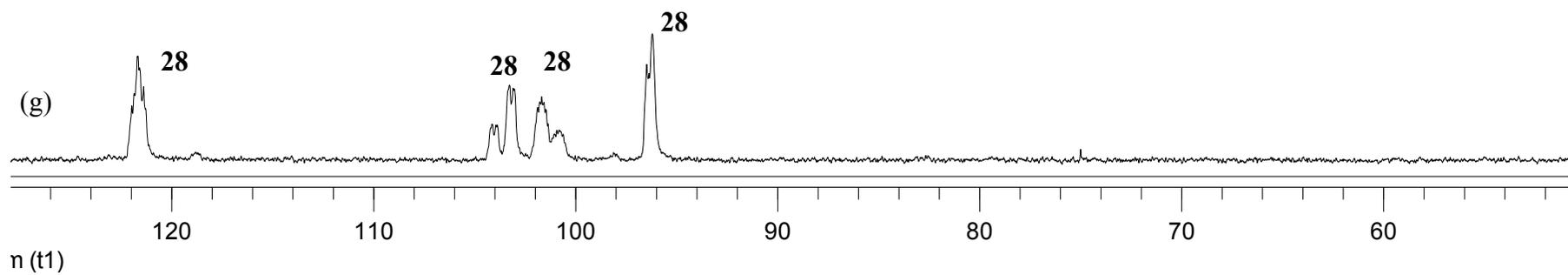
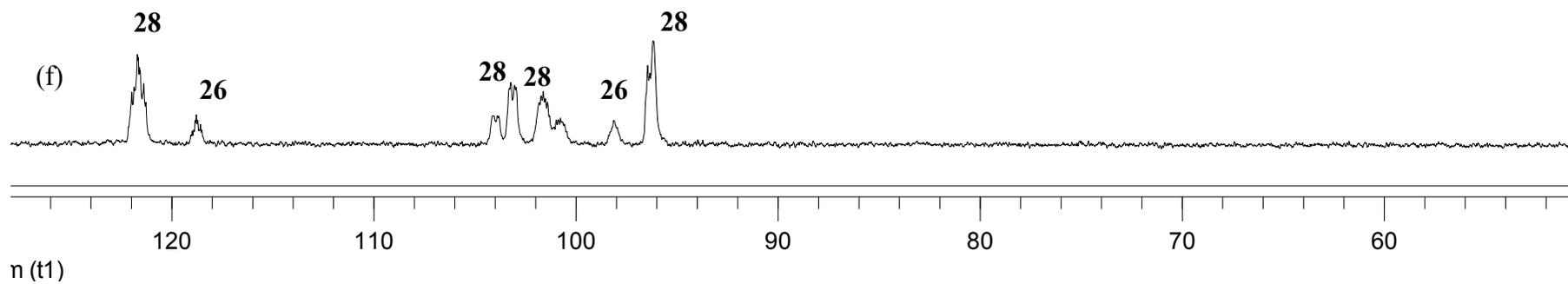
In the first part of the experiment, 15.0 mg of *cis-α*-[Fe(NCMe)<sub>2</sub>(*rac*-P4)](BF<sub>4</sub>)<sub>2</sub> (**25**) were dissolved in CD<sub>3</sub>OD (2.5 mL) and the resulting solution was placed into a 10 mm HPNMR sapphire tube. 20 μL of NEt<sub>3</sub> were added to the mixture. The mixture was then pressurized with 30 bar H<sub>2</sub> and analyzed by multinuclear NMR at 293 K. The temperature was slowly raised to 353 K and the course of the reaction monitored by <sup>31</sup>P{<sup>1</sup>H} and <sup>1</sup>H NMR. Finally, the mixture was cooled to 293 K. After overnight standing at 293 K, the variable temperature sequence was repeated as above and the reaction monitored by <sup>31</sup>P{<sup>1</sup>H} and <sup>1</sup>H NMR.

**Figure A8.** <sup>31</sup>P{<sup>1</sup>H} NMR spectra measured during the *in situ* reaction monitoring. (a) Complex **25** (15.0 mg) + NEt<sub>3</sub> (20 μl) dissolved in CD<sub>3</sub>OD (2.5 mL) at 293 K. (b) Reaction mixture after pressurization with 30 bar H<sub>2</sub> at 293 K. (c) Reaction mixture heated to 313 K. (d) Reaction mixture heated to 333 K. (e) Reaction mixture heated to 353 K for 1h. (f) Reaction mixture after standing overnight (17h) at room temperature. (g) Reaction mixture after further 3.5 h at 293 K.

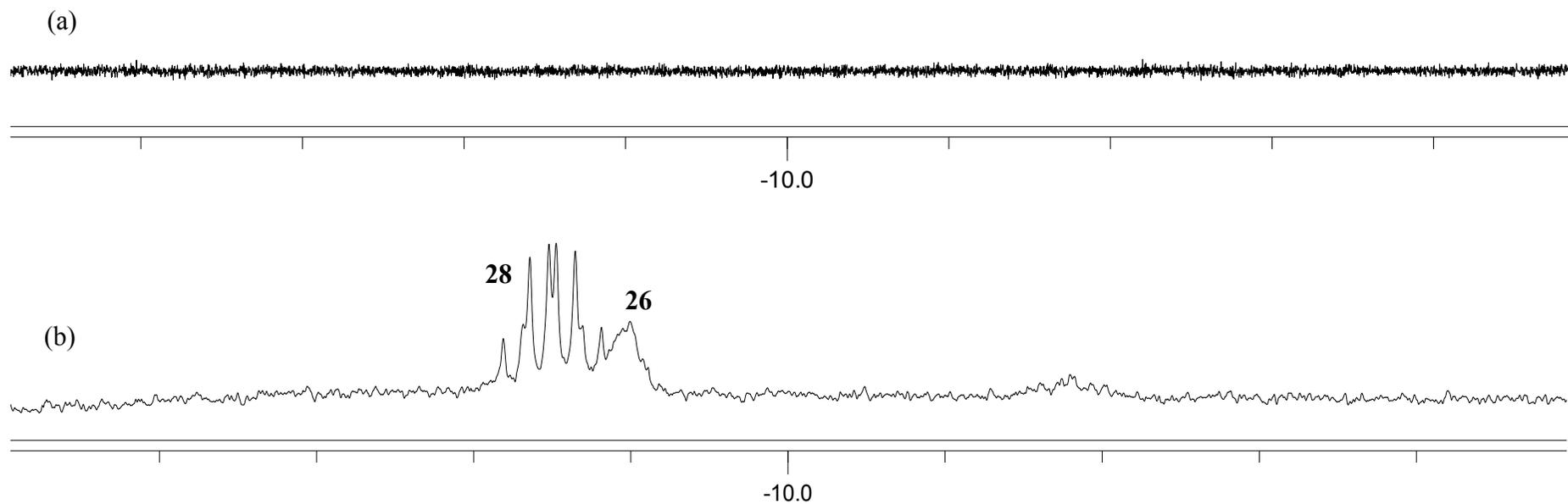


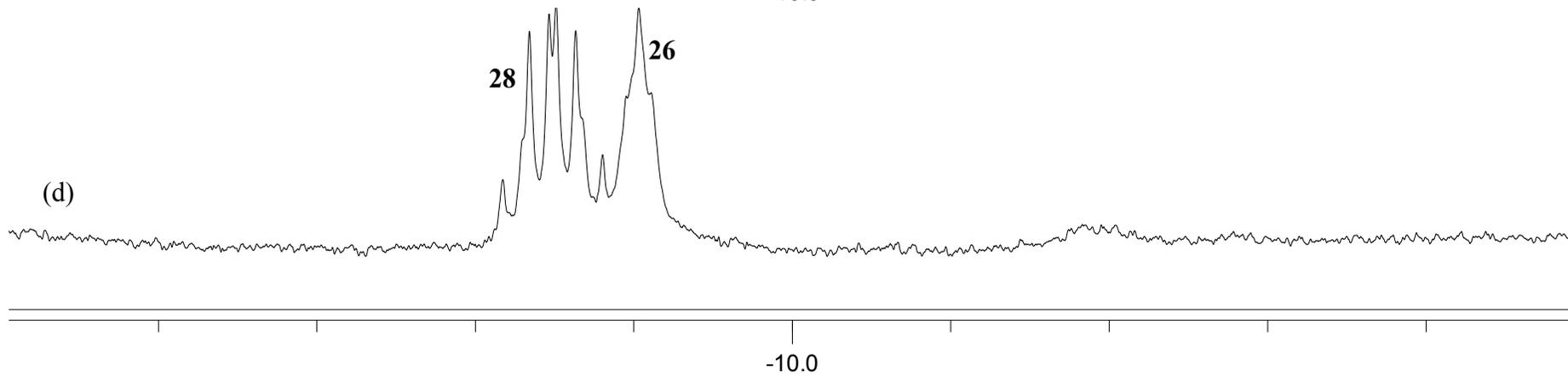
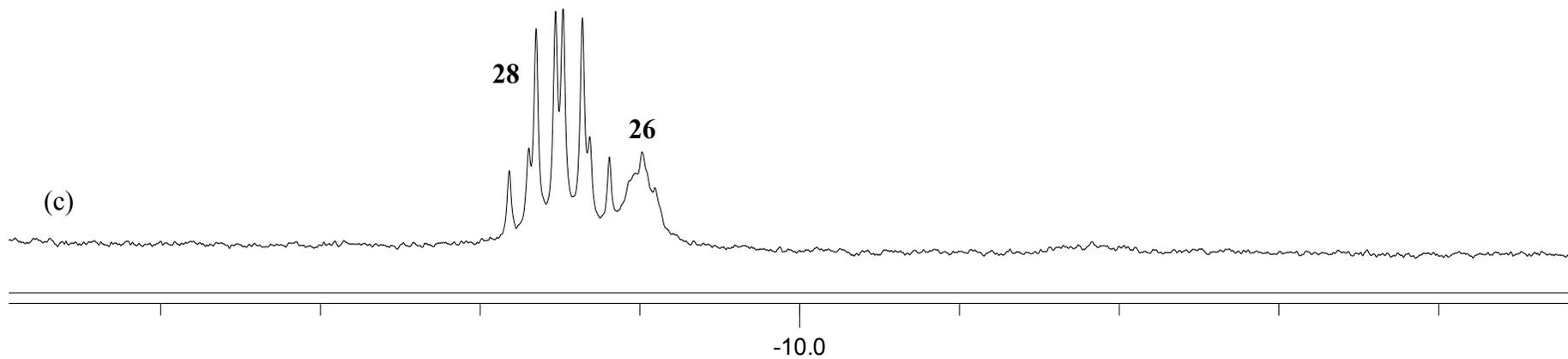


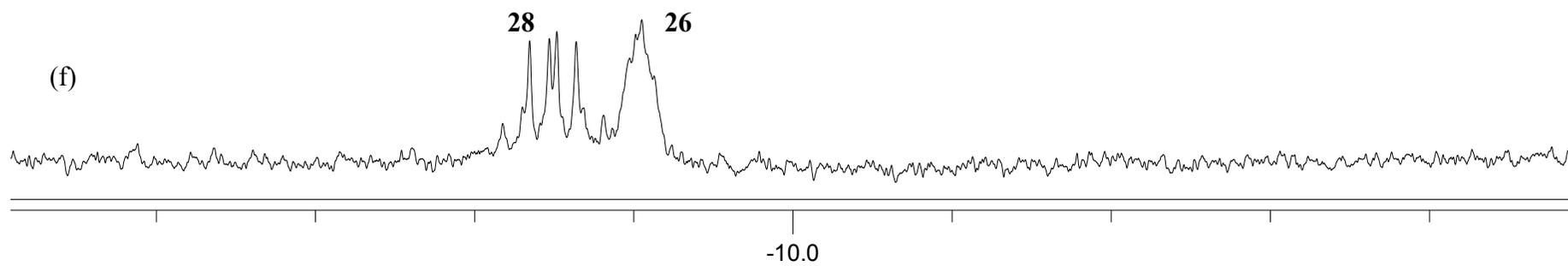
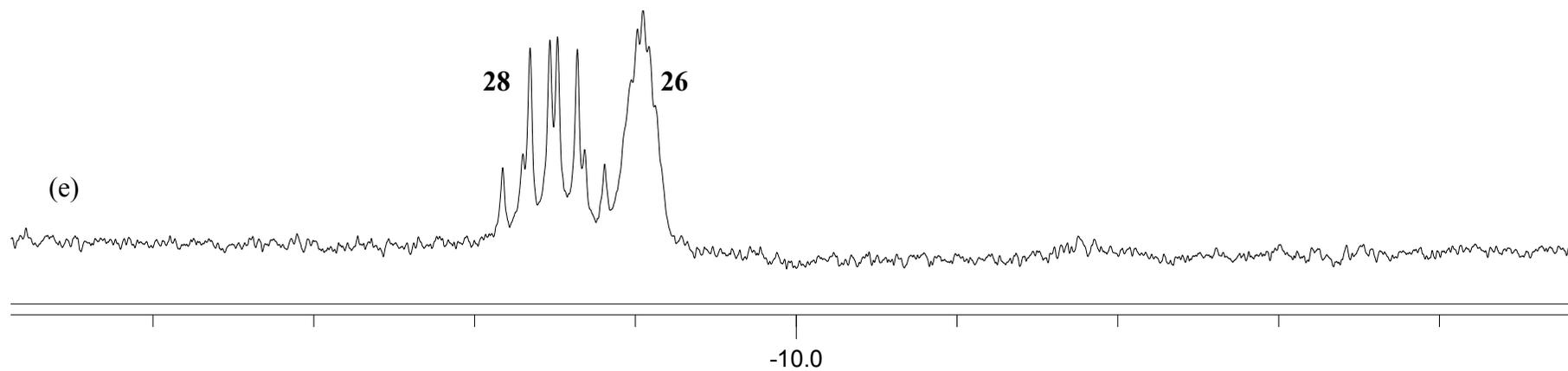


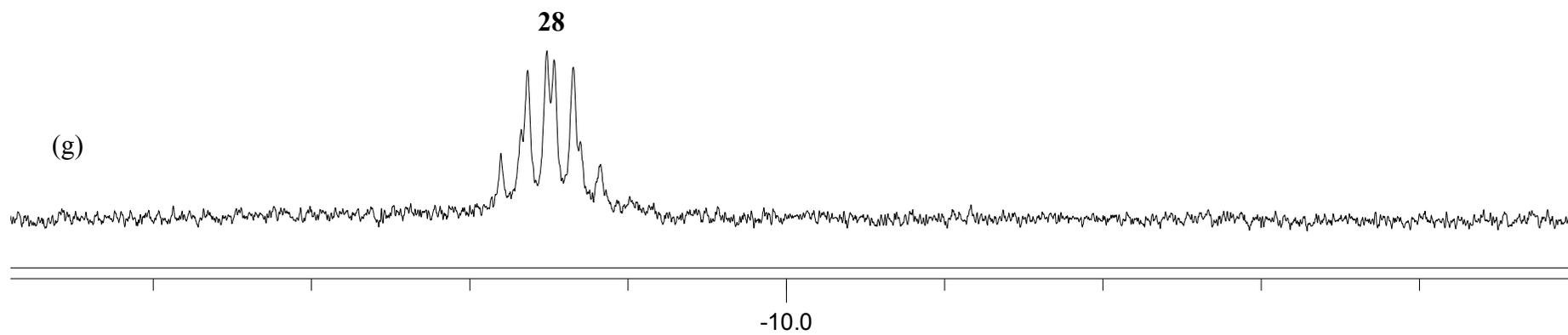


**Figure A9.**  $^1\text{H}$  NMR spectra measured during the *in situ* reaction monitoring. (a) Complex **2** (15.0 mg) +  $\text{NEt}_3$  (20  $\mu\text{l}$ ) dissolved in  $\text{CD}_3\text{OD}$  (2.5 mL) at 293 K. (b) Reaction mixture after pressurization with 30 bar  $\text{H}_2$  at 293 K. (c) Reaction mixture heated to 313 K. (d) Reaction mixture heated to 333 K. (e) Reaction mixture heated to 353 K for 1h. (f) Reaction mixture after standing overnight (17h) at room temperature. (g) Reaction mixture after further 3.5 h at 293 K.





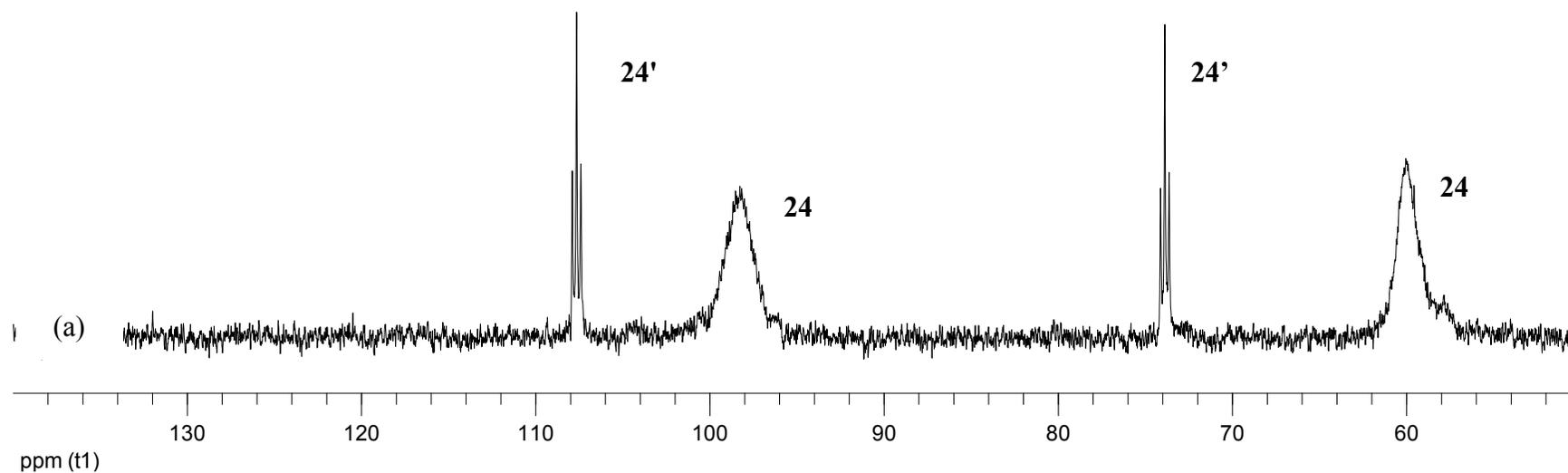


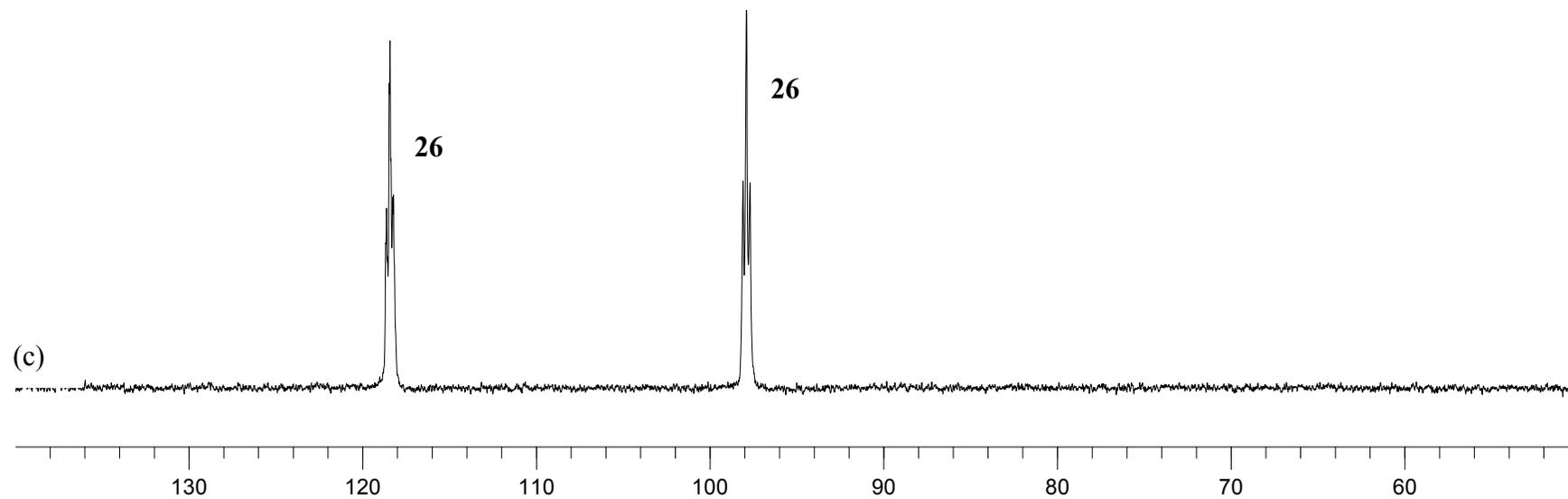
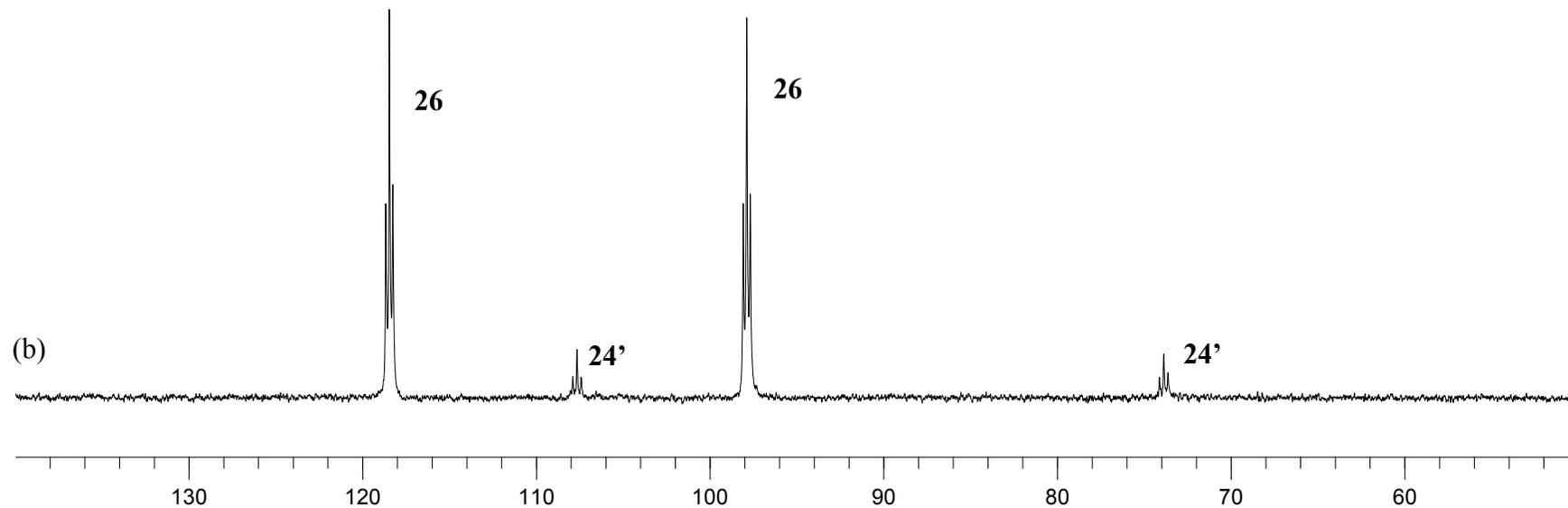


**Reaction of the complex formed *in situ* from the reaction of *rac*-P<sub>4</sub> and Fe(BF<sub>4</sub>)<sub>2</sub>·6H<sub>2</sub>O (**1**) with H<sub>2</sub>**

1.5 mL of a 0.01M solution of Fe( $\eta^1$ -FBF<sub>3</sub>)(*rac*-P<sub>4</sub>)](BF<sub>4</sub>) (**1**) in PC and 0.5 mL of CD<sub>3</sub>OD were placed in the HPNMR tube under Ar. The tube was pressurized with H<sub>2</sub> (30 bar), after which the formation of monohydride **3**·BF<sub>4</sub> was observed. The reaction was monitored by <sup>31</sup>P{<sup>1</sup>H} and <sup>1</sup>H NMR.

**Figure A10.** <sup>31</sup>P{<sup>1</sup>H} NMR spectra measured during the *in situ* reaction monitoring. (a) Complexes **1** and **1'** in PC + CD<sub>3</sub>OD. (b) Reaction mixture, after pressurization with 30 bar H<sub>2</sub> at 293 K. (c) Reaction mixture, after 1h at RT.

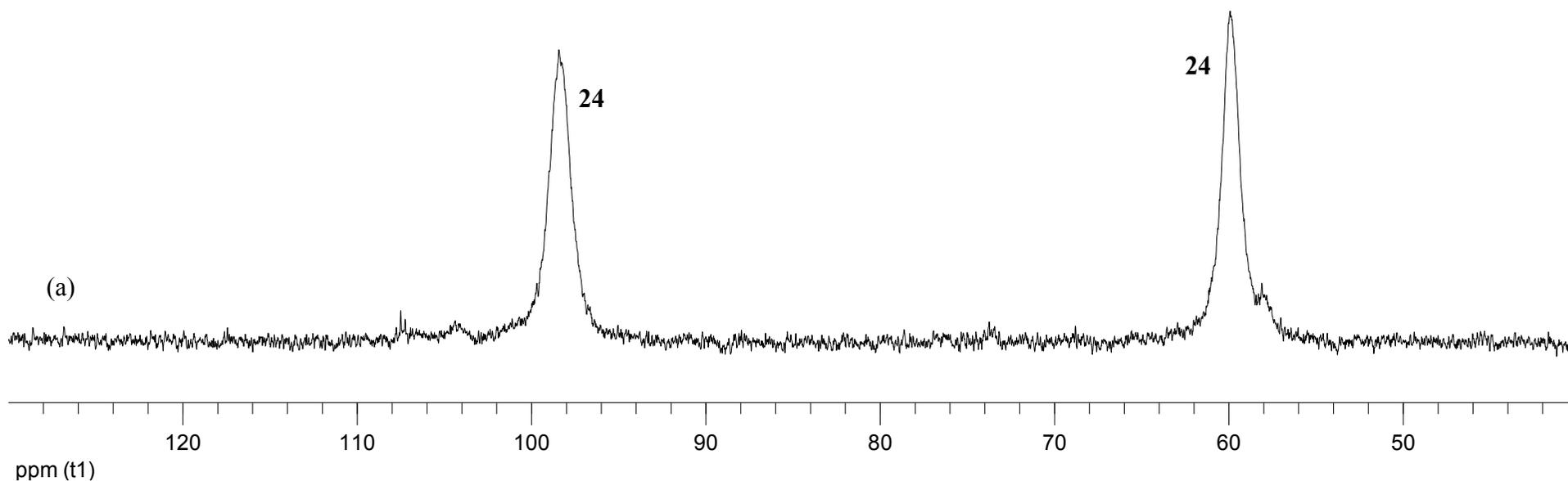


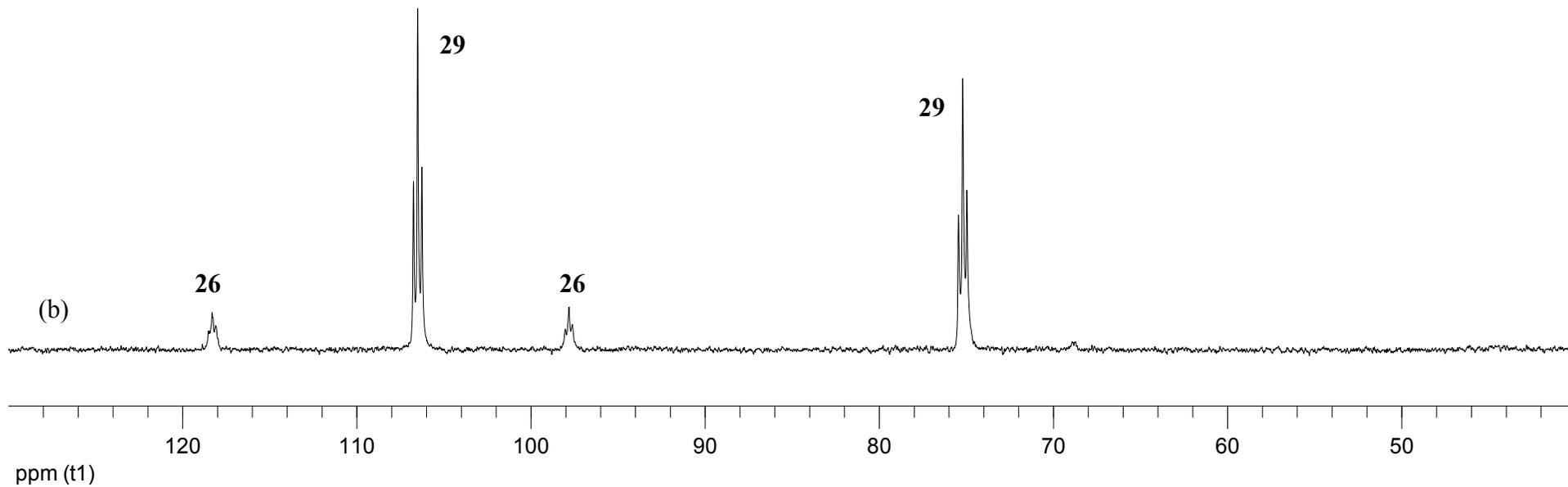


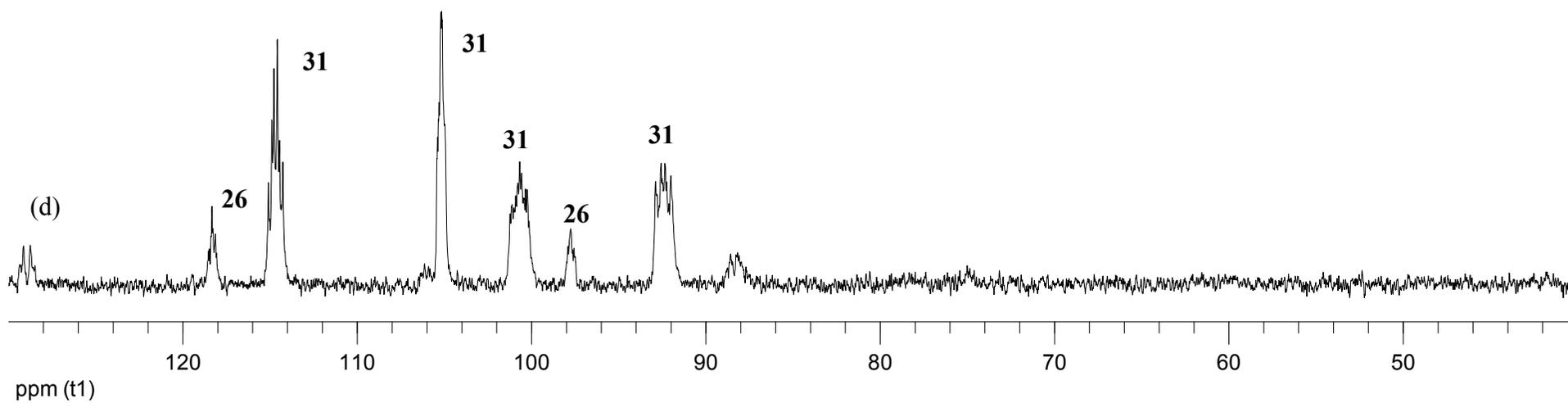
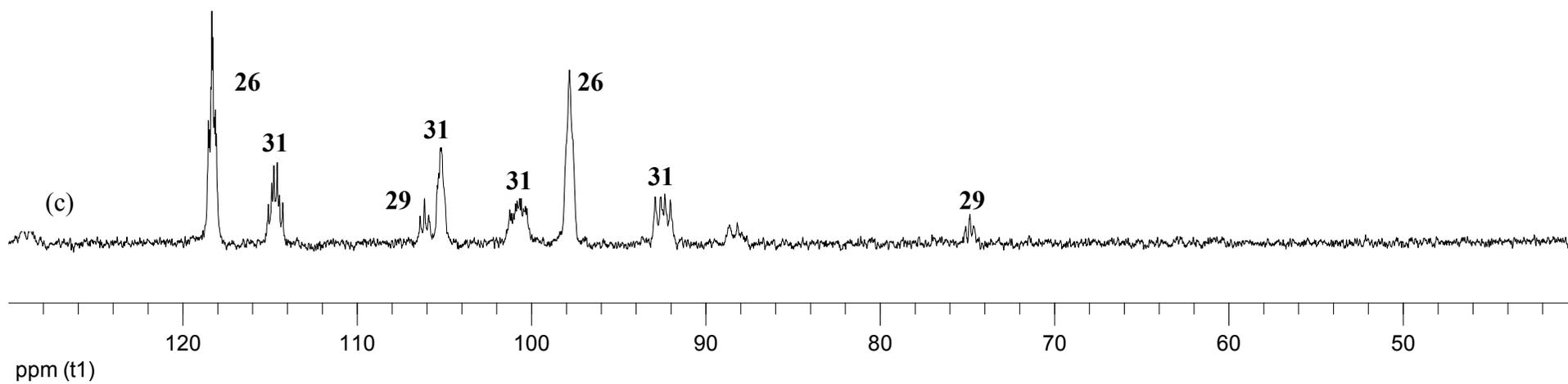
**FA dehydrogenation with the complex formed *in situ* from *rac*-P4 and Fe(BF<sub>4</sub>)<sub>2</sub> in PC (1)**

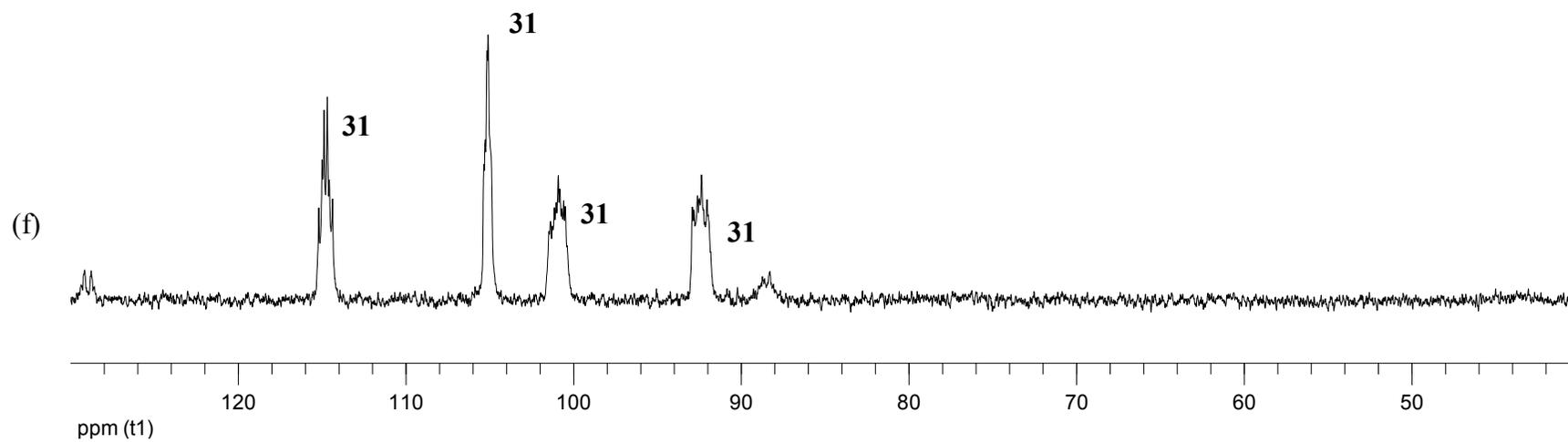
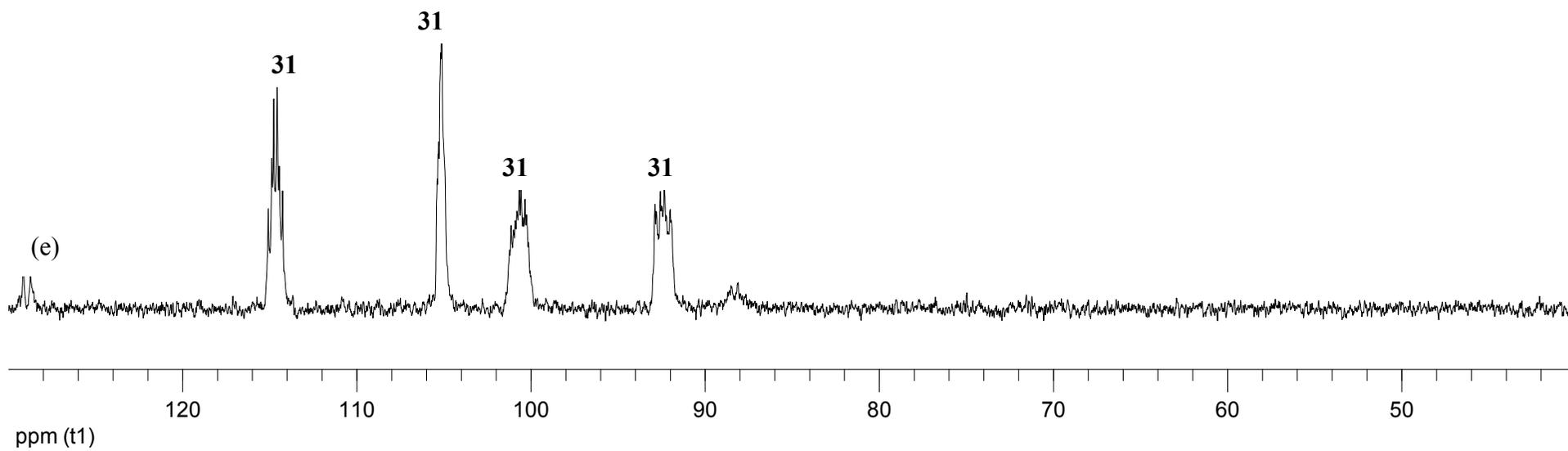
A 10mm HPNMR sapphire tube was charged with a solution of Fe(BF<sub>4</sub>)<sub>2</sub>·6H<sub>2</sub>O (14 mg; 0.0415 mmol) and *rac*-P4 (28 mg; 0.0415 mmol) in propylene carbonate (1.8 mL) under argon. CD<sub>3</sub>OD (0.4 mL) was added to the solution for deuterium lock, followed by HCOOH (4.15 mmol; 0.150 mL; 100 equiv.). The reaction mixture was gradually heated to 333 K and monitored by <sup>31</sup>P{<sup>1</sup>H} NMR.

**Figure A11.** <sup>31</sup>P{<sup>1</sup>H} NMR spectra measured during the *in situ* reaction monitoring. (a) Reaction mixture, immediately after the preparation of the sample, before addition of HCOOH, 293 K; (b) Reaction mixture, immediately after addition of 100 equivalents of HCOOH, 293 K; (c) Reaction mixture, after heating to 333 K; (d) Reaction mixture, after 1h at 333 K; (e) Reaction mixture, after 2h 30min at 333 K; (f) Reaction mixture, cooled to 293 K.









## X-ray crystal structure determinations

**X-Ray Structure Determination:** A summary of the crystal data are given in Table A1, A2 and A3. The data collection of **25** and **26**·BPh<sub>4</sub> was performed on an Oxford Diffraction Excalibur 3 diffractometer equipped with Mo-K $\alpha$  radiation at 150K and 100K respectively. Instead for **27**, **28** and **30'** an Oxford Diffraction Excalibur 3 diffractometer equipped with Cu-K $\alpha$  radiation was used. Data collections, data reductions and absorption corrections were performed with the program CrysAlisPRO<sup>1</sup>. The structure was solved using direct methods using Sir97<sup>2</sup> and refined on F<sup>2</sup> by full-matrix least squares techniques with SHELXL program<sup>3</sup>.

Generally all non-hydrogen atoms were refined anisotropically. The hydrogen atoms were included in calculated positions and refined riding on the respective Carbon atoms with isotropic displacement parameters. In **26**, **27** and **28** structures, the hydride atoms were located on Fourier maps. In structure **25**, one acetonitrile solvent molecule is disordered and the central Carbon atom sits on an inversion center, being almost impossible to distinguish between the contributions of the nitrogen and carbon atoms. In **26**·BPh<sub>4</sub>, a solvent molecule (probably Et<sub>2</sub>O or pentane) was disordered and its contribution was removed using the SQUEEZE procedure.<sup>4</sup> In **30'** the atoms of two methanol and a THF solvent molecules were refined isotropically. Also it was impossible to locate from Fourier maps the hydrogen atoms of the methanol molecules. Finally for **28** in the *rac*-P4 ligand one Phosphorus atom, one Carbon atom of an alkyl chain and four of six phenyl rings were found heavily disordered over two position with an occupancy factor between 52 to 61%. We tried to collect data with different crystals and using Mo-K $\alpha$  radiation but the results were similar with the refinement reported here. Also attempts to use larger unit cell with more than one complex in the asymmetric unit do not improve the overall quality of the refinement.

**Table A1. Crystal data and structure refinement for 25 and 26·BPh<sub>4</sub>.**

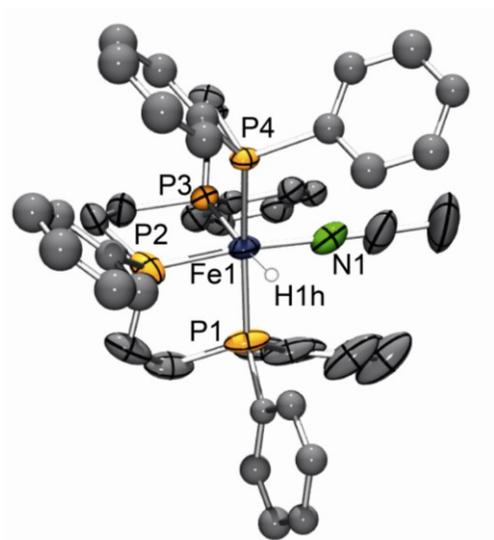
	<b>25</b>	<b>26·BPh<sub>4</sub></b>
Empirical formula	C103 H117 B4 F16 Fe2 N7 P8	C66 H63 B Fe P4
Formula weight	2159.73	1046.7
Temperature	150(2) K	100(2) K
Wavelength	0.71069 Å	0.71073 Å
Crystal system	Monoclinic	Triclinic
Space group	C 1 2/c 1	P -1
Unit cell dimensions	a = 33.6116(14) Å b = 14.8734(8) Å c = 20.7957(10) Å α = 90°. β = 105.833(4)°. γ = 90°.	a = 12.4918(6) Å b = 13.5351(7) Å c = 19.2058(9) Å α = 92.091(4)°. β = 105.612(4)°. γ = 94.273(4)°.
Volume	10001.7(8) Å <sup>3</sup>	3113.4(3) Å <sup>3</sup>
Z	4	2
Density (calculated)	1.434 Mg/m <sup>3</sup>	1.117 Mg/m <sup>3</sup>
Absorption coefficient	0.5 mm <sup>-1</sup>	0.381 mm <sup>-1</sup>
F(000)	4480	1100
Crystal size	0.3 x 0.2 x 0.18 mm <sup>3</sup>	0.2 x 0.18 x 0.1 mm <sup>3</sup>
Theta range for data collection	4.18 to 29.33°.	4.285 to 27.647°.
Index ranges	-46 ≤ h ≤ 22, -20 ≤ k ≤ 9, -27 ≤ l ≤ 27	-15 ≤ h ≤ 16, -17 ≤ k ≤ 17, -25 ≤ l ≤ 24
Reflections collected	21696	32826
Independent reflections	11442 [R(int) = 0.0427]	13325 [R(int) = 0.0536]
Completeness to theta	(25.242°) 99.5 %	(25.242°) 99.2 %
Absorption correction	Semi-empirical from equivalents	Semi-empirical from equivalents
Max. and min. transmission	1 and 0.5047	1 and 0.79474
Refinement method	Full-matrix least-squares on F <sup>2</sup>	Full-matrix least-squares on F <sup>2</sup>
Data / restraints / parameters	11442 / 0 / 613	13325 / 0 / 655
Goodness-of-fit on F <sup>2</sup>	1.018	1.028
Final R indices [I > 2σ(I)]	R1 = 0.0771, wR2 = 0.2042	R1 = 0.0551, wR2 = 0.1512
R indices (all data)	R1 = 0.1202, wR2 = 0.2393	R1 = 0.08, wR2 = 0.1659
Largest diff. peak and hole	1.868 and -0.639 e.Å <sup>-3</sup>	0.774 and -0.445 e.Å <sup>-3</sup>

**Table A2. Crystal data and structure refinement for 27 and 30'.**

	<b>27</b>	<b>30'</b>
Empirical formula	C42 H44 Fe P4	C144 H154 B2 Fe3 O13 P8
Formula weight	728.5	2529.59
Temperature	100(2) K	100(2) K
Wavelength	1.54184 Å	1.54184 Å
Crystal system	Triclinic	Triclinic
Space group	P -1	P -1
Unit cell dimensions	a = 11.3961(4) Å b = 11.8042(4) Å c = 14.9611(4) Å $\alpha$ = 88.014(2)° $\beta$ = 81.462(2)° $\gamma$ = 63.904(3)°	a = 14.7034(6) Å b = 15.3502(7) Å c = 30.5317(13) Å $\alpha$ = 81.607(4)° $\beta$ = 77.192(4)° $\gamma$ = 79.041(4)°
Volume	1786.33(11) Å <sup>3</sup>	6558.1(5) Å <sup>3</sup>
Z	2	2
Density (calculated)	1.354 Mg/m <sup>3</sup>	1.281 Mg/m <sup>3</sup>
Absorption coefficient	5.299 mm <sup>-1</sup>	4.029 mm <sup>-1</sup>
F(000)	764	2660
Crystal size	0.3 x 0.2 x 0.18 mm <sup>3</sup>	0.1 x 0.07 x 0.05 mm <sup>3</sup>
Theta range for data collection	4.173 to 72.255°.	4.33 to 62.007°.
Index ranges	-14<=h<=14, -14<=k<=14, -17<=l<=18	-13<=h<=16, -16<=k<=17, -34<=l<=34
Reflections collected	19769	41607
Independent reflections	6816 [R(int) = 0.0432]	20039 [R(int) = 0.1023]
Completeness to theta	(25.242°) 99.8 %	(67.684°) 84.4 %
Absorption correction	Semi-empirical from equivalents	Semi-empirical from equivalents
Max. and min. transmission	1 and 0.15503	1 and 0.53604
Refinement method	Full-matrix least-squares on F <sup>2</sup>	Full-matrix least-squares on F <sup>2</sup>
Data / restraints / parameters	6816 / 0 / 430	20039 / 6 / 1486
Goodness-of-fit on F <sup>2</sup>	0.976	0.988
Final R indices [I>2sigma(I)]	R1 = 0.0362, wR2 = 0.0882	R1 = 0.0938, wR2 = 0.2255
R indices (all data)	R1 = 0.0467, wR2 = 0.0985	R1 = 0.1915, wR2 = 0.286
Largest diff. peak and hole	0.371 and -0.59 e.Å <sup>-3</sup>	0.626 and -0.674e.Å <sup>-3</sup>

**Table A3. Crystal data and structure refinement for 28.**

<b>28</b>	
Empirical formula	C <sub>49</sub> H <sub>48</sub> B <sub>4</sub> Fe N <sub>4</sub> P <sub>4</sub>
Formula weight	917.42
Temperature	100(2) K
Wavelength	1.54184 Å
Crystal system	Triclinic
Space group	P -1
Unit cell dimensions	a = 11.6311(4) Å b = 12.2422(4) Å c = 18.0737(3) Å α = 104.224(3)° β = 98.681(3)° γ = 106.392(3)°
Volume	2325.11(13) Å <sup>3</sup>
Z	2
Density (calculated)	1.31 Mg/m <sup>3</sup>
Absorption coefficient	4.315 mm <sup>-1</sup>
F(000)	952
Crystal size	0.15 x 0.11 x 0.07 mm <sup>3</sup>
Theta range for data collection	4.285 to 72.276°
Index ranges	-11 ≤ h ≤ 14, -13 ≤ k ≤ 15, -22 ≤ l ≤ 21
Reflections collected	18456
Independent reflections	8857 [R(int) = 0.0428]
Completeness to theta	(67.684°) 99.7 %
Absorption correction	Semi-empirical from equivalents
Max. and min. transmission	1 and 0.30546
Refinement method	Full-matrix least-squares on F <sup>2</sup>
Data / restraints / parameters	8857 / 4 / 414
Goodness-of-fit on F <sup>2</sup>	1.081
Final R indices [I > 2σ(I)]	R1 = 0.1001, wR2 = 0.2711
R indices (all data)	R1 = 0.126, wR2 = 0.2987
Largest diff. peak and hole	1.324 and -0.763 e.Å <sup>-3</sup>

**Figure A12. X-ray crystal structure of 28.**

### 3. References

- <sup>1</sup> CrysAlisPro, Agilent Technologies, Version 1.171.36.28 (release 01-02-2013 CrysAlis171.NET)
- <sup>2</sup> Altomare, A.; Burla, M. C.; Camalli, M.; Casciarano, G. L.; Giacovazzo, C.; Guagliardi, A.; Moliterni, A. G. G.; Polidori, G.; Spagna, R., *J. Appl. Cryst.*, **1999**, *32*, 115-119.
- <sup>3</sup> Sheldrick, G. M., *Acta Cryst.* **2008**, *A64*, 112-122.
- <sup>4</sup> Spek, A. L. *J. Appl. Cryst.* **2003**, *36*, 7-13.



## **PERSONAL DETAILS**

### **IRENE MELLONE**

Date and Place of Birth: 11.08.1984, Firenze, Italy

Home Address: via A.F. Doni n° 4, Firenze, Italy

Telephone and Mobile: 055363528, +39.3398885960

Electronic Mail: irene.mellone@libero.com

irene.mellone@iccom.cnr.it

## **EDUCATION**

- Doctoral Candidate (Dottorato in Scienze Chimiche, Ciclo XXVII, a.a. 2014, University of Florence). Supervisors: Dr. Luca Gonsalvi, Dr. Luca Rosi.
- Masters Degree in Chemistry, at University of Florence in April 2011. Final mark: 110/110. Degree thesis on “Formic Acid Dehydrogenation catalyzed by Ru complexes” Supervisors: Dr. Luca Rosi, Dr. Luca Gonsalvi.
- Bachelors Degree in Technologies for the conservation and restoration of cultural heritages, at University of Florence in February 2008. Final mark: 110/110. Degree thesis on “Fluorinated Dispersions of Mg(OH)<sub>2</sub> Nanoparticles. Application on Archeological Wood” Supervisors: Prof. Piero Baglioni, Dr. Rodorico Giorgi.
- High school diploma, Maturità Scientifica at liceo Scientifico Leonardo da Vinci of Firenze. Final mark: 69/100.

## **EXPERIENCES**

2011: CNR Research Grant on “Hydrgen Production from renewable sources and release on demand via chemical storage (PIRODE), at Istituto di Chimica dei Composti OrganoMetallici (ICCOM-CNR) Supervisor: Dr. Luca Gonsalvi.

## TECHNICAL SKILLS

- Good knowledge of organometallic synthetic procedures; manipulation and purification of air-sensitive compounds.
- Purification of solvents and purification of compounds through distillation, sublimation, crystallization and column chromatography.
- Use of NMR (multinuclear, variable temperature), GC, GC-MS and IR instruments.
- Use of autoclaves for reactions under pressure of gas.

## FOREIGN LANGUAGES

- Good knowledge of oral and written English.
- Elementary knowledge of oral and written German.

## COMPUTER SKILLS

- Good knowledge of Windows 95/98/2000/XP (Excel, Word, Power Point, Outlook), ChemDraw (software of graphic chemistry), Beilstein Commander and SciFinder (bibliographical search), Internet.

## PUBLICATIONS

1. "Formic Acid Dehydrogenation Catalysed by Ruthenium Complexes bearing the Tripodal Ligands Triphos and NP<sub>3</sub>" I. Mellone, M. Peruzzini, L. Rosi, D. Mellmann, H. Junge, M. Beller, L. Gonsalvi, *Dalton Trans.*, **2013**, 42, 2495.
2. "Inner vs Outer-sphere Ru-catalyzed Formic Acid Dehydrogenation: A Computational Study" G. Manca, I. Mellone, F. Bertini, M. Peruzzini, L. Rosi, D. Mellmann, H. Junge, M. Beller, A. Ienco, L. Gonsalvi, *Organometallics* **2013**, 32, 7053–7064.
3. "Iron(II) Complexes of the Linear rac-tetraphos-1 Ligand as Homogeneous Catalysts for Sodium Bicarbonate Hydrogenation and Formic Acid

Dehydrogenation” F. Bertini, I. Mellone, A. Ienco, M. Peruzzini, L. Gonsalvi, *ACS Catal.* **2014**, under revision.

4. L. Gonsalvi, F. Bertini, A. Guerriero, I. Mellone, Chapter 14 in W.-Y. Wong (Ed.), *Organometallics and Related Molecules for Energy Conversion, Green Chemistry and Sustainable Technology Series*, Springer Heidelberg (1st Edition), expected end 2014.

**In preparation:**

1. “Hydrogen Storage and Release by HCOOH Dehydrogenation and NaHCO<sub>3</sub> Hydrogenation Catalyzed by Ru(II) Complexes Bearing Bulky Polydentate Phosphines” I. Mellone, D. Mellmann, F. Bertini, R. J. Gilbert-Wilson, L. D. Field, H. Junge, M. Beller, M. Peruzzini, L. Gonsalvi.

**ORAL COMMUNICATIONS - Personally presented**

Mellone, I.; Mellmann, D.; Bertini, F.; Gilbert-Wilson, R.J.; Field, L.D.; Junge, H.; Beller, M.; Peruzzini, M.; Gonsalvi, L. “Hydrogen Storage and Release by HCOOH Dehydrogenation and NaHCO<sub>3</sub> Hydrogenation Catalyzed by Ru(II) Complexes Bearing Bulky Polydentate Phosphines” IGCS-2. Second International Green Symposium & Advanced School on Green Chemistry, Rennes, France, 02-04 April 2014.

**POSTER PRESENTATIONS**

- 8th International School of Organometallic Chemistry , Camerino (MC), 27-31 Agosto 2011. “Selective Formic Acid Dehydrogenation catalyzed by Ru Complexes” Mellone, I.; Rosi, L.; Gonsalvi, L.; Peruzzini, M.
- X Congresso del Gruppo Interdivisionale di Chimica Organometallica della Società Chimica Italiana, Padova, 5-8 Giugno 2012. “Selective Formic Acid Dehydrogenation catalyzed by Ru Complexes bearing Multidentate Ligands” Mellone, I.; Rosi, L.; Peruzzini, M.; Gonsalvi, L.

- XVIII Congresso Nazionale della Divisione di Chimica Industriale della Società Chimica Italiana, Firenze, 11-14 Giugno 2012. “Selective Formic Acid Dehydrogenation catalyzed by Ru Complexes bearing Multidentate Ligands” Mellone, I.; Rosi, L.; Peruzzini, M.; Gonsalvi, L.
- XL Congresso Nazionale della Divisione di Chimica Inorganica della Società Chimica Italiana, Sestri Levante (GE), 9-13 Settembre 2012. “Selective Formic Acid Dehydrogenation catalyzed by Ru Complexes bearing Multidentate Ligands” Mellone, I.; Rosi, L.; Peruzzini, M.; Gonsalvi, L.
- XLI Congresso Nazionale della Divisione di Chimica Inorganica della Società Chimica Italiana, Parma, 3-6 Settembre 2013. “A Combined VT-NMR and DFT Computational Studies on Ru-catalyzed Formic Acid Dehydrogenation” Mellone, I.; Manca, G.; Ienco, A.; Peruzzini, M.; Rosi, L.; Mellmann, D.; Junge, H.; Beller, M.; Gonsalvi, L.
- IGCS-2. Second International Green Symposium & Advanced School on Green Chemistry, Rennes, France, 02-04 April 2014. “Hydrogen Storage and Release by HCOOH Dehydrogenation and NaHCO<sub>3</sub> Hydrogenation Catalyzed by Ru(II) Complexes Bearing Bulky Polydentate Phosphines” Mellone, I.; Mellmann, D.; Bertini, F.; Gilbert-Wilson, R.J.; Field, L.D.; Junge, H.; Beller, M.; Peruzzini, M.; Gonsalvi, L.
- ICPC-2014 - 20th International Conference on Phosphorus Chemistry, Dublin, Ireland, 28 June - 2 July 2014. “Hydrogen Storage and Release by NaHCO<sub>3</sub> Hydrogenation and HCOOH Dehydrogenation Catalyzed by Fe(II) Complexes of the Linear Tetrachos-1 Ligand” Bertini, F.; Mellone, I.; Ienco, A.; Peruzzini, M.; Gonsalvi, L.
- CO<sub>2</sub>-FORUM, Large Volume CO<sub>2</sub> Utilization : Enabling Technologies for Energy and Resource Efficiency, Lyon, France, 25-26 September 2014. “Efficient NaHCO<sub>3</sub> Hydrogenation and HCOOH Dehydrogenation Catalyzed by Fe(II) Complexes Stabilized by a Linear Tetrachosphine Ligand” Gonsalvi, L.; Bertini, F.; Mellone, I.; Ienco, A.; Peruzzini, M.

## **OTHER**

### **Active participation in the projects:**

- CNR per il Mezzogiorno “EFOR – Energia da Fonti Rinnovabili” (2011-2015);
- PRIN 2009 “Nuove strategie per il controllo di reazioni metallo assistite: interazioni non convenzionali di frammenti molecolari” (2010-2012);
- COST Action CM1205 CARISMA “Catalytic Routines for Small Molecule Activation” (2013-2017);
- “FIRENZE HYDROLAB2 - Programma di ricerca avanzata per la produzione, immagazzinamento ed utilizzazione dell'idrogeno come vettore energetico” (progetto motu proprio dell'Ente Cassa di Risparmio di Firenze, 2010-2014).